

CHARACTERIZATION AND MODELING OF ACTIVE METAL-MATRIX COMPOSITES WITH EMBEDDED SHAPE MEMORY ALLOYS

DISSERTATION

Presented in Partial Fulfillment of the Requirements for the Degree Doctor of
Philosophy in the Graduate School of The Ohio State University

By

Ryan M. Hahnlen, B.S., M.S.

Graduate Program in Mechanical Engineering

The Ohio State University

2012

Dissertation Committee:

Professor Marcelo J. Dapino, Advisor

Professor Sudarsanam Suresh Babu

Professor Manoj Srinivasan

Professor Mark E. Walter

© Copyright by
Ryan M. Hahnen
2012

ABSTRACT

Shape Memory Alloys (SMAs) can recover up to 6% of induced strain, undergo an increase in elastic modulus of over 100%, and generate large levels of stress through a temperature and stress-dependent transformation between their martensite and austenite phases. In this research, SMAs are embedded within an aluminum matrix through Ultrasonic Additive Manufacturing (UAM), a rapid prototyping process. Being a low temperature process, UAM enables the construction of metal-matrix composites with embedded thermally sensitive materials such as SMAs. Six composites were constructed by embedding NiTi ribbons within an Al 3003-H18 matrix with fiber volume fractions of up to 20% and various levels of NiTi prestrain. The resulting composites are the subject of modeling and experimental characterization.

A model is developed which describes the response to thermomechanical loading of an SMA composite with arbitrary fiber volume fractions and prestrain levels. The model is based on a new bivariant SMA formulation which has a continuous kinetic law through the mixed stress and temperature-induced transformation region of the phase diagram. This model is used to analyze experimental data and aid in the design of NiTi-Al UAM composites.

The experimental characterization of the composites has the primary focus of (i) controlling thermally-induced strain, (ii) tuning the response of the composites to static and dynamic mechanical loads via temperature changes, and (iii) characterization of the NiTi-Al interface. Through analysis of the thermally-induced strain responses of the composites, two key parameters for controlling the Coefficient of Thermal Expansion (CTE) were identified: NiTi fiber volume fraction and prestrain of the embedded NiTi. Using a 15.2% fiber

volume fraction of fully detwinned NiTi ribbons, a minimum CTE of $7.6 \mu\epsilon/^\circ\text{C}$ is obtained compared to $23.2 \mu\epsilon/^\circ\text{C}$ for Al 3003.

The change in static stiffness, natural frequency, and damping ratio of composites 1-4 were observed as a function of temperature. These composites exhibit a maximum increase in static stiffness of 10.0% at 100°C due to the increased modulus of the austenitic phase. Dynamic behavior was observed for clamped-free and clamped-clamped boundary conditions. The inclusion of NiTi mitigated the decrease in natural frequency associated with the decreasing Al modulus at elevated temperatures under the clamped-free boundary condition. Under the clamped-clamped boundary condition, the maximum change in natural frequency is +25.0% due to the blocking stress generated by the NiTi ribbons. In both boundary conditions, the composites exhibit a damping ratio similar to that of solid Al.

The NiTi-Al interface was characterized through scanning electron microscopy and differential scanning calorimetry. These methods were used to investigate the possibility of metallurgical bonding between the ribbon and matrix and determine interface shear strength. The investigation indicates that the interface is dominated by friction and has a shear strength of 7.36 MPa.

This research provides three primary contributions. The first is a new model that can guide the design of SMA composites using only material and composite properties. The second contribution is the development and construction of SMA metal-matrix composites at low temperatures with variable thermally-induced strain and tunable static and dynamic properties. The third contribution is the experimental characterization of the unique thermally-dependent behaviors and analysis of the SMA-matrix interface.

To my wife, Marie.

ACKNOWLEDGMENTS

I would not have been able to complete this work without the support of many other individuals. First, I would like to express my gratitude to my advisor, Professor Marcelo Dapino, for giving me the opportunity to work on this project. In addition to his technical help and encouragement, I am also appreciative of the opportunities he provided to present the research we have done through publications and conferences. I am very grateful for the technical and professional growth I have received while under Professor Dapino's guidance. I also want to thank my committee, Professors Suresh Babu, Manoj Srinivasan, and Mark Walter, for their input and comments on this research project. I would also like to thank Professor Babu for allowing me to use the metallurgical preparation facilities in the Welding Engineering department and providing his insight on the UAM process.

The research would not have been possible without Mark Norfolk from Fabrisonic and Dr. Karl Graff from the Edison Welding Institute. I thank them for allowing me to use the UAM system and their technical support. I also want to thank Dr. Phillip Evans from MIT Lincoln Laboratory for his support of UAM research and insightful discussions regarding composite behaviors. Collaboration with the Edison Welding Institute and MIT Lincoln Laboratory was possible through the Smart Vehicle Concepts Center, an NSF Industry/University Cooperative Research Center. I want to thank the members of the SVC Industrial Advisory Board for their continued interest in UAM research and the SVC fellowship that has supported me over the past four years.

I have enjoyed working with my past and present colleagues in the Smart Materials and Structures Lab, notably the UAM group, Chris Hopkins, Paul Wolcott, Justin Scheidler, Daniel Foster, Josh Pritchard, and Qian Zhang for our work-related and often sidetracked

discussions. Also John Larson, Surya Chakrabarti, Gordon Fox, Sheng Dong, Arjun Mahadevan, and Tom Walters with whom I could commiserate when the models wouldn't work and experiments didn't pan out. You helped make coming into the lab each day enjoyable. I also want to thank David Schick and Adam Truog for their assistance in preparing microscopy samples and Jason Dreyer for his input on experimental setups.

Starting the graduate program, let alone finishing, would not have happened without the love and support of my family. I thank my parents for instilling in me a love for learning and who taught me that, through hard work, I can accomplish nearly anything. Lastly, and as much as anyone else, I want to thank my wife, Marie, for celebrating the small victories with me and for her support and encouragement throughout these past years.

VITA

June 8, 1984	Born—Toledo, OH
June, 2007	B.S., Mechanical Engineering, Minor, Aviation, Cum Laude, The Ohio State University, Columbus, OH
June, 2009	M.S., Mechanical Engineering, The Ohio State University, Columbus, OH
2008 - 2012	NSF I/UCRC Smart Vehicle Concepts Center Fellow, The Ohio State University

Publications

Journal Publications

R. Hahnlen and M. J. Dapino. NiTi-Al interface strength in ultrasonic additive manufacturing composites. *Composites Part B*, in review.

R. Hahnlen, G. Fox, and M. J. Dapino. Fusion Welding of nickel-titanium and 304 stainless steel tubes: Part I: Laser welding. *Journal of Intelligent Material Systems and Structures*, doi:10.1177/1045389X12461075, 2012.

G. Fox, R. Hahnlen, and M. J. Dapino. Fusion Welding of nickel-titanium and 304 stainless steel tubes: Part II: Tungsten inert gas welding. *Journal of Intelligent Material Systems and Structures*, doi:10.1177/1045389X1246107, 2012.

R. Hahnlen, G. Fox, and M. Dapino. Ultrasonic soldering of shape memory NiTi to aluminum 2024. *Welding Journal*, 91:1–7, 2012.

D. E. Schick, R. M. Hahnlen, R. Dehoff, P. Collins, S. S. Babu, M. J. Dapino, and J. C. Lippold. Microstructural characterization of bonding interfaces in aluminum 3003 blocks fabricated by ultrasonic additive manufacturing. *Welding Journal*, 89:105–115, 2010.

Conference Publications

R. Hahnlen and M. J. Dapino. Thermomechanical behavior of low CTE metal-matrix composites fabricated through ultrasonic additive manufacturing. Proc. ASME SMASIS, Stone Mountain, GA, September 19-21, 2012.

R. Hahnlen and M. J. Dapino. Stress-induced tuning of ultrasonic additive manufacturing Al-NiTi composites. Proc. SPIE 8342, San Diego, CA, March 11-15, 2012.

R. Hahnlen, G. Fox, and M. J. Dapino. Laser welding of nickel titanium and 304 stainless steel tubes. Proc. ASME SMASIS, Scottsdale, AZ, September 18-21, 2011.

G. Fox, R. Hahnlen, and M. J. Dapino. TIG welding of nickel titanium and 304 stainless steel tubes. Proc. ASME SMASIS, Scottsdale, AZ, September 18-21, 2011.

R. Hahnlen and M. J. Dapino. Performance and modeling of active metal-matrix composites manufactured by ultrasonic additive manufacturing. Proc. SPIE 7979, San Diego, CA, March 6-10, 2011.

R. Hahnlen and M. J. Dapino. Active metal-matrix composites with embedded smart materials by ultrasonic additive manufacturing. Proc. SPIE 7645, San Diego, CA, March 7-11, 2010.

R. Hahnlen and M. J. Dapino. Joining of shape memory NiTi to structural materials using ultrasonic soldering. Proc. ASME SMASIS, Oxnard, CA, September 21-23, 2009.

R. Hahnlen, M. J. Dapino, M. Short, and K. Graff. Aluminum-matrix composites with embedded Ni-Ti wires by ultrasonic consolidation. Proc. SPIE 7290, San Diego, CA, March 8-12, 2009.

Fields of Study

Major Field: Mechanical Engineering

Studies in:

Active Metal-Matrix Composites	Professor Marcelo J. Dapino
Joining of Shape Memory Alloys	Professor Marcelo J. Dapino

Table of Contents

	Page
Abstract	ii
Dedication	iv
Acknowledgments	v
Vita	vii
List of Figures	xii
List of Tables	xviii

Chapters

1 Introduction	1
1.1 Overview and Motivation	1
1.2 Shape Memory Alloys	2
1.3 Ultrasonic Additive Manufacturing	8
1.4 Literature Review	11
1.4.1 SMA Composites	11
1.4.2 UAM Interface Studies	19
1.5 Research Objectives and Outline	21
2 SMA and SMA Composite Constitutive Modeling	24
2.1 Introduction	24
2.2 Shape Memory Alloy Modeling	25
2.2.1 Background	25
2.2.2 Change of Dependent Variable	32
2.2.3 Stress-Temperature Phase Diagram	32
2.2.4 Calculation of Martensitic Volume Fractions	34
2.2.5 SMA Model Implementation and Example Load Paths	41
2.3 Shape Memory Alloy Composite Modeling	52
2.3.1 Background	52
2.3.2 Addition of Matrix Constraint	55
2.3.3 Composite Model Implementation	58
2.4 Summary	65
3 SMA Characterization and UAM Composite Construction	67
3.1 Introduction	67

3.2	SMA Characterization	67
3.2.1	Transformation Temperature Determination	68
3.2.2	Determination of Mechanical Properties	71
3.2.3	NiTi Ribbon Characterization Summary	77
3.3	UAM Composite Construction	78
3.4	Summary	84
4	Thermally-Induced Strain	87
4.1	Introduction	87
4.2	Experimental Setup	87
4.3	Results and Discussion	89
4.3.1	Thermally-Induced Strain Experiments	89
4.3.2	Thermally-Induced Strain Modeling	96
4.4	Summary	105
5	Static and Dynamic Tuning	106
5.1	Introduction	106
5.2	Experimental Setup	107
5.2.1	Static Tuning	107
5.2.2	Dynamic Tuning	107
5.3	Results and Discussion	110
5.3.1	Static Tuning	110
5.3.2	Dynamic Tuning	113
5.4	Summary	132
6	SMA-Matrix Interface Characterization	134
6.1	Introduction	134
6.2	Experimental Setup	135
6.2.1	Scanning Electron Microscopy	135
6.2.2	Differential Scanning Calorimetry	137
6.3	Results and Discussion	137
6.3.1	Scanning Electron Microscopy	137
6.3.2	Differential Scanning Calorimetry	141
6.4	Summary	149
7	Conclusion	151
7.1	Summary of Findings	151
7.2	Contributions	155
7.3	Future Work	158
 Appendices		
A	Additional Numerical SMA Load Path Simulations	162
A.1	Piecewise Stress and Temperature Loading	162

A.2	Proportional Loading	165
A.3	SMA Model Code	168
B	High Temperature and Stress Cycles of NiTi Ribbons	179
C	Stiffening Effect of Strain Gages on HPUAM Composites	181
D	Characterization of Pseudoelastic NiTi Ribbon	184
D.1	Monotonic Tensile Test	184
D.2	Isothermal Stress Cycles	185
D.3	Blocking Stress Characterization	189
D.4	Summary	190
E	Fixture Drawings	191
E.1	C-F Dynamic Fixture	191
E.2	C-C Dynamic Fixture	194
E.3	HPUAM Mounting Plate	198
F	Composite Transient Dynamic Behavior	200
G	Maximum Fiber Volume Fraction	202
G.1	UAM Composite Constraints	202
G.2	Volume Fraction Calculations	203
	Bibliography	210

List of Figures

Figure	Page
1.1 Relationship between temperature, load, and crystal structure of an SMA. .	3
1.2 An example stress-temperature phase diagram for a typical shape memory alloy.	5
1.3 Modeled (a) load path with overlaid phase diagram and (b) stress-strain plot of an SMA exhibiting the shape memory effect.	6
1.4 Modeled (a) load path with overlaid phase diagram and (b) stress-strain plot of an SMA exhibiting the pseudoelastic effect.	6
1.5 Schematic of ultrasonic metal welding process.	8
1.6 A High Power Ultrasonic Additive Manufacturing (HPUAM) system and rendering of the transducer and horn during the additive and subtractive processes.	9
1.7 UAM build with a 76 μm diameter NiTi wire embedded within an Al 3003-H18 matrix. Plastic flow of the matrix has completely enveloped the NiTi wire.	10
1.8 Stress versus temperature plots for SMA wires with different levels of prestrain for (a) the first heating/cooling cycle and (b) the second heating/cooling cycle.	12
1.9 Stress versus temperature plots comparing the effect of SMA fiber volume fraction for (a) a reference composite specimen with no wires and SMA composites with prestrain levels of (b) 1%, (c) 2%, (d) 3%, (e) 4%, and (f) 5%.	13
1.10 Strain versus temperature plots comparing the effect of SMA fiber volume fraction for SMA composites with prestrain levels of (a) 0%, (b) 1%, (c) 3%, (d) 4%, and (e) 5%. Subfigure (f) compares prestrain levels for composites with an SMA volume fraction of 11.8%.	15
1.11 Strain versus temperature plots comparing the effect of SMA fiber prestrain levels embedded in glass fiber-epoxy composites.	16
1.12 Strain versus temperature plots showing SMA-matrix interface failure for different levels of SMA prestrain. Failure is characterized by the increase in strain after a given composite reaches its minimum strain.	17
1.13 DSC analysis data (a) of SMA wires subject to different prestrains; (b) of an SMA composite and interpretation of composite behavior.	17

1.14 Relationship between the experimental and analytical work discussed in this dissertation.	23
2.1 Stress-temperature phase diagram for SMAs as defined by the bivariant model.	29
2.2 Stress-temperature phase diagram in (a) original bivariant model [9]; (b) new bivariant model.	33
2.3 Stress-temperature phase diagram used in calculating total martensitic volume fraction, ξ	34
2.4 Total martensitic volume fraction $A - M$ transformation surface for $\xi \geq 0$. .	35
2.5 Total martensitic volume fraction $M - A$ transformation surface for $\xi \leq 0$. .	36
2.6 Low temperature stress-induced transformation surface for $\xi_s \geq 0$	39
2.7 Stress-induced transformation surfaces through regions 1, 2a, 2b, and 3 for initial volume fractions of: (a) $\xi_{so} = 0$; (b) $\xi_{so} = 0.5$; (c) $\xi_{so} = 0.8$	42
2.8 Overview of the process used in SMA Numerical Integration (N.I.) code. . .	44
2.9 Flow chart for determining total martensitic volume fraction evolution in SMA code.	45
2.10 Flow chart for determining total stress-induced martensitic volume fraction evolution in SMA code.	45
2.11 Low stress isobaric temperature cycle of initially temperature-induced martensitic SMA.	46
2.12 Low stress isobaric temperature cycle of initially stress-induced martensitic SMA.	47
2.13 Low temperature isothermal stress cycle of initially temperature-induced martensitic SMA.	48
2.14 Proportional stress-temperature load path traversing multiple transformation regions.	50
2.15 Proportional stress-temperature partial transformation load path.	51
2.16 The effect of SMA prestrain illustrated for an unconstrained SMA element and for a composite with an embedded SMA element.	56
2.17 Load path for an SMA composite subject to a thermal cycle modeled using the incremental approach with $\xi_{so} = 0$. Load path is superimposed on the SMA phase diagram.	61
2.18 Numerical instability for a composite with $\xi_{so} = 0.01$ numerically modeled through the incremental approach.	61
2.19 Interpolation approach, small circles represent the starting and ending points of transformation and green line represents the stress-temperature path through transformation.	63
2.20 Comparison of the interpolation method and incremental method.	64
2.21 Comparison of the simultaneous equation method and interpolation method for modeling SMA composites.	65
3.1 DSC curve with linear regressions used to find the austenite transformation temperatures for shape memory NiTi ribbon.	69
3.2 Relative change in bridge voltage containing a NiTi ribbon as it cools from 149°C.	71
3.3 Room temperature stress-strain plot of NiTi ribbon.	72

3.4	Isothermal stress-strain plots for NiTi ribbon: (a) $T=24^{\circ}\text{C}$, (b) $T=41^{\circ}\text{C}$, (c) $T=57^{\circ}\text{C}$, (d) $T=74^{\circ}\text{C}$, (e) $T=90^{\circ}\text{C}$, (f) Comparison of all temperatures. . .	73
3.5	Critical detwinning start and finish stresses (σ_{cr}^s , σ_{cr}^f) versus temperature. .	74
3.6	Tensile test of NiTi ribbon to failure.	75
3.7	Stress versus temperature for prestrained and constrained NiTi ribbon. Dashed line is the linear regression of cycle 2.	77
3.8	(a) Al 3003-H14 build plate attached to steel base plate used for fabricating the HPUAM NiTi-Al composites. (b) NiTi ribbons clamped in place on top of previously welded tape layers.	80
3.9	HPUAM system used to create NiTi-Al composites.	81
3.10	NiTi ribbons after detwinning fixed to a backing plate to avoid reorientation of the martensite variants during transportation. Ribbons held in place by polyimide tape.	83
3.11	Failure of first attempt on composite 4 showing delamination between tapes 2 and 3.	84
3.12	NiTi-Al composite 1 during the machining process used to attain the final composite width.	85
3.13	NiTi-Al composite 4 after final machining process used to remove the Al build plate: (a) top and (b) bottom. (c) Final geometry of composite 4. . .	85
4.1	Thermally-induced strain experimental setup showing composite 4 and an aluminum reference.	89
4.2	Temperature versus strain plots for cycles 1 through 3 of NiTi-Al: (a) composite 1; (b) composite 2; (c) composite 3; (d) composite 4.	90
4.3	Temperature versus strain plots for cycles 2 and 3 of NiTi-Al: (a) composite 1; (b) composite 2; (c) composite 3; (d) composite 4.	91
4.4	Top, bottom, and average strain response from the first heating cycle of composite 4.	94
4.5	Thermally-induced strain model for NiTi-Al: (a) composite 1; (b) composite 2; (c) composite 3.	97
4.6	Thermally-induced strain model with new A_f for NiTi-Al: (a) composite 1; (b) composite 2; (c) composite 3.	98
4.7	Thermally-induced strain model compared to thermally-induced strain data for composite 4: (a) cycle 1; (b) cycle 2 and 3.	100
4.8	Modeled stress-temperature load path of NiTi in composite 4 during heating, partial transformation, and cooling overlaid on the NiTi phase diagram. At 100°C , the location between the A_s^{σ} and A_f^{σ} lines correspond to a martensitic volume fraction of 0.81. Upon cooling, the stress-induced martensitic volume fraction returns to 1.	101
4.9	Updated thermally-induced strain model of composite 4 with hysteretic strain recovery after a partial transformation from heating to 100°C	101
4.10	Stress versus temperature plot for a blocked pseudoelastic NiTi ribbon. . .	102
4.11	Modeled thermally-induced strain for a composite with 15.2% pseudoelastic NiTi ribbon by volume. Model based on properties found in Appendix D. .	102

4.12	Comparison of modeled thermally-induced strain for difference fiber volume fraction in a composite with: (a) shape memory NiTi ribbons; (b) pseudoelastic NiTi ribbons.	103
4.13	Modeled thermally-induced strain for composite 4 showing the effect of pre-stress on the embedded NiTi ribbons.	104
5.1	Composite 4 prepared for the temperature-dependent stiffness test. Sample is instrumented with a thermocouple and strain gages. Loading is controlled through displacement of the top grip.	108
5.2	Composite sample installed in fixtures for dynamic testing: (a) Clamped-Free (C-F) fixture; (b) Clamped-Clamped (C-C) fixture.	109
5.3	Load versus displacement plot for NiTi-Al composites 1, 2, and 3 at 100°C. Composite 3 exhibits a loading plateau and pseudoelastic behavior.	112
5.4	Relative change in stiffness versus temperature for NiTi-Al composites 1-4.	114
5.5	Frequency response of X/F transfer function measured for composite 4 under the C-C boundary condition at room temperature. Natural frequency and -3 dB frequencies used to find the damping ratio.	114
5.6	Comparison of the relative change in natural frequencies versus temperature for solid Al and composite 1-4 when subject to the C-F boundary condition: (a) heating and cooling values displaying hysteretic response; (b) average of heating and cooling values.	119
5.7	Comparison of the damping ratios versus temperature for solid Al and composite 1-4 when subject to the C-F boundary condition: (a) heating and cooling values displaying hysteretic response; (b) average of heating and cooling values.	119
5.8	Comparison of the relative change in damping ratios versus temperature for solid Al and composite 1-4 when subject to the C-F boundary condition: (a) heating and cooling values displaying hysteretic response; (b) average of heating and cooling values.	120
5.9	Comparison of the relative change in natural frequencies versus temperature for solid Al and composite 1-4 when subject to the C-C boundary condition: (a) heating and cooling values displaying hysteretic response; (b) average of heating and cooling values.	122
5.10	Comparison of the damping ratios versus temperature for solid Al and composite 1-4 when subject to the C-C boundary condition: (a) heating and cooling values displaying hysteretic response; (b) average of heating and cooling values.	123
5.11	Comparison of the relative change in damping ratios versus temperature for solid Al and composite 1-4 when subject to the C-C boundary condition: (a) heating and cooling values displaying hysteretic response; (b) average of heating and cooling values.	123
5.12	Calculated relative change in natural frequency for the C-C boundary condition using the thermally-induced strain model.	128
5.13	Comparison of calculated relative change in natural frequency for composite 2 under the C-C boundary condition using the thermally-induced strain model and experimentally observed strain.	129

5.14	Comparison of calculated relative change in natural frequency for composite 3 under the C-C boundary condition using the thermally-induced strain model and experimentally observed strain.	130
5.15	Comparison of calculated relative change in natural frequency for composite 4 under the C-C boundary condition using the thermally-induced strain model and experimentally observed strain.	130
5.16	Comparison of thermally-induced strain models for composite 2. The amount of initial stress-induced martensite, ξ_{so} , is varied: solid line is the estimate after composite construction, 0%; dashed line is the estimate after analysis of thermally-induced strain experiments, 1.9%; dotted line is the final estimate after dynamic testing, 1.0%.	131
6.1	NiTi-Al composite samples for interface studies: (a) cross-section of composite 5 in removable polishing mount after final polishing; (b) sample 1 from composite 6 prior to DSC analysis.	136
6.2	SEM images of NiTi-Al composite 5 showing locations of EDS line scans.	136
6.3	SEM image of NiTi-Al composite 5 showing plastic flow of Al matrix enveloping the NiTi ribbon and close contact over the entire interface.	138
6.4	EDS line scan results of NiTi-Al composite 5 showing the relative atomic percent of Al, Ni, Ti, and O as a function of distance from the interface.	140
6.5	Combining the atomic percents of Ni and Ti to obtain a relative percent of NiTi. EDS line scan results of NiTi-Al composite 5 showing the relative atomic percent of Al, NiTi, and O as a function of distance from the interface.	140
6.6	DSC results for composite 6 (a) sample 1, (b) sample 2, and (c) sample 3.	142
6.7	DSC results for UAM Al 3003-H18 matrix sample with no embedded NiTi.	142
6.8	DSC heating cycles 1 and 2 of NiTi-Al composite 6 samples 2.	143
6.9	Representation of regions identified in DSC curve.	144
6.10	Model of NiTi-Al composites: (a) stress versus temperature, “x” marks interface failure; (b) strain versus temperature.	147
6.11	Model of failure temperature versus embedded length of NiTi ribbon.	149
7.1	Thermally-invariant HPUAM SMA-Al composite components under development.	161
A.1	Clockwise stress-temperature load path. $\xi_{To} = 1$, $T_o = 25^\circ\text{C}$, $\sigma_o = 0$ MPa.	163
A.2	Counter-clockwise stress-temperature load path. $\xi_{To} = 1$, $T_o = 25^\circ\text{C}$, $\sigma_o = 0$ MPa.	164
A.3	Proportional stress-temperature load path traversing multiple transformation regions starting as martensite. $\xi_{To} = 1$, $T_o = 52^\circ\text{C}$, $\sigma_o = 0$ MPa.	165
A.4	Proportional stress-temperature load path traversing multiple transformation regions starting as austenite. $\xi_o = 0$, $T_o = 52^\circ\text{C}$, $\sigma_o = 0$ MPa.	166
A.5	Proportional stress-temperature load path with minor loop. $\xi = 0$, $T_o = 100^\circ\text{C}$, $\sigma_o = 0$ MPa.	167
B.1	Stress-strain cycle plots for NiTi ribbon at: (a) 90°C ; (b) 100°C ; (c) 120°C ; (d) 150°C . Blue plots represent the first five cycles and red represent the last five cycles.	180

D.1	Tensile failure stress-strain plot of pseudoelastic NiTi ribbon.	185
D.2	Isothermal load cycles of pseudoelastic NiTi ribbon at (a) 23°C, (b) 40°C, (c) 60°C, and (c) 80°C. Last five cycles shown in red.	186
D.3	Critical detwinning and recovery stresses versus temperature for a pseudoelastic NiTi ribbon.	187
D.4	Linear regression of critical detwinning and recovery stresses versus temperature for a pseudoelastic NiTi ribbon.	188
D.5	Blocking stress versus temperature for the pseudoelastic NiTi ribbon. . . .	190
E.1	Diagram of C-F Fixture.	191
E.2	Schematic for bottom of C-F Fixture. Dimensions in inches.	192
E.3	Schematic for top of C-F Fixture. Dimensions in inches.	193
E.4	Diagram of C-C Fixture.	194
E.5	Schematic for bottom of C-C Fixture. Dimensions in inches.	195
E.6	Schematic for middle pieces of C-C Fixture. Dimensions in inches.	196
E.7	Schematic for top pieces of C-C Fixture. Dimensions in inches.	197
E.8	HPUAM steel base plate (a) without build plate and (b) with build plate. Machined pockets at the corners of the build plate were machined after NiTi-Al composites for an unrelated embedding study.	198
E.9	Schematic for HPUAM base plate. Dimensions in inches, holes are all threaded for 8-32 bolts.	199
F.1	Comparison of the first heating cycle responses of solid Al and composite 1-4 when subject to the C-C boundary condition: (a) Natural frequency; (b) Relative change in natural frequency.	201
G.1	Cross-section of a hypothetical rectangular ribbon multi-layer UAM composite with 5 courses and a maximum of 4 ribbons per course ($m = 5$, $n = 4$).	203
G.2	Surface plot of normalized volume fraction as a function of number of ribbon courses, m , and maximum number of ribbons per course, n	205
G.3	Normalized volume fraction as a function of (a) maximum number of ribbons per course for prescribed number of courses; (b) number of courses for a prescribed maximum number of maximum ribbons per course.	206
G.4	Surface plot of shape memory NiTi volume fraction as a function of number of ribbon courses, m , and maximum number of ribbons per course, n	207
G.5	Volume fraction of shape memory NiTi as a function of (a) maximum number of ribbons per course for prescribed number of courses; (b) number of courses for a prescribed maximum number of maximum ribbons per course.	208
G.6	Surface plot of pseudoelastic NiTi volume fraction as a function of number of ribbon courses, m , and maximum number of ribbons per course, n	208
G.7	Volume fraction of pseudoelastic NiTi as a function of (a) maximum number of ribbons per course for prescribed number of courses; (b) number of courses for a prescribed maximum number of maximum ribbons per course.	209

List of Tables

Table		Page
2.1	Material properties used for the bivariant SMA model.	31
2.2	Material properties used for SMA model numerical examples.	36
2.3	Material properties used for the phenomenological SMA model.	53
2.4	Matrix properties used for SMA composite model numerical examples. Values are for Al 3003-H18 [38].	60
3.1	Martensitic transformation temperatures as determined from electrical resistivity tests.	71
3.2	NiTi material properties obtained from characterization experiments.	78
3.3	Design characteristics and experimental plan for NiTi-Al composites.	79
3.4	Weld parameters used for different tape layers.	82
3.5	Dimensions and NiTi content of NiTi-Al composites.	84
4.1	Comparison of experimentally observed strain at maximum temperature and modeled strain for composites 1-4. The parenthetical value for composite 2 corresponds to the model with $\xi_{so} = 1.9\%$	105
5.1	Expected natural frequencies for the solid Al sample and composites 1-4 for the C-F and C-C boundary conditions.	110
5.2	Results from axial stiffness tests for the solid Al reference sample and composites 1-4.	111
5.3	Test temperature, natural frequency, and damping ratio for the solid Al sample and composites 1 and 2 with the C-F boundary condition.	115
5.4	Test temperature, natural frequency, and damping ratio for composites 3 and 4 with the C-F boundary condition.	116
5.5	Test temperature, natural frequency, and damping ratio for the solid Al sample and composites 1 and 2 with the C-C boundary condition.	117
5.6	Test temperature, natural frequency, and damping ratio for composites 3 and 4 with the C-C boundary condition.	118
5.7	Critical buckling loads, P_{crit} , for composites 1-4 when subject to the C-C boundary condition.	126

5.8	Calculated natural frequency ratio, ω_{np}/ω_{no} , for composites 1-4 when subject to the C-C boundary condition.	127
5.9	Calculated unloaded natural frequencies of composites 1-4 when subject to the C-C boundary condition.	127
5.10	Calculated relative change in natural frequencies for composites 1-4 under the C-C boundary condition considering the axial load from thermally-induced strain models	128
6.1	Transformation and failure temperatures for composite 6 samples 1, 2, and 3.	146
6.2	Failure temperature, embedded length, NiTi stress at failure, and interface shear strength for samples 1, 2, and 3.	147
A.1	Material properties used for SMA model numerical examples.	163
C.1	Properties used to quantify strain gage reinforcement.	182
D.1	NiTi material properties obtained from characterization experiments.	190
F.1	Calculated, initial, post-heating, and relative difference between room temperature natural frequencies of C-C dynamic test samples.	200
F.2	Comparison of the natural frequencies of composites 1-4 for the first and second heating cycles during C-C dynamic testing.	201
G.1	NiTi ribbon and matrix tape dimensions used in the maximum volume fraction analyses.	206

Chapter 1

INTRODUCTION

1.1 Overview and Motivation

Composite structures have made it possible to develop components with unique thermomechanical characteristics, directional strengths, and anisotropic stiffness. These properties allow for the development of components designed for specific loading conditions with high stiffness to weight ratios. Due to the ability to tailor the mechanical properties of composite materials, their use is surpassing that of traditional isotropic engineering materials [11] in many applications. With the introduction of smart materials, materials with uniquely coupled behaviors across different physical domains, it is possible to create multi-functional composite structures that have sensing and actuation properties allowing for the development of components that can adapt to their environment. One such smart material is NiTi, a Shape Memory Alloy (SMA) that can generate large stresses and recover between 4% and 8% of induced strain [20, 27, 36, 53, 57] through a stress and temperature dependent phase transformation.

By creating composites with embedded SMAs it is possible to vary their stiffness, tune the composites' dynamic properties, and tailor the Coefficient of Thermal Expansion (CTE). Through being able to adjust these mechanical properties, advanced concepts such as on-demand vibration attenuation, thermal-invariance, and solid-state actuation can be built into a monolithic composite structure. However, before these concepts can be fully realized, the coupled thermal and mechanical behavior of an SMA composite system must be understood.

This research focuses on the characterization, development, and modeling of the behaviors of SMA-Al composites constructed through Ultrasonic Additive Manufacturing (UAM), an emerging solid-state rapid prototyping technology that enables the construction of metallic structures at or near room temperature. The resulting composites are characterized in terms of their variable thermal expansion, mechanical stiffness, dynamic properties, and fiber-matrix interface strength. Using the observed results, a model has been developed which can be used to aid in the development of future SMA composites.

The following sections provide background to the key issues surrounding the development and characterization of SMA Metal-Matrix Composites (MMCs) constructed via UAM and a literature review to discuss the state-of-the-art research in SMAs, SMA composites, and the UAM process.

1.2 Shape Memory Alloys

SMAs are a unique class of smart materials that can be subjected to and recover between 4% and 8% strain without permanent deformation. This phenomenon is due to a temperature and stress-dependent phase transformation between the martensite and austenite phases. At low temperatures, SMAs are in the martensitic phase which has a monoclinic crystal structure. The martensitic phase can form in the “self-accommodating” or “twinned” orientation in which the monoclinic unit cells alternate orientations. When sufficient stress is applied, the martensite variants will reorient to form “preferentially-oriented” or “detwinned” martensite. While both the twinned and detwinned variants of martensite will undergo elastic deformation, the deformation contributed by reorientation of the variants is the source of the larger recoverable strain. In contrast to the martensitic phase, the high temperature austenite phase has a cubic crystalline structure. In transforming between twinned martensite and austenite, there is little deformation aside from thermal expansion or contraction, however, transforming from detwinned martensite to austenite recovers the strain induced during detwinning. The relationship between stress, temperature, and crystal structure is illustrated in Figure 1.1.

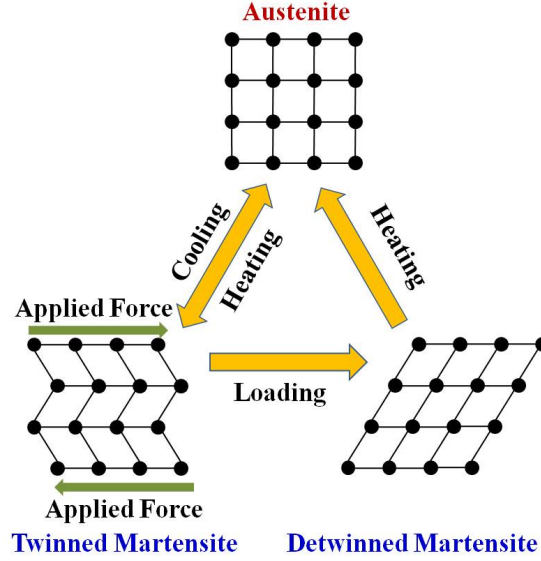


Figure 1.1: Relationship between temperature, load, and crystal structure of an SMA. Starting with twinned martensite, the application of load will cause the monoclinic structure to detwin resulting in a large macroscale deformation. This deformation is recovered by heating the detwinned martensite, forming austenite. As austenite cools, it transforms to twinned martensite when under no load. Heating the twinned martensite will cause a transformation to austenite with no large changes in strain.

Transformation between martensite and austenite can be accomplished through changes in temperature or stress. If there is no stress applied, increasing the temperature of an SMA in the martensite phase will start the martensite to austenite transformation ($M - A$) at the austenite start temperature, A_s , and transformation will be complete at the austenite finish temperature, A_f . Conversely, in decreasing the temperature of an austenitic SMA, the austenite to martensite transformation ($A - M$) will begin at the martensite start temperature, M_s , and will end at the martensite finish temperature, M_f .

Detwinned martensite is formed from twinned martensite by applying stress in excess of the critical start stress, σ_{cr}^s . Similar to the temperature-induced transformation, the stress-induced transformation occurs over a finite range which ends at the critical finish stress, σ_{cr}^f . Unlike the temperature-induced transformation, detwinned martensite will not spontaneously transform back to twinned martensite upon a decrease in stress.

The transformation temperatures are stress dependent: as increasing stress is applied

to the SMA, the transformation temperatures increase. In most SMA models the transformation temperatures are assumed to increase linearly with stress given by the following equations:

$$M_f^\sigma = M_f + \frac{\sigma}{C_M}, \quad (1.1)$$

$$M_s^\sigma = M_s + \frac{\sigma}{C_M}, \quad (1.2)$$

$$A_s^\sigma = A_s + \frac{\sigma}{C_A}, \quad (1.3)$$

and

$$A_f^\sigma = A_f + \frac{\sigma}{C_A} \quad (1.4)$$

where the superscript “ σ ” denotes the stress dependence of the transformation temperature. In the preceding equations, C_M and C_A are the martensitic and austenitic stress-influence coefficients, respectively. The transformation temperatures, critical stresses, and stress influence coefficients are determined experimentally. This is discussed in more detail in the context of alloys used for this research in Chapter 3 and Appendices B and D. Due to the stress-dependent transformation temperatures, it is possible for the austenitic phase to be transformed to martensite by only applying stress. As stress increases, the effective transformation temperatures also increase. Once the effective martensite transformation temperatures are greater than the ambient temperature, the $A - M$ transformation will commence despite the ambient temperature being greater than M_s .

Using the critical stresses and transformation temperatures, a stress-temperature phase diagram for a given alloy, such as the example given in Figure 1.2, can be constructed. Depending upon the stress and temperature of the SMA, the phase is identified by the martensitic volume fraction, ξ . This volume fraction is further divided into the stress-induced volume fraction, ξ_s , and temperature-induced volume fraction, ξ_T . When the SMA is fully austenitic, $\xi = 0$, and when it is fully martensitic, $\xi = 1$. Depending on stress and temperature, both the stress-induced and temperature-induced volume fractions can be any

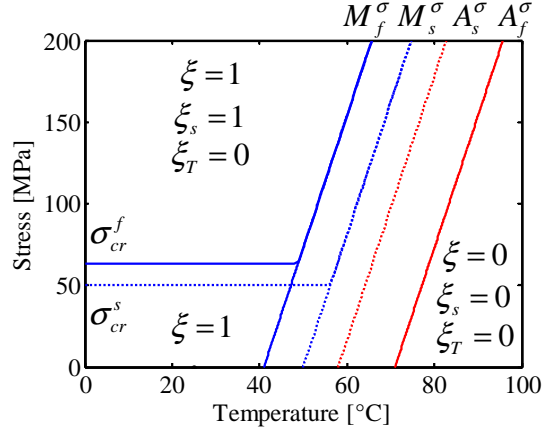


Figure 1.2: An example stress-temperature phase diagram for a typical shape memory alloy.

value between zero and one as long as they satisfy the inequality

$$0 \leq \xi_s + \xi_T \leq 1. \quad (1.5)$$

The phase diagram shown in Figure 1.2 is typical for an SMA exhibiting the “shape memory effect”. At room temperature under no load, the SMA will be fully martensitic and may be either twinned or detwinned. By changing the composition of the SMA, it is possible to shift the transformation temperatures below room temperature. In this case, the SMA will be austenitic at room temperature and exhibit the “superelastic” or “pseudoelastic” response. The key difference in the behavior of shape memory and pseudoelastic SMAs stems from their behavior to induced stresses. SMAs operating under the shape memory effect will undergo large deformations when subjected to sufficient load and the deformation will remain until the SMA is heated above the austenite transformation temperatures. In contrast, pseudoelastic material will accommodate large deformations under stress which are immediately recovered when the stress is released. To illustrate this difference, a load cycle from 0-500 MPa and back to 0 MPa is applied to hypothetical shape memory and pseudoelastic materials. The load path and resulting stress-strain curve for a shape memory material are shown in Figure 1.3(a) and (b), respectively. The corresponding plots for a pseudoelastic material are shown in Figure 1.4. It is noted that these behaviors assume

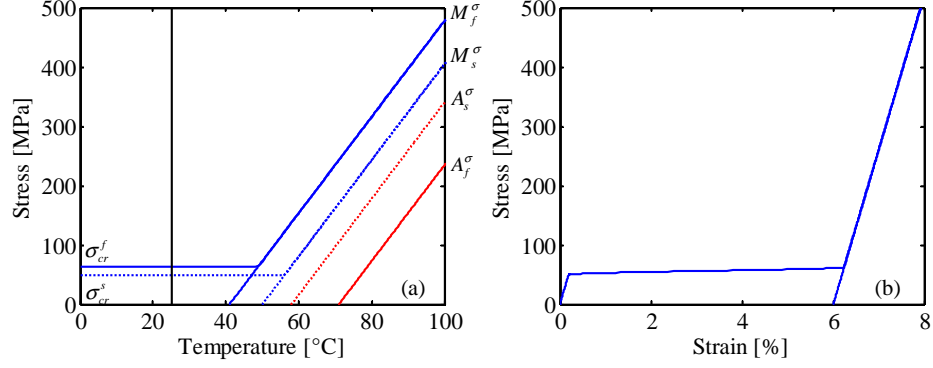


Figure 1.3: Modeled (a) load path with overlaid phase diagram and (b) stress-strain plot of an SMA exhibiting the shape memory effect.

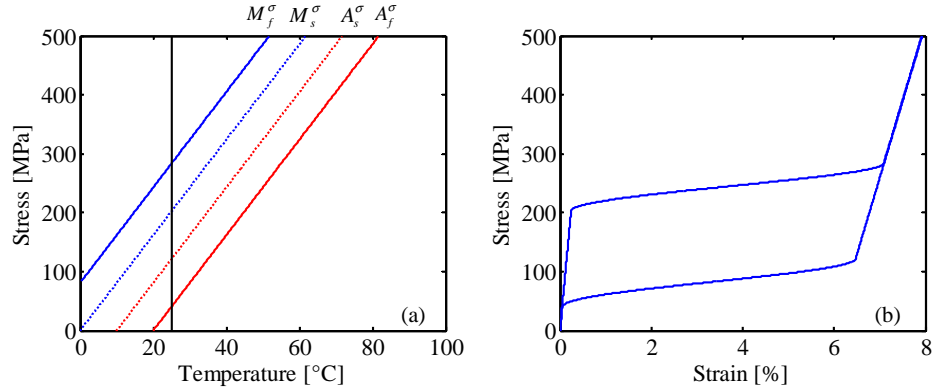


Figure 1.4: Modeled (a) load path with overlaid phase diagram and (b) stress-strain plot of an SMA exhibiting the pseudoelastic effect.

a fixed ambient temperature at 25°C. An alloy that exhibits the shape memory effect at room temperature may be made to exhibit the pseudoelastic effect at higher temperatures and similarly, a pseudoelastic material at room temperature may exhibit the shape memory effect at low temperatures. The specific behavior of an SMA is a function of not only its material properties but its operational environment as well.

While strain recovery is the more commonly utilized behaviors associated with SMAs, they can also generate large amounts of stress if the strain recovery is constrained. To utilize the “blocked” behavior of SMAs, the material must first be in the stress-induced or detwinned martensite phase. While in this phase, the strain is held constant while tem-

perature is increased. If a single crystal SMA is held under perfect constraint, once the temperature reaches A_s^σ , the stress will begin to increase linearly with increasing temperature as given by the Clausius-Clapeyron equation [9]:

$$\frac{d\sigma}{dT} = -\frac{\Delta H}{T_o \epsilon_L} \quad (1.6)$$

where ϵ_L is the transformation strain associated with the detwinning of martensite, ΔH is the change in enthalpy during the transformation from martensite to austenite, and T_o is the temperature at which the martensite and austenite temperatures are in equilibrium. This equation is simplified by considering $\frac{d\sigma}{dT} = C_A$, an assumption frequently used in SMA models [77]. The result is a linear relationship between blocking stress (also called transformation or recovery stress), σ_B , and temperature:

$$\sigma_B = C_A (T - A_s). \quad (1.7)$$

This can be visualized on the stress-temperature phase diagram as a load path that remains at an initial value until it intercepts and follows the A_s^σ line. The perfect constraint prevents strain recovery which must occur with transformation from detwinned martensite to austenite. Theoretically, this stress increases until the SMA yields. However, in practice, the stress level eventually reaches a maximum due to imperfect constraint, thermal expansion, and the polycrystalline nature of practical SMA materials.

In addition to strain recovery and blocking stress generation, SMAs exhibit large changes in material properties associated with the transformation between martensite and austenite. The austenitic phase of SMAs typically has an elastic modulus over 100% greater than that of the martensitic phase. Further, there are large changes in the electrical resistivity between the two phases which has been studied extensively for possible use as an SMA based strain sensing element [25, 52, 86].

While SMAs have unique properties and behaviors, the key to their utilization is dependent upon the repeatability of the behavior. Commercial SMAs are often trained to obtain a predictable thermomechanical response over a given range of loads and tempera-

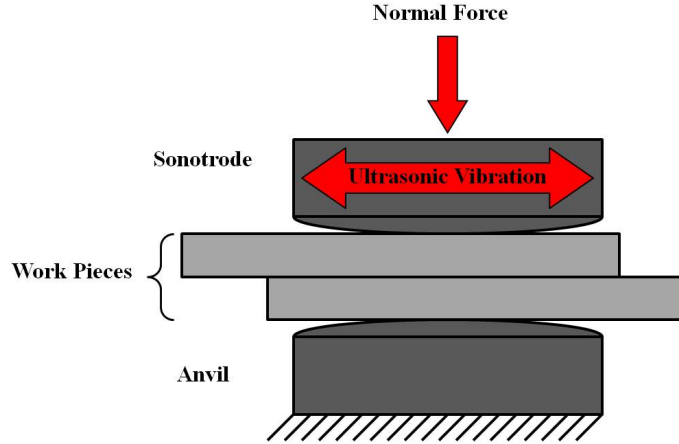


Figure 1.5: Schematic of ultrasonic metal welding process.

tures. If the SMA is overloaded or if it is heated to an excessive temperature, the repeatable behavior, or training, can be undone and the material will no longer behave in the same manner [21, 22, 93, 96].

1.3 Ultrasonic Additive Manufacturing

UAM is an emerging process through which MMCs can be fabricated at or near room temperature. The basis for UAM is ultrasonic metal welding, a solid-state joining process in which two metallic work pieces are joined without creating a liquid phase. During ultrasonic metal welding, the work pieces are held together under a normal force, bringing surface asperities in contact, and ultrasonic vibrations are applied to the top piece through a sonotrode or “horn”, shown in Figure 1.5. The vibrations are transmitted through the top piece to the interface between the work pieces causing a relative motion which creates plastic deformation and shearing of surface asperities. These actions, in turn, create nascent surfaces at the interface which lead to clean metal to clean metal contact, resulting in metallic bonding between the two pieces [19, 26, 39, 64, 71, 99, 100].

The ultrasonic metal welding process has been adapted in UAM through the use of a rolling transducer and sonotrode system. In UAM a thin metal tape or sheet is placed on the work surface and the horn presses the new material to the surface of the build. Piezo-

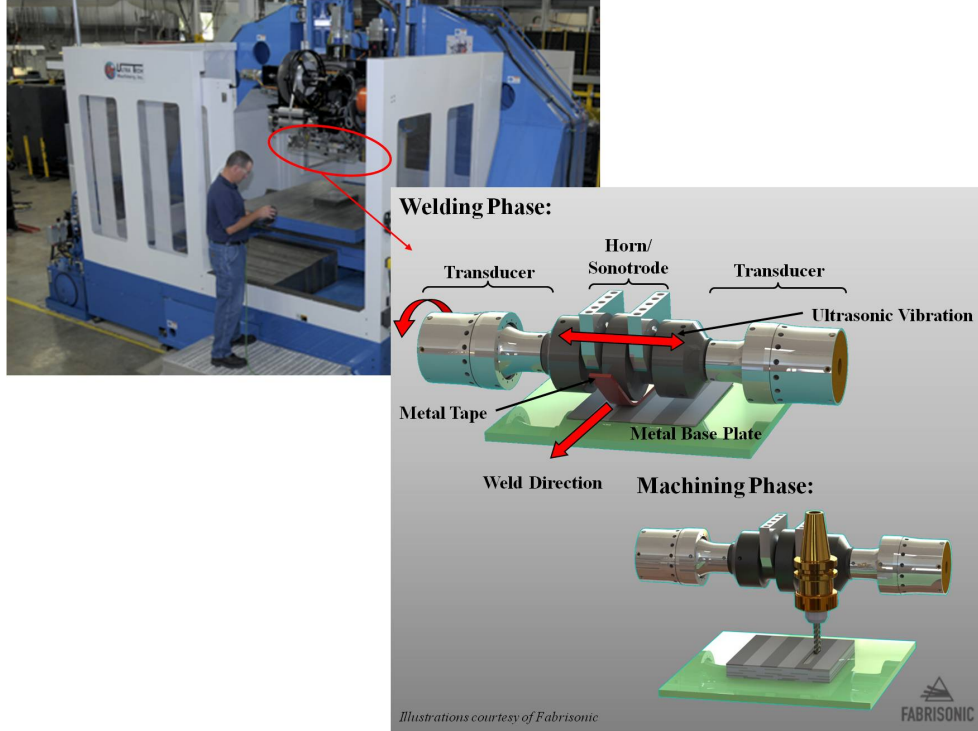


Figure 1.6: A High Power Ultrasonic Additive Manufacturing (HPUAM) system and rendering of the transducer and horn during the additive and subtractive processes. Images courtesy of EWI and Fabrisonic.

electric ultrasonic transducers are used to generate oscillations in the horn perpendicular to the rolling direction thus creating the friction-like action needed for ultrasonic welding, as shown in Figure 1.6. The rolling sonotrode allows for ultrasonic welds of arbitrary length to be created. By welding subsequent tapes on top of or next to previously welded layers, prismatic blocks of UAM material can be created. In conjunction with subtractive processes, such as Computer Numerically Controlled (CNC) or laser machining capabilities included in the latest systems, UAM can be used to create three-dimensional metallic components with arbitrary internal and external geometries. By including intermittent machining steps, unique features such as three-dimensional channels, embedded pockets, or internal structural members can be created using UAM.

Being a solid-state process, UAM is uniquely suited to create components with dissimilar materials such as Ti-Al laminates [28, 29] and Cu-Al builds [82]. Further, UAM is a low

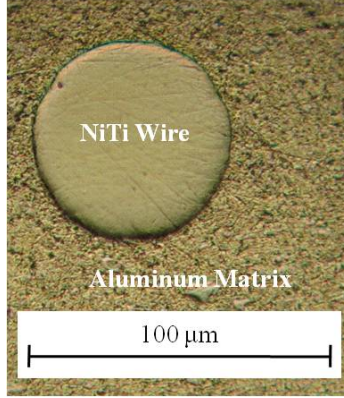


Figure 1.7: UAM build with a $76\text{ }\mu\text{m}$ diameter NiTi wire embedded within an Al 3003-H18 matrix. Plastic flow of the matrix has completely enveloped the NiTi wire.

temperature process, with maximum temperatures at foil interfaces measured between 25-50% of the matrix melting temperature and significantly lower temperatures within the bulk material during subsequent welds [40, 67, 68, 99]. The low process temperatures allow for embedding temperature sensitive materials such as electronics, fiber optic sensors, and polymers [39, 41, 56, 72].

Depending upon the objects being placed within the metal matrix, embedding can be accomplished in two ways. First, if the items are relatively small and can withstand the normal force involved with welding, materials may be directly embedded. This is best suited for long fibers or wires. In this procedure, the fibers are clamped in place at the desired layer in the UAM build and the subsequent matrix layer is welded on top. During welding of this layer, plastic flow of the matrix flows around the embedded material creating close contact and mechanical interlocking, as seen in Figure 1.7.

The second process involves subtractive steps and works well for larger items such as sensors, blocks of secondary material, and fragile materials such as fiber optics or brittle alloys. First, a pocket or groove is machined to allow the embedded items to rest partially or fully below the weld level. If the depth of the embedded object is precisely determined, plastic flow of the matrix can still envelop the secondary material without the compressive stresses associated with the direct method of embedding.

1.4 Literature Review

1.4.1 SMA Composites

The characteristic behaviors of SMAs can be used to create composites with unique properties. To date, the research on SMA composites can be divided into two main categories: those with a polymer matrix, generally epoxy, and those with a metallic matrix. When constructed with a polymer matrix, the SMA elements are held in place with a fixture while the polymer matrix is cured. SMA MMCs found in the literature have been constructed through high temperature processes such as casting, hot pressing, and powdered metallurgy processes. The key difference between the polymer matrix and metal-matrix SMA composites resides in the process temperatures, with polymer processes around 100-200°C and MMC processes several times greater [18, 24, 55, 63, 76, 94, 95, 104].

In the literature surveyed, there is experimental study on SMA composites in terms of the stress-strain behavior, stress-temperature behavior, strain-temperature behavior, and dynamic behavior. There has been limited work on SMA metal-matrix composites and that which has been accomplished focuses on construction methods and increases in yield strength over the parent matrix material. The relative lack of SMA MMC study is likely due to the fact that SMAs are temperature sensitive and, through high temperature construction processes, their stabilized behavior has been compromised.

Epoxy-Matrix Composites

Stress-Temperature Behavior

If a strain is induced on an SMA and then it is heated while mechanically constrained, the $M - A$ transformation will be inhibited and a blocking stress, or recovery stress, will be generated. In considering SMA composites, the matrix serves to restrict the transformation of an SMA that has been prestrained before embedding. Tsoi et al. [83] observed the constrained behavior of SMAs as a precursor to creating SMA epoxy composites. SMA wires were prestrained to 1%, 3%, and 6%, then subjected to thermal cycling while stress was monitored. Results for tests on a NiTiCu wire are shown in Figure 1.8. At the two lower

prestrain values, 1%, and 3%, stress generation does not begin until the temperature reaches the A_s temperature, 55°C. At 6% prestrain, the wire immediately generates recovery stress as temperature increases, an observation corroborated by other studies [75, 76, 84]. The authors also note that the rate of stress generation with respect to temperature is reduced for 6% prestrain when compared to 1% and 3%.

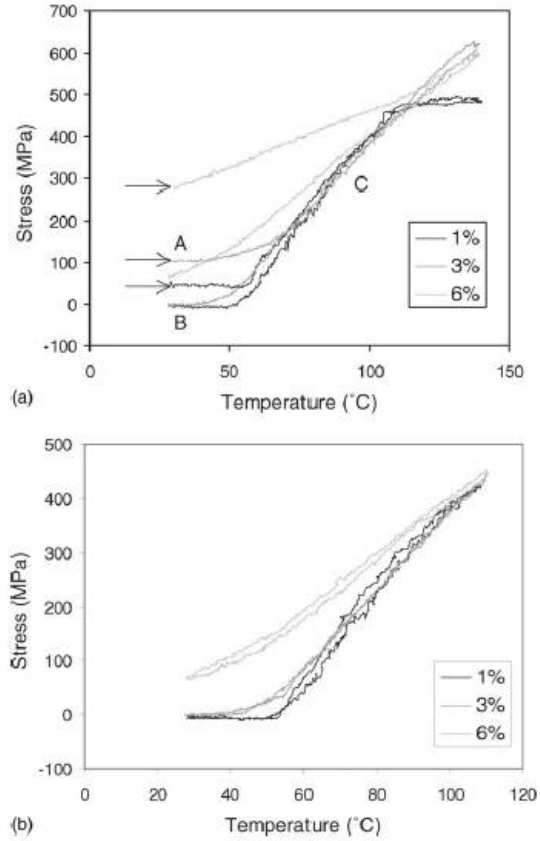


Figure 1.8: Stress versus temperature plots for SMA wires with different levels of prestrain for (a) the first heating/cooling cycle and (b) the second heating/cooling cycle. Reproduced from [83].

In a follow-up study, Tsoi et al. [84]. embedded NiTiCu SMA wires in a Kevlar epoxy matrix. In this study the wires were fixtured at prestrain values ranging from 1% to 5% before applying the matrix. In this instance, the prestrain did not have much effect as the Kevlar matrix already has a negative CTE and generates tensile recovery stresses when

heated and constrained. The study also observed different the effect of SMA volume fractions. As the volume fraction of SMA increased from 2.95% to 11.8% the maximum recovery stresses increased, illustrated in Figure 1.9.

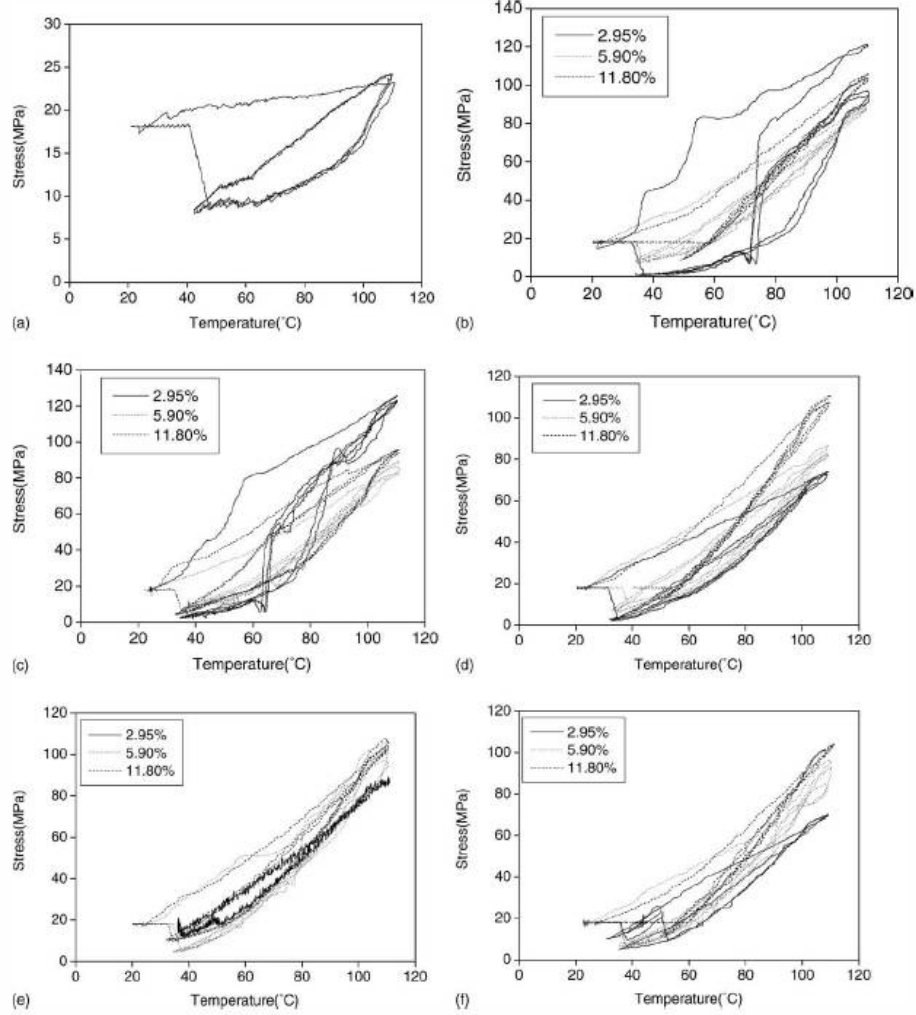


Figure 1.9: Stress versus temperature plots comparing the effect of SMA fiber volume fraction for (a) a reference composite specimen with no wires and SMA composites with prestrain levels of (b) 1%, (c) 2%, (d) 3%, (e) 4%, and (f) 5%. Reproduced from [84].

Strain-Temperature Behavior

The net negative strains generated by SMAs as they are heated presents an opportunity to create a composite with a negative CTE or actuation properties. Tsoi et al. [84] observed

the strain-temperature behavior of SMA/Kevlar epoxy composites as a function of prestrain and volume fraction. As seen in Figure 1.10, increasing volume fraction of the SMA for all composites increased the amount of recovery strain. Similar to what is observed in stress-temperature behavior, at low prestrains, 1% and 3%, the composites have a strain response governed mostly by the matrix at temperatures below A_s . At temperatures above A_s , the recovery stresses associated with the $M - A$ transformation increased the strain recovery as temperature increased. For composites with 6% prestrain, the strain recovery rate becomes more consistent over the temperature range.

Similar behaviors were observed by Zheng et al. [106] in studying SMA/glass fiber-epoxy composites. Seen in Figure 1.11, at prestrains of 1% and 3% the positive CTE causes an increase in strain with increasing temperature until A_s when blocking stresses cause strain recovery. At 6% prestrain, the strain response is uniformly negative over the observed temperature range.

Dynamic Behavior

The dynamic behavior of SMA composites can be tuned through two primary methods. The first method utilizes the stress generation of partially constrained SMA elements. Multiple studies have utilized this recovery stress generated in the constrained wires with increasing composite temperature to develop axial loads on the composite [4, 23, 59, 60]. Studies found in the literature observe the dynamic behavior of clamped-clamped beams which produce a net tensile force in the composite, due to net negative thermal strains, which induces a subsequent increase in natural frequency. This concept was applied to a complex structures by using an SMA-Kevlar epoxy composite as the skin of an airfoil [73]. By activating the SMA wires in the skin of the airfoil, the natural frequency was increased by nearly 7%.

The second method of tuning the dynamic properties of SMA composites take advantage of the change in material properties as SMA elements transform between martensite and austenite. Lau et al. [44, 45] investigated the effect of SMA wires on the dynamic properties of glass fiber and carbon fiber reinforced epoxy composites focusing on the natural frequency and damping of clamped-clamped and simply supported beams. Using 4%

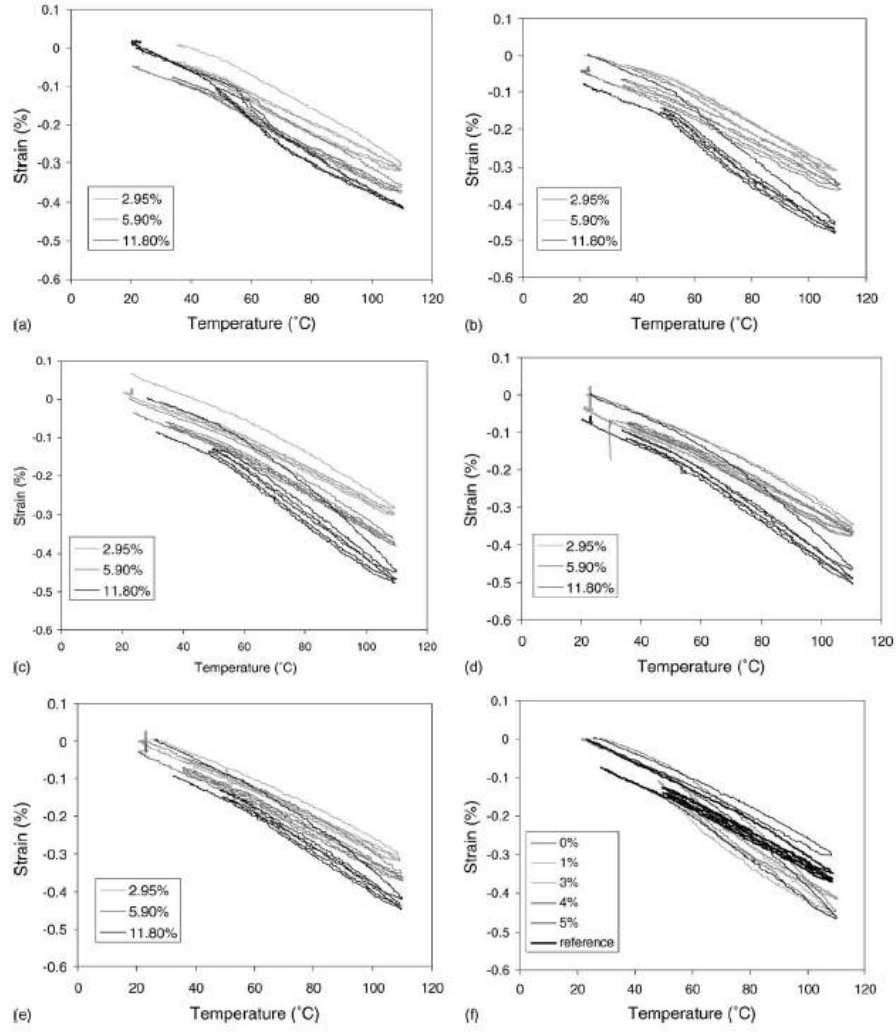


Figure 1.10: Strain versus temperature plots comparing the effect of SMA fiber volume fraction for SMA composites with prestrain levels of (a) 0%, (b) 1%, (c) 3%, (d) 4%, and (e) 5%. Subfigure (f) compares prestrain levels for composites with an SMA volume fraction of 11.8%. Reproduced from [84].

prestrain SMA elements, Lau observed up to 16.9% increase in natural frequencies with temperature. With non-prestrained SMA elements, an increase was observed due to the increase in the SMA elastic modulus and total composite stiffness, though it was not as large as the increase observed with prestrained SMA composites. It was noted that non-prestrained SMA composites had increased damping ratios as the number of SMA fibers were increased.

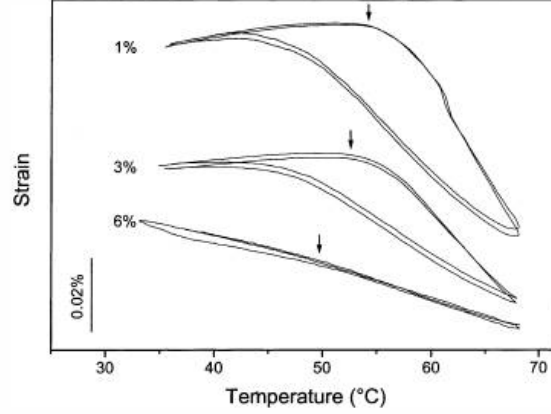


Figure 1.11: Strain versus temperature plots comparing the effect of SMA fiber prestrain levels embedded in glass fiber-epoxy composites. Reproduced from [106].

Composite Failure

The generation of recovery stresses and net thermal contraction of SMAs causes significant stresses to develop at the interface of the SMA and matrix. In the studies on SMA-epoxy composites, Zheng et al. found this interface was found to be a consistent point of failure [48, 104–106]. Failure has been identified through observing strain-temperature behavior as well as through Differential Scanning Calorimetry (DSC) analysis. In observing strain behavior, failure is observed when the strain reaches a minimum value and then suddenly begins to increase with increasing temperature, as shown in Figure 1.12. This indicates that the SMA is no longer transmitting a compressive load to the matrix and further strain response is dictated by the matrix properties through thermal expansion.

Analysis through DSC is possible due to the endothermic nature of the $M - A$ transformation. As the martensite transforms to austenite, the power required to heat an SMA sample relative to a comparative reference sample increases and is visualized as a negative heat flow in the DSC output. As prestrain is increased in a constrained wire, the heat flow minimum value becomes less pronounced, indicating that there is less martensite transforming to austenite, as shown in Figure 1.13 (a). This is due to the amount of twinned martensite decreasing due to increased prestrain. Because the SMA samples were constrained, only the twinned martensite transforms as transformation of the detwinned

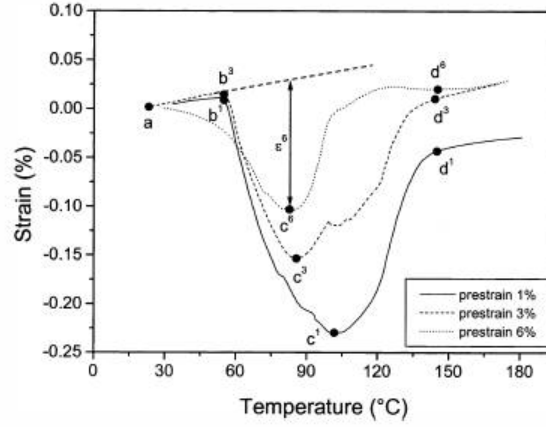


Figure 1.12: Strain versus temperature plots showing SMA-matrix interface failure for different levels of SMA prestrain. Failure is characterized by the increase in strain after a given composite reaches its minimum strain. Reproduced from [106].

martensite requires a recovery of the prestrain. A composite undergoing thermal loading until failure is shown in Figure 1.13 (b). An initial endothermic minimum is observed as the twinned martensite transforms to austenite. After this point the SMA generates recovery stresses and compresses the matrix. At interface failure, the SMA is able to move relative to the matrix, recovering its prestrain as detwinned martensite transforms to austenite which is observed on the DSC analysis as an additional local endothermic minimum.

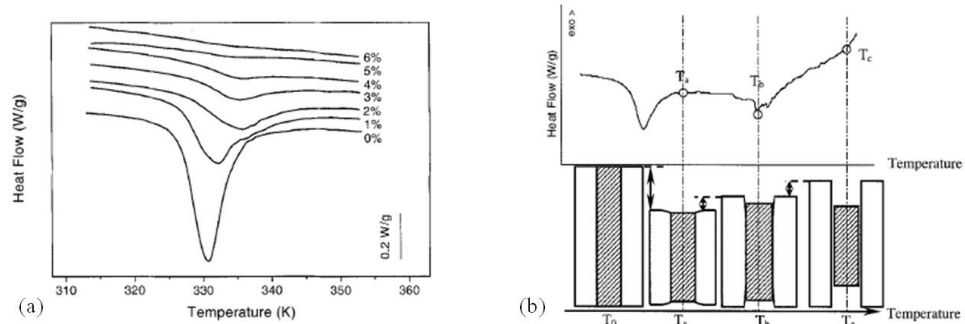


Figure 1.13: DSC analysis data (a) of SMA wires subject to different prestrains; (b) of an SMA composite and interpretation of composite behavior. Reproduced from [105].

Metal-Matrix Composites

The construction and characterization of SMA MMCs has also been investigated, however the primary focus is on enhanced yield strength, ultimate strength, and fatigue life. Little focus has been given to repeatable or cyclic thermomechanical behavior or dynamic properties of the composites. Further, the high temperatures involved in the manufacturing processes discussed in the current literature likely alter the repeatable behavior of SMAs making. Methods for creating these composites include solid-state methods such as hot pressing [2, 3] and powdered metallurgy processes [55, 63, 95] as well as casting methods using a liquid matrix phase to create the composite [18, 24] with temperatures up to 900°C.

In observing increases in strength, a common construction procedure involves the consolidation of the composite components at high temperature followed by a deformation step through tensile elongation [2, 24, 46, 63], extrusion processes, or cold rolling [55] and a second heating step. The deformation step serves to create stress-induced martensite and plastic deformation of the matrix while the second heating process causes strain recovery of the SMA elements resulting in a residual compressive stress in the matrix. The compressive stress in the matrices of the finished composites increases the tensile yield and ultimate strengths as the residual stress must first be overcome before tensile stresses in the matrix develop. Armstrong and Kino [2] also noted a bimodal yield in SMA MMCs arising from the initial yielding of the matrix followed by the detwinning of the SMA reinforcement material. The same study also noted a strongly non-linear temperature-strain relationship of the SMA MMC samples. The dependence of strength on temperature was also studied by Mizuuchi [55]. Mizuuchi found that by increasing composite temperature, the yield strength of the composites increased significantly. This was attributed to the increase in modulus of the SMA inclusions at high temperature due to the $M - A$ transformation.

Fatigue life of MMCs can also be significantly increased through the inclusion of SMA reinforcement. Coughlin et al. [18] created a unique pseudoelastic SMA MMC by casting Sn around SMA fibers to try and alleviate the low fatigue life of Pb-free solder joints. Results showed that low cycle fatigue life was dominated by the pseudoelastic response of the

NiTi fibers with an essentially vertical S-N curve at 1000-5000 cycles for strain amplitudes from 0.3% to 1.2%. Porter et al. [63] also investigated fatigue life of SMA-Al composites constructed through powder metallurgy. While NiTi bearing composites had 2-3 orders of magnitude increases in fatigue life at high stress amplitudes, the composite S-N curve converged with that of the matrix material at low stress amplitudes.

The studies conducted on SMA polymer based and metal based composites are vastly different. The key to unifying the unique behaviors observed in the polymer and metal-matrix composites is within maintaining a low process temperature. Low temperatures are critical to avoid loss of training of the SMA elements as well as enabling the control of SMA prestrain during construction, thereby eliminating the need to plastically strain the matrix after consolidation. Through UAM, it is possible to create SMA MMCs at low process temperatures and embed the SMA elements with a desired amount of prestrain in one step. This enables the creation of an MMC that has stiffness tuning and repeatable thermally-induced strain characteristics of polymer based SMA composites but with the benefits of a metal matrix such as insensitivity to moisture, broader operational temperature ranges, higher thermal conductivity, and higher stiffness [1, 65].

1.4.2 UAM Interface Studies

While there is little evidence in the literature of melting of the matrix material during UAM, the nature of contacting microscopic asperities and high strain rates dictate that there are likely very high temperatures at the local level [69]. However, in regard to embedding thermally sensitive materials, the critical scope of temperature increase is between that of the bulk material and microscale. There have been several studies in which the temperature at the weld interface is found through directly embedding small thermocouples between layers being consolidated. Kong et al. studied the interface temperature during welding of Al 3003 foils. They found that interface temperatures varied linearly with vibration amplitude between 60°C and 140°C [40]. Yang et al. reported significantly lower temperatures, between 68°C and 98°C, citing that the range of temperatures are due to changes in weld parameters [99]. Schick et al. observed the effect of build preheat on the temperature increase in

Al 3003 at not only the interface of the current weld, but also at the interface of previously welded layers. In this study, maximum temperature of 140°C were observed with build preheat temperature of 65°C while interface temperatures increased to a maximum of 220°C at build preheat levels of 149°C . In observing the temperatures of the previously welded interfaces, it was found that temperature increases were substantially smaller, indicating that the highest temperatures of any given interface are experienced during the welding of that interface [67, 68].

Being a solid-state process, UAM and ultrasonic metal welding are useful for bonding dissimilar materials. There have been several studies on the bonding mechanisms present between welds of dissimilar matrix materials as well as between the matrix and fibers in UAM composites. Diffusion is often used as a metric to determine if two dissimilar materials have bonded. However diffusion based bonding typically requires higher temperatures and longer time durations than are present in UAM [103]. Despite low temperatures observed in UAM and ultrasonic metal welding, Gunduz et al. [98] observed enhanced diffusion between Al and Zn in ultrasonic welds. Zn atoms were found to have diffused $3.5\text{ }\mu\text{m}$ into the Al foil. Using the diffusion lengths, an effective diffusivity for Zn was found to be five orders of magnitude higher than typical diffusivity at the weld temperature. Gunduz et al. conclude that the enhanced diffusivity is due to high strain rates present in ultrasonic welding results in higher instantaneous vacancy concentrations than are present at rest, indicating that given materials may have a critical strain rate at which enhanced diffusion may occur.

Yang et al. [99] observed the bonding mechanisms between Al 3003 and Ni 201 foils, Al 3003 and Cu foils, and an Al 3003 with embedded SiC fibers. In both dissimilar foil studies, there was no evidence of diffusion or chemical reactions between elements as investigated with Energy Dispersive X-ray Spectroscopy (EDS), nor was there significant evidence of mechanical interlocking between foils. Yang concludes that the bonding mechanism between the foils is due to intimate contact of atomically clean surfaces creating metallic bonding at the atomic level. In studying the interface between SiC fibers and the Al matrix, EDS analysis again indicated that there was no bulk diffusion of elements across the fiber/matrix interface. Further analysis of the interface after SiC fibers were removed showed that the

Al matrix created a negative image of the surface of the SiC fiber. This indicates that there was close contact and mechanical interlocking between the fiber and matrix, but no metallurgical or chemical bonding. If bonding was present, plastic or brittle deformations would have been expected upon removal of the fiber.

In further studies of dissimilar UAM welds, Truog [82] found that there was no significant diffusion between Al and Cu UAM welds as supported by EDS measurements across Al-Cu interface. Hopkins [28] and Schick [67] had similar findings for Al-Ti and Al braze metal UAM builds, respectively. These studies concluded that mechanical interlocking between the dissimilar metals is the primary contributor to the bond strength in UAM.

1.5 Research Objectives and Outline

The presented research has the following key objectives:

- Development of a model to describe the behavior of current composites and aid in the development of future SMA composites
- Design and manufacturing of high SMA volume fraction ($>15\%$) MMCs with different levels of SMA prestrain
- Experimental characterization of the thermally-dependent behaviors and properties of NiTi-Al composites including characterization of the interface between the NiTi fiber and Al matrix

The objectives aim at improving current modeling techniques, SMA MMC manufacturing techniques, as well as studying an area that, to date, has not received much attention: the repeatable thermomechanical behavior of SMA MMCs.

The developed model is able to describe the behavior of an SMA composite subjected to coupled thermal and mechanical loads. A key feature of the model is its reliance on only material properties of the SMA and matrix and two composite properties, SMA fiber volume fraction and SMA prestrain. The general nature of the model allows it to be applied to any SMA long-fiber reinforced composite.

The literature reveals substantial study on the thermally-induced strain behavior and dynamic behavior of SMA polymer based composites, but as mentioned, a majority of SMA MMC research focuses on manufacturing and monotonic properties such as yield and ultimate strength improvements. The root cause of this is likely the high temperatures involved in MMC processing which are detrimental to the unique behaviors attributed to SMAs [93, 96]. Since UAM is a low temperature process, it is now possible to create SMA MMCs without overheating the alloys, allowing retention of the SMAs repeatable behavior, thus enabling the unique behaviors characterized by SMA polymer based composites. The end result is a unique material that has the active properties of SMA-polymer based composites combined with the advantages of a metallic matrix: wider operational temperature ranges, higher thermal conductivity, higher stiffness [65], and negligible effects from moisture absorption [1]. These properties make MMCs favorable for structural applications and exposure to harsh environments. The composite manufacturing described herein outlines a method for creating long-fiber reinforced SMA MMCs through UAM with arbitrary fiber volume fraction and SMA prestrain with low process temperatures.

The thermally-dependent behaviors of the SMA MMCs are experimentally characterized. Thermally-induced strain is quantified as a function of fiber volume fraction and SMA prestrain as is the response of composites to static and dynamic loads. In considering static loads, composite stiffness as a function of temperature is quantified while dynamic studies focus on tuning natural frequencies and measuring composite damping ratios as a function of temperature.

While not a functional behavior, a key concern in any SMA composite is the interface between the SMA fiber and matrix. As such, characterizing the interface between the NiTi elements and Al matrix is an additional objective of this study. Through a combination of a series of experiments and modeling, the nature of the bonding between NiTi and Al via UAM and the strength of the NiTi-Al interface are determined. The method of bonding and interface strength do not immediately affect the characterized behaviors but do represent a potential failure mode which is not readily detected externally though will drastically alter composite behavior. As such, the interface strength is treated as a critical composite

material property providing an operational envelop for the NiTi-Al UAM composites.

The outline of this dissertation follows the key objectives in order. Discussion will start with the development of the SMA composite model in Chapter 2 followed by the characterization of the SMA elements and creation of the UAM composites in Chapter 3. Thermally-induced strain experiments, analysis, and modeling are presented in Chapter 4 with a similar presentation for composite stiffness tuning given in Chapter 5. Characterization of the interface, including suggestions for improving interface strength, is presented in Chapter 6. Lastly, the findings and contributions to the state-of-the-art are summarized in Chapter 7 with a discussion of on-going and suggested future work provided.

On a closing note to this introduction, the composite experiments and model were largely developed in parallel with insight from experiments aiding model construction and modeled simulations giving context to experimental results. Figure 1.14 provides a general overview to the relationship between experimental and modeling efforts discussed herein. Contributions to and/or from the model for each experiment will be highlighted in the discussions of the respective chapter.

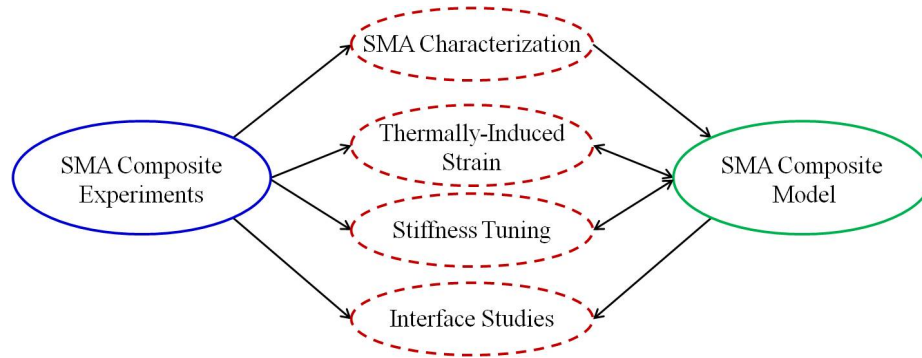


Figure 1.14: Relationship between the experimental and analytical work discussed in this dissertation.

Chapter 2

SMA AND SMA COMPOSITE CONSTITUTIVE MODELING

2.1 Introduction

The modeling used in this research combines the phenomenological SMA composite framework described by Sittner [75–78] for SMA composites but utilizes a new underlying SMA formulation based upon a bivariant constitutive SMA model developed by Brinson [9, 10]. The combination of the two approaches combines the computational efficiency of the numerical integration approach and strain matching strategy in the phenomenological composite model with the basis on thermodynamic principles, stress and temperature dependent martensitic volume fractions, and the reliance on easily obtainable SMA material properties as present in the bivariant model. The end result is an SMA composite model that depends only on material and composite properties and can describe the behavior of a long-fiber reinforced SMA composite when subjected to an arbitrary stress-temperature loading.

Multiple modifications are made to the original bivariant model to integrate it into a composite framework. The modifications include the change of the dependent variable from stress to strain, adjustment of the stress-temperature phase diagram, reformulation of the volume fraction equations and their conditions to account for the previous two changes, and a new kinetic law for the mixed stress and temperature-induced transformation region. Since the differential forms of the volume fraction equations are used for numerical integration, the time derivatives of the equations are also provided as each equation is discussed. This

chapter will provide background on the original models, detail the modifications, discuss an algorithm for implementing the new model equations, and provide example load paths for a hypothetical SMA material. After the SMA model is explained, the application of the matrix constraint, demonstration loading, and different algorithmic approaches for the composite scenario are discussed.

2.2 Shape Memory Alloy Modeling

2.2.1 Background

There are several different frameworks for modeling SMAs, some are empirically based, relying on a mixture of fitting parameters and experimentally determined properties, while others derived from the first principles of thermodynamics are described by a similar amount of determined material properties. Of the latter, derivations are commonly accomplished by using Gibbs free energy or Helmholtz free energy. Derivations utilizing Gibbs free energy, such as models based off of the work by Boyd and Lagoudas [6, 7, 42, 51], result in strain as the dependent variable being a function of stress, temperature, and martensitic volume fraction while models based on Helmholtz free energy, built upon the derivations given by Tanaka [9, 10, 49, 50, 80, 81] result in a dependent stress variable as a function of strain, temperature, and martensitic volume fraction. In this research, modeling work is based on a modified version of a bivariant one-dimensional SMA model developed by Brinson [9, 10]. The bivariant model was chosen because it considers both temperature and stress-induced martensite, has defined transformation start and end conditions, and has been shown to be accurate when modeling long fiber SMAs while maintaining relative simplicity through its one-dimensional assumption.

Bivariant Constitutive Model for Shape Memory Alloys

The bivariant constitutive model by Brinson [9, 10] for one dimensional SMAs is based on prior models developed by Tanaka [80, 81] and Liang and Rogers [49, 50]. The model relates the macro scale stress, strain, temperature and martensitic volume fraction of an

SMA through the constitutive law

$$\sigma - \sigma_o = E(\xi)\epsilon - E(\xi_o)\epsilon_o + \Omega(\xi_s)\xi_s - \Omega(\xi_o)\xi_{so} + \Theta(T - T_o) \quad (2.1)$$

where $E(\xi)$ is the elastic modulus, $\Omega(\xi)$ is the transformation tensor, and Θ is related to the CTE. The main contribution of this model is the separation of the martensitic volume fraction into temperature-induced and stress-induced components, ξ_T and ξ_s , respectively where

$$\xi = \xi_T + \xi_s \quad (2.2)$$

The constitutive law for stress in the SMA was derived by Tanaka [80, 81] from thermodynamic principles. In considering a one-dimensional SMA, the first law of thermodynamics is considered,

$$\rho\dot{u} = \sigma\dot{\epsilon} + \frac{\partial q_{sur}}{\partial x} + \rho q \quad (2.3)$$

and the second law of thermodynamics is expressed through the Clausius-Duhem inequality [9]:

$$\rho\dot{s} - \rho\frac{q}{T} + \frac{\partial}{\partial x}\left(\frac{q_{sur}}{T}\right) \geq 0. \quad (2.4)$$

Here, ρ is the material density, u is the internal energy, q_{sur} is the heat flux, x is the material coordinate, s is the entropy, and q is the heat production with overhead dots representing a derivative with respect to time. By rearranging (2.3) and substituting it into (2.4), a new expression is obtained:

$$\rho\dot{s} - \rho\frac{q}{T} + \frac{1}{T}(-\rho\dot{u} + \sigma\dot{\epsilon} + \rho q) \geq 0. \quad (2.5)$$

Using Helmholtz free energy, $\psi = u - Ts$ and $\dot{\psi} = \dot{u} - T\dot{s} - s\dot{T}$, (2.5) is rewritten as

$$-\rho\dot{\psi} + \sigma\dot{\epsilon} - \rho s\dot{T} \geq 0. \quad (2.6)$$

If the Helmholtz function is assumed to be a function of strain, temperature, and martensitic volume fraction, its derivative is given by

$$\dot{\psi} = \dot{\psi}(\epsilon, T, \xi) = \frac{\partial \psi}{\partial \epsilon}\dot{\epsilon} + \frac{\partial \psi}{\partial T}\dot{T} + \frac{\partial \psi}{\partial \xi}\dot{\xi}. \quad (2.7)$$

Combining the above equation with (2.6) gives

$$-\rho \left[\frac{\partial \psi}{\partial \epsilon} \dot{\epsilon} + \frac{\partial \psi}{\partial T} \dot{T} + \frac{\partial \psi}{\partial \xi} \dot{\xi} \right] + \sigma \dot{\epsilon} - \rho s \dot{T} \geq 0. \quad (2.8)$$

At this point, if the thermoelastic condition is considered (no transformation, $\dot{\xi} = 0$, and the second law takes the equality),

$$-\rho \frac{\partial \psi}{\partial \epsilon} \dot{\epsilon} + \sigma \dot{\epsilon} - \rho \frac{\partial \psi}{\partial T} \dot{T} - \rho s \dot{T} = 0 \quad (2.9)$$

must hold true for any strain rate, $\dot{\epsilon}$, and temperature rate, \dot{T} . This requires the following:

$$\sigma = \rho \frac{\partial \psi}{\partial \epsilon} \quad (2.10)$$

and

$$s = -\frac{\partial \psi}{\partial T}. \quad (2.11)$$

The inequality from the second law now depends only on the transformation term:

$$-\rho \frac{\partial \psi}{\partial \xi} \dot{\xi} \geq 0. \quad (2.12)$$

In the bivariant model, the dependent variable, stress, is dependent upon strain, temperature, and volume fraction by definition, as proposed by Liang and Rogers [49, 50]. As such, the derivative is given by

$$d\sigma = \frac{\partial \sigma}{\partial \epsilon} d\epsilon + \frac{\partial \sigma}{\partial T} dT + \frac{\partial \sigma}{\partial \xi} d\xi \quad (2.13)$$

which with (2.10) expands to

$$d\sigma = \rho \frac{\partial^2 \psi}{\partial \epsilon^2} d\epsilon + \rho \frac{\partial^2 \psi}{\partial \epsilon \partial T} dT + \rho \frac{\partial^2 \psi}{\partial \epsilon \partial \xi} d\xi. \quad (2.14)$$

The volume fraction variable is split into two terms and the following definitions are created:

$$\rho \frac{\partial^2 \psi}{\partial \epsilon^2} = E, \quad (2.15)$$

$$\rho \frac{\partial^2 \psi}{\partial \epsilon \partial T} = \Theta, \quad (2.16)$$

$$\rho \frac{\partial^2 \psi}{\partial \epsilon \partial \xi_T} = \Omega_T, \quad (2.17)$$

and

$$\rho \frac{\partial^2 \psi}{\partial \epsilon \partial \xi_s} = \Omega_s. \quad (2.18)$$

Using the material definitions, (2.13) is rewritten as

$$d\sigma = E d\epsilon + \Theta dT + \Omega_T d\xi_T + \Omega_s d\xi_s. \quad (2.19)$$

Given current $(\sigma, \epsilon, T, \xi_T, \xi_s)$ and initial $(\sigma_o, \epsilon_o, T_o, \xi_{To}, \xi_{so})$ conditions for stress, strain, temperature, and volume fractions, (2.19) becomes

$$(\sigma - \sigma_o) = E(\epsilon - \epsilon_o) + \Theta(T - T_o) + \Omega_T(\xi_T - \xi_{To}) + \Omega_s(\xi_s - \xi_{so}). \quad (2.20)$$

Values for the material functions can be determined by considering different beginning and end states. For instance, considering the induction of the maximum amount of recoverable strain, ϵ_L , from an initially austenitic phase, the initial conditions are $\sigma_o = \epsilon_o = 0$, $T_o = T$, $\xi_{To} = 0$, and $\xi_{so} = 0$ while the final conditions are $\sigma = 0$, $\epsilon = \epsilon_L$, $\xi_T = 0$, and $\xi_{so} = 1$, (2.20) becomes

$$\begin{aligned} (0) &= E(\epsilon_L) + \Theta(0) + \Omega_T(0) + \Omega_s(1) \\ &\Rightarrow \Omega_s = -E\epsilon_L. \end{aligned} \quad (2.21)$$

Considering the induction of the maximum amount of recoverable strain, ϵ_L , from an initially martensitic phase, the initial conditions are $\sigma_o = \epsilon_o = 0$, $T_o = T$, $\xi_{To} = 1$, and $\xi_{so} = 0$ while the final conditions are $\sigma = 0$, $\epsilon = \epsilon_L$, $\xi_T = 0$, and $\xi_{so} = 1$, (2.20) becomes

$$\begin{aligned} (0) &= E(\epsilon_L) + \Theta(0) + \Omega_T(0 - 1) + \Omega_s(1) \\ &\Rightarrow \Omega_s - \Omega_T = -E\epsilon_L \\ &\Rightarrow \Omega_T = 0. \end{aligned} \quad (2.22)$$

With the material function Ω depending on only ξ_s , the constitutive stress equation is found to equal (2.1).

The thermal term, Θ , can be found by considering a free thermal expansion condition without transformation where $\sigma = \sigma_o = \epsilon_o = 0$, $\xi_s = \xi_{so}$, and strain is governed by linear thermal expansion, $\epsilon = \alpha (T - T_o)$:

$$\begin{aligned} (0) &= E (\alpha (T - T_o)) + \Theta (T - T_o) + \Omega_s (0) \\ &\Rightarrow -E\alpha = \Theta. \end{aligned} \quad (2.23)$$

Transformations in this model are based upon the cosine kinetic functions described by Liang and Rogers [49, 50], however with the separation of stress-induced and temperature-induced martensitic volume fractions, the transformation equations are modified and occur over a different stress-temperature phase diagram, shown in Figure 2.1. While the $M - A$ transformation occurs over the same transformation band, between A_s^σ and A_f^σ , the $A - M$ is separated between conversion to twinned martensite and detwinned martensite.

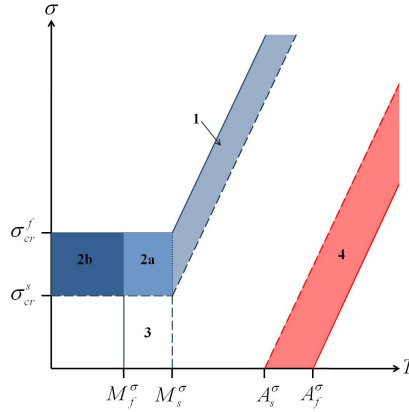


Figure 2.1: Stress-temperature phase diagram for SMAs as defined by the bivariant model.

From the phase diagram in Figure 2.1, transformation to martensite can occur in regions 1, 2a, 2b, and 3. In region 1, $T > M_s$ and $\sigma_{cr}^s + C_M (T - M_s) < \sigma < \sigma_{cr}^f + C_M (T - M_s)$, conversion to detwinned martensite is given by

$$\xi_s = \frac{1 - \xi_{so}}{2} \cos \left(\frac{\pi}{\sigma_{cr}^s(T) - \sigma_{cr}^f(T)} \left(\sigma - \sigma_{cr}^f(T) \right) \right) + \frac{1 + \xi_{so}}{2} \quad (2.24)$$

and the temperature-induced volume fraction derivative is given by:

$$\xi_T = \xi_{To} - \frac{\xi_{To}}{1 - \xi_{so}} (\xi_s - \xi_{so}). \quad (2.25)$$

Below M_s , both the stress and temperature-induced volume fractions evolve. When $T < M_s$ and $\sigma_{cr}^s < \sigma < \sigma_{cr}^f$, regions 2a and 2b, the stress-induced volume fraction is given by

$$\xi_s = \frac{1 - \xi_{so}}{2} \cos \left(\frac{\pi}{\sigma_{cr}^s - \sigma_{cr}^f} (\sigma - \sigma_{cr}^f) \right) + \frac{1 + \xi_{so}}{2} \quad (2.26)$$

with the temperature-induced volume fraction given by

$$\xi_T = \xi_{To} - \frac{\xi_{To}}{1 - \xi_{so}} (\xi - \xi_{so}) + \Delta_{T\xi}. \quad (2.27)$$

In (2.27), the determination of $\Delta_{T\xi}$ changes depending on the temperature. In region 2a, $M_f < T < M_s$, if temperature is decreasing,

$$\Delta_{T\xi} = \frac{1 - \xi_{To}}{2} (\cos(a_M(T - M_f)) + 1), \quad (2.28)$$

where

$$a_M = \frac{\pi}{M_s - M_f}. \quad (2.29)$$

Else, in region 2b or if temperature is not decreasing in region 2a, $\Delta_{T\xi} = 0$.

This model assumes that M_s and M_f are stress invariant for stresses below σ_{cr}^s . As such, when $M_f < T < M_s$ with decreasing temperatures, the temperature-induced volume fraction is given by

$$\xi_T = \frac{1 - \xi_{To}}{2} (\cos(a_M(T - M_f)) + 1). \quad (2.30)$$

In this case, since $\sigma < \sigma_{cr}^f$, there is no evolution of the stress-induced volume fraction and it remains equal to its initial value.

In the phase diagram shown in Figure 2.1, transformation to austenite can occur in region 4. In this case, the total volume fraction is decreasing when $T > A_s$ and $C_A(T - A_f) < \sigma < C_A(T - A_s)$:

$$\xi(T, \sigma) = \frac{\xi_o}{2} [\cos(a_A(T - A_s^\sigma)) + 1], \quad (2.31)$$

Table 2.1: Material properties used for the bivariant SMA model.

Property	Description [Units]
M_f	Martensitic Finish Temp [$^{\circ}\text{C}$]
M_s	Martensitic Start Temp [$^{\circ}\text{C}$]
A_s	Austenitic Start Temp [$^{\circ}\text{C}$]
A_f	Austenitic Finish Temp [$^{\circ}\text{C}$]
σ_{cr}^s	Detwinning Critical Start Stress [MPa]
σ_{cr}^f	Detwinning Critical Finish Stress [MPa]
C_M	Martensitic Stress Influence Coefficient [MPa/ $^{\circ}\text{C}$]
C_A	Austenitic Stress Influence Coefficient [MPa/ $^{\circ}\text{C}$]
E_M	Martensite Elastic Modulus [GPa]
E_A	Austenite Elastic Modulus [GPa]
α	Coefficient of Thermal Expansion [$\mu\epsilon/^{\circ}\text{C}$]
ϵ_L	Maximum Transformation Strain [non-dimensional]

where

$$a_A = \frac{\pi}{A_f - A_s}. \quad (2.32)$$

In this case, the total volume fraction is decreasing with increasing temperature over the range of A_s^{σ} to A_f^{σ} due to phase transformation to austenite. The stress induced and temperature induced components of the volume fraction are given by 2.33 and 2.34, respectively:

$$\xi_s = \xi_{so} - \frac{\xi_{so}}{\xi_o} (\xi_o - \xi) \quad (2.33)$$

and

$$\xi_T = \xi_{To} - \frac{\xi_{To}}{\xi_o} (\xi_o - \xi). \quad (2.34)$$

A key strength of the bivariant model is its dependence exclusively on material properties which can be determined through a modest number of thermomechanical experiments. In fact, it is possible to obtain all the necessary properties through stress-strain tests at different temperatures. These methods are discussed more in Chapter 3 and Appendices B and D. The main contribution of the model is the separation of stress and temperature-induced martensitic volume fractions. The discrimination between the two volume fractions allows for the modeling of the shape memory effect in addition to the pseudoelastic effect [9, 47, 102].

2.2.2 Change of Dependent Variable

The first modification to the original bivariant model is the dependent variable change from stress to strain. This is done from the constitutive strain equation given in (2.19) expanded using the material functions in (2.21) and (2.23):

$$\begin{aligned}
 d\sigma &= E d\epsilon + \Theta dT + \Omega_s d\xi_s \\
 d\sigma &= E d\epsilon - E\alpha dT - E\epsilon_L d\xi_s \\
 \frac{1}{E} d\sigma &= d\epsilon - \alpha dT - \epsilon_L d\xi_s \\
 \Rightarrow d\epsilon &= \frac{1}{E} d\sigma + \alpha dT + \epsilon_L d\xi_s.
 \end{aligned} \tag{2.35}$$

Using current and initial conditions as done for (2.20), a constitutive strain equation with elastic, thermal, and transformation components is given:

$$(\epsilon - \epsilon_o) = \frac{1}{E} (\sigma - \sigma_o) + \alpha (T - T_o) + \epsilon_L (\xi_s - \xi_{so}). \tag{2.36}$$

2.2.3 Stress-Temperature Phase Diagram

One feature of the phase diagram used in the original bivariant model is the stress-independence of the martensite start and finish temperatures at loads below the critical start stress, σ_{cr}^s , seen in Figure 2.2 (a). There are, however, several models that maintain stress-dependent martensitic transformation temperatures below σ_{cr}^s as supported by experimental characterization of SMA specimens [10, 14, 27, 34, 35, 107]. The presented model is based on a phase diagram with martensitic transformation temperatures that vary linearly with stress with a slope equal to C_M down to zero stress. As such, the critical stresses intersect the martensitic transition temperatures at different values than in the original phase diagram and require modification to the conditions for transformation. The modified phase diagram is seen in Figure 2.2 (b).

For both phase diagrams, in the region bound on the bottom by the critical finish stress, σ_{cr}^f , and on the right by the stress dependent martensitic finish temperature, M_f^σ , the NiTi material is completely detwinned martensite. The area bound on top by the critical start

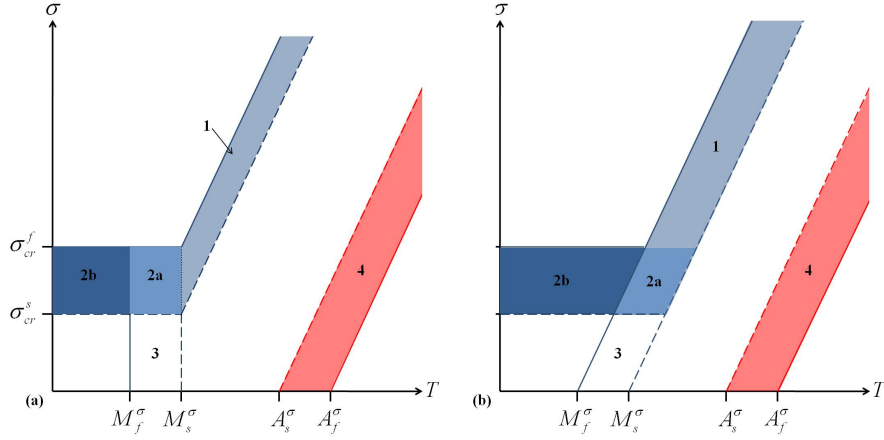


Figure 2.2: Stress-temperature phase diagram in (a) original bivariant model [9]; (b) new bivariant model.

stress, σ_{cr}^s , and M_f^σ also represents a completely martensitic material though whether it is stress induced or temperature-induced depends upon the loading history. Similarly, if the stress and temperature conditions are between the region bound by M_s^σ and A_s^σ , the phase is history dependent; any valid mixture ($0 \leq \xi_s + \xi_T \leq 1$) of twinned martensite, detwinned martensite, and austenite is possible. If the stress and temperature conditions fall to the right of the temperature dependent austenitic finish line, A_f^σ , the material is completely austenitic.

Both phase diagrams have four main regions over which stress and/or temperature-induced transformation can occur. The transformation from austenite to stress-induced martensite ($A - M^+$) occurs over region 1, transformation from austenite to temperature-induced martensite ($A - M$) occurs over region 3, transformation from temperature-induced to stress-induced martensite ($M - M^+$) occurs over region 2b, while a mixed transformation region is defined in region 2a. The martensite to austenite ($M - A$) transformation occurs in region 4 for both temperature and stress-induced martensite variants. Total volume fraction, ξ , can only increase over regions 1, 2a, and 3 while it can only decrease over region 4. The parent phase diagram, shown in Figure 2.3, is used for calculating the total volume fraction for SMAs or the combined total and stress-induced volume fraction in pseudoelastic alloys.

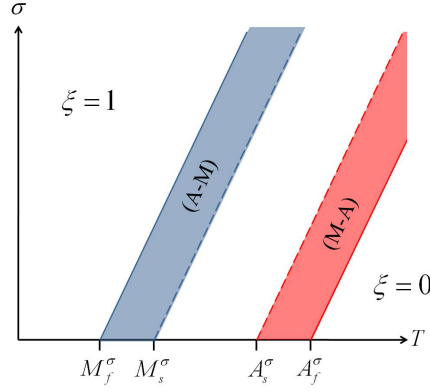


Figure 2.3: Stress-temperature phase diagram used in calculating total martensitic volume fraction, ξ .

2.2.4 Calculation of Martensitic Volume Fractions

Total Martensitic Volume Fraction

In this model, the total volume fraction is first calculated and the stress and temperature-induced volume fractions are defined in terms of the total volume fraction. The following total volume fraction evolution follows the equations determined by Liang and Rogers [49, 50].

For the reverse ($A - M$) transformation:

$$\xi = \frac{1 - \xi_o}{2} \cos [a_M (T - M_f^\sigma)] + \frac{1 + \xi_o}{2} \quad (2.37)$$

where M_f^σ is the stress-dependent martensitic start temperature given by 1.1 and a_M is given by (2.29). When stress and temperature are varying with time, the evolution of total volume fraction, $\dot{\xi}$, during the reverse transformation is:

$$\dot{\xi} = -\frac{1 - \xi_o}{2} \sin [a_M (T - M_f^\sigma)] a_M \left(\dot{T} - \dot{\sigma}/C_M \right). \quad (2.38)$$

For the forward ($M - A$) transformation:

$$\xi = \frac{\xi_o}{2} [\cos [a_A (T - A_s^\sigma)] + 1] \quad (2.39)$$

where A_s^σ is the stress-dependent austenitic start temperature given by 1.3 and a_A is given by (2.32). For the forward transformation, the evolution becomes:

$$\dot{\xi} = -\frac{\xi_o}{2} \sin[a_A (T - A_s^\sigma)] a_A \left(\dot{T} - \dot{\sigma}/C_A \right). \quad (2.40)$$

In considering the $A - M$ transformation, the transformation surface showing the total volume fraction in terms of stress and temperature is shown in Figure 2.4. This surface was made considering an initial total volume fraction of 0 using equation (2.37). Total volume fraction increases only as the stress-temperature location is between M_s^σ and M_f^σ . A similar surface is shown in Figure 2.5 for the $M - A$ transformation. Over the $A - M$ surface, ξ may only increase while, conversely, over the $M - A$ surface, it may only decrease. Material properties used for these transformation surfaces as well as all other numerical simulations in this chapter are given in Table 2.2.

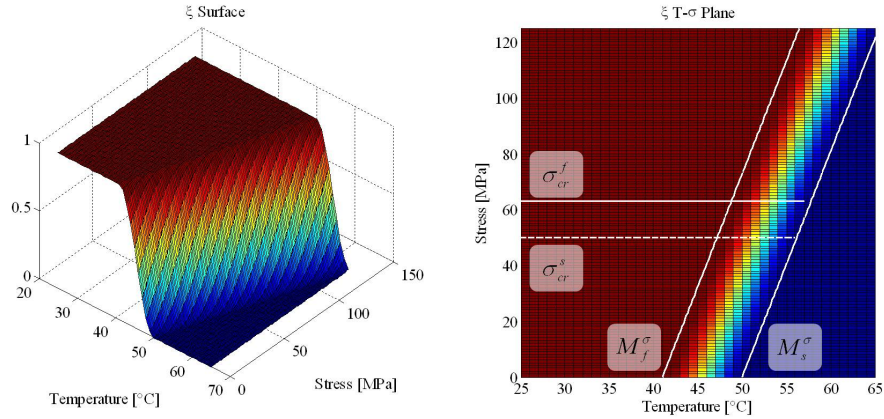


Figure 2.4: Total martensitic volume fraction $A - M$ transformation surface for $\dot{\xi} \geq 0$. Created using (2.37) with $\xi_o = 0$.

After the total volume fraction is determined the stress-induced and temperature-induced components can be determined. When considering the $M - A$ transformation, determining the evolution of the stress-induced and temperature-induced volume fraction is dependent only upon the total volume fraction and the initial volume fractions prior to

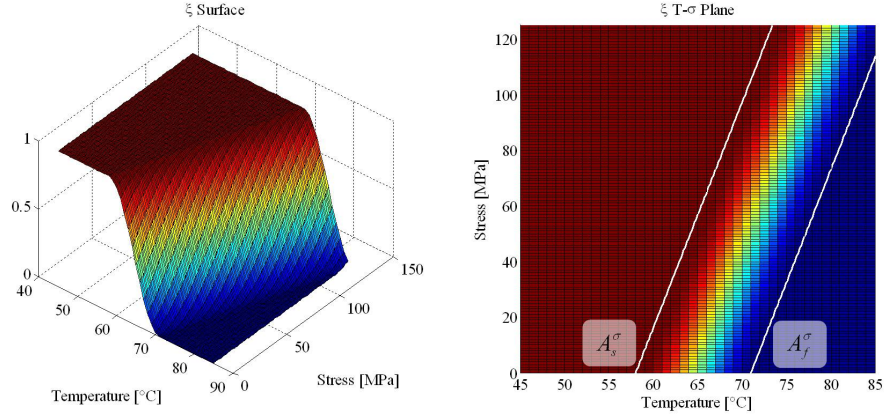


Figure 2.5: Total martensitic volume fraction $M - A$ transformation surface for $\dot{\xi} \leq 0$. Created using (2.39) with $\xi_o = 1$.

Table 2.2: Material properties used for SMA model numerical examples.

Property	Description	Value
M_f	Martensitic Finish Temp	41°C
M_s	Martensitic Start Temp	50°C
A_s	Austenitic Start Temp	58°C
A_f	Austenitic Finish Temp	71°C
σ_{cr}^s	Critical Start Stress	50 MPa
σ_{cr}^f	Critical Finish Stress	63 MPa
C_M	Martensitic Stress Influence Coefficient	8.1 MPa/°C
C_A	Austenitic Stress Influence Coefficient	8.1 MPa/°C
E_M	Martensite Elastic Modulus	26 GPa
E_A	Austenite Elastic Modulus	83 GPa
α	Coefficient of Thermal Expansion	10 $\mu\epsilon/^\circ\text{C}$
ϵ_L	Maximum Transformation Strain	6%

transformation. For temperature induced volume fraction [9]

$$\xi_T = \xi_{To} - \frac{\xi_{To}}{\xi_o} (\xi_o - \xi) \quad (2.41)$$

which yields the evolution equation

$$\dot{\xi}_T = \frac{\xi_{To}}{\xi_o} \dot{\xi}. \quad (2.42)$$

Similarly, the stress-induced fraction is given by [9]

$$\xi_s = \xi_{so} - \frac{\xi_{so}}{\xi_o} (\xi_o - \xi) \quad (2.43)$$

which yields an evolution equation of:

$$\dot{\xi}_s = \frac{\xi_{so}}{\xi_o} \dot{\xi}. \quad (2.44)$$

When considering the $A - M$ transformation in region 3, only the temperature-induced volume fraction will evolve. Any change in total volume fraction through (2.38) is equal to the change in temperature-induced volume fraction.

Stress-Induced Martensitic Volume Fraction

Aside from region 4, the stress-induced volume fraction will only evolve in regions 1, 2a, and 2b in Figure 2.2 (b) and then, only if it is increasing, $\dot{\xi}_s > 0$. As a general rule to be observed in all transformations in this model, the evolutions the stress-induced volume fraction, $\dot{\xi}_s$, and total volume fraction, $\dot{\xi}$, cannot be less than zero unless the load path traverses the phase diagram region bound by the austenite transformation temperatures, region 4 in Figure 2.2 (b) and the $M - A$ region in Figure 2.3.

Region 1 is defined as the region bound at the bottom by σ_{cr}^f and on either side by M_f^σ and M_s^σ . This region is bound at the top by the material yield strength which may or may not be temperature dependent, however this model does not yet take this into account. In region 1, any increasing evolution in ξ causes an increase in ξ_s , though this does not exclude the possibility of ξ_s forming at the expense of ξ_T .

Region 2a is bound on top and bottom by σ_{cr}^f and σ_{cr}^s , respectively, and on the left

and right by M_f^σ and M_s^σ , respectively. In this region it is possible to have both ξ_s and ξ_T increasing at different rates. While related in this region, one volume fraction need not increase at the expense of the other.

If the temperature is below M_f^σ and the stress-induced volume fraction is not already 1, an increase in stress between σ_{cr}^s and σ_{cr}^f will cause the stress-induced volume fraction to increase as well. This occurs in region 2b as defined in Figure 2.2 (b). Since $\xi = 1$ by definition of this region, ξ_s evolves at the expense of ξ_T .

The three regions are described in more detail in the following sections. However, for clarity of the equations used, They will be described in the following order: Region 1, Region 2b, Region 2a.

Region 1: High Temperature Stress-Induced Transformation

If the load path is such that the sample temperature reaches M_s^σ at a stress greater than or equal to σ_{cr}^f and the loading path remains in region 1, the stress-induced volume fraction is governed by an equation similar to that of the total volume fraction given in (2.37). The primary difference is in the initial volume fraction coefficients; the initial total volume fraction is replaced by the initial stress-induced volume fraction:

$$\xi_s^{R1} = \frac{1 - \xi_{so}}{2} \cos [a_M (T - M_f^\sigma)] + \frac{1 + \xi_{so}}{2} \quad (2.45)$$

which yields the evolution function

$$\xi_s^{\dot{R}1} = -\frac{1 - \xi_{so}}{2} \sin [a_M (T - M_f^\sigma)] a_M (\dot{T} - \dot{\sigma}/C_M). \quad (2.46)$$

The temperature-induced volume fraction evolution in this region is given by:

$$\xi_T^{\dot{R}1} = \dot{\xi} - \xi_s^{\dot{R}1}. \quad (2.47)$$

In the case that $\xi_o = 0$ then (2.37) and (2.45) are equivalent as are their differential forms, (2.38) and (2.46) ($\xi = \xi_s$ and $\dot{\xi} = \dot{\xi}_s$). The transformation surface looks identical to that presented in Figure 2.4 from the line representing σ_{cr}^f and above.

Region 2b: Low Temperature Stress-Induced Transformation

To describe this transformation, it is assumed that the starting point is any stress less than σ_{cr}^s and temperature below M_f^σ resulting in $\xi_o = 1$. The equation describing the stress-induced volume fraction between σ_{cr}^s and σ_{cr}^f is given in the original bivarient model [9]:

$$\xi_s^{R2b} = \frac{1 - \xi_{so}}{2} \cos \left[\frac{\pi}{\sigma_{cr}^s - \sigma_{cr}^f} (\sigma - \sigma_{cr}^f) \right] + \frac{1 + \xi_{so}}{2} \quad (2.48)$$

which yields the evolution function

$$\xi_s^{R2b} = -\frac{1 - \xi_{so}}{2} \sin \left[\frac{\pi}{\sigma_{cr}^s - \sigma_{cr}^f} (\sigma - \sigma_{cr}^f) \right] \left(\frac{\pi}{\sigma_{cr}^s - \sigma_{cr}^f} \right) \dot{\sigma}. \quad (2.49)$$

In this region, the stress-induced fraction increases explicitly at the expense of the temperature-induced fraction resulting in the expressions:

$$\xi_T^{R2b} = \xi_o - \xi_s^{R2b} \quad (2.50)$$

and

$$\xi_T^{R2b} = -\xi_s^{R2b}. \quad (2.51)$$

For illustrating the transformation in region 2b, this transformation surface is extended into region 2a to be bounded in the temperature range by M_s^σ and is illustrated in Figure 2.6.

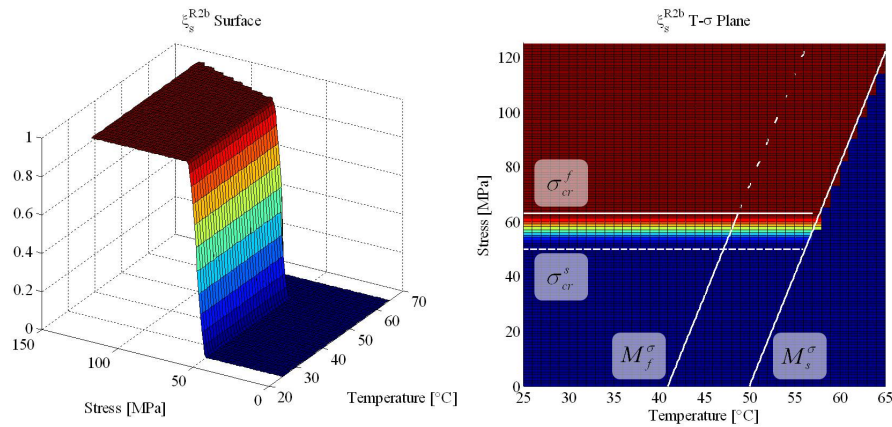


Figure 2.6: Low temperature stress-induced transformation surface for $\xi_s \geq 0$. Created using (2.48) with $\xi_{so} = 0$.

Region 2a: Mixed Stress and Temperature-Induced Transformation

In this region both the temperature-induced and stress-induced volume fractions can vary independently based upon the loading path. Total volume fraction is increasing based upon the current temperature in relation to M_s^σ and M_f^σ and follows (2.38). While the total volume fraction surface may remain the same in this region as it does in region 1 or in the low stress $A - M$ transformation region, the stress-induced volume fraction surface does not.

If isobaric thermal paths are considered, assuming an initially austenitic material, the stress-induced fraction will begin to increase with decreasing temperature when $T = M_s^\sigma$ and reach a maximum value when $T = M_f^\sigma$. This maximum value is dependent upon the constant stress value and its relation to σ_{cr}^s and σ_{cr}^f . This maximum value can be found through (2.48) describing the low temperature stress-induced transformation, region 2b. Above σ_{cr}^f all volume fraction evolution goes to forming ξ_s ; conversely, below σ_{cr}^s , all volume fraction evolution goes to forming ξ_T and there is no evolution of ξ_s . Therefore, at any point within region 2a, the stress-induced volume fraction will increase from its initial value at $T = M_s^\sigma$ to a maximum value determined by (2.48) at $T = M_f^\sigma$.

The concept behind the mixed stress-induced transformation region is to have a smooth function that depends on both temperature and stress, each varying through a cosine function to match the existing kinematic equations from the original bivariant model and provide a smooth, continuous transition between the transformation surfaces of regions 1 and 2b. To accomplish this, the following form for ξ_s is given:

$$\xi_s^{R2a} = \xi_T^{Mod} \times \xi_s^{Mod} + \xi_{so} \quad (2.52)$$

where ξ_T^{Mod} is the temperature modifier, ξ_s^{Mod} is the stress modifier, and ξ_{so} is used to account for the initial stress-induced volume fraction. The equations for the temperature and stress modifiers are given by

$$\xi_T^{Mod} = \left(\frac{1}{2}\right) [\cos [a_M (T - M_f^\sigma)] + 1] \quad (2.53)$$

and

$$\xi_s^{Mod} = \left(\frac{1 - \xi_{so}}{2} \right) \left[\cos \left[\frac{\pi}{\sigma_{cr}^s - \sigma_{cr}^f} (\sigma - \sigma_{cr}^f) \right] + 1 \right]. \quad (2.54)$$

By combining regions 1, 2a, and 2b, the resulting transformation surfaces are continuous for any value of ξ_{so} and provide continuity with the surfaces for regions 1 and 2b as shown in Figure 2.7.

The evolution of the stress-induced volume fraction in region 2a is found using the chain rule:

$$\xi_s \dot{R}_{2a} = \xi_T \dot{M} \xi_s^{Mod} + \xi_T^{Mod} \xi_s \dot{M}. \quad (2.55)$$

This is expanded and rearranged to give

$$\xi_s \dot{R}_{2a} = - \left(\frac{1 - \xi_{so}}{4} \right) \sin(\chi) \dot{\chi} [\cos \beta + 1] - \left(\frac{1 - \xi_{so}}{4} \right) \sin(\beta) \dot{\beta} [\cos \chi + 1] \quad (2.56)$$

where

$$\chi = a_M (T - M_f^\sigma), \quad (2.57)$$

$$\dot{\chi} = a_M (\dot{T} - \dot{\sigma}/C_M), \quad (2.58)$$

$$\beta = \frac{\pi}{\sigma_{cr}^s - \sigma_{cr}^f} (\sigma - \sigma_{cr}^f), \quad (2.59)$$

and

$$\dot{\beta} = \frac{\pi}{\sigma_{cr}^s - \sigma_{cr}^f} \dot{\sigma}. \quad (2.60)$$

2.2.5 SMA Model Implementation and Example Load Paths

In implementing the SMA model, a numerical integration approach is taken. Using this approach, the time derivatives of stress and temperature are provided and the respective load vectors are constructed as a function of time. This approach has multiple advantages. First, the loading conditions are simplified as the direction of stress and temperature loads are known by whether their respective time derivatives are positive or negative. Second, without observing the relative rates of stress and temperature loading, it is possible to

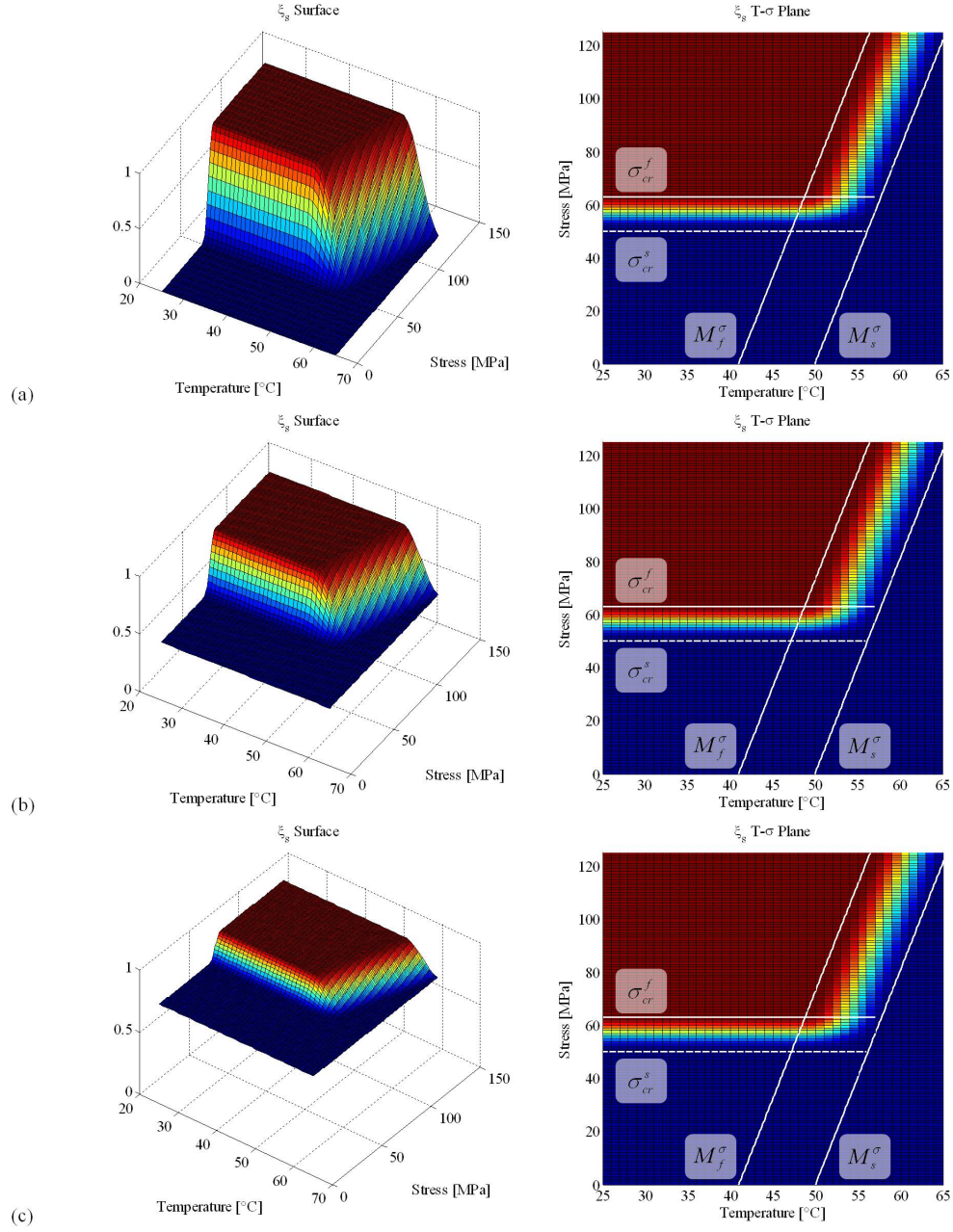


Figure 2.7: Stress-induced transformation surfaces through regions 1, 2a, 2b, and 3 for initial volume fractions of: (a) $\xi_{so} = 0$; (b) $\xi_{so} = 0.5$; (c) $\xi_{so} = 0.8$.

inadvertently calculate an evolving volume fraction when the transformation is not actually occurring. An example is in region 2a of the original bivariant model in the determination of $\Delta_{T\xi}$, (2.28), which increases for decreasing temperature. However, if the loading is such that temperature is decreasing while $\dot{\sigma}/\dot{T} > C_M$, the load path is exiting the martensitic transformation region rather than traversing through it. Situations similar to this arise with proportional stress-temperature load paths and are more easily identified by observing the time derivatives of the applied loads. An additional advantage to this approach is the dependence of all variables on time. While the current model is rate independent with respect to time, the inclusion of a time variable allows for future additions to the model that account for rate dependencies on the reaction to stress and temperature loads. One example is high mechanical loading rates which increase the internal temperature of the SMA, thereby affecting the critical stresses [27, 107].

The SMA code can be implemented following the flow charts given in Figures 2.8, 2.9, and 2.10. First the time vector is initialized by selecting a time step. The user inputs the initial conditions (σ_o , T_o , ξ_{so} , and ξ_{To}) and the stress-temperature load path as a series of time derivatives. Material properties are included in the script but can be changed to model different alloys. Next, the stress and temperature load vectors are calculated through numerical integration. Using the calculated stress and temperature vectors, the stress-dependent transformation temperatures and temperature-dependent critical stresses are determined. For each time step, the time derivative of the total volume fraction is calculated followed by the time derivative for stress-induced volume fraction. From (2.2), if two of the volume fraction values are known, the third can be determined. From this it follows that if two of the values for the volume fraction derivatives are known, the third can be determined, thus it is sufficient to only calculate $\dot{\xi}$ and $\dot{\xi}_s$ independently. Numerical integration is again utilized to determine the values of the martensitic volume fraction components which are in turn used to determine the strain response in the modeled SMA:

$$\epsilon = \frac{1}{E(\xi)} (\sigma - \sigma_0) + \alpha (T - T_0) + \epsilon_L (\xi_s - \xi_{so}). \quad (2.61)$$

The strain equation takes into account elastic, thermal, and transformation strains. Elastic

modulus does vary with phase and is calculated as a rule of mixtures:

$$E = \xi E_M + (1 - \xi) E_A. \quad (2.62)$$

The model currently assumes CTE does not vary with phase and since thermal expansion is a small component in many loading paths. This is a sufficient assumption for the time being as the change in the CTE between the martensite and austenite phase of NiTi, the specific alloy studied herein, is $4.4\mu\epsilon/^\circ\text{C}$ [36]. This could be implemented into the model in a manner similar to the change in elastic modulus in (2.62).

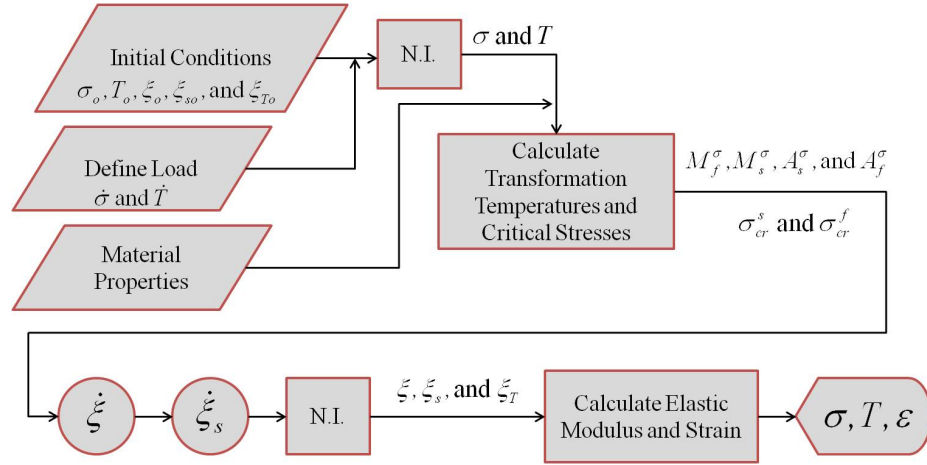


Figure 2.8: Overview of the process used in SMA Numerical Integration (N.I.) code.

The SMA model is used to generate example load paths, using an m-code provided in Appendix A, such as isobaric temperature cycles (Figures 2.11 and 2.12), an isothermal stress cycle (Figure 2.13), and paths with proportional load-temperature inputs similar to loadings observed in composites (Figures 2.14 and 2.15) are demonstrated. Additional loading scenarios including piecewise closed-loop load paths and minor loops are further discussed in Appendix A.

Figure 2.11 presents a simulation of an initially temperature-induced martensitic SMA undergoing a thermal cycle at low stress. The load path traverses regions 4 and 3 on the phase diagram, Figure 2.2 (b), first inducing the $M - A$ transformation upon heating, then

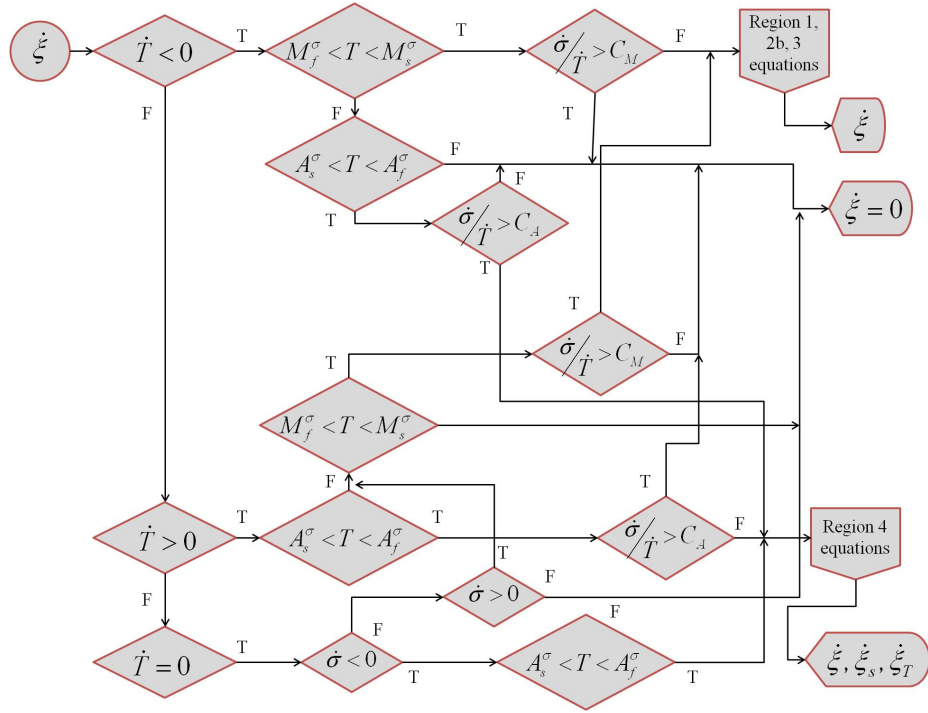


Figure 2.9: Flow chart for determining total martensitic volume fraction evolution in SMA code.

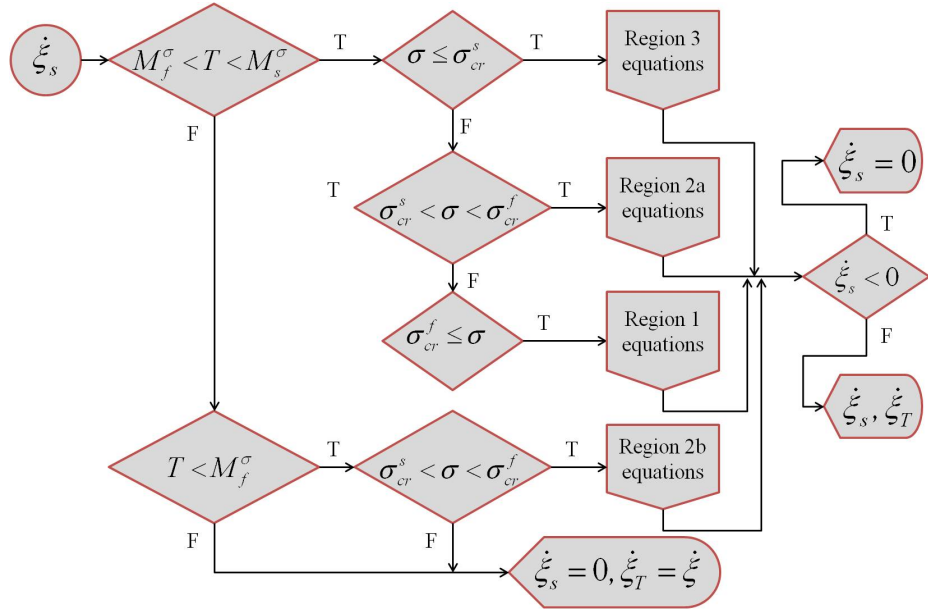


Figure 2.10: Flow chart for determining total stress-induced martensitic volume fraction evolution in SMA code.

the $A - M$ transformation on cooling. Because the martensite is initially temperature-induced, there is no strain recovery and the major contribution to strain is thermal expansion. A slight hysteretic region is observed in the strain-temperature plot but this is due to the change in modulus of the SMA as it transforms from the low modulus martensitic phase to high modulus austenite phase. Since there is a low stress maintained on the SMA, there is a corresponding change in strain as the transformation affects the SMA modulus. If a free-heating scenario was observed with no applied mechanical load, there would be no hysteretic region and only a linear temperature-strain relationship as the model assumes that both phases have the same CTE.

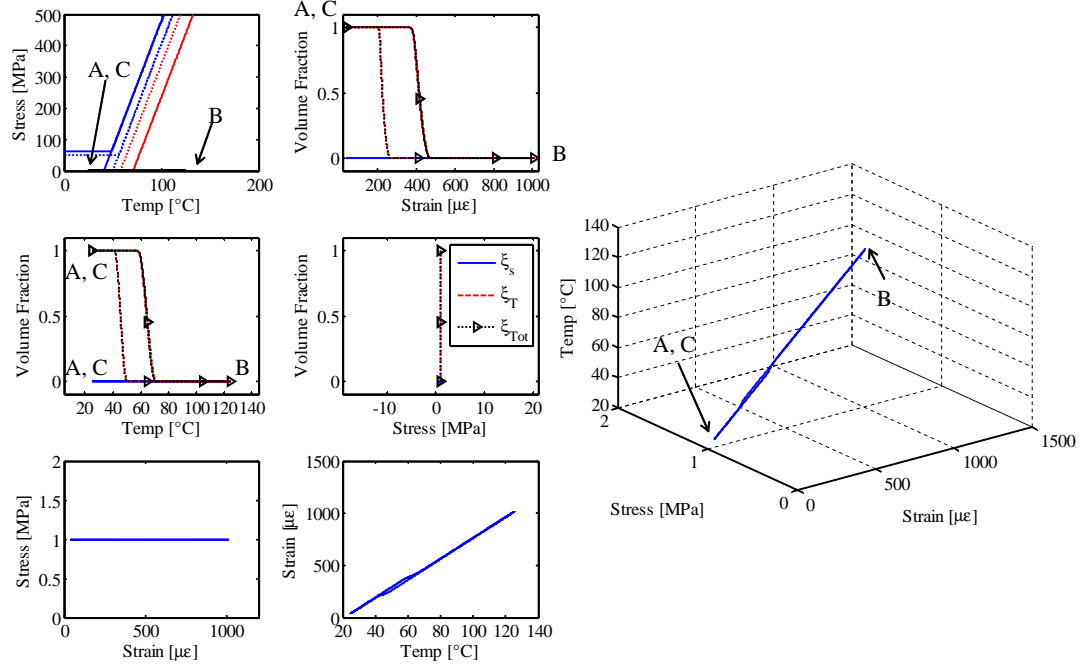


Figure 2.11: Low stress isobaric temperature cycle of initially temperature-induced martensitic SMA. $\xi_{T_o} = 1$, $T_o = 25^\circ\text{C}$, $\sigma_o = 1$ MPa. Load follows points A, B, and C in order.

A similar condition is modeled in Figure 2.12 with the only difference being the initial phase of the SMA, fully detwinned martensite, $\xi_o = \xi_{so} = 1$. In this case the transforma-

tion through region 4 of the phase diagram causes a 6% strain recovery as the detwinned martensite transforms to austenite. Upon cooling, the SMA undergoes the same decrease in strain with decreasing temperature as observed in the previous case.

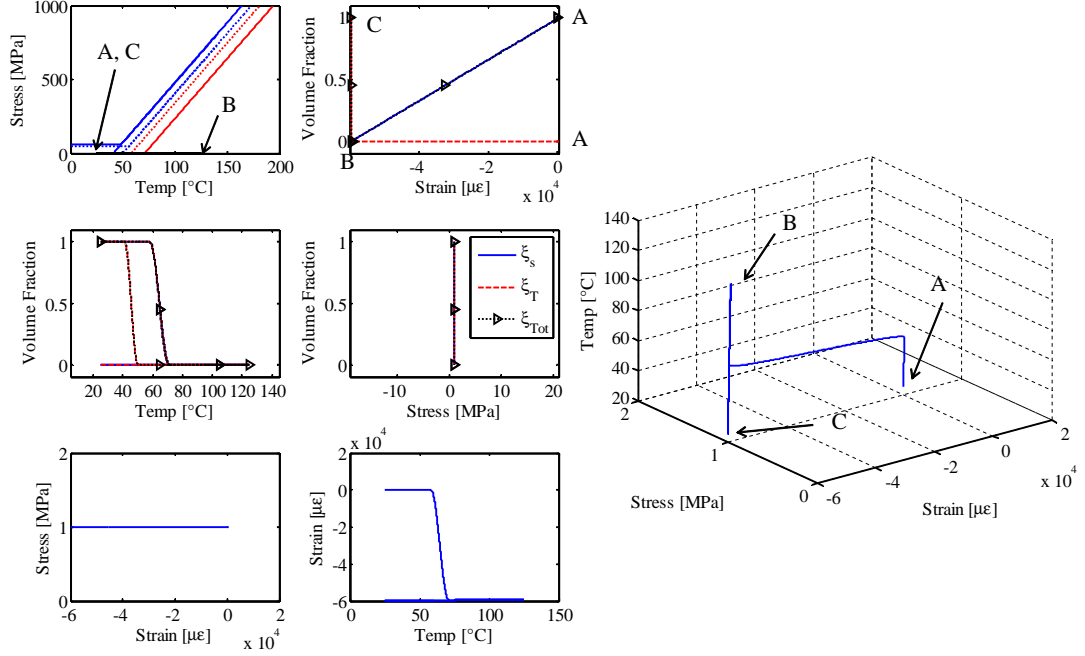


Figure 2.12: Low stress isobaric temperature cycle of initially stress-induced martensitic SMA. $\xi_{so} = 1$, $T_o = 25^\circ\text{C}$, $\sigma_o = 1$ MPa. Load follows points A, B, and C in order.

The next case is a low temperature isothermal stress cycle which demonstrate the one-way behavior of the detwinning process. The SMA in this case is initially temperature-induced martensite, $\xi_o = \xi_{T_o} = 1$, and loading above the critical start stress causes a large increase in strain for little increase in stress. As seen in Figure 2.13, neither the temperature-induced volume fraction, nor the transformation strain is recovered upon release of the load. This loading condition followed by the low temperature isobaric thermal cycle in Figure 2.12 constitutes a single cycle of the one-way shape memory effect.

When combined with a second material in a composite structure, it is unlikely that

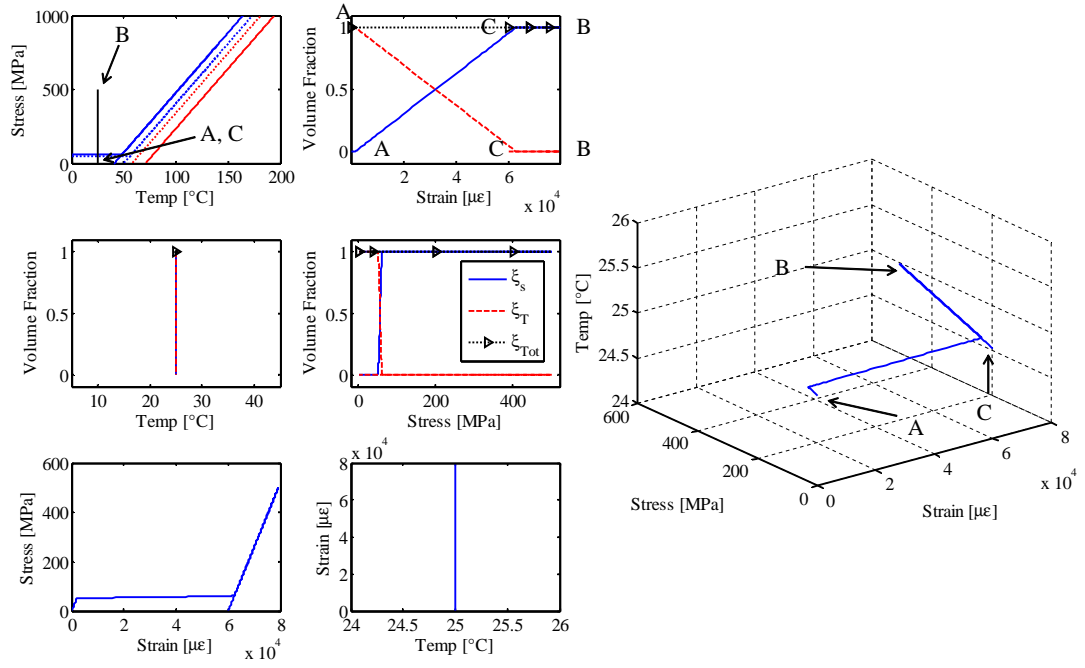


Figure 2.13: Low temperature isothermal stress cycle of initially temperature-induced martensitic SMA. $\xi_{T_o} = 1$, $T_o = 25^\circ\text{C}$, $\sigma_o = 0$ MPa. Load follows points A, B, and C in order.

an SMA will be subjected to an isobaric thermal load as differences in CTEs will cause a proportional increase in stress with temperature. To that end, Figure 2.14 describes a proportional thermal-mechanical load path. To further investigate the effect of different transformation regions, this load path was chosen such that multiple phase diagram regions are traversed. An initially temperature-induced martensitic SMA is proportionally loaded, first encountering the low temperature stress-induced transformation region (2a), then nearly completes the detwinning process in the mixed transformation region (2b). Further increases in temperature cause a mixed temperature-induced and stress-induced transformation to austenite, recovering any transformation strain induced during low temperature loading. Upon cooling, the SMA begins to undergo a partial $A - M^+$ transformation in region 1, however stress becomes too low to fully transform the austenite to stress-induced martensite. As temperature continues to drop, the remaining austenite is transformed, instead, to temperature-induced martensite.

The final example load path, Figure 2.15, performs two cycles of a proportional stress-temperature loading taking the SMA only partially through the martensitic transformation region. The observed load path partially traverses the mixed transformation region (2b), and the high stress transformation region (region 1). On unloading, none of the stress-induced martensite is recovered and the SMA has an initially mixed stress and temperature-induced volume fraction to begin the second loading cycle. While traversing the same phase diagram regions, the amount of additional stress-induced martensite is proportional to the remaining temperature-induced martensite (or combined with remaining austenite if initially present). This type of loading may be significant if sufficient stress is developed at low temperature due to unequal CTEs between an SMA and matrix material in a composite sample.

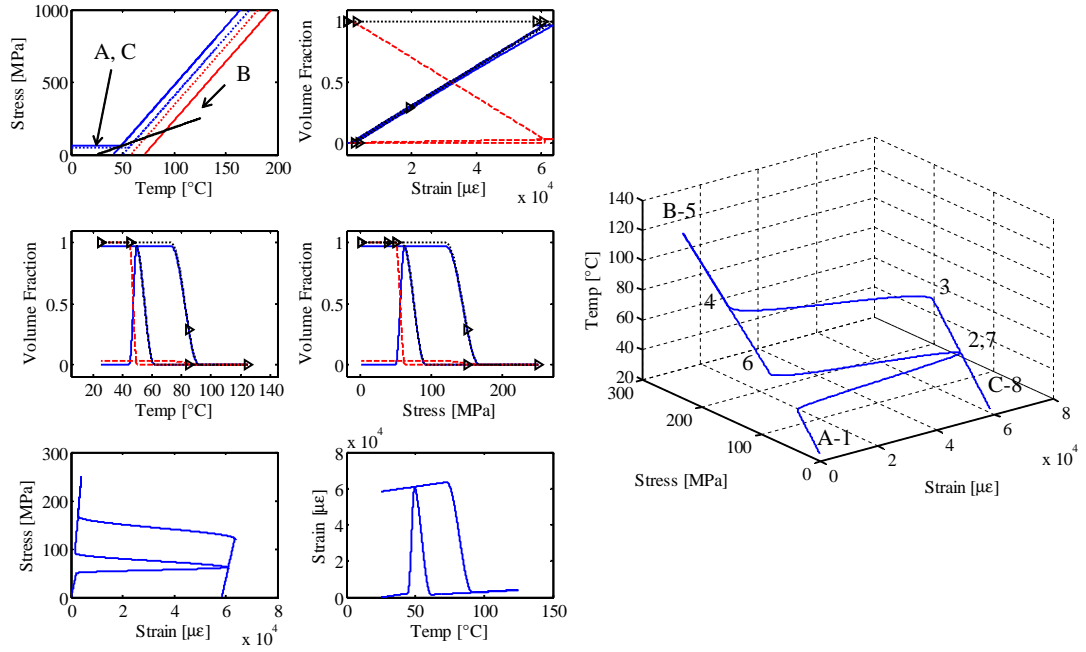


Figure 2.14: Proportional stress-temperature load path traversing multiple transformation regions. $\xi_{T_o} = 1$, $T_o = 25^\circ\text{C}$, $\sigma_o = 0$ MPa. Load follows points A, B, and C in order with intermediate points 1-8 in ascending order.

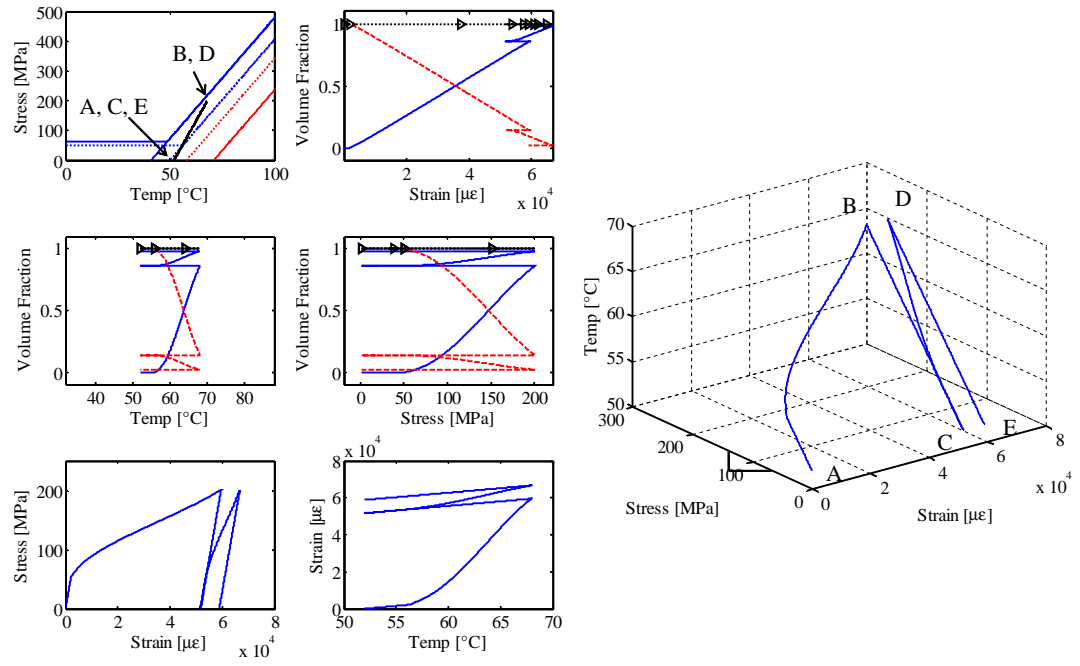


Figure 2.15: Proportional stress-temperature partial transformation load path. $\xi_{T_0} = 1$, $T_0 = 52^\circ\text{C}$, $\sigma_0 = 0$ MPa. Load follows points A-E in order.

2.3 Shape Memory Alloy Composite Modeling

2.3.1 Background

The new bivariant model presented in section 2.2 is integrated into an SMA composite modeling framework by Sittner [74–77]. The composite framework initially uses a phenomenological SMA model to describe the behavior of composites. The SMA model is reliant on fitting parameters adjusted such that model output matches experimental SMA data. The phenomenological SMA composite framework is used because of its success in predicting the behavior of SMA-epoxy based composites and its basis on the time derivatives of stress and temperature loads simplifies transformation conditions.

Phenomenological Model for SMAs and SMA Composites

Sittner et al. [74–77] developed a model for the hysteretic response of SMAs. This model differs significantly from the bivariant model in that it does not distinguish between twinned and detwinned martensite and bases the direction of transformation on an equilibrium temperature. Further, the phenomenological model uses several parameters to capture the effects due to the polycrystalline nature of SMA elements. This model utilizes a minimum of seven material parameters which are determined through experimental characterization of a stable SMA specimen. In addition to material properties, this model uses seven fitting parameters which are used to match the model output to an isothermal stress-strain curve of the material of interest. The addition of the fitting parameters are necessary as the material properties do not provide sufficient information on the thermomechanical hysteresis of the SMA since only the martensite and austenite start temperatures are used in the model formulation. The seven material properties and seven fitting parameters are summarized in Table 2.3.

The phenomenological model does not distinguish between thermally-induced and stress-induced martensite because the authors cite that while the separation of thermal and stress-induced martensite evolution is well modeled in single crystal SMA elements, the separation creates difficulties in continuum modeling of polycrystalline elements. To this end, they

Table 2.3: Material properties used for the phenomenological SMA model.

Property	Description [Units]	Source
E	Elastic Modulus [GPa]	Experimental Characterization
α	Coefficient of Thermal Expansion [$\mu\epsilon/^\circ\text{C}$]	
γ_m	Maximum Transformation Strain [non-dimensional]	
M_s	Martensitic Start Temp [$^\circ\text{C}$]	
A_s	Austenitic Start Temp [$^\circ\text{C}$]	
s	Temperature Dependence of Transformation Stress [$\text{MPa}/^\circ\text{C}$]	
σ^{re}	Reorientation Stress Below M_f [MPa]	Fit to $\sigma - \epsilon$ Plot
G	Fitting Term for ξ	
c	Fitting Term for Hysteresis	
n	Exponential Term for $\dot{\xi}$	
m	Exponential Term for $\dot{\xi}$	
l	Exponential Term for $\dot{\xi}$	
k_1	Fitting Term for ϵ^{tr}	
k_2	Fitting Term for ϵ^{tr}	

present a general thermomechanical driving force for the martensitic transformation and martensitic volume fraction, ξ . All transformations are assumed to be rate independent. The rate of change of the martensitic volume fraction is taken as a function of an internal variable,

$$\phi = T - \sigma/s, \quad (2.63)$$

and its derivative with respect to time,

$$\frac{d\phi}{dt} = \frac{dT}{dt} - \frac{1}{s} \frac{d\sigma}{dt}, \quad (2.64)$$

where T and σ are arbitrary time dependent temperature and stress loads, respectively. This internal variable serves to combine the effects of temperature and stress in the NiTi transformation. An equilibrium between the two phases of the NiTi are assumed to exist when

$$\phi - T_o(\xi) = 0 \quad (2.65)$$

where

$$T_o(\xi) = \left(M_s - \frac{\sigma_{re}}{s}\right) (1 - \xi) + \left(A_s - \frac{\sigma_{re}}{s}\right) \xi. \quad (2.66)$$

If $\phi - T_o(\xi)$ is not equal to zero there is a driving potential which will cause a change

in the volume fraction. The volume fraction rates are given as:

$$\dot{\xi} = \begin{cases} -c \frac{G}{s} \xi^l (1 - \xi)^{m+n} e^{-G(\phi - T_o)} \dot{\phi} & \text{for } \dot{\phi} \geq 0 \text{ (} A - M \text{)} \\ -c \frac{G}{s} \xi^{n+l} (1 - \xi)^m e^{G(\phi - T_o)} \dot{\phi} & \text{for } \dot{\phi} \leq 0 \text{ (} M - A \text{)}. \end{cases} \quad (2.67)$$

The change in martensitic volume fraction is driven by the internal variable which is driven by arbitrary thermal and mechanical loads. As such, the model is able to describe the volume fraction evolution of an SMA under an arbitrary stress-temperature load path. The martensitic volume fraction at any point in time is found by numerically integrating the time derivatives in (2.67).

Strain in the SMA is modeled as a constitutive equation with elastic, thermal, and transformation components, ϵ^{el} , ϵ^{th} , and ϵ^{tr} , respectively:

$$\epsilon^{SMA} = \epsilon^{el} + \epsilon^{th} + \epsilon^{tr} = \frac{\sigma}{E} + \alpha (T - T_s) + \xi \gamma_m \tanh \left(k_1 \frac{\sigma}{\sigma_{re} - k_2} \right). \quad (2.68)$$

In (2.68), T_s is the initial temperature and k_1 and k_2 are additional fitting parameters to match the hyperbolic tangent function to the shape of the transformation regions in the stress-strain curve of the SMA being modeled.

This model has been expanded to include the modeling of SMA composite structures [75–78] by matching the strain in a well defined thermoelastic matrix material to the strain of the SMA element:

$$\epsilon^{SMA}(\sigma, T, \xi) = \epsilon^c + \frac{\sigma}{E_c} + \alpha^c (T - T_s). \quad (2.69)$$

Here, ϵ^c is the transformation strain or prestrain in the SMA when the constrain of the matrix is applied, E_c is the elastic modulus of the matrix, and α_c is the CTE of the matrix. The generalized nature of the phenomenological model allows it to be used for any type of matrix material whose thermomechanical properties are readily defined. This model has been used as a design tool and to calculate the stress state of SMA wires within epoxy based composites.

While this model is useful for the strain response of an SMA or SMA composite to arbitrary thermal and mechanical loads, it relies heavily on fitting parameters which must

be reevaluated from specimen to specimen. While parameters G , c , l , m , and n have a basis in the underlying behavior of polycrystalline SMAs, the parameters k_1 and k_2 do not. These fitting parameters are freely varied to match the transformation strain, ϵ^{tr} , to observed transformation behavior where as other models can accomplish this through the use of additional material properties.

2.3.2 Addition of Matrix Constraint

The effect of the matrix constraint on the SMA is dependent upon the SMA prestrain. The contribution of SMA prestrain level to the overall behavior of the composite is illustrated in Figure 2.16. In considering an SMA in an unconstrained state, if there is no prestrain, the twinned martensitic phase will transform to austenite upon heating, though the only change in sample strain will be a small increase through thermal expansion. If an identical SMA sample is first prestrained to completely detwin the martensitic phase, upon heating and subsequent transformation to austenite, it will recover all of the induced prestrain, 6% for NiTi, in the opposite direction of thermal expansion.

If both SMA samples are embedded in a matrix to create two composites, equal except for the level of SMA prestrain, they will exhibit different thermally-induced strain behaviors. The SMA composite with no prestrain will undergo thermal expansion and a relatively small increase in strain as the composite is heated and the SMA transforms to austenite. However, the composite with the prestrained SMA embedded within the matrix will experience a reduced and possibly negative thermally-induced strain due to the partial constraint of the SMA. Through transformation, the SMA will recover strain or generate a compressive stress on the matrix if strain recovery is inhibited. The exact behavior and magnitude of strain is dependent upon the modulus and CTE of both the fiber and matrix in addition to the prestrain of the SMA and is discussed further in this section.

Modeling SMA composites represents a unique challenge because the SMA is partially constrained by the surrounding matrix. Using the new bivariant constitutive model described, the strain-matching algorithm utilized in the phenomenological SMA composite model is applied to calculate the thermally-induced strain behavior and stresses developed

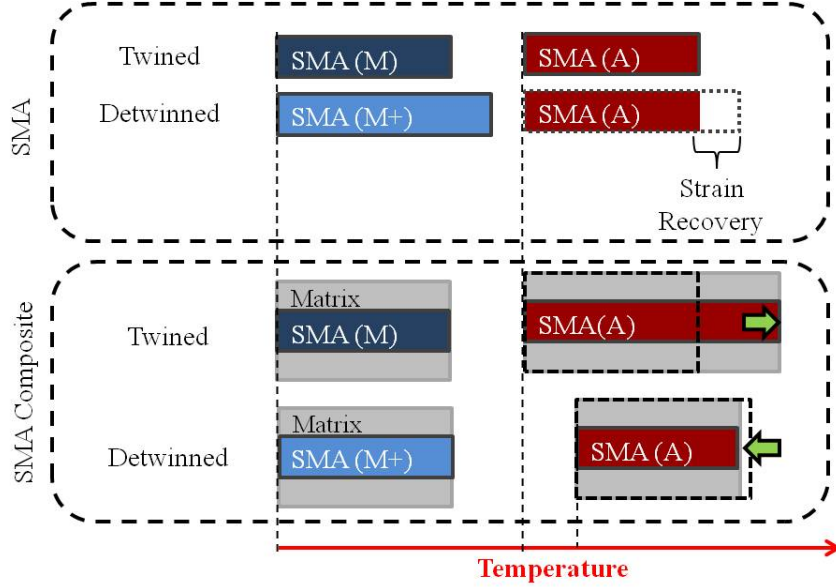


Figure 2.16: The effect of SMA prestrain illustrated for an unconstrained SMA element and for a composite with an embedded SMA element. In the unconstrained state, the SMA will recover any strain induced during detwinning. When constrained by the composite matrix, the recovery of the strain or generation of blocking stresses reduce the amount of thermally-induced composite strain.

within the SMA elements when embedded in a thermoelastic matrix. In the strain-matching algorithm, the thermomechanical load is represented by the rate of change of the temperature and the stress applied to the composite. While an external stress can be applied in the model, the time derivative of stress also is a function of temperature if the CTEs of the SMA and matrix are not equal. Similar to the SMA-only model, numerical integration is used to determine the stress, temperature, and volume fractions of the composite at any given point in time. The resulting values are then used to determine composite strain, ϵ_{comp} which is equal to the strain in the matrix, ϵ_m , and strain in the fiber/SMA, ϵ_f :

$$\epsilon_{comp} = \epsilon_m = \frac{1}{E_m}(\sigma_m - \sigma_{mo}) + \alpha_m(T - T_o) = \epsilon_f \quad (2.70)$$

where E_m is the elastic modulus of the matrix, σ_m is the stress in the matrix, and α_m is the the matrix CTE. Expanding the above equation with (2.61) substituted for ϵ_f provides

$$\frac{1}{E_f}(\sigma_f - \sigma_{fo}) + \alpha_f(T - T_o) + \epsilon_L(\xi_s - \xi_{so}) = \frac{1}{E_m}(\sigma_m - \sigma_{mo}) + \alpha_m(T - T_o) \quad (2.71)$$

where σ_f is the stress in the fiber/SMA. Assuming no external loads, a force balance is used to obtain the stress in the matrix in terms of SMA stress:

$$\begin{aligned} \sigma_f A_f + \sigma_m A_m &= 0 \\ \sigma_m &= -\frac{A_f}{A_m} \sigma_f \\ \sigma_m &= \frac{-v}{(1-v)} \sigma_f, \end{aligned} \quad (2.72)$$

where A_f and A_m are the cross-sectional areas of the SMA and matrix, respectively. The variable change from cross-sectional area to fiber volume fraction, v , can be made by assuming the SMA fibers provide long-fiber reinforcement of the matrix and the lengths of both components are equal, $L_f = L_m = L$:

$$\begin{aligned} v &= \frac{v_f}{v_{tot}} \\ v &= \frac{v_f}{v_f + v_m} \\ v &= \frac{A_f L}{A_f L + A_m L} \\ v &= \frac{A_f}{A_f + A_m}. \end{aligned} \quad (2.73)$$

Assuming zero initial stress, the stress in the SMA can be obtained as a function of temperature, material properties, volume fraction, and transformation terms by substituting (2.72) into (2.71),

$$\frac{1}{E_f} \sigma_f + \alpha_f(T - T_o) + \epsilon_L(\xi_s - \xi_{so}) = \frac{1}{E_m} \left(\frac{-v}{(1-v)} \sigma_f \right) + \alpha_f(T - T_o) \quad (2.74)$$

and solving for σ_f :

$$\sigma_f = \frac{(\alpha_m - \alpha_f)(\Delta T)}{\frac{1}{E_f} + \frac{1}{E_m} \frac{v}{(1-v)}} - \frac{\epsilon_L(\xi_s - \xi_{so})}{\frac{1}{E_f} + \frac{1}{E_m} \frac{v}{(1-v)}}. \quad (2.75)$$

This equation has two components: the first is the thermoelastic component which applies to any long-fiber reinforced composite; the second is due to the transformation-induced strain recovery of the SMA if it is embedded in a detwinned state ($\xi_{so} \neq 0$). If the embedded SMA elements are not prestrained before fabrication, only the thermoelastic stress component remains but is non-linear due to the change in modulus during transform between martensite and austenite. Once the SMA stress is calculated it can be used in (2.61) to determine total composite strain:

$$\epsilon_{comp} = \epsilon_f = \frac{1}{E_f} \left[\frac{(\alpha_m - \alpha_f)(\Delta T)}{\frac{1}{E_f} + \frac{1}{E_m} \frac{v}{1-v}} - \frac{\epsilon_L(\xi_s - \xi_{so})}{\frac{1}{E_f} + \frac{1}{E_m} \frac{v}{1-v}} \right] + \alpha_f(\Delta T) + \epsilon_L(\xi_s - \xi_{so}). \quad (2.76)$$

Expanding (2.76) gives

$$\epsilon_{comp} = \frac{E_f v \alpha_f + E_m (1-v) \alpha_m}{E_f v + E_m (1-v)} \Delta T - \frac{E_f v \epsilon_L (\xi_{so} - \xi_s)}{E_f v + E_m (1-v)}. \quad (2.77)$$

The same result is obtained by calculating the matrix stress and using it in (2.70). Again, if the stress-induced martensitic volume fraction term is ignored, the first component of the strain equation in (2.77) describes the thermally-induced strain for a typical long-fiber reinforced composites [66, 79]. The second term is unique to SMA composites.

2.3.3 Composite Model Implementation

Due to the mutual dependence of stress and martensitic volume fraction in the composite model, the stress derivative cannot be prescribed but rather must be calculated for each time step. In addition to the temperature dependence of stress via the martensitic volume fraction, the model allows for a varying elastic modulus of the matrix as a function of temperature which causes stress to change even if the volume fraction is constant and $\alpha_f = \alpha_m$.

The stress from (2.75) is simplified to by

$$\sigma_f = \lambda\theta + \kappa\theta \quad (2.78)$$

where

$$\lambda = (\alpha_m - \alpha_f) (T - T_o), \quad (2.79)$$

$$\kappa = -\epsilon_L (\xi_s - \xi_{so}), \quad (2.80)$$

and

$$\theta = \frac{1}{\frac{1}{E_f} + \frac{1}{E_m} \frac{v}{1-v}}, \quad (2.81)$$

which, considering the variable SMA modulus, becomes

$$\theta = \frac{1}{\frac{1}{E_M \xi + E_A (1 - \xi)} + \frac{1}{E_m} \frac{v}{1-v}}. \quad (2.82)$$

The derivative of (2.78) is found through the chain rule:

$$\dot{\sigma}_f = \dot{\lambda}\theta + \lambda\dot{\theta} + \dot{\kappa}\theta + \kappa\dot{\theta} \quad (2.83)$$

where

$$\dot{\lambda} = (\alpha_m - \alpha_f) \dot{T}, \quad (2.84)$$

$$\dot{\kappa} = -\epsilon_L \dot{\xi}_s, \quad (2.85)$$

and

$$\dot{\theta} = \left[\frac{(E_M - E_A) \dot{\xi}}{E_f^2} + \frac{\frac{dE_m}{dT} \dot{T}}{\left(E_m^2 \frac{v}{1-v} \right)} \right] \left(\frac{1}{E_M \xi + E_A (1 - \xi)} + \frac{1}{E_m} \frac{v}{1-v} \right)^{-2}. \quad (2.86)$$

Table 2.4: Matrix properties used for SMA composite model numerical examples. Values are for Al 3003-H18 [38].

Property	Description	Value
E_m	Matrix Elastic Modulus at 25°C	69 GPa
$\frac{dE_m}{dT}$	Matrix Modulus Temperature Coefficient	-46.7 MPa/°C
α_m	Coefficient of Thermal Expansion	23.2 $\mu\epsilon$ /°C

These version of the stress and its time derivative are used in all three of the described implementations below. All numerical simulations of SMA composites in this chapter use the same material properties for the SMA component given in Table 2.2 and material properties for the matrix given in Table 2.4.

Incremental Approach

Initial implementation of the matrix constraint utilized an incremental approach: for each time step, a temperature value and temperature derivative were calculated and the stress derivative was calculated based upon the previous time step's values for temperature and martensitic volume fractions. Using these values, new martensitic volume fraction derivatives were calculated and used to determine the current values of the martensitic volume fractions. While this incremental approach works well for composites with very little or no SMA prestrain and hence, little effect from stress-induced martensite recovery (Figure 2.17), the algorithm becomes unstable for values of $\xi_{so} \approx 0.01$. This instability is caused by using previous values of stress to calculate current volume fraction values. At moderate levels of prestrain, stress can increase quickly for a small increase in temperature and the underlying assumption that $\sigma(i-1) \approx \sigma(i)$ is no longer valid. This causes large swings in stress and martensitic volume fraction as seen in Figure 2.18. The exact value of ξ_{so} at the onset of instability depends on material properties, the size of the time increment, and rate of temperature change. As such, the incremental approach is best used for composites with $\xi_{so} = 0$.

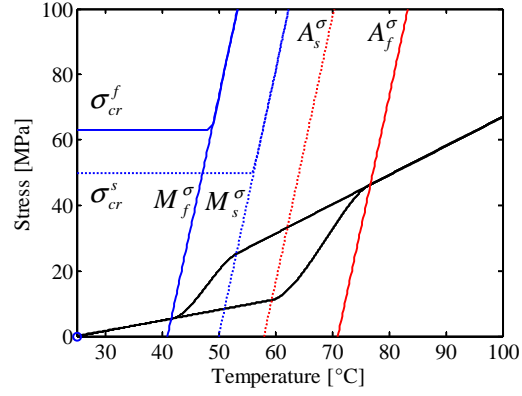


Figure 2.17: Load path for an SMA composite subject to a thermal cycle modeled using the incremental approach with $\xi_{so} = 0$. Load path is superimposed on the SMA phase diagram.

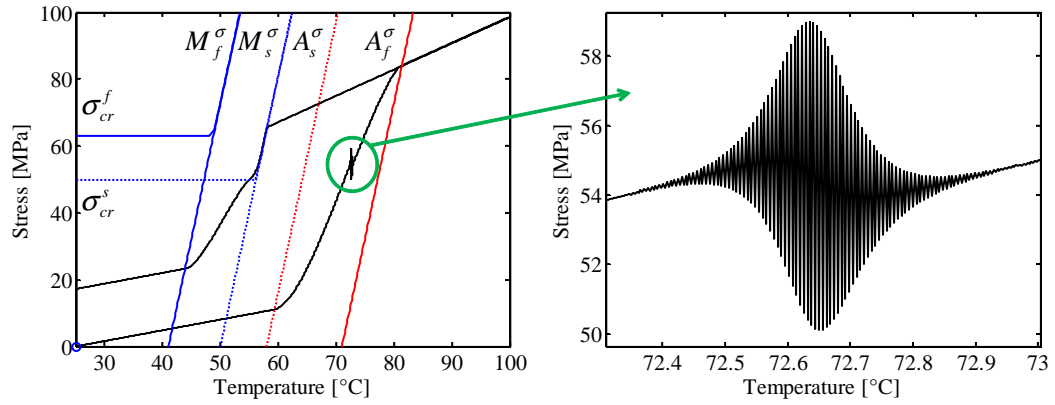


Figure 2.18: Numerical instability for a composite with $\xi_{so} = 0.01$ numerically modeled through the incremental approach.

Volume Fraction Dependent and Interpolation Approach

The second approach for composite model implementation is based of of using the martensitic volume fraction as an independent variable. In considering the transformations for a given composite with well defined properties, any value of martensitic volume fraction between 0 and 1 has a unique set of stress and temperature coordinates on the SMA phase diagram for both the $M - A$ and $A - M$ transformation. Further, when the martensitic volume fractions are equal to 0 or 1, temperature changes that do not cause transformation create a thermoelastic response with composite strain varying only through temperature.

To illustrate the concept, Figure 2.19 (a) shows a stress-temperature plot with A_s^σ and A_f^σ lines plotted to mark the boundaries of the $M - A$ transformation. A series of dotted lines represent the thermoelastic response of a given SMA composite with various martensitic volume fraction values. These lines are plotted using (2.75) varying temperature only, fixing a specific value of ξ , and keeping $\xi_s = \xi_{so} = 0$. Note that these lines do not represent valid stress-temperature coordinates over their entire length; for rising temperatures the $\xi = 1$ line is valid only until it intersects the A_s^σ line and the $\xi = 0$ line is valid at temperatures only beyond its intersection with the A_f^σ line. All other lines are only valid at one point within the transformation region.

Next, lines of constant martensitic volume fraction are determined between A_s^σ and A_f^σ and are denoted by $A_x(\xi, \sigma)$. The $\xi = 1$ and $\xi = 0$ values of A_x are coincident with A_s^σ and A_f^σ , respectively. All other A_x lines have a slope equal to C_A on the temperature-stress phase diagram but intersect the temperature axis at zero stress at different temperatures determined by solving (2.39) for T at different values of ξ :

$$T = A_s + \frac{1}{a_A} \arccos \left(\frac{2}{\xi_o} \xi - 1 \right). \quad (2.87)$$

The equation of the constant martensitic volume fraction lines are given by

$$A_x(\xi, \sigma) = A_s + \frac{1}{a_A} \arccos \left(\frac{2}{\xi_o} \xi - 1 \right) + \frac{\sigma}{C_A}. \quad (2.88)$$

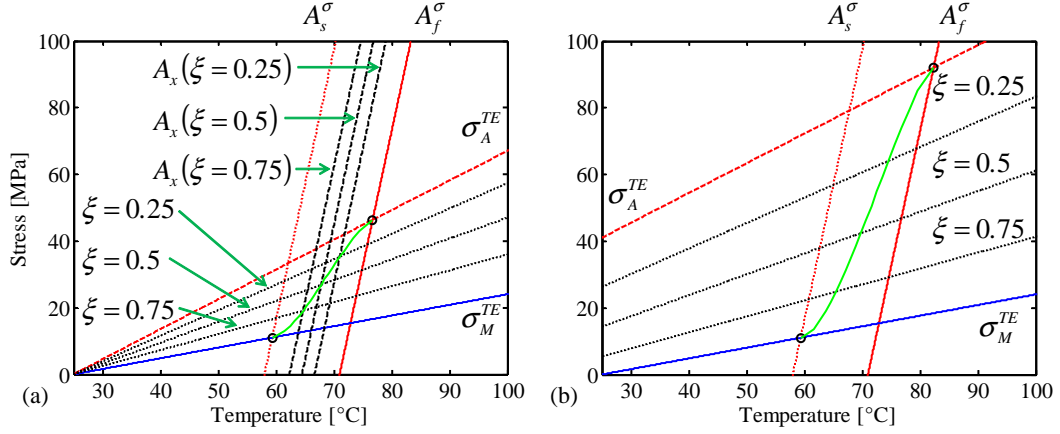


Figure 2.19: Interpolation approach, small circles represent the starting and ending points of transformation and green line represents the stress-temperature path through transformation: (a) Thermoelastic stress lines, σ^{TE} , for fixed values of ξ intersecting constant martensitic volume fraction lines, A_x ; (b) Effect of $\xi_{so} = 0.01$ on thermoelastic stress lines.

For a value of ξ between 0 and 1, the intersection of A_x and the corresponding thermoelastic stress line provides a coordinate in (ξ, T, σ) space. By finding a series of these data points, a look-up tables is created which can be used to find the stress and volume fraction of the SMA in a composite for any given temperature in the $M - A$ transformation region. The same approach can be done for the $A - M$ transformation region using M_x found from (2.37):

$$T = M_f + \frac{1}{a_M} \arccos \left[\frac{2}{1 - \xi_o} \left(\xi - \frac{1 + \xi_o}{2} \right) \right]. \quad (2.89)$$

The equation of the constant martensitic volume fraction lines are given by

$$M_x(\xi, \sigma) = M_f + \frac{1}{a_M} \arccos \left[\frac{2}{1 - \xi_o} \left(\xi - \frac{1 + \xi_o}{2} \right) \right] + \frac{\sigma}{C_M}. \quad (2.90)$$

The effect of stress-induced prestrain gives the thermoelastic stress lines a positive offset from the temperature axis. The amount of offset is equal to the stress-induced volume fraction component in (2.75) for fixed values of ξ , ξ_{so} , and ξ_s . In this case, ξ_s is proportional to ξ through (2.43). The effect of initial stress-induced martensite is shown in Figure 2.19 (b).

This method does not suffer from the numerical instability of the incremental method,

shown in Figure 2.20. However, there are a few disadvantages. First, a new look-up table must be made for every composite. A change in volume fraction, initial external stress, or SMA prestrain will change the data points. Second, it will only work for repeatable behavior; the evolution of stress-induced martensite cannot change over multiple thermal cycles.

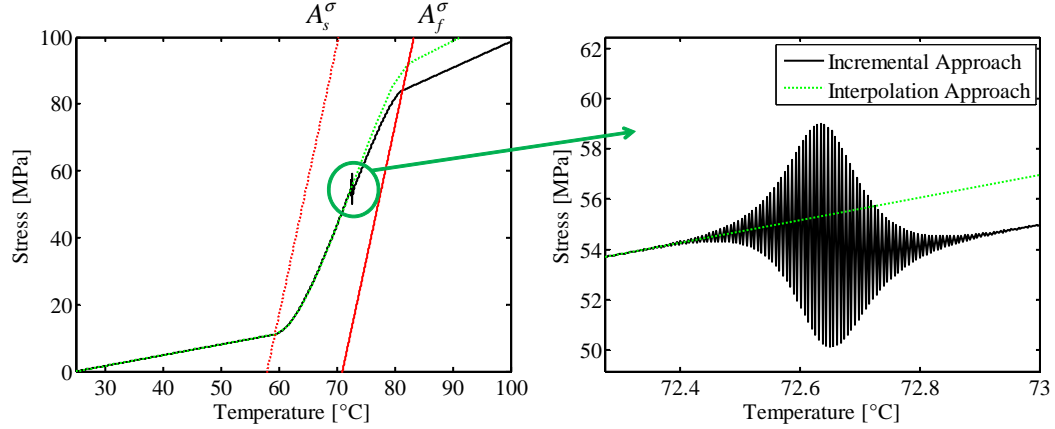


Figure 2.20: Comparison of the interpolation method and incremental method.

Simultaneous Equation Approach

The last model implementation directly addresses the linked nature of SMA stress and martensitic volume fraction when considering a composite structure and solves them simultaneously. Best results are found by simultaneously solving for a total of six equations, ξ , ξ_s , σ , and their derivatives, $\dot{\xi}$, $\dot{\xi}_s$, and $\dot{\sigma}$. The benefit versus interpolation is seen in Figure 2.21. Since the interpolated model is based on an independent martensitic volume fraction value, the data points in on the stress-temperature plot are not equally spaced through the transition region. From the cosine-based transformation functions, small changes in temperature have little effect at the beginning and end of transformation on ξ , but ξ becomes very sensitive to temperature changes mid-transformation. The primary concern is not capturing the onset or completion of transformation very near the transformation temperatures.

The main drawback to the simultaneous equation approach is the time needed to solve the equations.

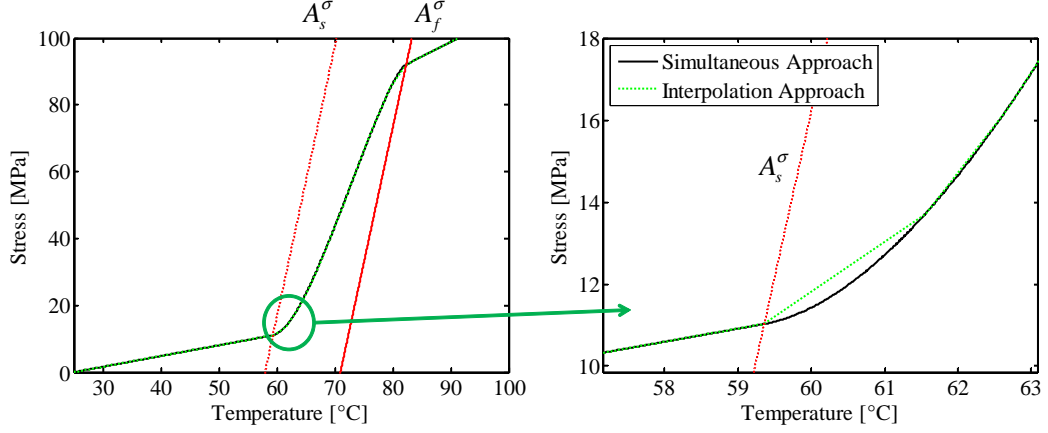


Figure 2.21: Comparison of the simultaneous equation method and interpolation method for modeling SMA composites.

2.4 Summary

In this chapter, a constitutive model was developed that can describe the behavior of an SMA composite in terms of material properties such as elastic modulus and CTE, and composite properties, including the SMA fiber volume fraction and SMA prestrain level. Three implementation methods have been discussed for determining the composite response to arbitrary thermal and mechanical loads.

The underlying SMA model is also a unique contribution. Based upon bivariant SMA models discussed in the literature, the presented formulation has a continuous mixed-transformation region and is applied to a commonly accepted version of the SMA stress-temperature phase diagram. The new model is able to describe both the pseudoelastic and shape memory responses of SMAs.

The developed SMA composite model is applied in the following chapters to describe the thermomechanical behaviors observed in characterization experiments and also aid in the

design of thermally-invariant composites. Since all material and composite properties can be freely varied, the model can be used to describe any long-fiber reinforced SMA composite system regardless of the fiber or matrix material.

Chapter 3

SMA CHARACTERIZATION AND UAM COMPOSITE CONSTRUCTION

3.1 Introduction

This chapter discusses the characterization of the NiTi alloy embedded in the composites studied in this research and the construction of the composites themselves. Material properties and behaviors observed from the NiTi characterization study were used in the models to analyze the responses observed in composites 1 through 3, aid in the design of composite 4, and analyze the results from composite 6. Composite construction methods discussed herein provide unique solutions to the challenges surrounding the fabrication of UAM composites.

3.2 SMA Characterization

The SMA used in this research is equiatomic NiTi provided by NDC in the form of rectangular ribbons 762 μm (0.030 in) wide by 254 μm (0.010 in) thick. Characterization was accomplished through a combination of DSC analysis, electrical resistance tests, isothermal tensile tests conducted at different temperatures, and blocked force tests. From these tests, values for transformation temperatures, the elastic modulus of martensite, critical detwinning stresses, stress-influence coefficients, and maximum transformation strain are determined.

3.2.1 Transformation Temperature Determination

DSC Characterization

In DSC testing, a test sample and a reference sample are heated to the same temperature at a prescribed rate. Both the test sample and reference are heated independently but the power to each heater is adjusted such that the two samples are at the same temperature. The difference in power required to maintain the same temperature is used to identify phase transformations and sample heat capacity as a function of temperature. The $M - A$ transformation of NiTi is endothermic meaning that the transformation can be observed as a significant drop in the relative power. For all DSC analysis presented, the convention for relative power is

$$\Delta P = P_R - P_S \quad (3.1)$$

where ΔP is the relative power, P_R is the power input to the reference sample, and P_S is the power input to the test specimen.

For DSC testing, a NiTi ribbon sample with a mass of 6.2 mg was placed in an Al sample pan. An additional empty Al sample pan was used as the reference. The prescribed heating and cooling rate was $10^\circ\text{C}/\text{min}$ and $-10^\circ\text{C}/\text{min}$, respectively, however the system used for testing did not have active cooling, the consequences of which are discussed momentarily. The heating cycle for the ribbon sample is shown in Figure 3.1. From the plot, the differential power is negative as the additional mass of the NiTi sample requires more power to heat to the same temperature as the empty reference pan by (3.1). As the temperature nears 45°C , the differential power becomes even more negative due to the endothermic $M - A$ transformation. At approximately 70°C the differential power levels off again indicating that the transformation to austenite is complete. From the DSC curve, linear regressions are made over the two flat regions representing the martensite and austenite stages of the heating curve and the falling and rising differential power side of the transformation “peak.” The A_s temperature is found at the intersections of the low temperature regressions of the martensitic region and low temperature side of the endothermic peak while the A_f tem-

perature is found at the intersection of the high temperature side of the peak and high temperature austenitic region of the curve.

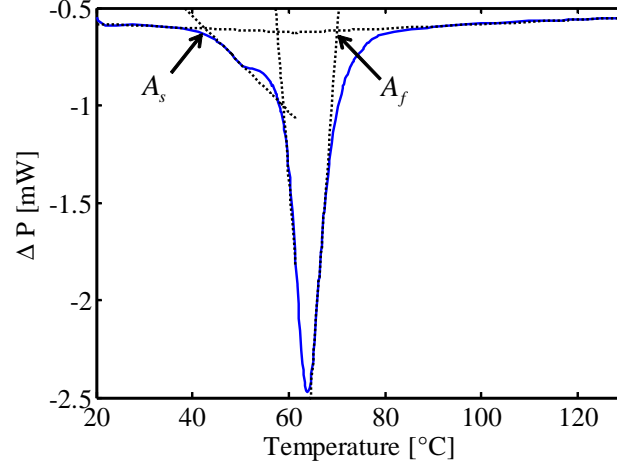


Figure 3.1: DSC curve with linear regressions used to find the austenite transformation temperatures for shape memory NiTi ribbon.

As seen in Figure 3.1, there appears to be a “leveling off” of the endothermic peak between 50°C and 55°C. This may be due to residual stresses in the ribbon as a result of forming the final geometry. Post-processing of SMAs, such as cold rolling, has been shown to change transformation temperatures [54, 61]. In this case, it may cause the $M - A$ transformation to occur in two main groups at slightly different temperatures. As such, the brief power plateau is considered part of the total $M - A$ transformation and the initiation of this phase is considered the effective A_s temperature of the alloy. From this plot, the A_s and A_f temperatures are found to be 45°C and 70°C, respectively.

Since finding the transformation temperatures requires sufficient steady-state behavior of the differential power in terms of temperature, it was not possible to determine the martensitic transformation temperatures with the available DSC equipment. Without active cooling, the system was not able to maintain a consistent cooling rate and as a result, the DSC curves for cooling were not able to provide reliable $A - M$ transformation data.

Electrical Resistance Characterization

Since the DSC cooling curves were unable to provide reliable martensitic transformation temperatures, a second characterization experiment was conducted to observe the change in electrical resistance of the NiTi ribbon. NiTi undergoes a significant change in electrical resistivity as it transforms between its martensite and austenite phase [25, 36, 52, 53, 86, 97]. By measuring the resistance of a NiTi sample as a function of temperature, the transformation temperatures can be determined in a manner similar to DSC.

In this experiment, a NiTi ribbon sample 11 cm long was suspended in an oven with leads attached to either end. The NiTi ribbon was placed in series with a potentiometer and the ribbon/potentiometer system was used as the active leg in a wheatstone bridge. The potentiometer was used to bring the active leg resistance up to $350\ \Omega$. The completed bridge was monitored by a signal conditioning amplifier as the oven was brought to a temperature of 149°C (300°F) and then allowed to cool slowly. Output from the amplifier and a J-type thermocouple placed near the ribbon were monitored to create the temperature versus change in bridge voltage (dV/V_o) plot shown in Figure 3.2. The ribbon was suspended from an acrylic block with a through-hole to prevent any contact with the metal oven shelves in order to avoid changes to the bridge voltage measurement.

While a change in resistance during heating is observed, signaling the $M - A$ transformation, the initial heating response of the oven is fast near the austenite transition temperatures. Since direct contact between the thermocouple and ribbon are avoided to prevent any corruption of the thermocouple or bridge signals, there is an underlying assumption that the ambient temperature surrounding the ribbon is the same as the ribbon temperature. During the fast initial heating of the oven, this assumption is likely not valid. However, during cooling from 149°C , the thermal response has slowed significantly in the expected vicinity of the martensitic transformation temperatures, less than 50°C . As a result, the only temperatures obtained from this experiment are M_s and M_f .

Similar to previous analysis, the the constant phase and transition regions of the resistance response to temperature plot are subject to linear regression. The intersection of the

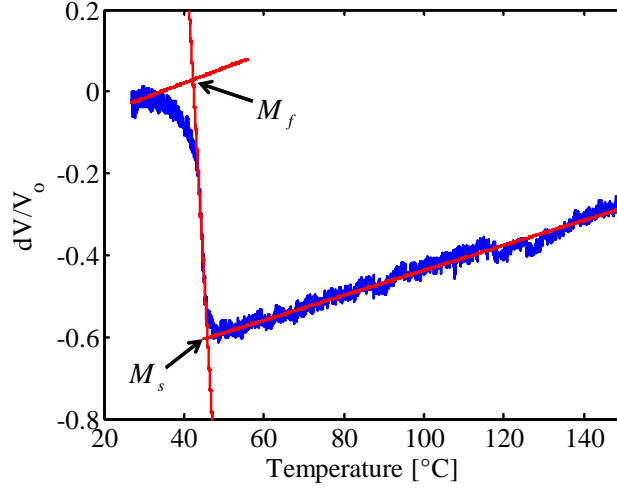


Figure 3.2: Relative change in bridge voltage containing a NiTi ribbon as it cools from 149°C.

Table 3.1: Martensitic transformation temperatures as determined from electrical resistivity tests.

Transformation Temperature	Test 1	Test 2	Test 3
M_s	45°C	45°C	46°C
M_f	41°C	41°C	42°C

resulting lines are taken as the martensitic transformation temperatures. The experiment was repeated a total of three times with resulting transformation temperatures listed in Table 3.1. From this experiment, the average martensite start and finish temperatures at zero stress were found to be 45°C and 41°C, respectively.

3.2.2 Determination of Mechanical Properties

Isothermal Tensile Characterization

Isothermal tensile tests were conducted on a tension/compression load frame with controllable thermal chamber at nominal temperatures of 24°C, 41°C, 57°C, 74°C, and 90°C (corresponding to 75°F, 105°F, 135°F, 165°F, and 195°F, increments of 30°F on the thermal chamber controller). The load profile consisted of a initial loading under displacement

control to 11.3 kg (25 lbf) at 1.27 mm/min (0.05 in/min). The initial ribbon length was 38 mm (1.5 in) as measured from a twinned martensitic state attained by heating the ribbon and allowing it to cool unloaded.

Using linear regression, the stiffness of different regions of the load-displacement plots was obtained and intersection points of linear regressions of the first elastic region, detwinning plateau, and second elastic region were used to find critical start and finish loads. With the cross-sectional area of the ribbon and the gage length, critical start and finish stresses were found as well as the elastic moduli at different portions of the load cycle for each temperature. An example of the linear regressions and intersection points are shown in Figure 3.3. A comparison of the stress-strain plots for each temperature is shown in Figure 3.4. As temperature increases above 41°C, so does the critical stresses that define the detwinning plateau and the slope of the initial linear region due to the temperature-induced $M - A$ transformation.

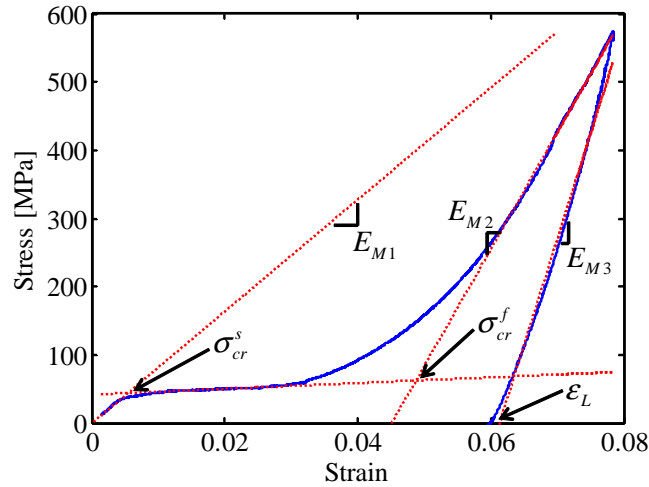


Figure 3.3: Room temperature stress-strain plot of NiTi ribbon. Dotted lines are linear regressions of the elastic and detwinning plateau regions.

Results from the tensile tests conducted at 24°C and 41°C were used to find the critical start and finish stresses by extending linear regressions of the initial elastic loading, de-

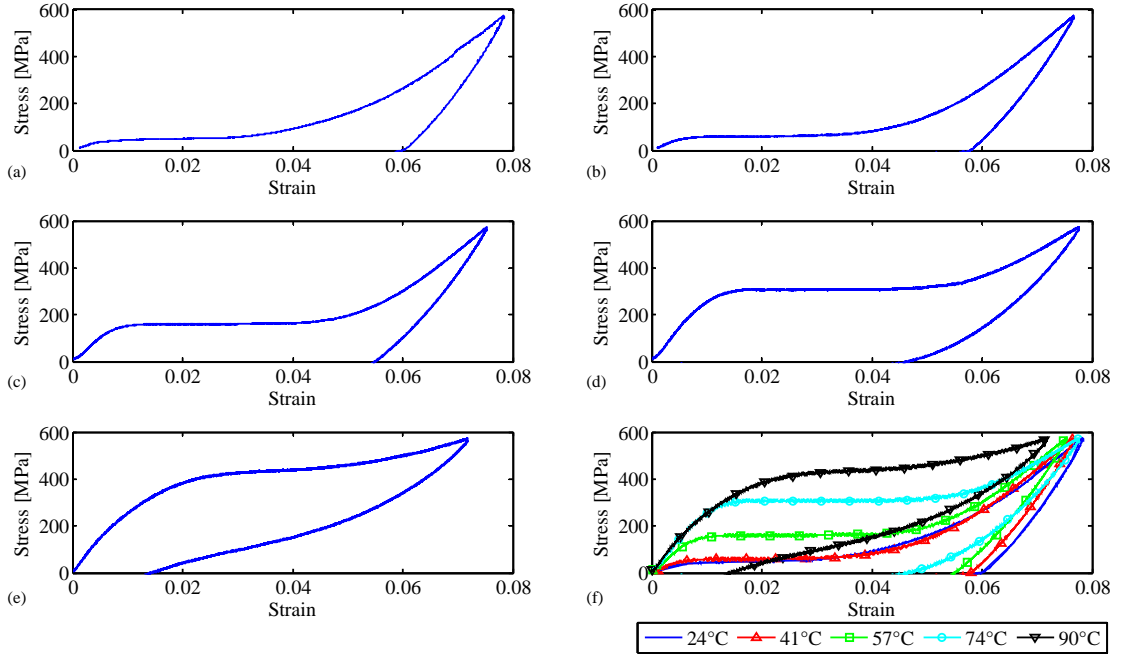


Figure 3.4: Isothermal stress-strain plots for NiTi ribbon: (a) $T=24^{\circ}\text{C}$, (b) $T=41^{\circ}\text{C}$, (c) $T=57^{\circ}\text{C}$, (d) $T=74^{\circ}\text{C}$, (e) $T=90^{\circ}\text{C}$, (f) Comparison of all temperatures.

twinning plateau, and second elastic region. At room temperature, the critical detwinning start and finish stresses were found to be 50 MPa and 63 MPa, respectively. The room temperature test was also used to quantify the maximum recoverable strain, ϵ_L . As seen from Figure 3.4 (a), the stress returns to zero with a residual strain of 6%. For all other temperatures, the critical detwinning start and finish stresses were recorded and plotted as a function of temperature. The resulting plot is shown in Figure 3.5. As seen in typical SMA phase diagrams (Figures 2.1 and 2.2), the critical stresses do not increase until temperatures exceed the martensite transition temperatures. Above 41°C , the critical stresses begin to increase linearly with temperature. The slope of the critical stress versus temperature plot gives the martensitic stress influence coefficient, C_M . For these experiments, the average of the slopes for both the critical start and finish stress plots gives $C_M=8.1 \text{ MPa}/^{\circ}\text{C}$.

After isothermal testing, the ribbon was axially loaded until failure as shown in Figure 3.6. Using a linear regression of the second linear region and applying a 0.2% offset [33],

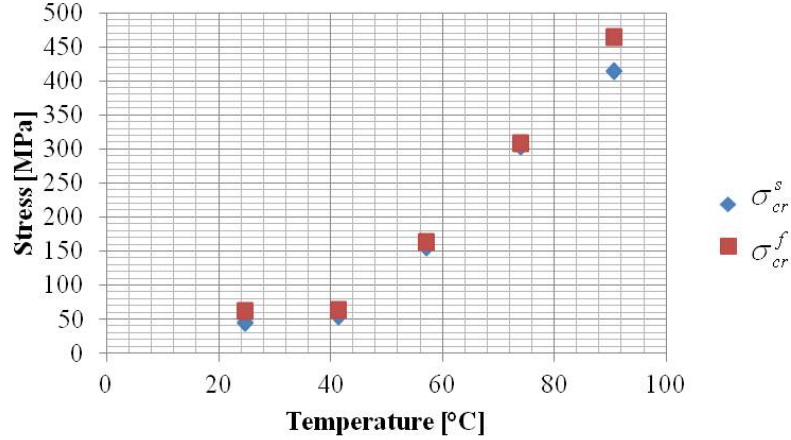


Figure 3.5: Critical detwinning start and finish stresses ($\sigma_{cr}^s, \sigma_{cr}^f$) versus temperature.

the yield strength of the ribbon was found to be 816 MPa. The maximum load provided a value of 963 MPa for the ultimate strength of the NiTi ribbon.

The average of the slopes from the initial linear region (E_{M1} in Figure 3.3) for tests at 24°C and the rising and falling slopes of the second linear regions (E_{M2} and E_{M3} , respectively, in Figure 3.3) for tests at temperatures of 24°C, 41°C, 57°C, and 74°C was used to determine the elastic modulus of the martensite phase, 17.9 GPa. This value falls in ranges given by the literature both from manufacturers and other researchers [20, 36, 37, 57]. The slopes of the initial elastic region for temperatures above 24°C were not used due to uncertainty of the initial stress-free phase. After the stress-induced ($M - M^+$ or $A - M$) transformation, the second linear regions are martensite and as such can be used to determine the elastic modulus of the phase. No data was used from the test at 90°C as the second linear region is not well defined under the maximum load used in the tensile tests, 110 N (25 lbf) resulting in a stress of 575 MPa (83.3 ksi).

In an attempt to obtain the elastic modulus of the austenite phase, a series of isothermal tensile tests were conducted at higher temperatures up to higher maximum loads. The hypothesis was that at higher temperatures, the ribbon could be made to behave as a pseudoelastic alloy: the stress-induced $A - M$ transformation could be completed due to increased tensile stresses, and the transformation back to austenite could be completed due

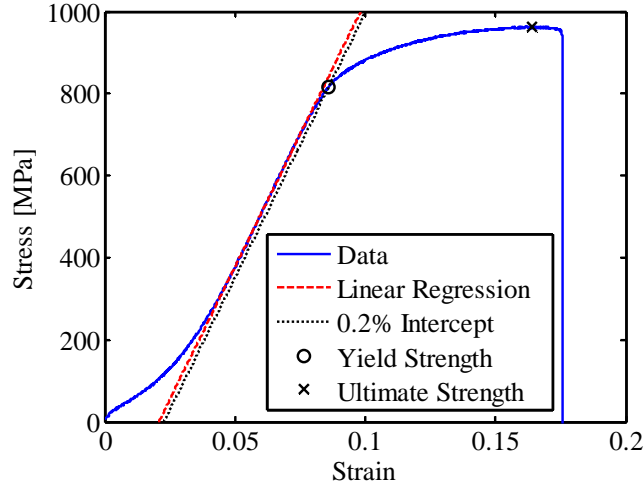


Figure 3.6: Tensile test of NiTi ribbon to failure. Dashed line is linear regression of second linear region, dotted line indicates the 0.2% yield criteria, circle indicates yield stress, and “x” indicates the ultimate stress.

to the higher temperatures. As seen in Figure 3.4, the ribbons were not fully returning to austenite upon unloading. The additional tests increased the maximum tensile load to 156 N (35 lbf) resulting in a tensile stress of 806 MPa (117 ksi), just below the observed yield strength. Test temperatures were also increased up to 149°C (300°F), however, as temperatures increased, the increased load was not able to complete the $A - M$ stress-induced transformation. Plots and additional details are provided in Appendix B. Since the austenite elastic modulus could not be determined in multiple linear regions similar to the procedure for the martensitic modulus, the literature value of austenite, 83 MPa [20, 36] was used for all calculations and modeling.

Blocking Stress Characterization

A second series of tensile characterization tests were conducted to observe the behavior of the NiTi ribbon when it is heated under a constraint. In these experiments, a ribbon 38 mm (1.5 in) long was axially loaded in tension to generate the detwinned martensitic phase. At a prescribed load, the strain was held constant while the temperature of the ribbon was increased by applying a DC electric current through the ribbon. Force was measured

through the load cell on the load frame while temperature of the ribbon was measured by a J-type thermocouple placed in contact with a high electrical resistance/high thermal conductivity thermal compound. The ribbon temperature was increased and decreased incrementally by adjusting the applied voltage.

An initial test was conducted with a NiTi ribbon with the load frame oven fan running to aid in temperature homogenization of the ribbon via convection. In the first test, the initially twinned ribbon was axially loaded to 44.5 N (10 lbf) and was subjected to two heating cycles while measuring load and temperature at 0.2 V increments. The resulting temperature/stress plot is seen in Figure 3.7. With the load frame fan on, the maximum temperature attained was 95°C, at which point the power supply used to heat the ribbon reached its maximum output. An additional test was conducted starting at an initial tensile load of 44.5 N with the load frame fan turned off and voltage increments of 0.5 V. This enabled observation of the behavior at a maximum temperature of 130°C. Since the NiTi ribbon is held at a constant length, it cannot complete the $M^+ - A$ transformation as this transformation requires the recovery of the strain induced by detwinning. As a result, the ribbon generates a temperature-dependent tensile load at temperatures above A_s .

On the the first cycle, the ribbon does not generate additional blocking stress until 52°C. This is due to the initial preload causing an increase in the austenite start temperature. Upon cooling, the stress decreases linearly to a level below the initial preload. This is a commonly observed phenomena with constrained SMAs [83–85] and is due to an intermediate “R-phase” transformation upon cooling which slightly reduces the amount of stress-induced martensite allowing the ribbon to reach a lower stress level upon cooling. The formation of the R-phase and recovery of prestrain is stable, it occurs only during the first heating cycle and will not occur to a greater extent unless new loading conditions are applied (i.e. higher stresses or temperatures) [83, 92]. Upon subsequent heating cycles, the stress-temperature curve is linear with a slope similar to the initial heating cycle. The observed slope of the force-temperature plots is 1.6 N/°C which, when considering the ribbon geometry, provides a value for the stress influence coefficient for austenite, C_A , of 8.2 MPa/°C. This is similar to the value of C_M obtained from the isothermal tension tests, as expected from literature

for NiTi [27, 37, 42]. One additional observation from the behavior is the low hysteresis of the blocked behavior. The heating and cooling paths for all cycles are nearly coincident. This behavior is also commonly observed in the literature [78, 83, 85].

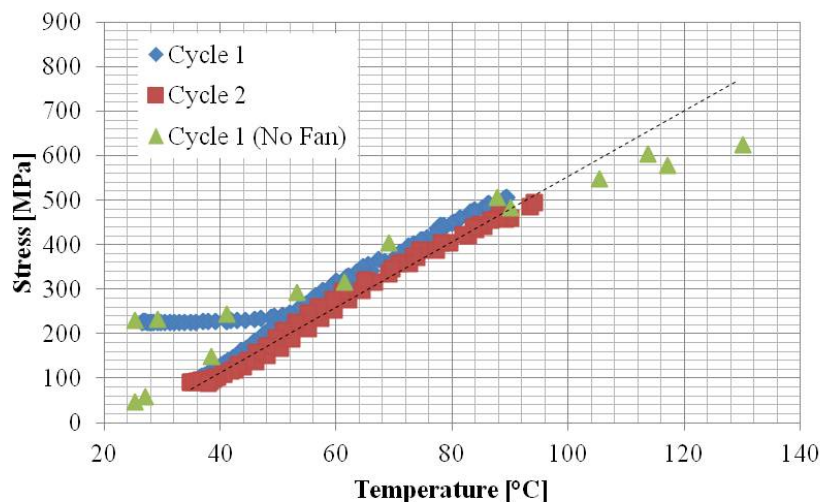


Figure 3.7: Stress versus temperature for prestrained and constrained NiTi ribbon. Dashed line is the linear regression of cycle 2.

3.2.3 NiTi Ribbon Characterization Summary

Through a series of thermomechanical tests, all material properties of the NiTi ribbon needed for characterization using the new bivariate model were determined except for the elastic modulus of austenite and the CTE. The elastic modulus of austenite and value for CTE are taken from the literature [20, 27, 36, 76, 77]. All obtained properties, summarized in Table 3.2, are within the range specified by manufacturers and ranges commonly cited in the SMA literature. The material properties were used in modeling and designing of the composites described in the following section and will be the only NiTi material properties used for analysis in the following chapters unless otherwise stated.

Table 3.2: NiTi material properties obtained from characterization experiments.

Property	Description	Value	Source
M_f	Mart. Finish Temp	41°C	Electrical Resistance
M_s	Mart. Start Temp	45°C	Electrical Resistance
A_s	Aust. Start Temp	45°C	DSC
A_f	Aust. Finish Temp	70°C/60°C ^a	DSC
σ_{cr}^s	Critical Start Stress	50 MPa	Tensile Test
σ_{cr}^f	Critical Finish Stress	63 MPa	Tensile Test
C_M	Mart. Stress Influence Coefficient	8.1 MPa/°C	Tensile Test
C_A	Aust. Stress Influence Coefficient	8.2 MPa/°C	Blocked Force Test
E_M	Mart. Elastic Modulus	17.9 GPa	Tensile Test
E_A	Aust. Elastic Modulus	83 GPa	Literature [20, 36]
α	Coefficient of Thermal Expansion	10 $\mu\epsilon$ /°C	Literature [27, 76, 77]
ϵ_L	Maximum Transformation Strain	6%	Tensile Test
σ_y (0.2%)	Yield Stress	816 MPa	Tensile Test
σ_u	Ultimate Stress	963 MPa	Tensile Test

^a A_f value found through DSC is later amended to 60°C. See sections 4.3.2 and 6.3.2.

3.3 UAM Composite Construction

A total of six NiTi-Al composites were constructed by embedding rectangular NiTi ribbons, $254 \mu\text{m} \times 762 \mu\text{m}$, in an Al 3003-H18 matrix. The primary design differences between the composites is the NiTi fiber volume fraction and the prestrain level of the embedded NiTi ribbons. NiTi fiber volume fraction is controlled through varying the number of embedded ribbons and changing the final cross-sectional area of the finished composite. The set of composites is considered in two primary groups: composites with embedded twinned martensite ribbons (1-3) and composites with detwinned martensite ribbons (4-6). Composites 1-3 were designed to have nominal fiber volume fractions of 5%, 15%, and 20%, respectively while composites 4 and 6 were designed to have nominal fiber volume fractions of 15%. Composite 5 was made for microscopic study of the NiTi-Al interface and as such, fiber volume fraction was not considered an important parameter. A composite with a fiber volume fraction of 20% represents approximately half of the theoretically possible volume fraction. Further discussion on this topic is presented in Appendix G. A summary of the composite design characteristics are given in Table 3.3.

Table 3.3: Design characteristics and experimental plan for NiTi-Al composites.

Composite	Ribbons	NiTi Vol. Fraction	Ribbon Phase	Characterization
1	1	5%	M	Thermomechanical
2	2	15%	M	Thermomechanical
3	2	20%	M	Thermomechanical
4	2	>15%	M^+	Thermomechanical
5	1	NA	M^+	Interface
6	1	>15%	M^+	Interface

While the overall procedure for creating all six composites is similar, maintaining the desired phase of the ribbons until embedding requires different considerations depending on whether the ribbon is to be embedded in a twinned or detwinned state. The composites are constructed on a 10.2 cm \times 7.6 cm (4 in \times 3 in) Al 3003-H14 sacrificial build plate 2.54 mm (0.100 in) thick. This build plate is bolted to a larger steel base plate which has accommodations for clamping embedding material in place as shown in Figure 3.8 (a). The base plate is then clamped to the table of a High Power UAM (HPUAM) system, shown in Figure 3.9. The HPUAM system used to construct the samples has two piezoelectric ultrasonic transducers oriented in a push-pull configuration with a combined power output of 10 kW.

Composites 1-3 were constructed by first welding two 152 μm (0.006 in) thick Al 3003-H18 tapes on the build plate, one on top of the other. After the consolidation of the first two layers, the NiTi ribbons are arranged on top of the welded tapes and clamped into place, similar to Figure 3.8 (b). Following the placement and clamping of the NiTi ribbons, two additional tapes were placed on the top surface and welded simultaneously.

It has been shown that welding more than one tape layer at a time generally has a negative impact on build strength [28–30], however the thickness of the ribbon makes welding a single 152 μm layer impossible. Assuming that the thickness of the embedded ribbon is split evenly between the top and bottom interfacing tapes, a 254 μm thick ribbon will leave only 25 μm (0.001 in) of tape between the ribbon and top of the build. Initial attempts to embed a ribbon with only one tape resulted in the ribbon tearing through the top of the tape, thus requiring the simultaneous consolidation of tape layers 3 and 4.

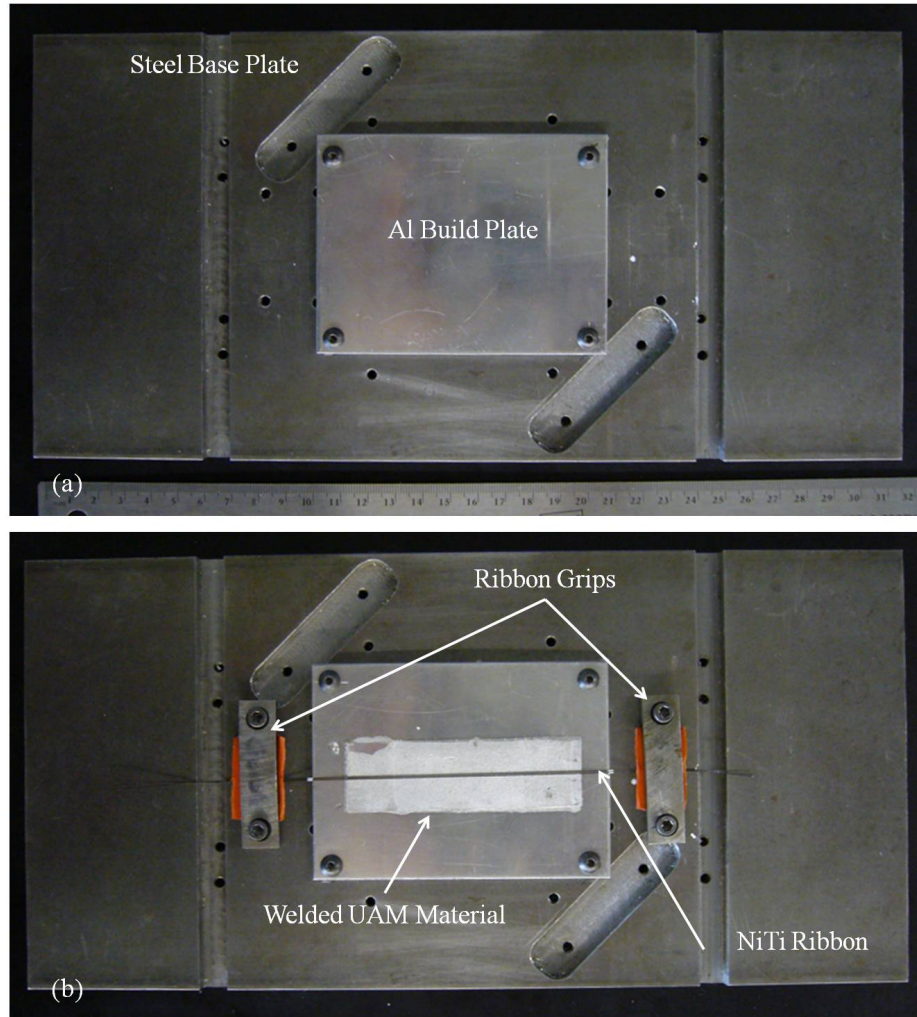


Figure 3.8: (a) Al 3003-H14 build plate attached to steel base plate used for fabricating the HPUAM NiTi-Al composites. (b) NiTi ribbons clamped in place on top of previously welded tape layers.

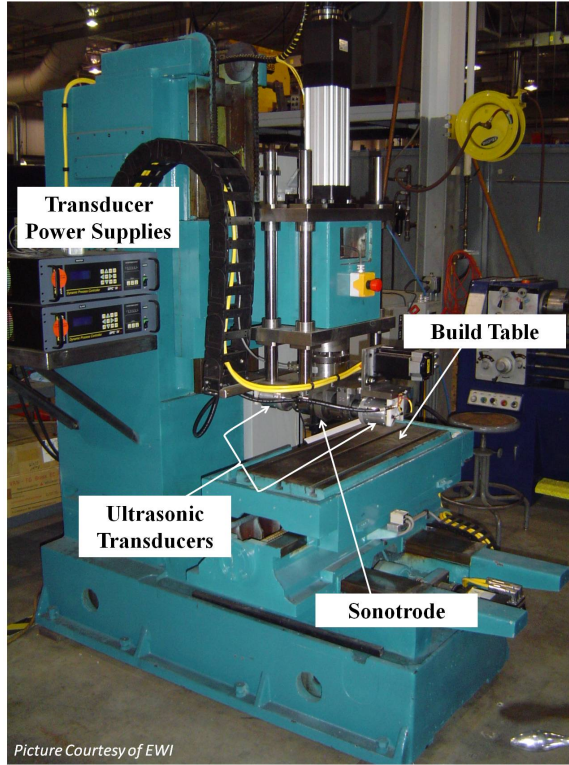


Figure 3.9: HPUAM system used to create NiTi-Al composites.

There are three main parameters that can be adjusted on the HPUAM system, normal force, transducer power, and weld rate. Since welding two tapes simultaneously welds twice the interface area, it follows that it will require more work than welding a single tape. As such, the parameters for welding tape layers 3 and 4 were increased to promote adequate bonding. A summary for the weld parameters is shown in Table 3.4. It is noted that while UAM is a low temperature process, there are significant normal loads applied as a line contact to the composite components. The result is high applied stress in the normal direction of the laminates. As will be shown in the forth coming chapters, there do not appear to be effects from the normal stress on the repeatable behavior of the NiTi ribbons, but this has not been explicitly investigated. Like exposure to excessive temperatures, SMA behavior can be altered by excessive loads. The effect of the forces in the UAM process on SMA behavior is left as an area of future work.

Composites 4-6 were constructed with detwinned NiTi ribbons. The ribbon detwinning

Table 3.4: Weld parameters used for different tape layers.

Tapes (Thickness)	Normal Force [N]	Power [%]	Weld Rt. [mm/s]	Composites
1 (152 μm)	4450	60	25.4	1-2,5,6
2 (152 μm)	5340	60	25.4	1-2,5,6
1 (304 μm)	4450	70	25.4	4

process was accomplished by first heating the ribbons and allowing them to cool unloaded to achieve a common starting state. The heating and cooling step is important to ensure that the ribbons are in the twinned form of martensite and do not have any detwinning-induced strain in any direction. Without the initial heating step, a prestrain ribbon may have detwinning-induced strain in directions other than the longitudinal direction. Following the stress-free cooling, ribbons were detwinned by applying a dead weight load. Based upon the critical detwinning finish stress found in the initial characterization, a load of 40 N (9 lbf) was applied for each ribbon. This load results in an axial tensile stress of 200 MPa, above the critical detwinning finish stress and into the second linear region of the stress-strain plot at room temperature (Figure 3.3). Once the ribbons were detwinned they were placed on a backing plate, seen in Figure 3.10, to prevent accidental stressing, which could result in reorientation of the martensite variants, during transposition to the HPUAM system. The ribbons remained on the backing plate until clamped in place on the base plate for final consolidation.

Consolidation of composites 5 and 6 was successfully completed using the same parameters as composites 1-3. Chronologically, composites 1-3 were constructed followed by composite 5 and 6. There was several months of testing and analysis in between the construction of composites 6 and 4. On the initial attempt to create composite 4, the build appears successful, but upon machining, the interface between tapes 2 and 3 began to separate, Figure 3.11, indicating that welding quality of composite 4 was substantially less than that of the other composites. This is attributed to wearing of the texture on the sonotrode over time. The HPAUM sonotrode system is periodically retextured via electro-discharge machining and this texture is what causes the sonotrode to grip the top tape. If this pattern

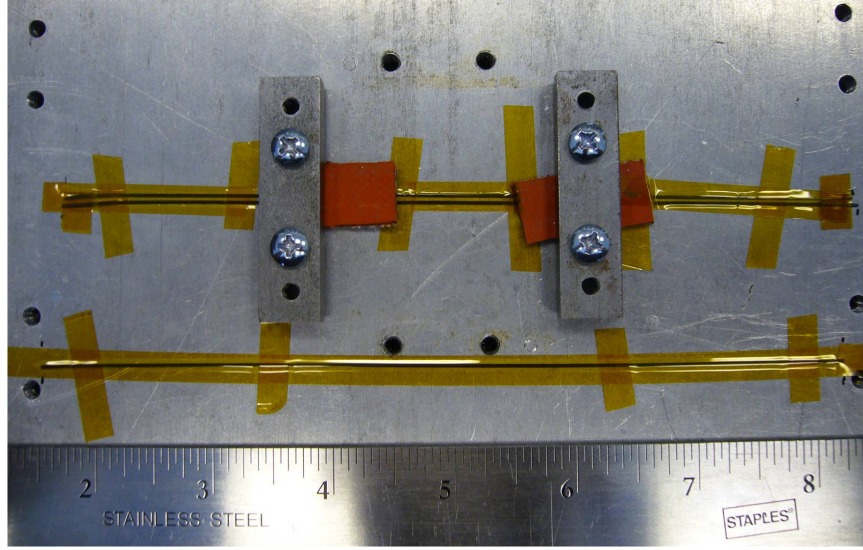


Figure 3.10: NiTi ribbons after detwinning fixed to a backing plate to avoid reorientation of the martensite variants during transportation. Ribbons held in place by polyimide tape.

becomes worn, it adversely affects the strength for the resulting welds. To overcome the worn texture, composite 4 was remade with $304\text{ }\mu\text{m}$ (0.012 in) thick Al 3003-H18 tapes. This allowed for ribbon embedding to be accomplished with a single top tape, reducing the total weld area and enabling a satisfactory bond at the embedding layer. Parameters for welding the $608\text{ }\mu\text{m}$ tapes in composite 4 are given in Table 3.4.

After consolidation, each composite was machined to final dimensions. This was accomplished by reinstalling the build plate on the steel base plate and first machining the consolidated layers to their final width, shown in Figure 3.12. Next, the build plate was reinstalled upside-down and then machined away from the consolidated layers, shown in Figure 3.13 (a) and (b). The composites were then cut away from the build plate using a low speed lubricated saw to prevent heat build up and ribbon transformation at the cutting plane. Finished composites were in a rectangular prismatic form, as shown in Figure 3.13 (c). The base plate was machined away from the composite for all composites except for composite 5 since it was used for microscopic studies as opposed to thermomechanical testing. For composite 5, a shear press was used to cut excess build plate material from either side and the remaining build plate was left attached. Following the machining processes, the

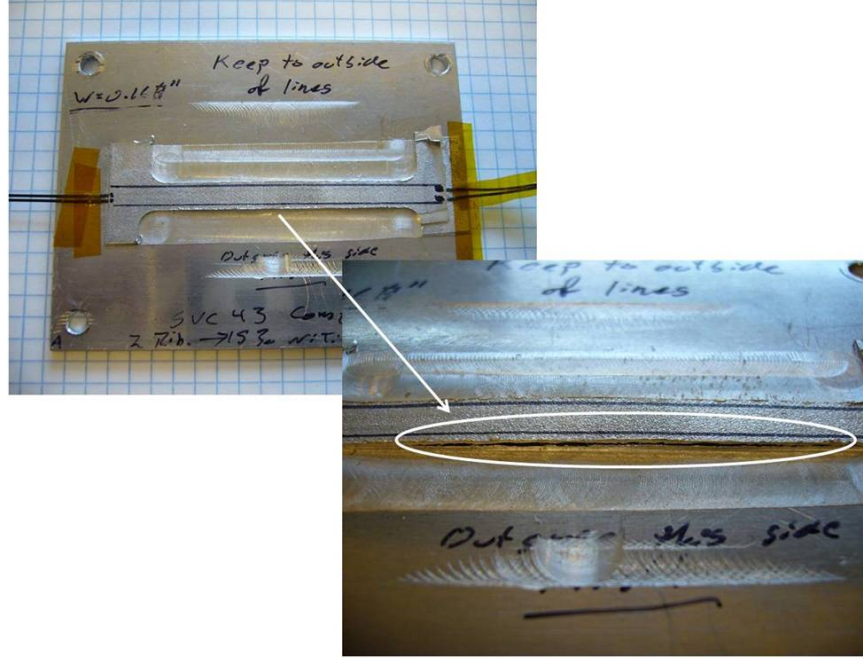


Figure 3.11: Failure of first attempt on composite 4 showing delamination between tapes 2 and 3.

Table 3.5: Dimensions and NiTi content of NiTi-Al composites.

Composite	Ribbons	Cross-Sectional Area [mm ²]	Length [mm]	NiTi Vol. Fraction
1	1	3.52	76.2	5.3%
2	2	2.54	74.0	15.2%
3	2	1.88	71.9	20.6%
4	2	2.53	57.9	15.2%
5	1	15.3	76.2	1.27%
6	1	1.28	76.2	15.1%

final dimensions and fiber volume fraction for each composite was determined. The actual dimensions and fiber volume fractions are provided in Table 3.5.

3.4 Summary

In this chapter, the shape memory alloy embedded within the composites studied in this research has been experimentally characterized to determine the material properties needed for analysis using the model presented in Chapter 2. A method for creating high fiber volume

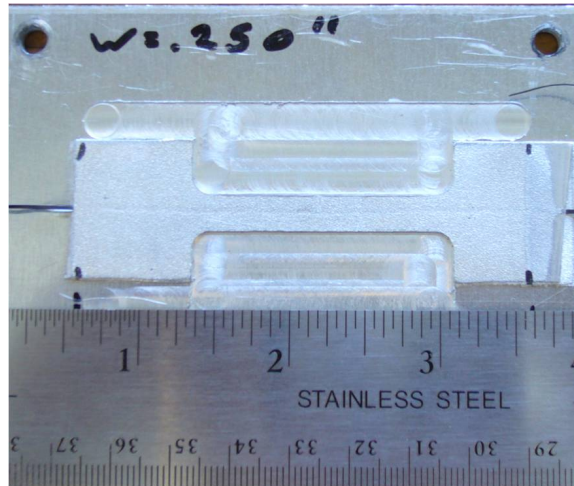


Figure 3.12: NiTi-Al composite 1 during the machining process used to attain the final composite width.

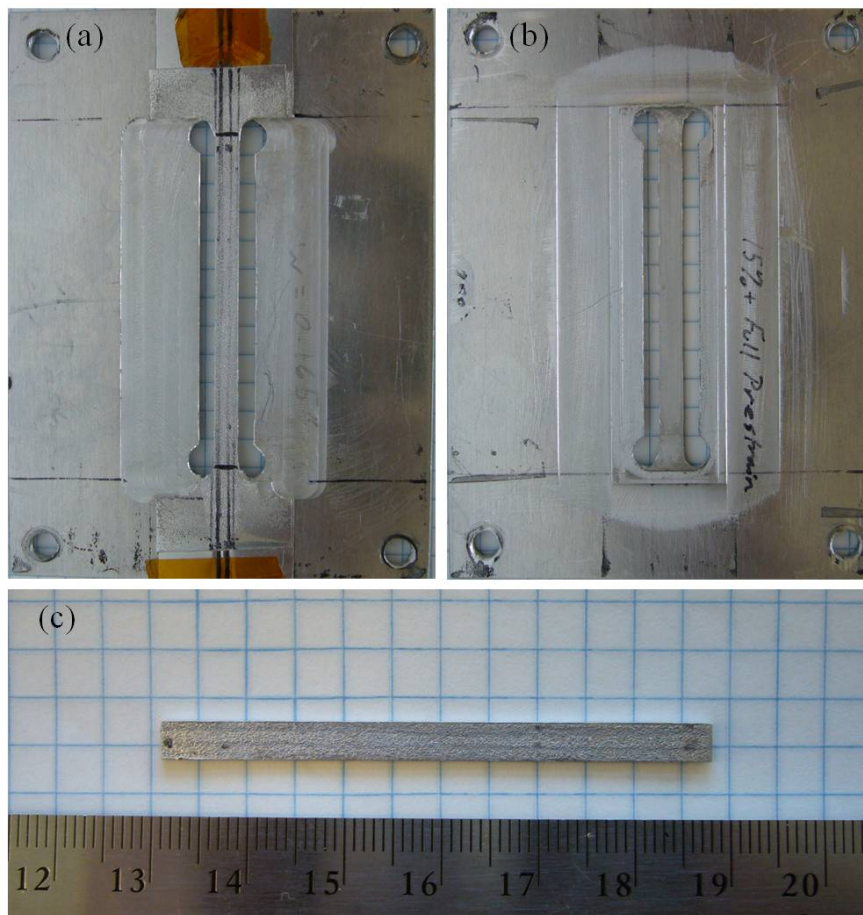


Figure 3.13: NiTi-Al composite 4 after final machining process used to remove the Al build plate: (a) top and (b) bottom. (c) Final geometry of composite 4.

fraction SMA MMCs has been discussed and demonstrated. The resulting composites are truly unique as the fiber volume fraction and NiTi phase can be controlled due to the additive nature of UAM and low process temperatures. The outlined process can be used to create components of arbitrary size with arbitrary volume fractions of embedded shape memory alloys.

Chapter 4

THERMALLY-INDUCED STRAIN

4.1 Introduction

In this chapter, the phase-dependent modulus of NiTi and its ability to generate transformation stresses when heated in an initially prestrained state are utilized to counteract the thermal expansion of the aluminum matrix. Changes in elastic modulus allow for variable matrix reinforcement while transformation stresses can create axial loads, both of which are utilized to create unique thermally-induced strain responses. These responses are characterized through experimentation and described using the analytical model presented in Chapter 2. A discussion on the necessary steps needed to achieve the goal of thermally-invariant components with an effective zero CTE is provided. Chronologically, composites 1-3 were first constructed and tested and these initial experimental results were used to aid in model development. After the model had been developed, composite 4 was constructed based upon guidance from the analytical model.

4.2 Experimental Setup

To measure the thermally-induced strain, composites 1-3 and an Al 3003-H18 reference sample were placed in a thermal chamber. The samples were subjected to three consecutive heating cycles from 24°C to 100°C. During thermal cycles, the strain of each composite was measured with a strain gage matched to aluminum alloys and the temperature of the composites was monitored with a J-type thermocouple placed next to the strain gages. The

strain gage model used in this experiment is WK-13-031CF-350, a general purpose linear pattern manufactured by Vishay Precision Group [88], was chosen for its small form factor (grid width of $1.57 \text{ mm} \times 1.57 \text{ mm}$), wide operational temperature range (up to 290°C), and aluminum-matched thermal output. An analysis on the stiffening effect of the gages on the composites was conducted, but the effect was found to be negligible. This analysis is provided in Appendix C. Thermal compound was used to increase thermal conductivity between the samples and thermocouples.

Composite 4 was tested in the same manner with one difference: both the composite and Al reference had two strain gages applied to opposite sides. The second strain gage enabled an analysis of and compensation for bending. Reasons for this addition are discussed in the following section.

The inclusion of the aluminum reference sample enables the determination of the composite CTE despite the thermal output of the strain gage. Since the CTE of the reference sample is known, the strain signal from the reference sample was used to remove the thermal dependency of the strain gages from the composite strain signals. To determine the composite strain response, the strain measured from the reference sample was subtracted from the strain measured from each composite and then the calculated thermal strain of the reference sample was added to the composite strain measurements [43]:

$$\epsilon_{comp} = \epsilon_{sig/comp} - \epsilon_{sig/ref} + \alpha_{ref} \times \Delta T. \quad (4.1)$$

Here, $\epsilon_{sig/comp}$ is the non-compensated strain signal from the composite, $\epsilon_{sig/ref}$ is the strain signal from the reference sample, α_{ref} is the CTE of the reference material ($23.2 \mu\epsilon/^\circ\text{C}$ [38]), and ΔT is the change in temperature. To avoid large discrepancies in temperature between the composites and reference, the reference sample was made from $635 \mu\text{m}$ (0.025 in) thick aluminum sheet and cut to 5 mm wide to approximate the size of the composites.

The thermal chamber was heated through forced convection and was constructed with a sensor lead exit port and air inlet baffles to avoid direct airflow on the composites. The test setup can be seen in Figure 4.1. A study on the thermal variation within the chamber

was also conducted and found that over the height of the chamber, the temperature varied by a maximum of 1.4°C .

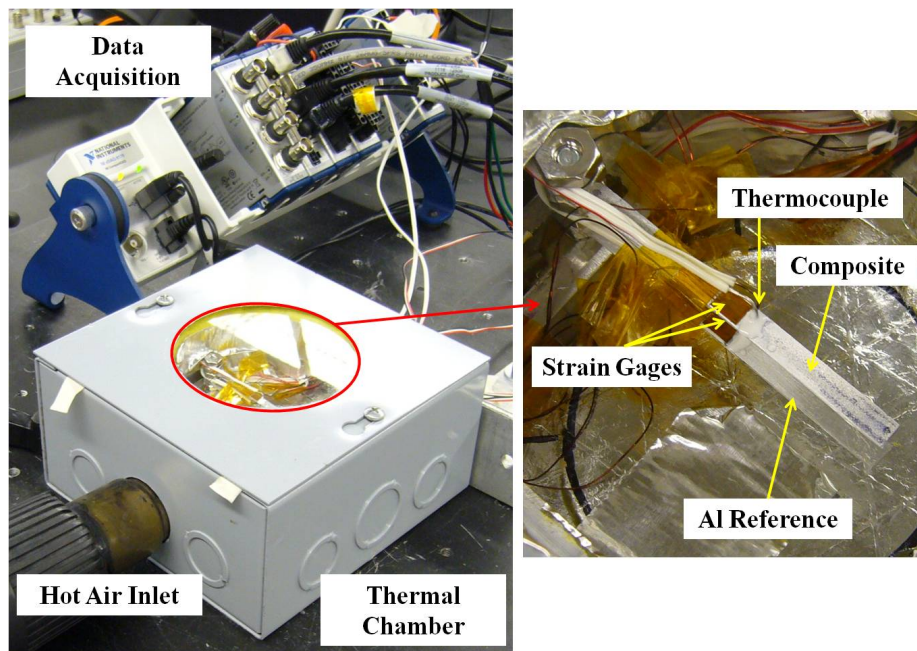


Figure 4.1: Thermally-induced strain experimental setup showing composite 4 and an aluminum reference.

4.3 Results and Discussion

4.3.1 Thermally-Induced Strain Experiments

The temperature versus strain plots of each composites are shown in Figure 4.2 (a)-(d). For each composite, the initial cycle is different than subsequent cycles, however cycles 2 and 3 exhibit stabilized behavior. This is similar to the initial transient behavior seen in thermal cycling of constrained shape memory alloys [92]. For clarity, cycles 2 and 3 for each composite are shown in Figure 4.3 (a)-(d) without the initial thermal cycles.

Composite 1 has a strain spike in the initial cycle after which its behavior becomes nearly linear. The spike in the initial cycle, seen at 42°C , is believed to be due to a stick-

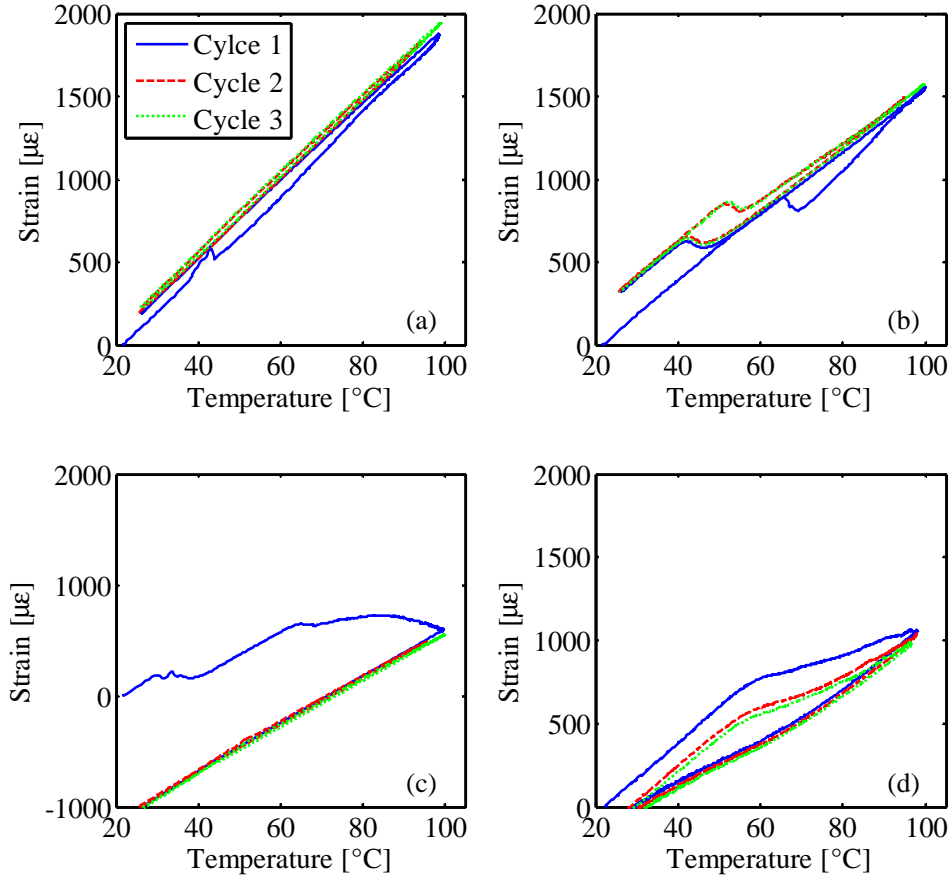


Figure 4.2: Temperature versus strain plots for cycles 1 through 3 of NiTi-Al: (a) composite 1; (b) composite 2; (c) composite 3; (d) composite 4.

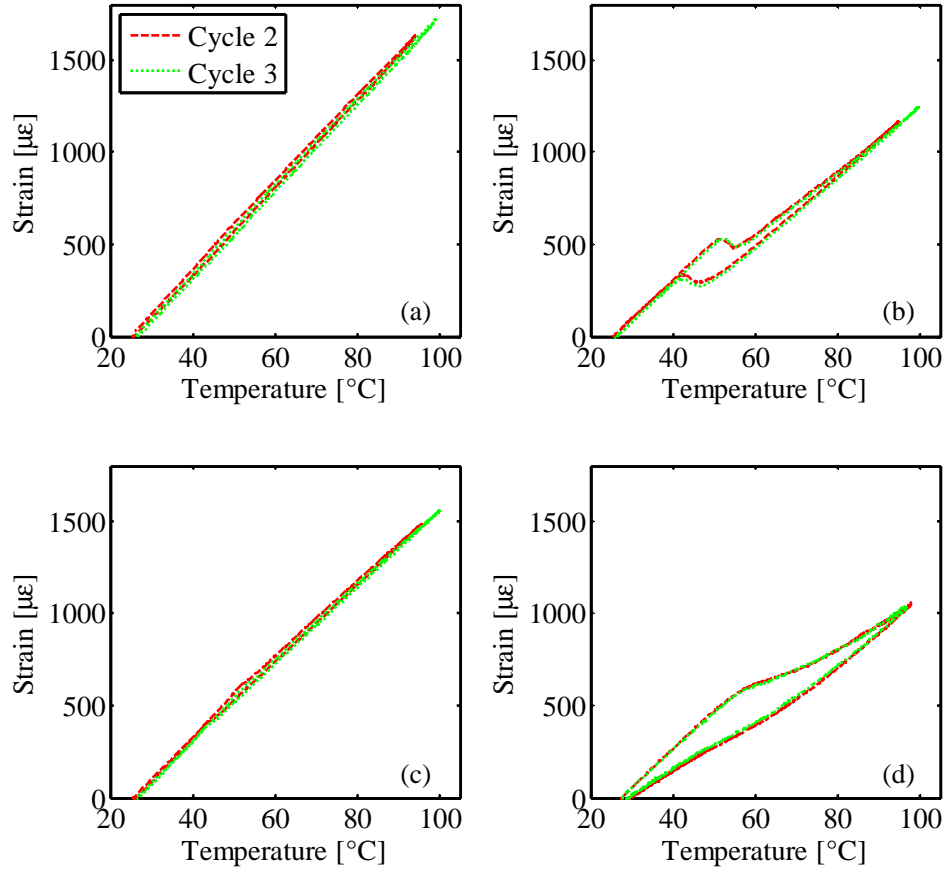


Figure 4.3: Temperature versus strain plots for cycles 2 and 3 of NiTi-Al: (a) composite 1; (b) composite 2; (c) composite 3; (d) composite 4.

slip condition that developed between the ribbon and matrix, allowing the embedded ribbon to contract slightly within the matrix. If this occurred, the matrix would have a momentary increase in strain before being constrained again by the NiTi ribbon, which coincides with what is observed.

The temperature-strain behavior of composite 2 is significantly different than that of composite 1. After an initial linear region the composite recovers some strain, starting at approximately 50°C until approximately 55°C, as observed by negative strain-temperature slope seen in Figure 4.2 (b) and Figure 4.3 (b). After a repeatable amount of contraction, the composite again behaves linearly with a different CTE than the initial low temperature region. Upon cooling, the process reverses with the exception of a hysteretic recovery of the thermal contraction. The strain recovery suggests that there is some amount of prestrain in the embedded NiTi. Upon heating through A_s and A_f , the $M - A$ transformation recovers the prestrain and generates recovery stresses, causing the observed contraction. Upon cooling, the $A - M$ transition occurs over M_s and M_f which produce the observed hysteresis. The first cycle of composite 2 undergoes the strain contraction over a higher temperature region than subsequent cycles. This, too, is described by the observed behavior of constrained SMAs. As seen in the stress-temperature plots of constrained prestrained SMAs, upon cooling from the first cycle, the stress level drops below its initial value [83, 92]. This decrease in stress for subsequent thermal cycles lowers the effective A_s temperature of the SMA and in this case, the composite.

Composite 3 has linear behavior similar to composite 1 in its second and third cycles. However since composite 3 has a higher NiTi volume fraction than composite 2, a similar response and larger magnitude of strain recovery would be expected. An explanation for the behavior of composite 3 is in the strain response from the initial thermal cycle. In the first cycle, Figure 4.3 (c), composite 3 exhibits an initial linear region followed by a strain recovery greater in magnitude than composite 2. After this recovery there is a gradual decrease in slope which becomes negative before cooling begins. This gradual slope change and strain recovery is hypothesized to be plastic deformation of the Al matrix from the generation of recovery stresses in the NiTi.

As shown in Chapter 3, a prestrained NiTi sample heated under constraint generates a recovery stress that increases with temperature. In being heated to 100°C, the NiTi ribbons in composite 3 appear to generate enough recovery stress to yield the matrix, allowing the ribbons to recover any induced prestrain. This scenario requires that the NiTi ribbons have an initial prestrain, similar to composite 2, as indicated by its hysteretic behavior. In subsequent thermal cycles, composite 3 had no remaining prestrain and therefore behaves in a piecewise fashion with two linear regions.

The behavior of composites 1, 2, and 3 suggest that although steps were taken to embed the NiTi ribbons without prestrain, manufacturing of the composites did induce strain in the NiTi ribbons during consolidation. The rolling action of the UAM horn and plastic embedding of the ribbons into the matrix likely induced detwinning of the martensitic structure of the NiTi thus creating a prestrain and non-zero initial stress-induced volume fraction. For composites 1 and 3, the initial heating cycles appear to have removed the initial prestrain through movement of the embedded ribbon in composite 1 or through deformation of the matrix in composite 3.

The first three composites each exhibit two linear regions corresponding to the martensite and austenite phases of the embedded NiTi ribbons. The difference between the slopes of the two linear regions is small in composite 1, however, the effect becomes more pronounced as NiTi fiber volume fraction increases as displayed in the behaviors of composites 2 and 3. Since NiTi has a lower CTE than the Al matrix, the inclusion of NiTi elements will reduce the total composite CTE, α_{comp} , to varying degrees based upon the fiber volume fraction and phase dependent modulus [15, 66, 79]:

$$\alpha_{comp} = \frac{(1 - \nu)(E_{Al})(\alpha_{Al}) + \nu(E_{NiTi})(\alpha_{NiTi})}{(1 - \nu)(E_{Al}) + \nu(E_{NiTi})}. \quad (4.2)$$

Here, E_{Al} , E_{NiTi} , α_{Al} , and α_{NiTi} are the elastic moduli and CTEs of Al and NiTi, respectively. At high temperatures, the modulus of the embedded NiTi increases, due to transformation to austenite, thus reducing the total composite CTE. This results in a higher strain-temperature slope at low temperatures and a lower slope at high temperatures corresponding to the higher and lower composite CTEs. A similar, yet less noticeable, effect is

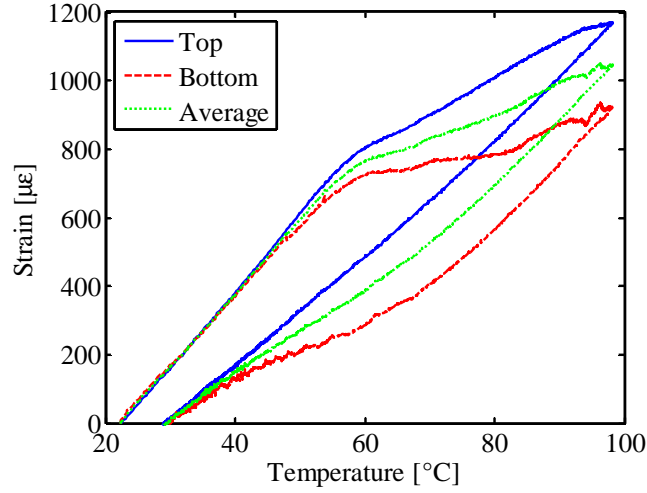


Figure 4.4: Top, bottom, and average strain response from the first heating cycle of composite 4.

the decreasing modulus of the Al matrix with increasing temperature. As the Al modulus decreases, the composite CTE also decreases.

The strain response for composite 4 was found by taking the average of the top and bottom strain gage signals. As seen in Figure 4.4, the overall shape of the strain-temperature plots for the top and bottom gages are similar but the bottom gage consistently gives a lower output than the top. Further, the discrepancy between the top and bottom increases with temperature. This indicates that there is some bending due to a small offset between the center-line of the NiTi ribbons and the center-line of the matrix. If it is assumed that this offset is small, the top and bottom strain gages are nearly equally spaced from the neutral axis of the composite and can be assumed to have equal and opposite strain signal components due to bending. By averaging the strain output of the two gages, the bending component is removed and the remaining strain signal is the longitudinal strain, in this case, due to thermal expansion of the composite.

The average strain responses of the three cycles of composite 4 exhibit a hysteretic three part response. First, the strain increases linearly with temperature like the low temperature regions present in composites 1-3. At temperatures beyond 54°C, the strain response

changes showing a region of significantly lower CTE. This response is due to the generation of blocking stresses in the fully prestrained NiTi ribbons above the effective A_s temperature of the composite. Beyond 70°C, there appears to be the start of a second high temperature linear region that does not fully develop over the temperature range of the conducted thermal cycles.

It is noted that the ribbon A_s temperature was found to be 45°C and composites 1-3 all show transformation regions beginning at approximately 45°C in the second and third cycles. This higher A_s temperature of composite 4 indicates that the NiTi ribbons are under a tensile preload, likely induced during embedding, which increases the austenite start temperatures through (1.3). The second and third cycles of the other composites do not show increased austenite start temperatures as the transient behaviors in the initial cycles relieved the induced tensile loads.

The second and third cycles of composite 4 are similar to each other, as observed in the previous composites. The additional cycles are generally similar to the first cycles except for an initial strain offset; in the first cycle, the strain returned to zero at a 29°C, indicating that there was strain recovery in the first cycle. In all cycles, at approximately 70°C-80°C, the composite appears to enter into a second linear strain region indicating that the blocking region is ending. This is hypothesized to be due to a non-linear blocking behavior. As seen in Figure 3.7, at high temperatures the blocking stress generated by the NiTi ribbon begins to deviate from the linear relationship with temperature. If this behavior is occurring, then the composite may be completing the $M - A$ transformation without recovering all of the induced strain. Further, without a blocking stress increase with increasing temperature, the composite will exhibit a second thermoelastic region as governed by (4.2).

4.3.2 Thermally-Induced Strain Modeling

Composites 1-3 were assumed to be consolidated in a twinned martensite state, having an initial stress-induced volume fraction of zero. As such, the initial models for thermally-induced strain do not include the transformation strain recovery components and (2.77) becomes:

$$\epsilon_{comp} = \frac{1}{E_{NiTi}} \left[\frac{(\alpha_{Al} - \alpha_{NiTi})(\Delta T)}{\frac{1}{E_{NiTi}} + \frac{1}{E_{Al}} \frac{v}{(1-v)}} \right] + \alpha_{NiTi}(\Delta T) \quad (4.3)$$

where the matrix property values are described by mechanical properties of aluminum, identified by the subscript “Al”, and fiber property values are described by the properties of NiTi, identified by the subscript “NiTi”. The strain calculation is completed by finding the elastic modulus of the NiTi ribbons as a function of martensitic volume fraction and the Al matrix as a function of temperature. The elastic modulus of the Al matrix is varied linearly using modulus values at different temperatures as found in the literature [38] and provided in Table 2.4.

The thermoelastic strains were modeled for each composite using the material properties found in Table 3.2 and 2.4. The model output can be seen for composites 1-3 in Figure 4.5 (a)-(c), respectively. For the given material properties, the incremental approach was able to be used without unstable regions. For composites 1 and 3 the strain model closely matches the strain observed in the experiments, including unique high and low temperature linear regions and a small amount of hysteresis. However, the model does not describe the negative strain-temperature regions observed in composite 2. This confirms that the zero prestrain assumption is not valid when considering composite 2 and there is residual prestrain that was induced by the rolling action of the sonotrode during fabrication. The amount of prestrain and subsequent stress-induced martensite is determined by observing the amount of strain recovered as the NiTi ribbons go through the $M - A$ transformation.

One discrepancy between the models and the results is the temperature at which the $M - A$ transformation regions ends upon heating. In Figure 4.3, strain data for composites 1

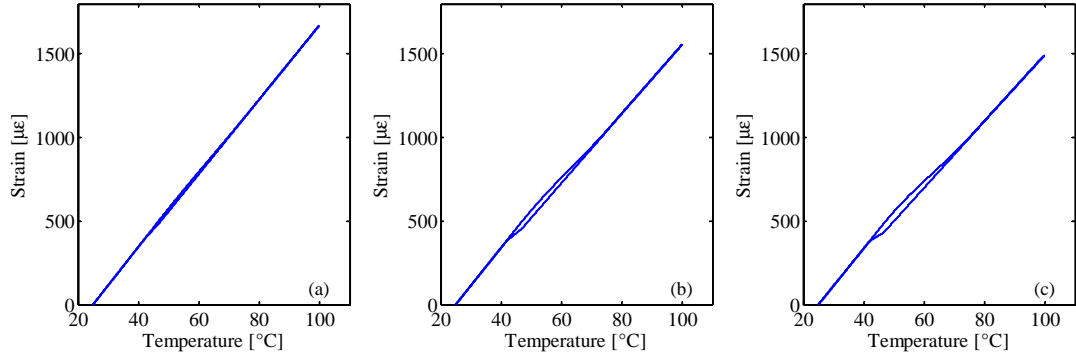


Figure 4.5: Thermally-induced strain model for NiTi-Al: (a) composite 1; (b) composite 2; (c) composite 3.

and 3 indicate that the transformation ends at approximately 60°C rather than the 70°C observed from the DSC tests. If the value for A_f in the model is changed to 60°C, the resulting strain responses for composites 1 and 3 are more accurately represented, Figure 4.6. The thermally-induced strain experiments strongly suggest that the A_s temperature should be 60°C but are in agreement with the other transformation temperatures as obtained through ribbon characterization experiments. The a possible cause of the discrepancy of the ribbon A_f temperature as found through DSC testing and the strain response is thought to be due external loading of the NiTi ribbon sample used for characterization. Additional DSC testing discussed in Chapter 6 provides additional evidence of the A_f temperature being 60°C. From this point forward, the A_s temperature as reported in Table 3.2 is replaced by 60°C.

The strain recovery region observed in composite 2 is consistent over multiple cycles. Because of this, the transformation is assumed to recover and induce a repeatable amount of stress-induced martensite as the composite is heated and cooled. To this end, an assumption is made that $\xi_s = \xi_{so} \times \xi$ where ξ is found from 2.39 and 2.37 for purposes of calculating composite strain. By taking the average strain of the rising and falling high temperature linear regions at $T=65^\circ\text{C}$, a temperature beyond the $M - A$ transformation region, and subtracting the modeled thermoelastic strain for composite 2 at 65°C, the total composite recovery strain, $\epsilon_{NiTi/X}$, is estimated to be 200 $\mu\epsilon$. To calculate the initial stress-induced

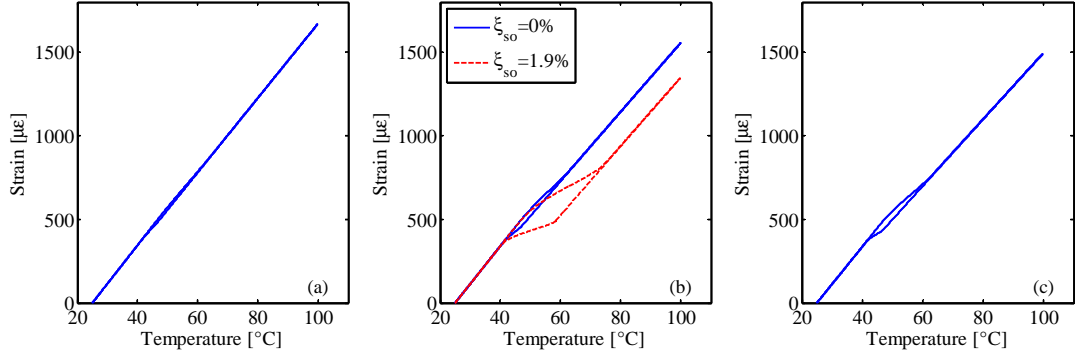


Figure 4.6: Thermally-induced strain model with new A_f for NiTi-Al: (a) composite 1; (b) composite 2; (c) composite 3.

volume fraction from the total observed strain recovery, the thermoelastic strain component from (4.3) is subtracted from the total strain from (2.76),

$$\epsilon_{NiTi/X} = \frac{1}{E_{NiTi}} (\sigma_{NiTi/X}) + \epsilon_L (\xi_s - \xi_{so}), \quad (4.4)$$

where $\sigma_{NiTi/X}$ is equal to the second term of (2.75). Considering $E_{NiTi} = E_A$ and $\xi_s = 0$ when the $M - A$ transformation is complete,

$$\begin{aligned} \epsilon_{NiTi/X} &= \frac{1}{E_{NiTi}} \left[\frac{-\epsilon_L (\xi_s - \xi_{so})}{\frac{1}{E_{NiTi}} + \frac{1}{E_{Al}} \frac{\nu}{(1-\nu)}} \right] + \epsilon_L (\xi_s - \xi_{so}) \\ &= -\epsilon_L \xi_{so} \left[1 - \frac{1}{1 + \frac{E_A}{E_{Al}} \frac{\nu}{(1-\nu)}} \right]. \end{aligned} \quad (4.5)$$

Using $200 \mu\epsilon$ for $\epsilon_{NiTi/X}$, the initial stress-induced martensitic volume fraction is found to be 1.9%. Using (2.76) with the calculated value for ξ_{so} , the red dashed line in Figure 4.6 (b) shows the thermally-induced strain model for composite 2 including the transformation strain component. With the inclusion of the transformation strain term, the model closely matches the experimental data and exhibits the expanded hysteretic region originally observed. Low prestrain models were obtained using the incremental model approach discussed in section 2.3.3, however, with the inclusion of the prestrain in composite 2 with $\xi_{so} = 1.9\%$, this approach becomes unstable. As such, the interpolation algorithm discussed in section 2.3.3 was used to determined the strain-temperature models for non-zero

stress-induced martensitic volume fractions.

While the second linear strain regions from Figure 4.6 (b) align with the linear region from Figure 4.3 (b), the modeled transition region does not have a negative strain-temperature slope as displayed by the strain data. Further, composite 4, which has a similar NiTi fiber volume fraction and a larger stress-induced volume fraction of martensite, does not show a negative strain-temperature slope over any region. The difference between the observed strain and model from composite 2 is further evidence that the composite is undergoing bending in addition to the thermal expansion and that the strain gage used to measure the strain is on the concave surface of the curvature. This observation was the impetus for installing two strain gages on composite 4 which allowed for the bending contribution to strain to be nullified. It is not possible to know the amount of bending experienced by composite 2 from the current data set. As such, a second thermally-induced strain experiment for composites 1-3 is to be the subject of future study with two strain gages installed on all samples.

Using the strain modeling techniques used to describe composites 1-3, the behavior of composite 4 was modeled prior to construction. Assuming a 15.2% NiTi volume fraction, the linear thermoelastic region was predicted to end at an A_s^σ temperature of 45.6°C followed by a region of continuously decreasing CTE. The model was extrapolated beyond the expected 100°C maximum temperatures and predicts a zero CTE at 118°C. Since the SMA was believed to operate in the blocked regime, the heating and cooling curves were initially expected to have low hysteresis similar the blocked stress testing results in section 3.2.2.

As compared to the thermally-induced strain data given in Figures 4.2 (d) and 4.3 (d), effective austenite start temperatures at the end of the thermoelastic response occur at 57.7°C, 54.7°C, and 54.4°C for the first, second, and third cycles, respectively. The increase in the A_s^σ can be attributed to a tensile load applied to the ribbons during the embedding process, similar to those observed in composite 1-3. Using (1.3) and the results from the steady-state behavior observed in cycles 2 and 3, the axial preload on the ribbons due to embedding is estimated to be 72.6 MPa. Using this preload and the NiTi fiber volume fraction of 15.2%, the model is compared to the thermally-induced strain data for

composite 4 in Figure 4.7.

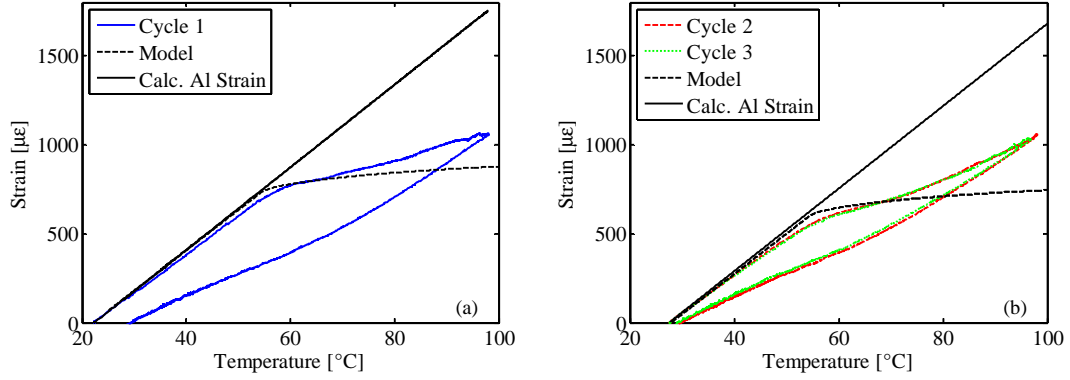


Figure 4.7: Thermally-induced strain model compared to thermally-induced strain data for composite 4: (a) cycle 1; (b) cycle 2 and 3.

The thermally-induced strain model and data are in close agreement until approximately 70°C where the composite appears to complete the $M - A$ transformation. This was not expected as even a modeled stress-temperature load path of the NiTi ribbon within the composite, Figure 4.8, shows a martensitic volume fraction of 0.81 at 100°C, corresponding to only a 19% transformation. A few hypotheses are put forth to describe the unexpected behavior. First, there may be a strain gradient through the thickness of the composite, allowing the SMA to contract further than predicted or observed by the surface mounted strain gages. However, since the composite is relatively thin, this strain gradient is not likely to be large. Second, high temperature/high stress blocking behavior of the SMA observed in Figure 3.7 show the start of a deviation from linear behavior at between 70°C and 80°C. If the blocking stress generated by the NiTi ribbon begins to reach a steady value, thermoelastic behavior of the composite will continue as the blocking stress no longer increases.

The hysteresis observed in the behavior of composite 4 is attributed to the partial transformation upon heating. The transformed austenite will not transform back to martensite until the temperature cools below the martensitic start temperature. The composite model

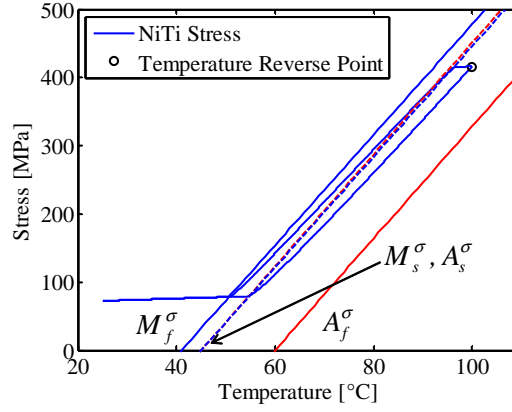


Figure 4.8: Modeled stress-temperature load path of NiTi in composite 4 during heating, partial transformation, and cooling overlaid on the NiTi phase diagram. At 100°C, the location between the A_s^σ and A_f^σ lines correspond to a martensitic volume fraction of 0.81. Upon cooling, the stress-induced martensitic volume fraction returns to 1.

was updated to account for this and is shown in Figure 4.9.

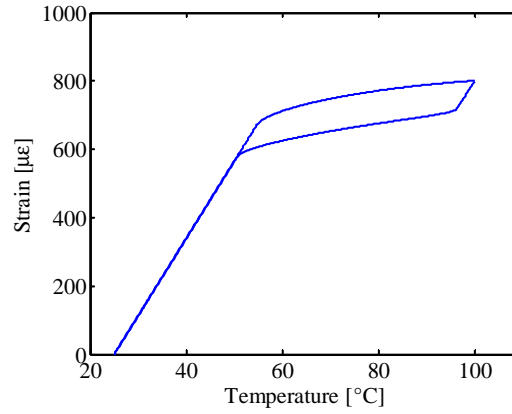


Figure 4.9: Updated thermally-induced strain model of composite 4 with hysteretic strain recovery after a partial transformation from heating to 100°C.

While it is not likely that composite 4 will attain a zero CTE behavior as described by the model, the lowest CTE found through linear interpolation of the transformation regions is $4.9 \mu\epsilon/^\circ\text{C}$ in the blocking region of cycle 1. If only the repeatable cycles 2 and 3 are considered, the average CTE in the blocking region is $7.6 \mu\epsilon/^\circ\text{C}$, over a 2/3 reduction

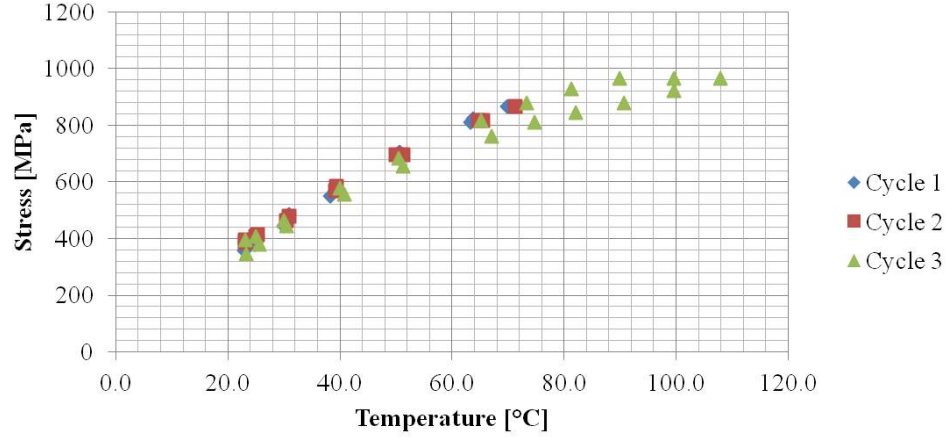


Figure 4.10: Stress versus temperature plot for a blocked pseudoelastic NiTi ribbon.

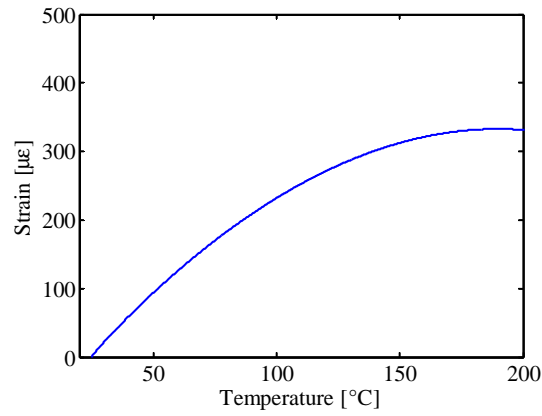


Figure 4.11: Modeled thermally-induced strain for a composite with 15.2% pseudoelastic NiTi ribbon by volume. Model based on properties found in Appendix D.

compared to the CTE of the Al 3003 matrix. With the results observed in these experiments, some considerations for future composites are given to obtain zero CTE behavior. While composite 4 begins to deviate from the linear blocked behavior at higher temperatures, it is believed that this can be avoided if the blocking behavior can be utilized at lower temperatures and stresses. By using a detwinned pseudoelastic alloy, the beginning of the blocking behavior can be made to occur at a lower temperature due to the inherently lower A_s values for pseudoelastic alloys. A pseudoelastic alloy has been characterized in

preparation for the next series of composites. Details of the characterization, similar to that conducted in Chapter 3, are given in Appendix D. This particular alloy demonstrates the immediate generation of blocking stress upon heating beyond room temperature as shown in Figure 4.10. The immediate generation of blocking stress effectively removes and linear thermoelastic region as observed in composite 4 below 54°C. A model of the thermally-induced strain for a hypothetical composite made with this pseudoelastic ribbon is shown in Figure 4.11.

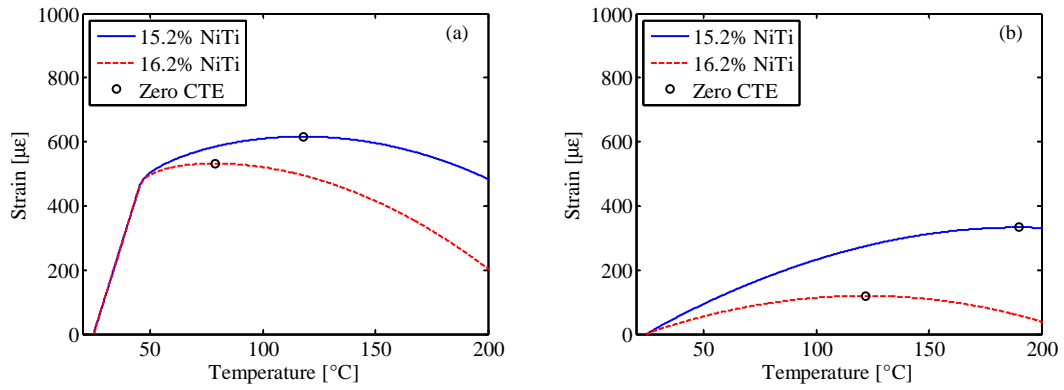


Figure 4.12: Comparison of modeled thermally-induced strain for difference fiber volume fraction in a composite with: (a) shape memory NiTi ribbons; (b) pseudoelastic NiTi ribbons.

In addition to lowering the transformation temperatures in the embedded NiTi ribbons, the composite CTE behavior can be adjusted by increasing the NiTi fiber volume fraction. Small increases in the volume fraction cause the zero CTE behavior to occur at lower temperatures, as shown in Figure 4.12 (a) for a composite similar to composite 4 and Figure 4.12 (b) for a composite made with the pseudoelastic NiTi previously discussed. While increasing the volume fraction does cause the zero CTE point to occur at lower temperatures, it also hastens the occurrence of the negative CTE region. A composite that contracts upon heating is useful for actuation purposes, however it may as undesirable as a positive CTE depending upon the design conditions. The effect of prestress on the NiTi

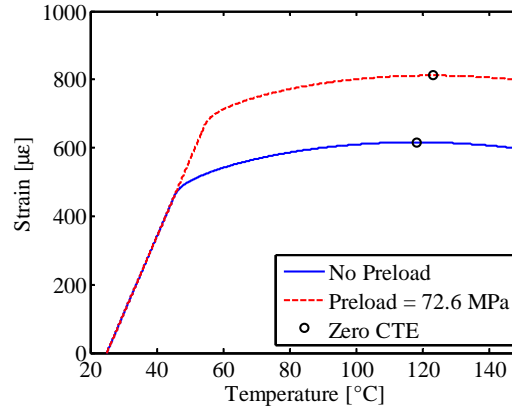


Figure 4.13: Modeled thermally-induced strain for composite 4 showing the effect of pre-stress on the embedded NiTi ribbons.

ribbons is also detrimental to achieving a zero CTE. The model for composite 4 is used to demonstrate the effect of a residual axial load on the composite behavior, Figure 4.13. The axial load effectively increases the temperature at which the blocking stresses are generated, allowing the linear thermal expansion region of the composite to further increase the total strain after the stress-free austenite start temperature. The estimated preload on composite 4 also causes the zero CTE point to occur at a higher temperature, 123°C versus 118°C. Due to the UAM process, it is not likely that prestress will ever be fully removed, however, its effect on ribbons needs to be quantified so it can be accounted for in future composites.

A summary comparison of the maximum strains observed in the composites at their respective maximum temperatures and the model output at each respective temperature is shown in Table 4.1. For low prestrain composites 1 and 3, the modeled strains are within 3.9% and 4.2% of the experimentally observed values, respectively. Composites 2 and 4 have more significant deviations due to the bending observed in composite 2 and the deviation from linear blocked behavior of NiTi in composite 4, as discussed.

Table 4.1: Comparison of experimentally observed strain at maximum temperature and modeled strain for composites 1-4. The parenthetical value for composite 2 corresponds to the model with $\xi_{so} = 1.9\%$.

Composite	Max. Temp. [$^{\circ}\text{C}$]	Exp. Strain [$\mu\epsilon$]	Modeled Strain [$\mu\epsilon$]
1	99	1720	1653
2	100	1244	1549 (1327)
3	100	1560	1495
4	98	1059	742

4.4 Summary

In this chapter, the thermally-induced strain behavior of NiTi-Al composites has been characterized and modeled. There is good agreement between the results and models for various levels of NiTi fiber volume fraction and NiTi prestrain level. Two factors that allow for tailoring the CTE of NiTi-Al composites have been identified and explored. The first is the variable modulus of the embedded NiTi ribbons. At high temperatures, the increased modulus of the austenite phase provides more resistance to the thermal expansion of the matrix. With a low prestrain composite, a bilinear hysteretic thermally-induced strain behavior is observed. The second method of tailoring the CTE is through the generation of blocking stress by prestrained NiTi ribbons. When prestrained and constrained by the matrix, the NiTi ribbons generate a temperature-dependent blocking stress above the effective austenite start temperature, directly opposing the CTE of the Al matrix.

Using shape memory NiTi, a CTE of $7.6 \mu\epsilon/^{\circ}\text{C}$ was obtained, a 67% reduction over the Al 3003 matrix material; however, the zero CTE behavior is not attained due to the high temperature/high stress deviation of the blocking stress behavior. Characterization and additional modeling suggest that it is possible to create a composite with a zero CTE near room temperature through embedding a pseudoelastic NiTi alloy. On-going work is focused on creating and characterizing such a composite.

Chapter 5

STATIC AND DYNAMIC TUNING

5.1 Introduction

In this chapter, both static and dynamic properties of the NiTi-Al composites are investigated as a function of temperature. In considering static properties, the change in elastic modulus of NiTi is utilized to change the stiffness of the NiTi-Al composites. A component with variable mechanical stiffness could be useful for adjusting clearances while under load and these composites are unique in that increasing temperatures can cause an increase in stiffness, opposite of typical structural materials that become more compliant with increasing temperature. The change in axial stiffness of composites 1-4 is characterized for static measurements.

In considering the dynamic properties, the natural frequencies and damping ratios of the composites are investigated. The natural frequency of the composites is impacted by the change in stiffness of the composites due to transformation of the NiTi ribbons as well as the generation of transformation stress of prestrained and constrained ribbons. By actively varying the resonant frequencies of a component, active vibration isolation mechanisms can be designed. Damping ratios are investigated as the composite nature of the samples and the hysteretic transformation of NiTi both provide mechanisms for energy dissipation. These properties are investigated through harmonic excitation experiments. The composite model introduced earlier is combined with analytical methods to describe the change in natural frequency of the composites as a function of temperature.

5.2 Experimental Setup

5.2.1 Static Tuning

The mechanical stiffness of each composite and a reference piece of Al 3003-H18 was measured at three different nominal temperatures, 23 °C, 60 °C, and 100 °C using a tension/compression load frame. Ambient temperature was controlled using the integrated thermal chamber on the tension/compression frame. Sample temperature, as measured with a J-type thermocouple contacting the sample near the strain gage, was allowed to stabilize prior to applying the load. At each temperature the composites were first given a nominal tensile reference load of 22 N (5.0 lbf), then load was increased to a nominal tensile load of 67 N (15.0 lbf) under displacement control at a rate of 2.54 mm/s (0.100 in/sec). During loading, the composites' strain was measured using strain gages. To find stiffnesses, the average values of load and strain were found at the low and high level load plateaus. Assuming a linear force-displacement relationship, the stiffness is found by dividing the change in force by the deflection over the length of the strain gage (787 μm , 0.031 in). Difference in the stiffness as a function of test temperature is then calculated relative to room temperature. This procedure assumes that the composites exhibit a linear stress-strain behavior which holds as long as the embedded NiTi ribbons are not stressed above the critical detwinning start stress during room temperature loading or do not undergo a stress-induced $A-M$ transformation during loading at elevated temperatures. The possibility of transformation is discussed in section 5.3.1.

5.2.2 Dynamic Tuning

The NiTi-Al composites and an Al 3003-H18 reference sample were subjected to dynamic testing. Dynamic tests consisted of applying a harmonic force to a clamping fixture while measuring displacement of the samples with a non-contact laser measurement system and the applied force with a piezoelectric load washer. For the solid Al samples and composite 1-3, a single point laser displacement sensor was used to measure deflection at a single point while for composite 4, a scanning laser vibrometer was made available for measurements

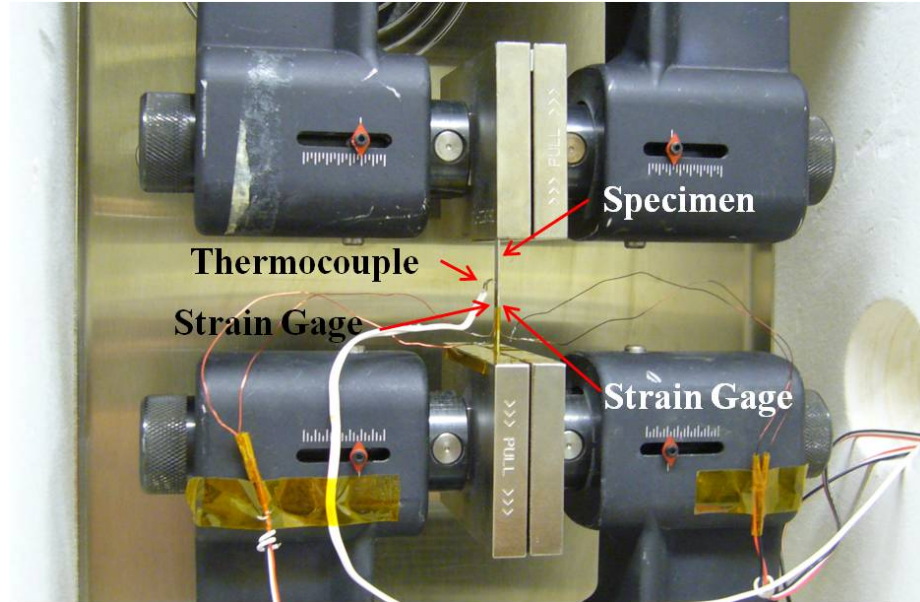


Figure 5.1: Composite 4 prepared for the temperature-dependent stiffness test. Sample is instrumented with a thermocouple and strain gages. Loading is controlled through displacement of the top grip.

over the entire sample surface. Two fixtures were used for dynamic testing. The first fixture creates a cantilevered condition (C-F) consisting of a clamp on one end and leaving the other end of the sample free. When installing beams on the C-F fixture, total length was set at 34.93 mm (1.375 in) with displacement measurements taken at 31.8 mm (1.25 in) from the fixed end. The second fixture holds both ends of the composite fixed with clamped boundary conditions (C-C). The distance between each clamp is 38.10 mm (1.500 in) and displacement measurements were taken at the mid-span of the beams. Both fixtures were constructed from Al 3003 and can be seen in Figure 5.2. Dimensions for these fixtures are provided in Appendix E.

For each boundary condition, the fixtures were attached to an electrodynamic shaker using a stinger that placed the fixtures and samples in a thermal chamber. For the solid Al sample and composites 1-3, dynamic excitation consisted of 50 chirps over a range of 200 to 500 Hz for the C-F tests and 1500 to 3000 Hz for the C-C tests. Excitation for composite 4 consisted of at least 5 chirp signals over the same frequency ranges for each scan point.

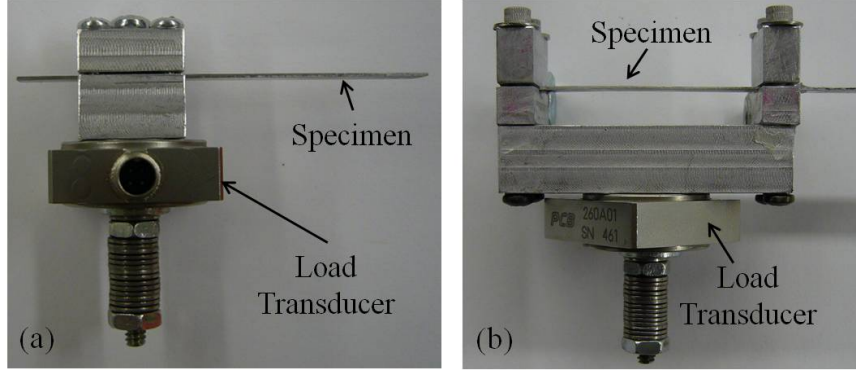


Figure 5.2: Composite sample installed in fixtures for dynamic testing: (a) Clamped-Free (C-F) fixture; (b) Clamped-Clamped (C-C) fixture.

Tests were conducted at nominal chamber temperatures of 24°C, 40°C, 60°C, 70°C, 90°C and 100°C in both heating and cooling sequences. Between each test, the thermal chamber was allowed to reach equilibrium to ensure that both the sample and fixture were at the same temperature before recording data. Temperature was monitored by a thermocouple attached to each fixture.

The frequency response function for displacement per force, X/F , was created using the average of the transfer functions from the chirp excitations in each experiment. System natural frequencies and damping ratios were identified from the resonant peaks and half-power frequencies. Prior the experiments, the expected natural frequencies were calculated using [5]

$$\omega_i = \frac{\lambda_i^2}{2\pi} \sqrt{\frac{EI}{mL^3}}. \quad (5.1)$$

In this equation, ω_i is the i^{th} natural frequency, λ_i is a dimensionless natural frequency parameter, E is the composite modulus, I is the composite area moment of inertia, m is the composite mass, and L is the composite length. In this study only the first natural frequency was observed which has a value for λ_1 of 1.87510407 and 4.73004074 for the C-F and C-C boundary conditions, respectively [5]. Mass for each composite beam was found via the rule of mixtures using the fiber volume fractions and densities for Al 3003-H18 and NiTi. The stiffness term, EI was calculated considering the Al matrix and NiTi ribbons

as two spring elements in parallel. Using this assumption, the composite value for EI was found by adding the respective values for the Al matrix and NiTi ribbons:

$$(EI)_{comp} = E_{Al}I_{Al} + E_{NiTi}I_{NiTi}. \quad (5.2)$$

As composites 2 and 4 have the same volume fractions and nearly identical dimensions, they are assumed to have the similar natural frequencies. The resulting expected first resonant frequencies at room temperature are summarized in Table 5.1.

Table 5.1: Expected natural frequencies for the solid Al sample and composites 1-4 for the C-F and C-C boundary conditions.

Sample	C-F [Hz]	C-C [Hz]
Al Reference	405.9	2170
Composite 1	391.2	2092
Composite 2/4	365.7	1955
Composite 3	353.7	1891

5.3 Results and Discussion

5.3.1 Static Tuning

The results from the static axial stiffness tests are seen in Table 5.2. The point of comparison between samples is the change in stiffness, Δk , given by:

$$\Delta k(T) = \frac{k(T) - k(RT)}{k(RT)} \times 100\% \quad (5.3)$$

where $k(RT)$ is room temperature sample stiffness and $k(T)$ is stiffness at test temperature, T . The change in stiffness is used as the comparison metric as it is not affected by the different cross-sectional area which varies from sample to sample. Assuming constant composite length and cross-sectional area during testing, relative change in axial stiffness is equal to relative change in elastic modulus. The sample stiffness is found considering the

Table 5.2: Results from axial stiffness tests for the solid Al reference sample and composites 1-4.

Sample	Temperature [°C]	Stiffness [N/mm]	Relative Δk
Al Reference	26	253.2	-
	60	248.0	-2.0%
	101	242.5	-4.2%
Composite 1	23	254.1	-
	59	254.7	0.3%
	98	261.2	2.8%
Composite 2	24	181.2	-
	58	184.4	1.7%
	99	199.3	10.0%
Composite 3	23	101.1	-
	58	102.9	1.7%
	98	64.9	-35.8%
Composite 4	24	220.0	-
	61	216.5	-1.6%
	100	216.9	-1.4%

Al matrix and NiTi ribbons as spring elements in parallel:

$$k_{tot} = k_{Al} + k_{NiTi} = \frac{E_{Al}A_{Al}}{L_{Al}} + \frac{E_{NiTi}A_{NiTi}}{L_{NiTi}}. \quad (5.4)$$

Since the matrix and ribbons have the same length and their respective cross-sectional areas are related through the NiTi volume fraction, v , equation 5.4 becomes:

$$k_{tot} = \frac{[E_{Al}(1-v) + E_{NiTi}v] A_{tot}}{L}. \quad (5.5)$$

Thus, relative change in stiffness is equivalent to change in modulus, allowing discussion of the stiffness change in terms of the change in elastic modulus of the matrix components.

The Al reference sample continually decreases in stiffnesses as temperature increases. This is due to the elastic modulus of the Al decreasing with increasing temperature. Composites 1 and 2 both exhibit increasing stiffness with increasing temperature. Further, composite 2 has a greater increase in stiffness than composite 1 at both elevated temperatures. The increase in stiffness indicates that the embedded NiTi ribbons are transforming to austenite as temperature increases. The increasing elastic modulus of NiTi through the

$M - A$ transformation is offsetting the decrease in modulus of the Al matrix, causing the net increase composite stiffness. As the NiTi content increases, the relative modulus change also increases.

Composite 3 shows an initial increase in stiffness at 58°C, consistent with composites 1 and 2, but then a significant decrease in stiffness is observed at 98°C. The load-displacement data from the load frame for this test shows that at the nominal 100°C test temperature, composites 1 and 2 exhibit a nearly linear trend while composite 3 shows a trend consistent with a superelastic shape memory alloy, Figure 5.3. Above 35 N, composite 3 exhibits a region with a much lower force-displacement slope, indicative of a stress induced $A - M$ transformation. This large increase in displacement is associated with a transformation to detwinned martensite which would cause composite 3 to exhibit a decrease in stiffness at 100°C. Composites 1 and 2 may also exhibit such behavior at this temperature but require a larger load to begin the $A - M$ transformation due to their smaller volume fractions of NiTi and larger cross-sections, as the smaller volume of NiTi will carry a smaller fraction of the applied stress.

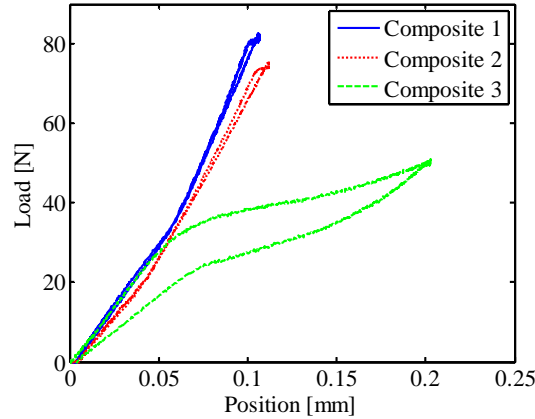


Figure 5.3: Load versus displacement plot for NiTi-Al composites 1, 2, and 3 at 100°C. Composite 3 exhibits a loading plateau and pseudoelastic behavior.

Composites 1-3 all have initially increasing mechanical stiffness with temperature be-

cause of the temperature-induced transformation to austenite. This transformation is enabled because of the low prestrain in the ribbons for each composite. Since composite 4 has completely detwinned martensite and it is constrained by the Al matrix, increasing temperature does not cause the same temperature-induced transformation. The stiffness for composite 4 at both 60°C and 100°C are less than the room temperature stiffness, indicating that the stiffness change is dominated by the decreasing modulus of the Al matrix. However, there is a slight stiffness increase between 60°C and 100°C, 0.2%, which indicates that the NiTi is partially transforming to austenite. This partial transformation hypothesis is supported by the observed second linear regions in the strain-temperature measurements from the thermally-induced strain tests discussed in Chapter 4.

A graphical comparison of the stiffnesses of composites 1-4 and Al 3003-H18 is given in Figure 5.4. Composites 1-3 all exhibit an increase in stiffness at 60°C due to a partial $M - A$ transformation while composite 4 and the solid aluminum sample shows a decrease. The stiffness decrease in composite 4 is not as large as the solid aluminum sample's decrease indicating that the martensitic phase of NiTi does not have the same decrease in modulus with increasing temperature that Al 3003-H18 does. While composite 4 is likely under a compressive load from the constrained NiTi ribbons at 60°C, the blocking stress that is generated does not contribute to the stiffness because the blocking load remains the same over the entire loading cycle for a given temperature.

5.3.2 Dynamic Tuning

Results from the C-F and C-C dynamic tests are compiled in Tables 5.3-5.6. The change in natural frequency, ω_n , and damping ratio, ζ , relative to their respective room temperature values are shown in Figures 5.6, 5.7, and 5.8 for the C-F boundary condition and in Figures 5.9, 5.10, and 5.11 for the C-C boundary condition. The percent change is used to normalize the results with respect to sample geometry since cross-sectional areas were varied to obtain specific NiTi volume fractions. The natural frequency is found from the maximum value of the frequency response of the displacement to force transfer function magnitude for each temperature. Damping ratio is found using half power points also found on the

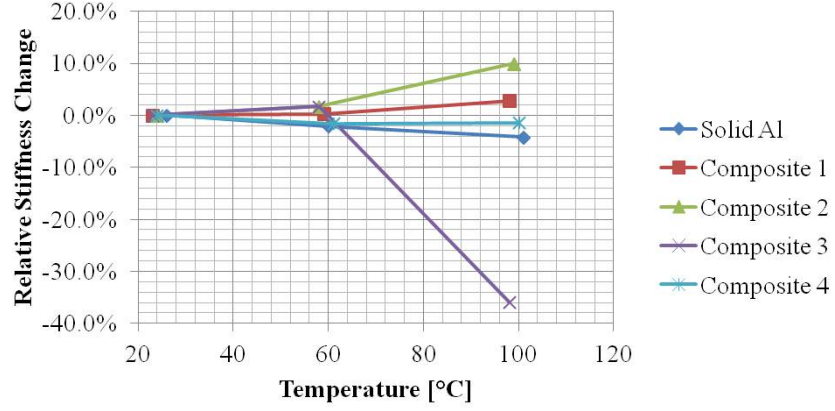


Figure 5.4: Relative change in stiffness versus temperature for NiTi-Al composites 1-4.

frequency response functions, as shown in Figure 5.5, as the points with magnitudes 3 dB less than the magnitude at the resonant frequency. The relationship between the half power points and ζ is given by

$$2\zeta = \frac{\omega_2 - \omega_1}{\omega_n} = \frac{\Delta\omega}{\omega_n} \quad (5.6)$$

where ω_1 and ω_2 are the -3 dB half power points in ascending order.

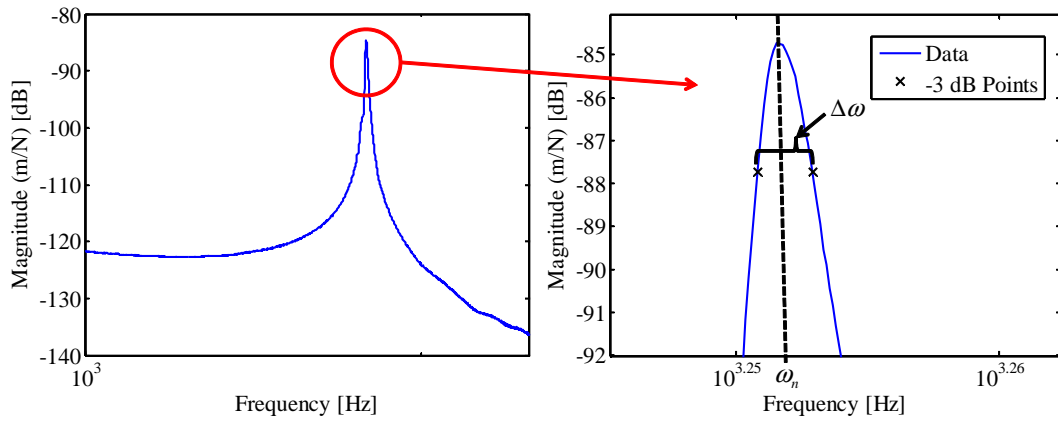


Figure 5.5: Frequency response of X/F transfer function measured for composite 4 under the C-C boundary condition at room temperature. Natural frequency and -3 dB frequencies used to find the damping ratio.

Table 5.3: Test temperature, natural frequency, and damping ratio for the solid Al sample and composites 1 and 2 with the C-F boundary condition.

Sample	Nom. Temp. [°C]	Temperature [°C]			Natural Frequency [Hz]			Damping Ratio ($\times 10^{-3}$)		
		Heating	Cooling	Average	Heating	Cooling	Average	Heating	Cooling	Average
Solid Al	25	24	24	24	414.1	414.1	414.1	1.802	1.1050	1.453
	40	38	41	39	414.1	412.5	413.3	2.703	2.502	2.603
	60	56	58	57	411.7	411.7	411.7	2.048	1.976	2.012
	70	73	72	72	410.9	410.9	410.9	2.285	2.169	2.227
	90	88	89	88	409.4	409.4	409.4	2.380	2.559	2.470
	100		101			408.6			2.186	
Comp. 1	25	24	23	24	362.5	362.5	362.5	0.875	0.882	0.879
	40	37	41	39	361.7	361.7	361.7	0.758	1.607	1.182
	60	54	57	56	360.9	360.9	360.9	0.919	1.474	1.196
	70	69	69	69	360.2	360.2	360.2	1.068	2.129	1.598
	90	88	90	89	359.4	359.4	359.4	2.224	1.538	1.881
	100		100			357.8			1.306	
Comp. 2	25	24	24	24	283.6	283.6	283.6	2.438	1.803	2.121
	40	37	38	38	282.8	282.8	282.8	3.648	2.074	2.861
	60	56	54	55	285.2	285.2	285.2	1.369	1.433	1.401
	70	67	71	69	285.2	285.2	285.2	1.395	1.546	1.470
	90	91	90	90	284.4	284.4	284.4	1.761	2.667	2.214
	100		100			283.6			3.593	

Table 5.4: Test temperature, natural frequency, and damping ratio for composites 3 and 4 with the C-F boundary condition.

Sample	Nom. Temp. [°C]	Temperature [°C]			Natural Frequency [Hz]			Damping Ratio ($\times 10^{-3}$)		
		Rising	Falling	Average	Rising	Falling	Average	Rising	Falling	Average
Comp. 3	25	23	24	24	339.1	339.1	339.1	2.639	2.253	2.446
	40	37	38	37	338.3	338.3	338.3	1.619	1.947	1.783
	60	55	57	56	339.1	339.1	339.1	1.436	1.745	1.591
	70	69	72	70	339.1	339.1	339.1	2.064	2.118	2.091
	90	91	90	91	337.5	337.5	337.5	1.703	1.693	1.698
	100		101			336.7			1.192	
Comp. 4	25	24	24	24	350.6	351.1	350.9	2.567	1.851	2.209
	40	37	38	38	349.1	350.1	349.6	2.578	2.142	2.360
	60	55	57	56	348.1	349.6	348.9	2.011	2.002	2.006
	70	70	69	69	348.6	350.1	349.4	1.865	1.857	1.861
	90	84	85	84	349.1	349.6	349.4	1.862	1.859	1.860
	100		101			348.6			1.865	

Table 5.5: Test temperature, natural frequency, and damping ratio for the solid Al sample and composites 1 and 2 with the C-C boundary condition.

Sample	Nom. Temp. [°C]	Temperature [°C]			Natural Frequency [Hz]			Damping Ratio ($\times 10^{-3}$)		
		Heating	Cooling	Average	Heating	Cooling	Average	Heating	Cooling	Average
Solid Al	25	24	24	24	2277	2273	2275	1.156	0.972	1.064
	40	40	38	39	2264	2264	2264	1.594	1.125	1.359
	60	57	56	56	2252	2252	2252	1.812	1.891	1.852
	70	69	71	70	2242	2236	2239	1.729	1.748	1.738
	90	95	98	97	2220	2217	2219	1.634	1.727	1.681
	100		100			2217			1.685	
Comp. 1	25	25	24	24	1945	1933	1939	1.561	1.444	1.503
	40	38	40	39	1950	1933	1941	1.531	2.186	1.858
	60	58	56	57	1978	1970	1974	2.354	2.328	2.341
	70	71	71	71	1989	1978	1984	2.283	2.154	2.218
	90	90	92	91	2000	1989	1995	2.493	2.224	2.358
	100		101			2003			2.474	
Comp. 2	25	23	24	23	1813	1800	1806	1.694	1.755	1.724
	40	41	39	40	1838	1819	1828	2.052	1.872	1.962
	60	59	57	58	1966	2009	1988	2.705	2.524	2.615
	70	75	73	74	2045	2052	2048	1.846	1.974	1.910
	90	90	98	94	2086	2092	2089	2.226	2.163	2.194
	100		103			2106			2.240	

Table 5.6: Test temperature, natural frequency, and damping ratio for composites 3 and 4 with the C-C boundary condition.

Sample	Nom. Temp. [°C]	Temperature [°C]			Natural Frequency [Hz]			Damping Ratio ($\times 10^{-3}$)		
		Heating	Cooling	Average	Heating	Cooling	Average	Heating	Cooling	Average
Comp. 3	25	24	24	24	1856	1844	1850	1.891	1.745	1.818
	40	39	39	39	1869	1848	1859	2.022	2.050	2.036
	60	59	59	59	1956	1963	1959	3.226	3.514	3.370
	70	72	74	73	1991	1988	1989	2.733	2.744	2.738
	90	92	90	91	2020	2005	2013	2.640	3.381	3.011
	100		102			2028			2.560	
Comp. 4	25	23	23	23	1785	1779	1782	2.400	2.298	2.349
	40	36	34	35	1809	1806	1808	2.129	2.106	2.118
	60	57	53	55	1842	1943	1893	2.362	2.056	2.209
	70	66	69	67	1950	2076	2013	2.367	1.920	2.144
	90	83	83	83	2131	2157	2144	1.789	1.882	1.836
	100		100			2228			2.011	

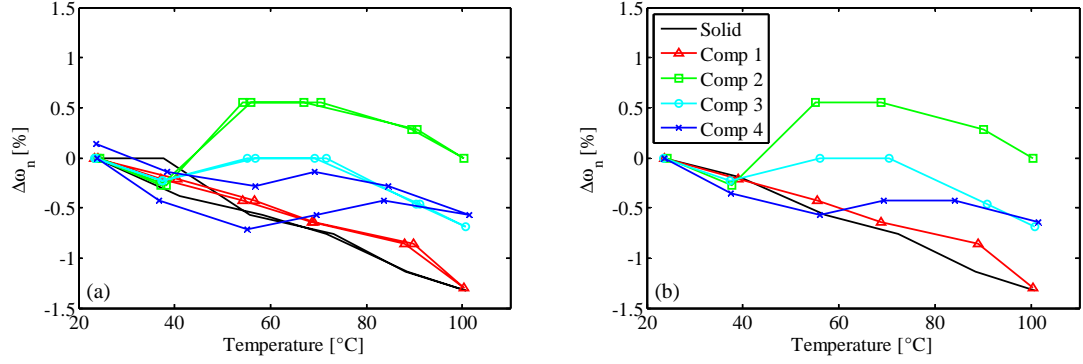


Figure 5.6: Comparison of the relative change in natural frequencies versus temperature for solid Al and composite 1-4 when subject to the C-F boundary condition: (a) heating and cooling values displaying hysteretic response; (b) average of heating and cooling values.

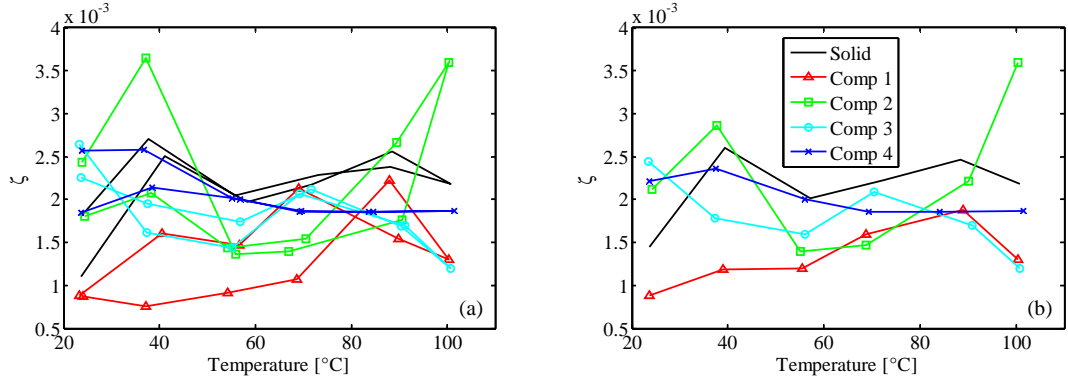


Figure 5.7: Comparison of the damping ratios versus temperature for solid Al and composite 1-4 when subject to the C-F boundary condition: (a) heating and cooling values displaying hysteretic response; (b) average of heating and cooling values.

The observed natural frequencies for the C-F boundary condition are similar to those described by the analytical equations with the exception of composite 2. The deviation of composite 2 is hypothesized to be a result of the partially detwinned martensite, though the exact mechanism is the subject of continued study. For the C-F boundary condition, the Al sample exhibits a linear decrease in natural frequency as temperature increases due to a drop in modulus, subsequently decreasing the sample's bending stiffness. The largest relative

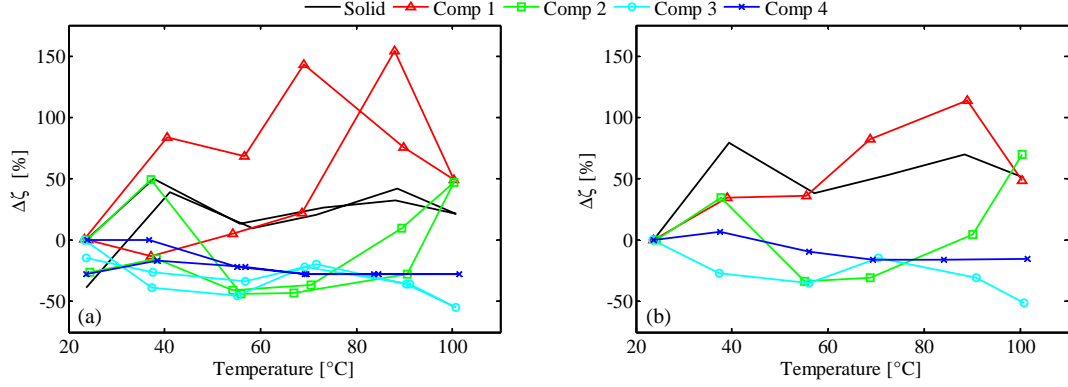


Figure 5.8: Comparison of the relative change in damping ratios versus temperature for solid Al and composite 1-4 when subject to the C-F boundary condition: (a) heating and cooling values displaying hysteretic response; (b) average of heating and cooling values.

change in natural frequency was -1.3% at 100 $^{\circ}\text{C}$. Composite 1 shows a similar decrease in natural frequency, reaching a relative change of -1.3% at 100 $^{\circ}\text{C}$. At a temperature between 60 $^{\circ}\text{C}$ and 90 $^{\circ}\text{C}$, composite 1 has a smaller relative decrease in natural frequency than the solid Al sample due to the $M - A$ transformation of the embedded NiTi ribbons; as a result of the transformation and higher modulus of the austenite phase, the loss in stiffnesses of the Al matrix due to increasing temperature is partially offset. This effect is expected to increase as NiTi volume fraction increases.

Composites 2 and 3 show a non-linear relationship between temperature and natural frequency. From Figure 5.6 both composites show a change in natural frequency similar to the solid Al sample and composite 1. However, at 60 $^{\circ}\text{C}$ composite 2 shows an increase in natural frequency relative to room temperature while composite 3 completely recovers all loss in natural frequency due to the drop in modulus of the Al matrix. Starting at 70 $^{\circ}\text{C}$, both composites continue a linear decrease in natural frequency with increasing temperature that is similar in rate to the Al sample and composite 1. The initial increase in natural frequency is due to the transformation of the embedded NiTi ribbons; at 60 $^{\circ}\text{C}$, the increase in bending stiffness of the ribbons is greater than the decreasing stiffness of the matrix due to heating. The effect is relatively small because while the change in NiTi modulus is significant, bending stiffness is also a function of the moment of inertia of all components.

The small cross-section of the ribbons as compared to the Al matrix combined with their placement near the neutral axis of the composite results in a relatively minute effect on natural frequency in the C-F boundary condition.

It is noted that composite 2, with 15.2% NiTi, has a net positive change in natural frequency at mid-range temperatures and no change in natural frequency at 100°C while the natural frequency of composite 3, with 20.6% NiTi, never exceeds the natural frequency recorded at room temperature. An examination of composite 2 showed that near the clamped end of the composite, total thickness was greater than expected, 0.69 mm (0.027 in) rather than 0.61 mm (0.024 in), indicating the presence of additional base plate material that was not fully removed. This extra material offsets the NiTi ribbons from the neutral axis causing the transformation to austenite to have a larger effect on the composite bending stiffness than if it were embedded at the neutral axis. This concept could be used to create composites with large natural frequency shifts through strategic placement of embedded SMAs rather than increasing the total SMA volume fraction.

Figure 5.6 shows the natural frequency of composite 4 initially starting to decrease with increasing temperature but then shows a momentary increase at 55°C. This is due to the onset of the $M - A$ transformation. As seen in the thermally-induced tests, the strain curve starts to change slope at approximately 55°C indicating that the transformation to austenite has begun. As with the C-F natural frequency of composites 2 and 3, the onset of transformation causes the natural frequency to increase, however with this composite, the detwinned NiTi cannot fully transform and therefore does not receive the full benefit of the increase in modulus associated with transformation. The increase in C-F natural frequency of composite 4 takes place at a higher temperature than the increase observed in composites 2 and 3. This is due to the tensile preload on the ribbons in composite 4 that are not present in composites 1-3. The effect of the preload is an increase in the effective austenite transformation temperatures. The lowest relative change in natural frequency for composite 4 is -0.7% at 55°C while at 101°C the drop in natural frequency is slightly less at -0.6%. The decrease in the natural frequency during transformation is less than that of the solid Al sample and composite 1, with 5.3% NiTi by volume, but greater than

the decrease observed by composite 3 with 20.6% NiTi by volume. This follows the trend expected by increasing NiTi volume fraction. It is also noted that composite 4 has a greater amount of hysteresis than composites 1-3. This is also true of the thermally-induced strain behavior and is believed to be due to the hysteresis induced by the extended partial $M - A$ transformation and resulting extended $A - M$ transformation upon cooling.

The damping ratios of all composites are similar in magnitude to that of the solid Al sample, as shown in Tables 5.3 and 5.4 and Figure 5.7. The values for damping ratio of the Al beam are within the range reported in the literature for aluminum alloys [16, 62, 87]. Both the solid Al sample and composite 1 have similar increases in average damping ratio with increasing temperature. Composite 2 shows an initial increase in damping ratio with temperature but exhibits a sharp decrease corresponding with the M-A transformation at 60°C. From 60°C on, the damping ratio increases with temperature. Composite 3 exhibits consistently lower damping ratios relative to the room temperature value at all elevated temperatures. When considering composite materials, the damping ratios are generally assumed to be higher than that of isotropic materials. This is attributed to friction between laminate layers, friction between the matrix and fiber, or damage to the composite [13, 32]. However, in this study it appears that UAM composites do not exhibit this characteristic of composite materials.

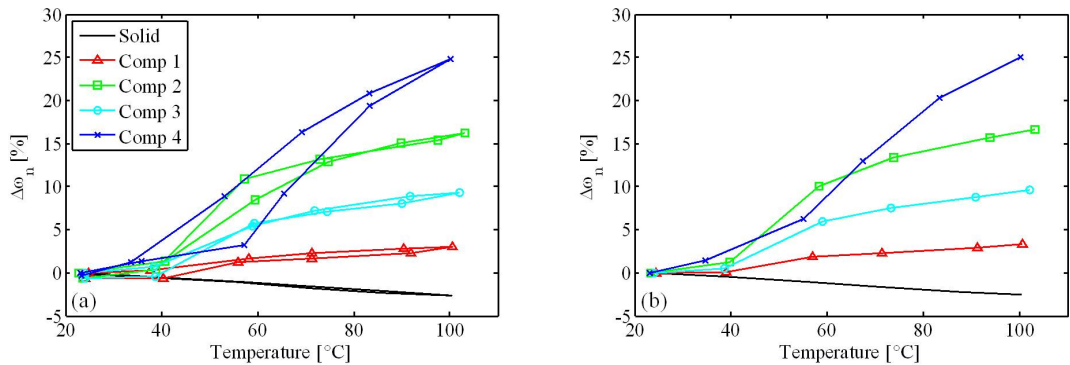


Figure 5.9: Comparison of the relative change in natural frequencies versus temperature for solid Al and composite 1-4 when subject to the C-C boundary condition: (a) heating and cooling values displaying hysteretic response; (b) average of heating and cooling values.

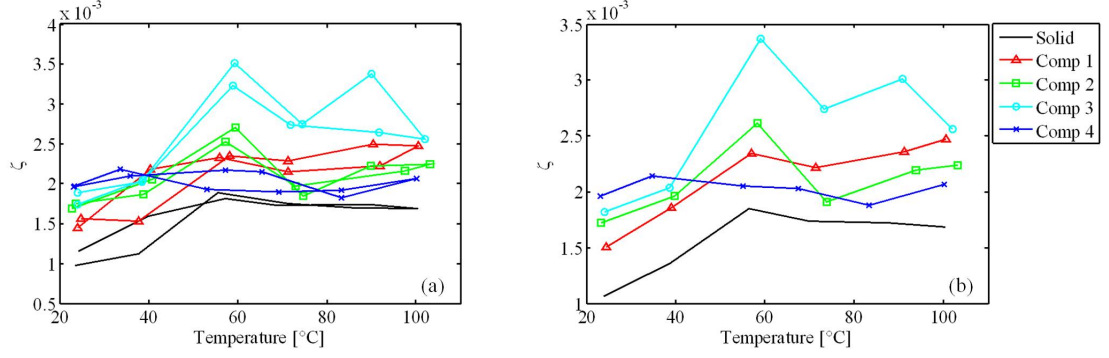


Figure 5.10: Comparison of the damping ratios versus temperature for solid Al and composite 1-4 when subject to the C-C boundary condition: (a) heating and cooling values displaying hysteretic response; (b) average of heating and cooling values.

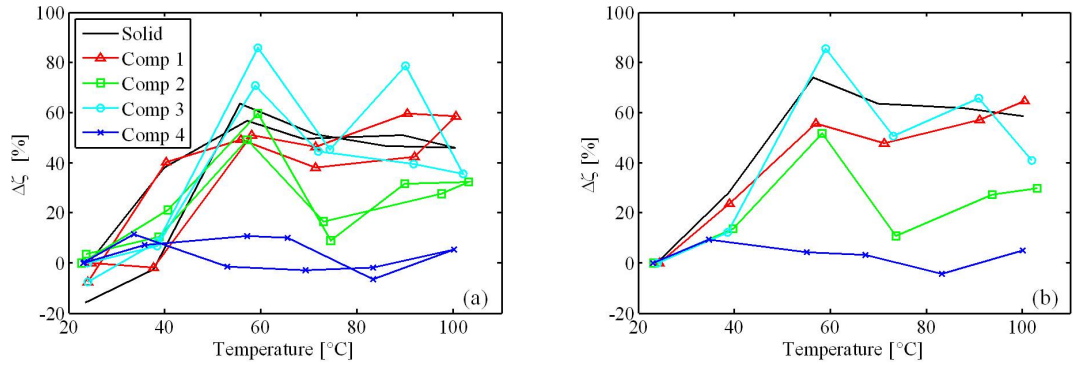


Figure 5.11: Comparison of the relative change in damping ratios versus temperature for solid Al and composite 1-4 when subject to the C-C boundary condition: (a) heating and cooling values displaying hysteretic response; (b) average of heating and cooling values.

Initial thermal cycles for the C-C tests showed that all four composites did not return to their initial natural frequency values upon cooling. In each case, the second room temperature natural frequency upon cooling was lower than the initial natural frequency prior to heating. The second thermal cycles, however, resulted in a return to the new initial room temperature natural frequency value. Since the composites are effectively constrained by the solid Al test fixture, this behavior is attributed to the previously observed transient behavior of constrained SMA composites. This behavior was not noted in the C-F tests due

to the unconstrained nature of the boundary condition and the transient response being already induced via the thermally-induced strain tests. Thus, it appears that when similar composites are in service, the first thermal cycle in a new boundary condition will not be representative of the repeatable behavior of subsequent cycles. The measured natural frequencies for the first cycles of the C-C boundary condition are close to the predicted values in Table 5.1. The initial transient behaviors are provided in more detail in Appendix F.

Dynamic test results from the C-C boundary condition show a significantly different composite behavior than the C-F boundary condition. While the solid Al sample exhibits a linear decrease in natural frequency with increasing temperature, all NiTi-Al composites exhibit increasing natural frequency with increasing temperature. Due to the C-C boundary condition, the lower CTE of the composites relative to the Al 3003 fixture causes a tensile stress to develop thereby creating an increase in natural frequency as temperature increases [5]. According to the zero prestrain assumption, composites 1, 2, and 3 should have increasing changes in natural frequency due to progressively higher NiTi fiber volume fractions creating progressively lower composite CTEs. The lower CTEs cause greater stresses to develop as temperature increases due to larger CTE mismatch between the sample and fixture. As observed by the thermally-induced strain study, composite 2 has a non-negligible prestrain and an apparent strain contraction as it is heated to 100°C. As a result, composite 2 generates larger tensile stresses in the C-C boundary condition than composite 3 even though it has a smaller NiTi volume fraction. This is reflected in the larger increase in natural frequency that composite 2 exhibits at temperatures above 60°C, up to 16.6%. Composite 1 and 3 have maximum increases in natural frequency of 3.3% and 9.6%, respectively, while the solid Al sample exhibits a change of -2.5%. In addition to the maximum relative increase in natural frequency, composites 1-3 have a sharp increase between 40°C and 60°C. This corresponds to the phase transformation of the embedded NiTi elements as the austenitic composites have a lower composite CTE, thereby creating higher tensile stresses.

Following this result, composite 4 shows the largest increase in natural frequency in the C-C boundary condition, 25.0%. While similar to composite 2 in terms of NiTi fiber

volume fraction, the fully prestrained NiTi ribbons generate larger blocking stresses and result in a smaller CTE, as discussed in Chapter 4. The smaller CTE results in larger tensile stresses generated in the composite. Similar to the C-F results, composite 4 does not begin to show a large change in natural frequency until after 60°C corresponding to the higher starting temperature for the $M - A$ transformation due to the initial preload on the ribbons. In addition, composite 4 has more hysteresis in the observed natural frequencies between heating and cooling segments of the experiment due to the incomplete $M - A$ transformation over the heating range between 60°C and 100°C.

Similar to the results for the C-F boundary condition, the composites have damping ratios similar in magnitude to the solid Al sample, shown in Figure 5.10. For the C-C boundary condition, all samples show an increase in damping ratio except for composite 4, which has a consistent damping ratio at all temperatures. The relatively constant damping ratio of composite 4 may stem from generation of recovery stresses creating larger tensile loads on the composite, reducing total deflection from bending.

The model developed for the thermally-induced strain of the composites is utilized to estimate the stresses on the composites in the C-C boundary condition. Since the fixture is significantly larger and stiffer than the composites, it is assumed that the strain induced in the fixture from the lower CTE of the composites is negligible. As such, the thermally-induced strain in the fixture is compared to the composite strain as given by (2.76) and (2.77). Any difference in strain, $\Delta\epsilon$, is resolved as elastic strain and external stress applied to the composite, σ_{ext} :

$$\Delta\epsilon = \epsilon_{fix} - \epsilon_{comp} = \alpha_{Al}\Delta T - \epsilon_{comp} = \frac{1}{E_{comp}}\sigma_{ext} \quad (5.7)$$

where E_{comp} is the elastic modulus of the composite calculated as a rule of mixtures between the NiTi fraction and Al fraction at each temperature. The additional stress will cause an increase in natural frequency as given by [5]:

$$\frac{\omega_{np}}{\omega_{no}} = \sqrt{1 - \frac{P}{P_{crit}}} \quad (5.8)$$

where ω_{np} is the natural frequency with applied axial load, ω_{no} is the unloaded natural

frequency, P is the applied axial load, and P_{crit} is the critical buckling load of the sample. For the C-C tests, the critical buckling load is calculated by [17]:

$$P_{crit} = \frac{\pi^2 EI}{(KL)^2}. \quad (5.9)$$

In the above equation, L is the beam length (38.10 mm for C-C tests), and K is a boundary condition dependent coefficient. For a beam clamped at both ends, K is 0.5. Similar to (5.1), the bending stiffness, EI , is calculated considering the Al matrix and NiTi ribbons as springs in parallel, adding their individual stiffnesses to get the total composite bending stiffness through (5.2). The temperature dependent load, P , for each composite is found by considering the composite modulus and total cross-sectional area, A_{tot} :

$$P = \sigma_{ext} A_{tot} = \Delta \epsilon E_{comp} A_{tot}. \quad (5.10)$$

The critical buckling loads and unloaded natural frequency change as a function of temperature due to the transformation of NiTi and the decreasing modulus of the matrix with increasing temperature. For each nominal test temperature, the buckling load, natural frequency ratio, unloaded natural frequency, and relative change were calculated and are provided in Tables 5.7, 5.9, 5.8, and 5.10, respectively. In these tables, both heating and cooling values are given as the hysteretic transformation of the embedded NiTi ribbons occasionally cause a different value at the same temperature depending upon the temperature trend.

Table 5.7: Critical buckling loads, P_{crit} , for composites 1-4 when subject to the C-C boundary condition.

Temp. [°C]	Comp. 1 [N]		Comp. 2 [N]		Comp. 3 [N]		Comp. 4 [N]	
	Heat	Cool	Heat	Cool	Heat	Cool	Heat	Cool
24	219	219	145	145	106	106	146	146
40	217	217	143	143	105	105	144	144
60	215	216	143	145	107	107	142	142
70	214	214	144	144	106	106	141	142
90	211	211	142	142	105	105	140	140
100	210		141		104		139	

Table 5.8: Calculated natural frequency ratio, ω_{np}/ω_{no} , for composites 1-4 when subject to the C-C boundary condition.

Temp. [°C]	Comp. 1		Comp. 2		Comp. 3		Comp. 4	
	Heat	Cool	Heat	Cool	Heat	Cool	Heat	Cool
24	1.000	1.000	1.000	1.000	1.000	1.000	1.000	1.000
40	1.015	1.015	1.017	1.017	1.018	1.018	1.017	1.017
60	1.030	1.032	1.092	1.080	1.074	1.080	1.065	1.108
70	1.037	1.037	1.167	1.187	1.099	1.099	1.161	1.205
90	1.048	1.048	1.214	1.214	1.136	1.136	1.348	1.386
100	1.053		1.228		1.154		1.437	

Table 5.9: Calculated unloaded natural frequencies of composites 1-4 when subject to the C-C boundary condition.

Temp. [°C]	Comp. 1 [Hz]		Comp. 2 [Hz]		Comp. 3 [Hz]		Comp. 4 [Hz]	
	Heat	Cool	Heat	Cool	Heat	Cool	Heat	Cool
24	2092	2092	1955	1955	1891	1891	1956	1956
40	2081	2081	1945	1945	1882	1882	1947	1947
60	2074	2076	1947	1957	1898	1902	1934	1935
70	2068	2068	1948	1951	1896	1896	1929	1929
90	2054	2054	1937	1937	1883	1883	1917	1918
100	2047		1931		1877		1911	

The relative change in natural frequency versus temperature as estimated from the thermally-induced strain model is provided in Figure 5.12. The modeled change in natural frequency for solid Al and composite 1 match the observed results with changes at 100°C of -2.6% and 3.1%, respectively. This experimentally obtained change in natural frequency for these samples are -2.5% for the solid Al beam and 3.3% for composite 1.

The C-C frequency model overestimates the change for composites 2, 3, and 4. This overestimation is due to an underestimate of the thermally-induced strain models for each of these composites. As discussed in Chapter 4, the negative strain-temperature slope over part of the response from composite 2 indicates that there may be bending that was unquantified. The underestimate of composite 3 may be due to a similar issue, though not to as great a

Table 5.10: Calculated relative change in natural frequencies for composites 1-4 under the C-C boundary condition considering the axial load from thermally-induced strain models

Temp. [°C]	Comp. 1		Comp. 2		Comp. 3		Comp. 4	
	Heat	Cool	Heat	Cool	Heat	Cool	Heat	Cool
24	0.0%	0.0%	0.0%	0.0%	0.0%	0.0%	0.0%	0.0%
40	1.0%	1.0%	1.2%	1.2%	1.3%	1.3%	1.2%	1.2%
60	2.1%	2.4%	8.7%	17.5%	7.8%	8.6%	5.2%	9.5%
70	2.6%	2.6%	16.3%	18.5%	10.1%	10.1%	14.4%	18.8%
90	2.9%	2.9%	20.3%	20.3%	13.1%	13.1%	32.1%	35.8%
100	3.1%		21.2%		14.6%		40.4%	

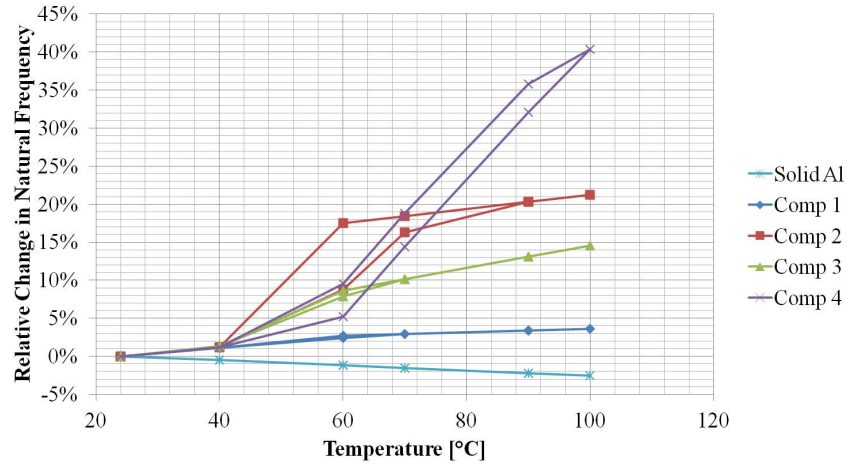


Figure 5.12: Calculated relative change in natural frequency for the C-C boundary condition using the thermally-induced strain model.

degree. Models for composite 4 assume a continued strain response in the blocking regime while the observed strain response indicates that the $M - A$ transformation is closer to completion at 100°C than predicted by the model. To overcome issues with the thermally-induced strain model assumptions, the experimentally determined strain for each of these composites is used to find strain values at the nominal dynamic test temperatures. These values are next used in (5.7) through (5.10) to calculate expected change from the observed strain data. The relative change in natural frequency versus temperature as calculated using the thermally-induced strain models is compared to the relative change as calculated from experimentally observed strain in Figures 5.13, 5.14, and 5.15.

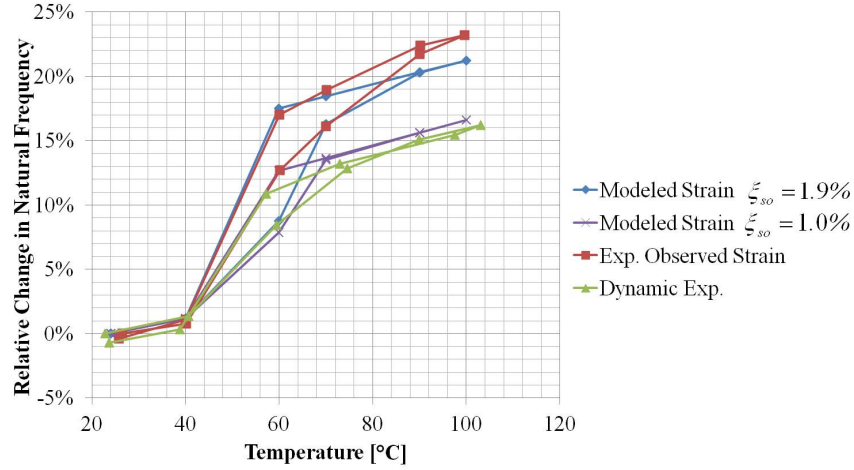


Figure 5.13: Comparison of calculated relative change in natural frequency for composite 2 under the C-C boundary condition using the thermally-induced strain model and experimentally observed strain.

The results for the modeled change in natural frequency for composites 3 and 4 using the observed strain data closely match the observed natural frequency shift. However, calculating the relative change in natural frequency for the C-C condition of composite 2 using experimentally observed strain still overestimates the frequency shift. This indicates that the calculated initial stress-induced volume fraction of 1.9% obtained in Chapter 4 is, itself, an overestimate due to neglecting the bending contribution to strain. However,

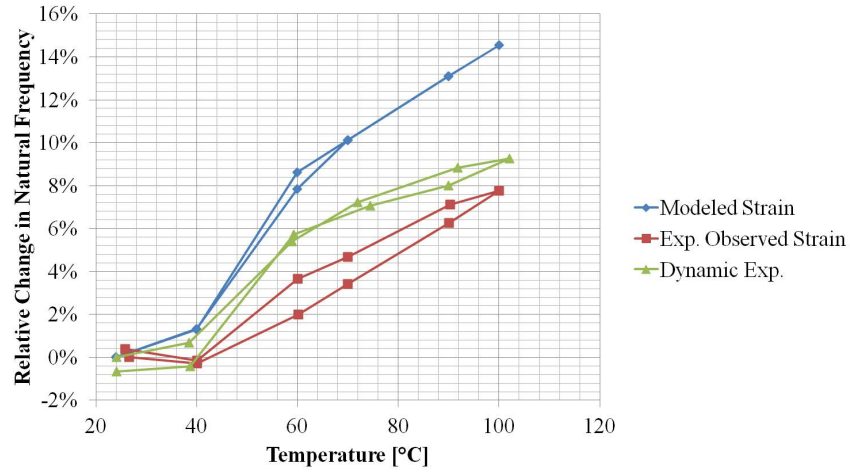


Figure 5.14: Comparison of calculated relative change in natural frequency for composite 3 under the C-C boundary condition using the thermally-induced strain model and experimentally observed strain.

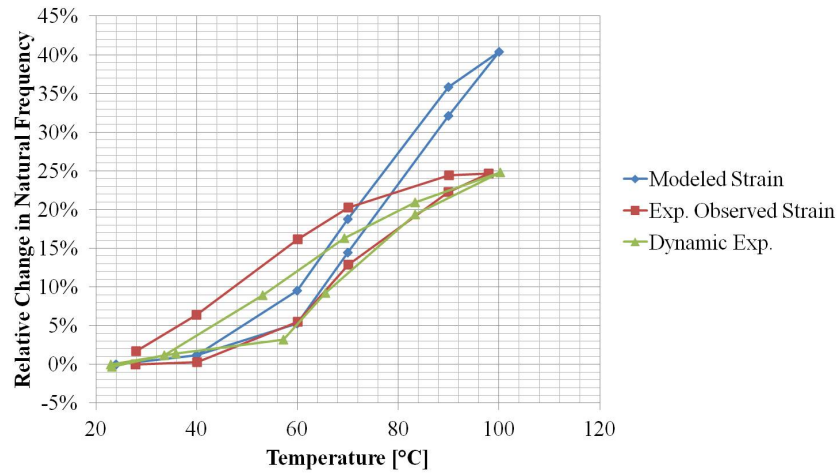


Figure 5.15: Comparison of calculated relative change in natural frequency for composite 4 under the C-C boundary condition using the thermally-induced strain model and experimentally observed strain.

by using the known frequency shift at 100°C, 16.6%, and the calculated unloaded natural frequency at 100°C from Table 5.9, the axial load on composite 2 can be found:

$$P = P_{crit} \left[1 - \left(\frac{\omega_{np}}{\omega_{no}} \right)^2 \right]. \quad (5.11)$$

The calculated value for P , 55.6 N, is in turn used to find the composite strain at 100°C through (5.10) and (5.7), 1442 $\mu\epsilon$. By subtracting the calculated strain required to cause the 16.6% frequency shift from the calculated strain for an equivalent composite with no stress-induced martensite (1557 $\mu\epsilon$), a value for transformation strain is obtained, 115 $\mu\epsilon$. Using (2.77) and the new transformation strain value, a new initial stress-induced volume fraction for composite 2 is found to be 1.0%. Using this final adjusted initial volume fraction for composite 2, the relative change in natural frequency closely matches the observed dynamic behavior as seen in Figure 5.13. Using the new initial stress-induced volume fraction value, the thermally-induced strain model is compared to previous version, Figure 5.16, put forth in section 4.3.2.

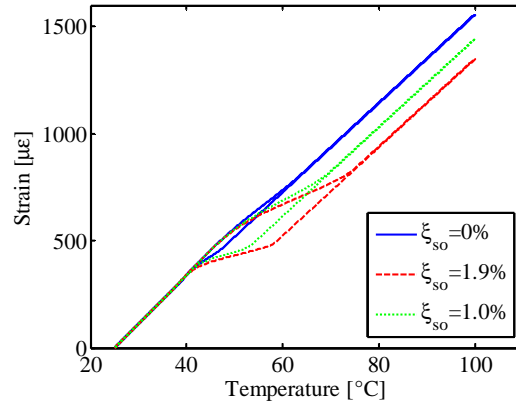


Figure 5.16: Comparison of thermally-induced strain models for composite 2. The amount of initial stress-induced martensite, ξ_{so} , is varied: solid line is the estimate after composite construction, 0%; dashed line is the estimate after analysis of thermally-induced strain experiments, 1.9%; dotted line is the final estimate after dynamic testing, 1.0%.

5.4 Summary

The mechanical stiffness of NiTi-Al composites was investigated through studying the effect of NiTi volume fraction and prestrain on the composites' thermomechanical static behavior. Low prestrain composites exhibit increases in stiffness due to the $M - A$ transformation of the embedded ribbons; the increase in modulus of NiTi overcomes the decrease in modulus of Al at higher temperatures. Composite 3 shows that this increase in stiffness only occurs below a critical load which is dependent upon NiTi fiber volume fraction. Above this critical load, the stress in the NiTi ribbons initiates the stress-induced $A - M$ transformation, bringing the NiTi elements into the detwinning plateau and their stiffness to several orders of magnitude below that of the matrix and causing the load to be entirely supported by the Al matrix. When the stress-induced transformation does not occur, increasing fiber volume fraction creates a larger increase in composite stiffness. In contrast to the low-prestrain composites, the constraint provided by the Al matrix prevents the completion of the $A - M$ transformation in composite 4 and as a result, the composite has a net negative change in stiffness at both 60°C and 100°C. As suggested by the thermally-induced strain behavior, there appears to be a partial $M - A$ transformation indicated by the higher stiffness of composite 4 at 100°C compared to 60°C.

Two different boundary conditions were considered in dynamic tests. For the C-F boundary condition, composites mitigate the decrease in natural frequency with increasing temperature exhibited by the solid Al reference sample. Composite 2 demonstrates the largest change, a 0.6% increase in natural frequency starting at 60°C relative to room temperature, due to the transformation of the embedded NiTi ribbons and their location slightly offset from the composite neutral axis. By placing SMA elements further from the composite neutral axis, it may be possible to create larger increases in natural frequency with smaller volume fractions. In the C-C boundary condition, all composites exhibit significant increases in natural frequency with temperature due to their lower CTE than the Al fixture. Composite 4 has the largest increase in natural frequency, 25.0% at 100°C relative to room temperature, due to the contribution of transformation stress generated by the

embedded pretrained NiTi elements. Composite 2 shows a similar increase, 16.6%, which is smaller than composite 4 due to the lower initial stress-induced volume fraction at room temperature. This demonstrates that by increasing prestrain in the embedded elements, natural frequency shifts can be substantially increased. In both boundary conditions, the damping ratios of the composites are found to be similar to that of the solid Al sample. This indicates that neither the composite nature of the specimens nor stress-induced martensitic transformations of the embedded NiTi ribbons cause a substantial change in damping properties over the parent matrix material under the tested conditions. At higher deflection, the $A - M$ transformation may occur, creating an increase in damping ratio.

Using analytical expressions, the thermally-induced strain models for composite 1-4 were utilized to describe the change in natural frequency of the C-C boundary condition tests. These expressions take into account the tensile stresses generated by the thermoelastic CTE of the composites as well as blocking behavior of initial stress-induced martensite volume fractions. If the properties of the composites are well known, these methods can be used in a predictive manner to design tunable dynamics systems. In the case of composite 2, the thermally-induced strain model was corrected through adjusting the initial stress-induced volume fraction using the observed change in natural frequency under the C-C boundary condition. This correction allows the model to overcome the error induced by the unknown bending component to thermally-induced strain originally discussed in Chapter 4.

Chapter 6

SMA-MATRIX INTERFACE CHARACTERIZATION

6.1 Introduction

Due to the difference in CTE of the Al matrix and NiTi elements as well as blocking stresses generated by the embedded SMA, the fiber-matrix interface is subject to significant temperature dependent stresses. The nature of the interface between the matrix and embedded SMA elements remains a critical issue in the designing and modeling of smart UAM composites. If the interface fails to maintain the constraint on the SMA elements, the NiTi fibers will be allowed to recover any induced prestrain through the $M^+ - A$ transformation and will not generate recovery stresses upon subsequent heating cycles, thus irrevocably changing the unique thermomechanical behavior of the composite.

In this chapter, interface of UAM NiTi-Al composite samples are studied through EDS and DSC. The EDS study investigates the possibility of metallurgical bonding between the NiTi ribbons and Al matrix, a key mechanism in the UAM process. Through the DSC study, samples from composite 6, with embedded fully prestrained NiTi ribbons, are heated until interface failure. The prestrain is critical because it creates the stress-induced martensite variant in the SMA. If left unconstrained, the induced prestrain will be recovered as the detwinned martensite transforms to austenite upon heating. If the SMA element is constrained, the transformation is extended over a larger temperature range and the SMA develops recovery stresses in lieu of phase transformation [78]. If there is no initial

prestrain in the SMA, the transformation from twinned martensite to austenite will not induce strain recovery and therefore will not generate recovery stresses even if the SMA element is constrained. Since the matrix cannot support the full strain recovery of the SMA, 6%, interface failure is coincident with the $M - A$ transformation of the embedded NiTi. This can be detected through DSC, an established method for observing behavior and failure in SMA-epoxy based composites [104–106].

6.2 Experimental Setup

6.2.1 Scanning Electron Microscopy

In preparing composite 5, all base plate material outside of the weld region was removed using a shear press and the resulting composite was cut in half with a lubricated low speed diamond precision saw to avoid transforming the NiTi ribbon near the cutting plane. To avoid the heating steps required for mounting the sample in a suitable conductive medium, a removable polishing clamp was created to polish the cross-section of composite 5, shown in Figure 6.1 (a). The interface was polished incrementally from 320 grit SiC sandpaper down to a 1 μm diamond paste. After polishing, the sample was cleaned in a methanol bath with ultrasonic excitation for 5 minutes and allowed to dry in air. SEM analysis was conducted with an electron accelerating voltage of 20.0 kV which was maintained for both general SEM observation and EDS analysis. A total of four EDS line scans were obtained, three on the top interface and one on the bottom with positions shown in Figure 6.2. Lines scans consisted of 50 individual analysis points spaced at most 0.8 μm apart. If bonding between NiTi and Al does occur during the UAM process, two key observations are expected. First, for metallic bonding to occur, the oxide layers of both workpieces must be removed. Second, diffusion is also expected to occur in conjunction with metallic bonding and thus, elements from the matrix and embedded SMA, namely Ni, Ti, and Al, are expected to migrate across the interface if such bonding is present. In the conducted line scans, the atomic percentage of Al, Ni, Ti, and O were recorded at each point in the scan and plotted as a function of distance from the interface.

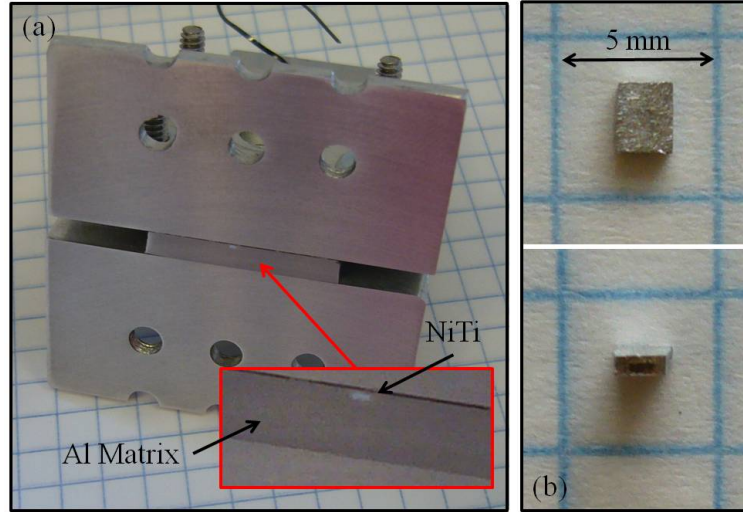


Figure 6.1: NiTi-Al composite samples for interface studies: (a) cross-section of composite 5 in removable polishing mount after final polishing; (b) sample 1 from composite 6 prior to DSC analysis.

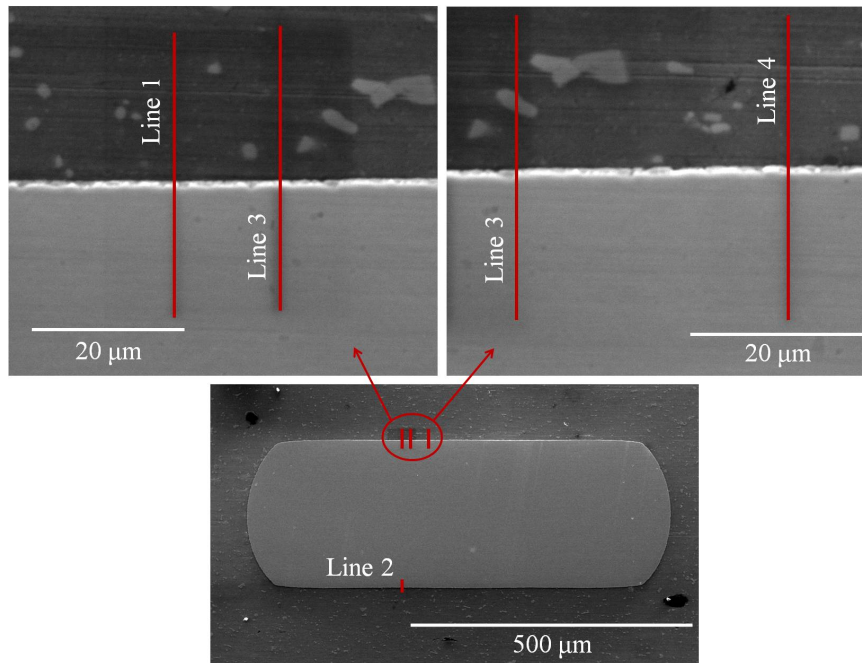


Figure 6.2: SEM images of NiTi-Al composite 5 showing locations of EDS line scans.

6.2.2 Differential Scanning Calorimetry

In preparation for DSC analysis, three samples were taken from composite 6 with an average length of 2.28 mm. The samples, seen in Figure 6.1 (b), were cut with a lubricated low speed diamond saw. Each sample from composite 6 was placed in an Al test pan and a single empty test pan was used as a comparative reference for all measurements. Using DSC analysis, the transformation of NiTi can be observed by measuring the difference in power needed to heat the test pan with the sample and the empty reference pan to the same temperature. The $M-A$ transformation for NiTi is endothermic and results in a well defined negative region termed an “endothermic peak” [104–106]. Since the embedded NiTi ribbon in composite 6 is highly prestrained, the $M-A$ transformation must be accompanied by a 6% strain recovery. The surrounding Al matrix is unable to accommodate a 6% contraction without plastic yielding or failure of the interface. Thus, by noting the temperature at which the endothermic transformation begins, a failure temperature can be measured and used in conjunction with the NiTi-Al composite models to determine the strength of the NiTi-Al interface.

For each sample, two heating cycles were recorded during DSC measurement. Temperature was increased at a rate of 10°C/min to 200°C for the first cycle of each sample and up to 120°C for the second cycle in anticipation of lower transformation temperatures. Cooling was augmented by compressed air between cycles but was not recorded.

6.3 Results and Discussion

6.3.1 Scanning Electron Microscopy

The NiTi-Al interface of composite 5 was investigated prior to conducting EDS analysis. As seen in Figure 6.3, there is intimate contact between the NiTi ribbon and Al matrix around the entirety of the ribbon perimeter. Top, bottom, and side surfaces as well as corner regions all show close contact even at high magnification. Further, a rough surface can be seen along the NiTi ribbon, indicating that the oxide layer on the ribbon surface has been ruptured creating areas of mechanical interlocking between the ribbon and matrix.

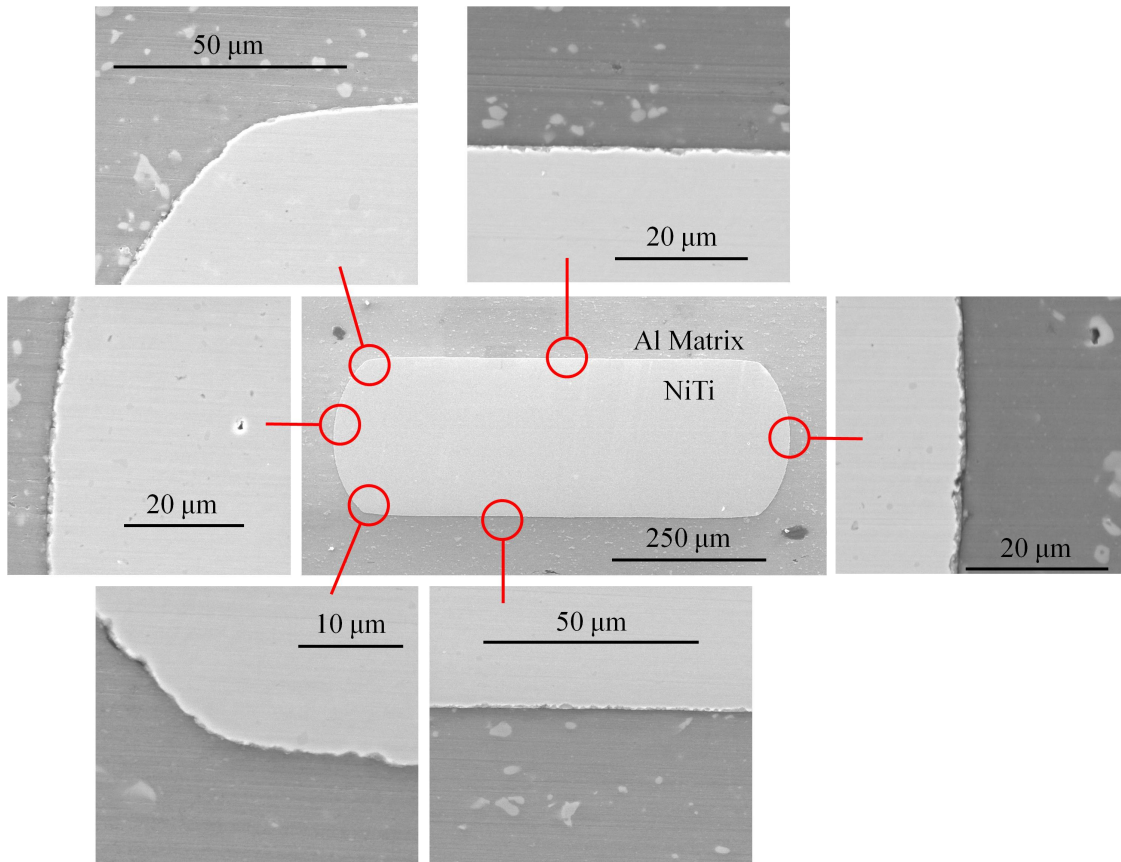


Figure 6.3: SEM image of NiTi-Al composite 5 showing plastic flow of Al matrix enveloping the NiTi ribbon and close contact over the entire interface.

There are several visible inclusions in the Al matrix in Figure 6.3. EDS point analyses were conducted on these regions and found consistent compositions of 85.9 at% Al, 6.8 at% Mn, and 7.3 at% Fe, all primary alloying elements in Al 3003 [12]. The inclusions are evenly dispersed and as a result appear to be naturally occurring precipitates within the Al tapes and not a result of the UAM process or embedding of the NiTi ribbon.

EDS line scan results are shown in Figures 6.4 and 6.5. Figure 6.4 shows atomic percent of all constituent elements while Figure 6.5 combines the Ni and Ti measurements to show compositional percent of equiatomic NiTi. The composite NiTi and Al atomic percent profiles were used to set a datum line equal to a distance of zero where the two profiles intersect. This is taken to be the interface between the NiTi ribbon and Al matrix and all EDS plots provide distance with respect to this assumed interface with negative values being within the Al and positive value being within the NiTi. While EDS line scan points were taken at intervals of less than 1 μm , the resolution of the line scan measurement is also dependent upon the electron interaction radii of the material being scanned. A Monte Carlo simulation of electron flight paths estimated interaction radii for Al and NiTi of 2.6 μm and 1.2 μm , respectively. The result of the interaction radii is that the EDS results will show a transition equal to the sum of the radii, 3.8 μm , as a scan transitions across a perfect, diffusionless interface between an Al and NiTi system. In considering the EDS results, a transition region greater than 3.8 μm indicates the presence of diffusion while a transition less than or equal to 3.8 μm indicates that there is no measurable diffusion between the materials.

The EDS line scans show Al-to-NiTi transition regions of 3.9 μm , 3.3 μm , 3.9 μm , and 3.5 μm for lines 1, 2, 3, and 4, respectively. The resulting transition widths are very close to the threshold for measurable diffusion indicating that there is likely no diffusion based bonding between the NiTi and Al constituents. Further, in all line scans there is a peak in oxygen content near the intersection of Al and NiTi composition lines. This indicates that at least one oxide layer, from either the Al or NiTi, is still present at the interface. A key aspect to bonding via UAM and solid-state joining in general is the removal of surface oxides at the interface of the workpieces. From the EDS results, the ultrasonic vibrations

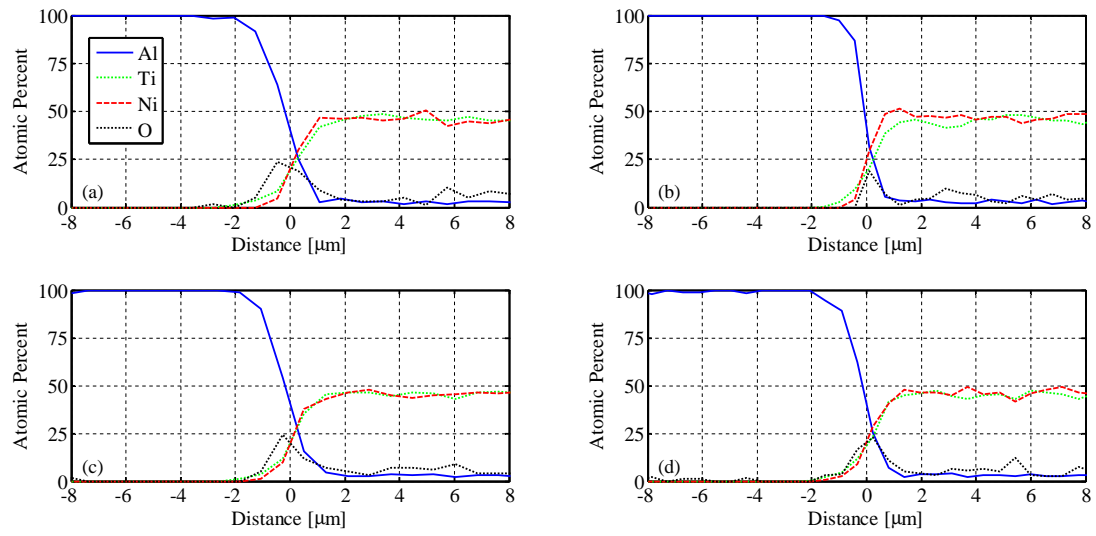


Figure 6.4: EDS line scan results of NiTi-Al composite 5 showing the relative atomic percent of Al, Ni, Ti, and O as a function of distance from the interface.

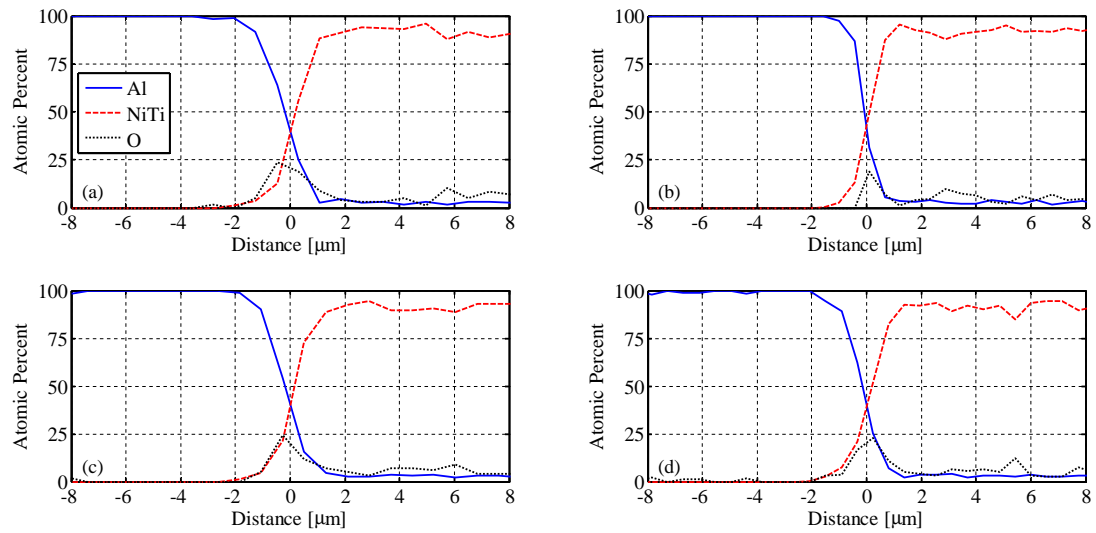


Figure 6.5: Combining the atomic percents of Ni and Ti to obtain a relative percent of NiTi. EDS line scan results of NiTi-Al composite 5 showing the relative atomic percent of Al, NiTi, and O as a function of distance from the interface.

generated for the consolidation process were not sufficient to create nascent surfaces at the NiTi-Al interface, thus making a metallurgical bond unlikely. While metallurgical bonding between NiTi and Al is doubtful, the SEM image in Figures 6.2 and 6.3 shows very close contact around the entire perimeter of the NiTi ribbon cross-section. This indicates that the load transfer necessary for the behaviors observed in the CTE testing is accomplished through a friction dominated interface.

6.3.2 Differential Scanning Calorimetry

Results from the DSC measurements are shown in Figure 6.6. The endothermic peaks observed in both cycles for each sample indicate the $M - A$ transformation temperature range of the embedded NiTi ribbons and display the change in temperatures between the first and second cycles. The decrease in bounding temperatures for the $M - A$ transformation and the magnitude decrease of the endothermic peak for the second cycle indicates that the NiTi ribbons in each sample have recovered the prestrain associated with stress-induced martensite through the first heating cycle. In both heating cycles of all samples, the contribution of NiTi can be observed when compared to a DSC measurement of a sample of UAM matrix material made from Al 3003-H18 with no embedded ribbons, Figure 6.7. The addition of NiTi causes a deviation from the nearly constant power versus temperature plot obtained from a sample of the matrix material.

There is slight variation in the first transformation peaks between samples. Both samples 1 and 2 show a single large peak while sample 3 exhibits a primary endothermic peak and a secondary peak beyond 80°C . This is likely due to stick-slip behavior within the composite caused by the interface maintaining a constraint on a portion of the NiTi ribbon until the interface stress develops further. Despite the differences in peak formation, all samples begin transformation at nearly identical temperatures. Further, all second cycle behaviors are also consistent, indicating that all three composites still have similar phases of NiTi after the first cycle.

Five key regions of interest are identified in the first cycles and are defined by either consistent behavior or transition points between areas of different behavior. These regions

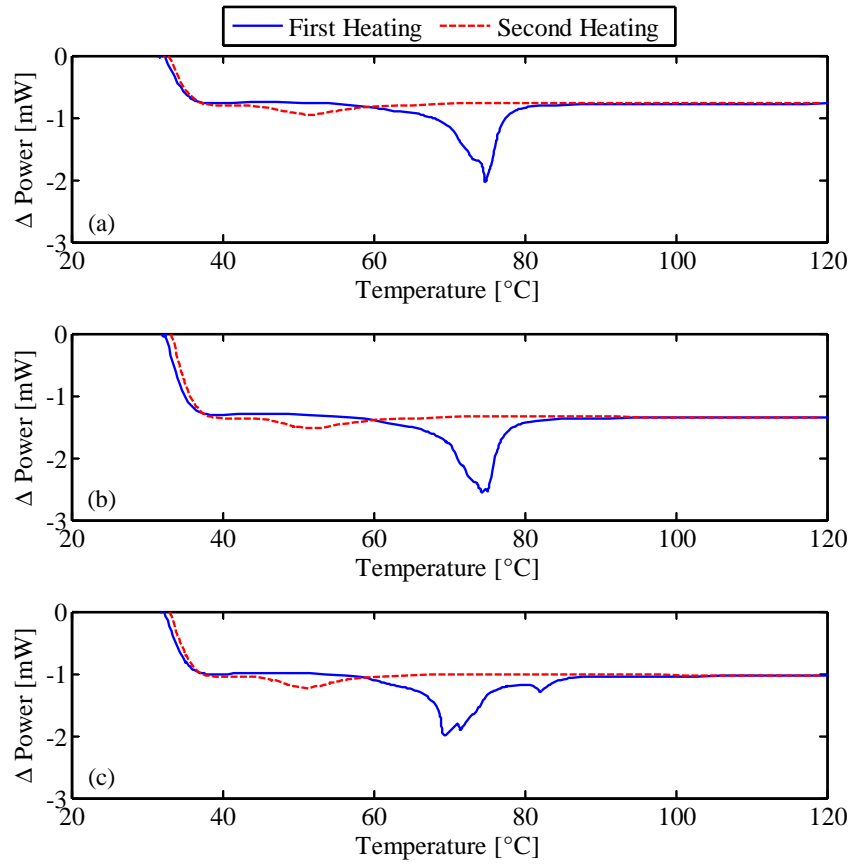


Figure 6.6: DSC results for composite 6 (a) sample 1, (b) sample 2, and (c) sample 3.

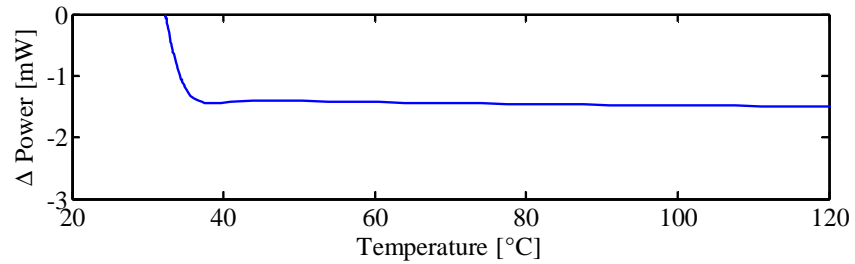


Figure 6.7: DSC results for UAM Al 3003-H18 matrix sample with no embedded NiTi.

are highlighted in Figure 6.8 for sample 2. Region (i) is the initial state and is characterized by the stabilization of the differential power measurement from the DSC system. Region (ii) is characterized by a nearly horizontal power versus temperature relationship. Region (iii) is defined by the a negative power-temperature slope prior to the endothermic transformation peak. Region (iv) is noted by the transition between region (iii) and the low temperature portion of the endothermic peak at temperature T_x . Region (v) is the intersection of linear interpolations of the high temperature portion of the endothermic transformation peak and the consistent behavior at higher temperature characterized by an approximately horizontal power versus temperature curve.

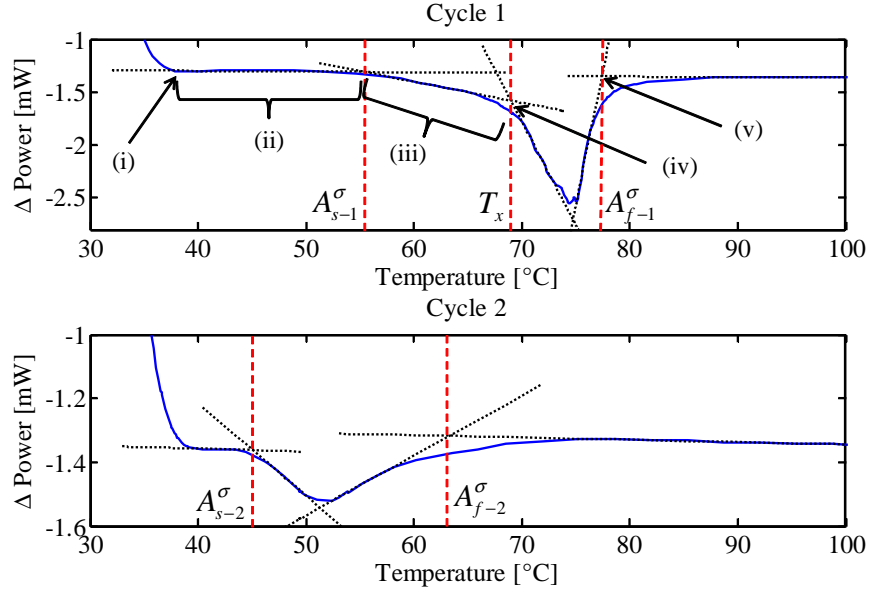


Figure 6.8: DSC heating cycles 1 and 2 of NiTi-Al composite 6 samples 2.

An interpretation of the composite behavior at each region is shown in Figure 6.9. At region (i), the composite is considered to be in a reference state to which all other regions are compared. Through region (ii), linear thermal expansion of the total composite is occurring. In region (iii), the temperature has surpassed the composite austenite start temperature, $A_{s-1}^σ$. As the composite temperature increases, the NiTi ribbon generates

recovery stress which is resolved as a compressive stress on the Al matrix. The result is an apparent reduction in CTE of the composite in this region due to the combined thermal and internal mechanical loading from transformation stresses. At region (iv) the generated stresses overcome the shear strength of the NiTi-Al interface and transformation of the detwinned martensite continues unrestrained. As the NiTi ribbons transform they recover the induced prestrain, contracting within the Al matrix while, simultaneously, the Al matrix is able to freely expand as governed by its CTE. At region (v) the NiTi transformation and strain recovery is complete. Additional heating results in linear thermal expansion of the composite. It is noted that while the NiTi ribbon has contracted within the Al matrix, there is still friction between the ribbon and matrix which allows load transfer and will govern thermomechanical properties of the composite. Region (vi) is cooling of the composite. During cooling and in subsequent cycles, the samples will behave similar to composites 1 and 3 due to the new zero prestrain condition and thermally-induced strain can be described by (4.3).

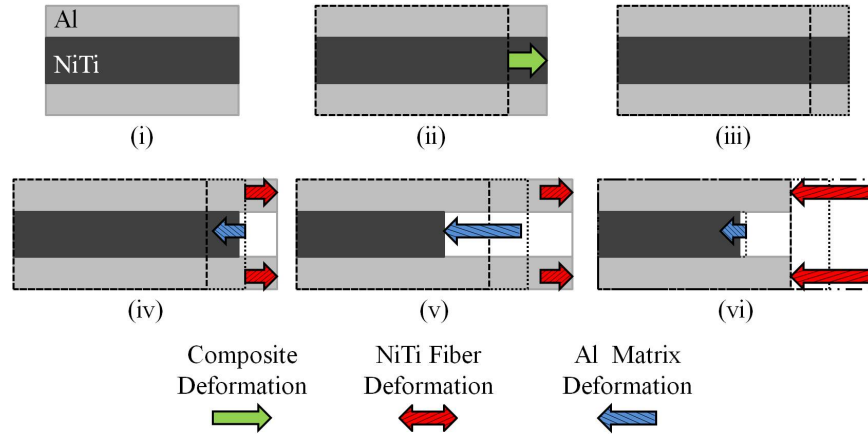


Figure 6.9: Representation of regions identified in DSC curve: (i) reference state; (ii) linear thermal expansion of total composite; (iii) reduced/suppressed expansion due to generation of blocking stresses; (iv) onset of NiTi-Al interface failure; (v) NiTi transformation complete; (vi) cool to reference temperature (not plotted).

Using the intersection of linear interpolations of different identified regions, several im-

portant temperatures are determined. The intersection of regions (ii) and (iii) is taken as the initial austenite start temperatures, A_{s-1}^σ , as previously noted. This is different than the austenite start temperature of the ribbon, A_s , due to the thermoelastic stresses generated by the different CTEs of the Al and NiTi components, thereby increasing the transformation temperatures as a function of temperature. In a similar manner, the initial austenite finish temperature, denoted A_{f-1}^σ , is different than the austenite finish temperature of the material, A_f , however in this case it is due to generated blocking stresses in addition to the thermoelastic stresses. The temperature at region (iv) is denoted T_x and represents the onset of the NiTi-Al interface failure. Region (v) denotes A_{f-1}^σ , the temperature at which the $M - A$ transformation is complete. At this temperature all prestrain has been recovered and further increases in temperature do not affect the NiTi phase.

The second thermal cycle in Figure 6.8 shows the shift in the endothermic peak and transformation temperatures, A_{s-2}^σ and A_{f-2}^σ . The austenite start temperature of cycle 2 is lower than that of cycle 1 indicating that there was a persistent preload on the NiTi ribbon after embedding. This preload is likely due to a combination of tension developed during the clamping process and the rolling action of the sonotrode imparting a tensile load during embedding similar to the load in composite 2 that created the stress-induced martensitic volume fraction. A_{f-2}^σ is significantly lower than A_{f-1}^σ due to the absence of blocking stresses generated during heating above A_{s-2}^σ . Further, cycle 2 does not exhibit a temperature range analogous to region (iii) in which blocking stresses were generated in the initial cycle. This is supporting evidence that all prestrain was recovered in the first cycle due to failure of the interface. The temperatures of interest for all 3 samples are given in Table 6.1. A_{f-2}^σ represents the austenite finish temperature of the temperature-induced NiTi composites. The results from these DSC tests have an average A_{f-2}^σ temperature of 61.9°C. As discussed in Chapter 4, this indicates that the A_f temperature of the NiTi ribbons is 60°C rather than the 70°C obtained from the original ribbon-only DSC test described in Chapter 2. It is most likely that the NiTi ribbon used in the initial characterization experiments was subject to an external stress causing the increase in the effective A_f temperature.

The NiTi stress in the DSC samples was calculated using (2.75) assuming an initial

Table 6.1: Transformation and failure temperatures for composite 6 samples 1, 2, and 3.

Temperature [°C]	Sample 1	Sample 2	Sample 3
A_{s-1}^σ	55.5	55.5	56.4
A_{f-1}^σ	77.7	77.4	77.5
A_{s-2}^σ	44.5	45.0	44.7
A_{f-2}^σ	62.6	63.2	60.0
T_x	69.2	69.0	68.4

stress induced volume fraction of 1 to obtain the stress-temperature load profile for the initial heating cycle shown in Figure 6.10(a). The plot shows two load paths: a profile in which the embedded NiTi has no initial preload and a profile that was made to intersect A_s^σ at the average A_{s-1}^σ temperature of 55.8°C. Both modeled cases have a stress-induced martensite volume fraction of 1, and therefore have the same amount of prestrain. The varied preload takes into account the amount of tensile stress applied to the SMA ribbon after it has been detwinned. Due to the transformation temperatures of this alloy and the stress-strain relationship of SMAs, the ribbon can be given a 6% prestrain and be unloaded to a zero preload condition while maintaining the prestrain level. Further, once fully detwinned, additional tensile loads will change preload without changing the prestrain value associated with detwinning. The DSC results combined with the NiTi composite model suggests that the NiTi ribbons were under a 83.9 MPa preload after embedding. It is noted that the zero preload profile begins the M-A transformation at 45.6°C, close to the average A_{s-2}^σ temperature of 44.7°C, indicating that the embedded ribbons have recovered all prestrain and preload after the initial DSC cycle. The stress-temperature load profile with the 83.9 MPa preload was used to determine the stress in the NiTi at interface failure, when $T = T_x$. The average interface failure temperature, 68.9°C, is marked by an “x” in the phase diagram and has an associated NiTi stress of 176 MPa. Using (2.77), the hypothetical thermally-induced strain of the DSC composites is shown in Figure 6.10 (b).

The EDS results indicate that there is no metallurgical bonding between the NiTi and Al and load transfer is accomplished via friction between the constituent components. Using the average tensile stress at failure, the ultimate shear strength at the interface is calculated:

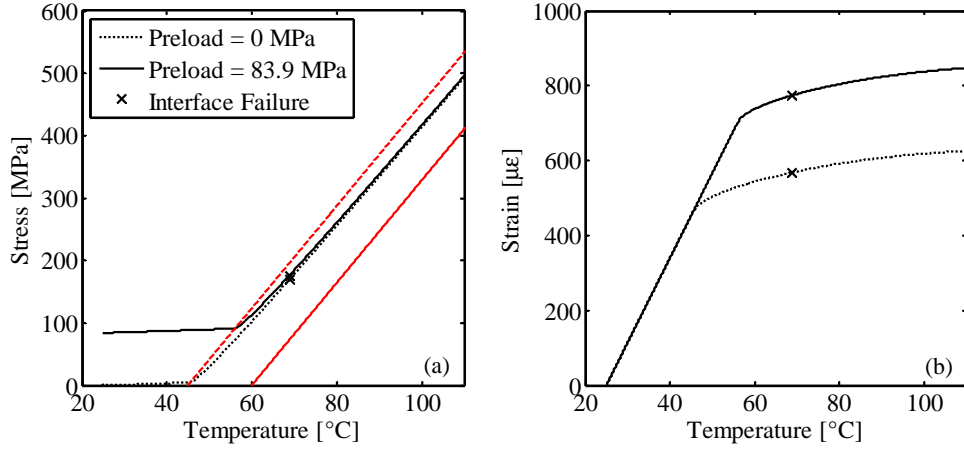


Figure 6.10: Model of NiTi-Al composites: (a) stress versus temperature, “x” marks inter-face failure; (b) strain versus temperature.

Table 6.2: Failure temperature, embedded length, NiTi stress at failure, and interface shear strength for samples 1, 2, and 3.

Parameter	Sample 1	Sample 2	Sample 3
T_x [°C]	69.2	69.0	68.4
L [mm]	2.21	2.37	2.25
σ_x [MPa]	178	177	172
τ_f [MPa]	7.68	7.10	7.29

$$\tau_f = \sigma_x \frac{A_{NiTi}}{A_{shear}} \quad (6.1)$$

where σ_x is the NiTi stress at failure, A_{NiTi} is the ribbon cross-sectional area, and A_{shear} is the interface surface area calculated by multiplying the ribbon cross-sectional perimeter by its embedded length. For each composite, observed failure temperature and the measured length in the fiber direction were used to find the NiTi stress at failure and shear stress at failure, respectively. These values are tabulated in Table 6.2. The average shear stress at failure is found to be 7.36 MPa.

The shear strength of the interface can be treated as a material property of the composite; it is a function of the UAM parameters used to create the sample as well as the materials being joined. Further, interfacial shear strength due to friction between the fiber

and matrix is not dependent upon the fiber length [70]. The shear stress at the interface, however, is a function of temperature, ribbon cross-sectional area, and embedded length. The composite temperature directly impacts the stress generated by the NiTi and the NiTi cross-sectional area is proportional to the amount of axial load the ribbon can apply to the matrix. While the recovery stress generated by the NiTi is not dependent upon ribbon length, the interface surface area is proportional to the length of ribbon embedded within the matrix. This implies that as composite length increases for similar NiTi-Al composites, so will the shear area, reducing shear stress for any given temperature, ultimately increasing failure temperature for a given sample. Eventually, the interface failure temperature may reach a point where composite failure may occur through yielding of the NiTi elements, compressive yielding of the Al matrix, or buckling of the composite rather than interfacial failure. The constant shear stress assumption used to determine the interfacial shear stress of the can be improved upon by using shear lag analysis which accounts for properties such as the coefficient of friction, fiber size, elastic moduli, and Poisson's ratios of the fiber and matrix [8, 70, 101]. However, before this can be applied, the coefficient of friction between NiTi and Al needs to be determined.

Using the model discussed in Chapter 2, failure temperatures of similar composites based upon the length of the embedded ribbon can be determined. In this approach, the NiTi stresses required to surpass the interface shear strength are calculated using prescribed lengths and proportional shear areas. The required stresses to induce interface failure have unique failure temperatures which are plotted in Figure 6.11. The plot accounts for the effect of the preload estimated in the DSC samples, however the difference between the failure temperature with and without preload is less than 1°C. With the 83.9 MPa preload, the minimum embedded length is 1.2 mm. Below this length, the stresses applied by the elastic preload are sufficient to cause interface failure without heating.

From Figure 6.11, a composite with a length of 20 mm has a sufficiently large shear area to be heated to over 240°C before interface failure. The implications of increasing the fiber length, and therefore operating temperature range, are demonstrated in the modeled strain-temperature behavior of these composites, shown in Figure 6.10 (b) for both the zero

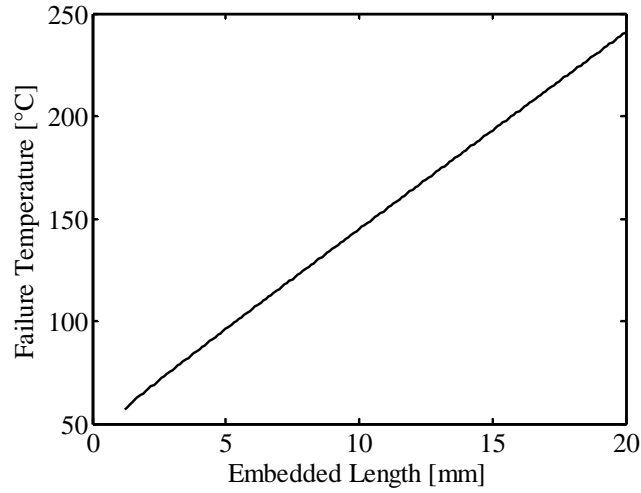


Figure 6.11: Model of failure temperature versus embedded length of NiTi ribbon.

preload and 83.9 MPa preload conditions. At the current failure temperature, the DSC samples are beginning to operate in their blocking stress and reduced CTE regime but are still several tens of degrees away from the thermally-invariant point. By increasing the failure temperature by making longer composites, it should be possible to delay interface failure until beyond the zero CTE temperature. The offset of interface failure by increasing composite length has already been demonstrated in the thermally-induced strain experiments: composite 4 could be repeatably heated beyond 68.9°C without observing composite failure due to the long embedded fiber length relative to the DSC sample studied in this chapter.

6.4 Summary

Work presented in this chapter characterizes the nature of the NiTi-Al interface in UAM composites. Observation through electron microscopy shows that the HPUAM process creates intimate contact between the NiTi ribbon and Al matrix around the perimeter of the ribbon cross-section. EDS analysis across the NiTi-Al interface at multiple points did not provide evidence of diffusion between NiTi and Al and, further, indicates that there is a persistent oxide layer between the fiber and matrix. The presence of the oxide layer is further evidence that there is no metallic bonding and load transfer between the fiber and

matrix are accomplished through mechanical interlocking or friction.

DSC analysis of three composite samples with fully detwinned NiTi ribbons shows a consistent interface failure temperature of 68.9°C. The lower transition temperatures observed in the second DSC heating cycle confirm that the embedded NiTi ribbons recovered the induced prestrain in the initial heating cycle and the composites have been irrecoverably changed as a result. Using the models described in Chapter 2, the blocking stress generated by the NiTi is estimated to be 176 MPa. Assuming a friction dominated interface, the ultimate shear strength of the NiTi-Al interface is determined to be 7.36 MPa. While the interfacial shear strength and the blocking force are not dependent upon length of the embedded NiTi elements, the shear stress at the interface is inversely proportional to ribbon length. This suggests that by increasing the composite length the interface failure temperature is increased significantly, avoiding irrecoverable composite damage. Ultimately, composite failure may not be limited by interface strength, but instead by material yield strengths and critical buckling loads.

Interfacial shear strength is a parameter of critical importance as significant stress levels are generated both by thermoelastic stresses and blocking stresses from the constrained NiTi ribbons. It may be possible to increase shear strength in future composites by either removing oxide layers mechanically or chemically immediately prior to consolidation to promote metallic bonding or through texturing the NiTi surface to improve mechanical interlocking. For high temperature zero CTE applications or composites with actuation properties, increasing the strength of the interface will likely be a primary concern to prevent composite failure in service.

Chapter 7

CONCLUSION

7.1 Summary of Findings

In this research, the modeling, creation, and characterization of a unique class of materials, SMA MMCs, has been accomplished. The new model was developed based upon bivariant constitutive SMA and phenomenological SMA composite frameworks from the literature. The new model has continuous functions describing the evolution of the martensitic volume fractions through the mixed temperature and stress-induced transformation region as described by a commonly utilized stress-temperature phase diagram. The SMA model is used to create a strain-matching framework to describe the thermomechanical behavior of an SMA composite. The total composite model is dependent only material and composite properties. The model requires 12 SMA material properties, 3 matrix material properties, and 2 composite properties (initial stress-induced volume fraction and SMA fiber volume fraction) for a total of 17 total necessary values. The model was used to analyze and describe the thermomechanical behavior of NiTi-Al composites with different stress-induced martensitic and fiber volume fractions in this research.

Using UAM, composites structures with Al matrices have been created that have over to 20% shape memory NiTi by volume. The key difference between the SMA MMCs developed and studied in this research and those previously described in the literature is in the low temperature construction process which allows for the study of unique, repeatable SMA-based behaviors. The process demonstrated in this work is not limited to these particular materials or fiber volume fractions. As such, the thermomechanical properties can

be further tailored using different matrix materials compatible with UAM (e.g. copper, titanium, steel) to tune the thermoelastic responses, SMAs of different compositions to adjust transformation temperatures and transformation hysteresis, and higher SMA fiber volume fractions to increase the magnitude of transformation related behaviors. Regardless of materials, the same principles, application of SMA prestrain, preload, and fixturing, can be applied for any future UAM composite to achieve similar behaviors.

The thermally-induced strain behavior of four NiTi-Al UAM composites was experimentally characterized. The composite have different fiber volume fractions of NiTi and different levels of initial stress-induced martensite or NiTi prestrain. Two primary behavioral regimes are observed. The first is the variable thermoelastic strain behavior where the composites exhibit a linear increase in strain with increasing temperature. In this regime, the NiTi ribbons provide different levels of constraint against the thermal expansion of the Al matrix depending upon their phase. At low temperatures, the constraint is relatively minor due to the low modulus of martensite while at high temperatures, the lower modulus of the Al matrix and increased modulus of the austenitic NiTi ribbons provide a greater restraint against the Al thermal expansion, leading to a reduced linear CTE of the composite. The effect of the NiTi ribbons is dependent upon the fiber volume fraction: more NiTi fiber volume results in a larger constraint and larger change in CTE.

The second behavioral regime in thermally-induced strain behavior is due to a non-zero initial stress-induced martensite volume fraction. As the temperature increases, the NiTi ribbons begin to under go a $M - A$ transformation which recovers strain induced through the stress-induced transformation to detwinned martensite. If this recovery is inhibited, a temperature dependent blocking or recovery stress is generated by the NiTi elements. In the case of composites 2 and 4, the stress-induced martensite created regions over which the composite has a significantly reduced CTE. At the minimum, composite 4 exhibits a CTE of $7.6 \mu\epsilon/^\circ\text{C}$, more than a two-thirds reduction of the CTE of the Al matrix. Using the developed composite model and properties obtained from characterization of a pseudoelastic NiTi alloy, a design has been created for a composite with a blocked strain behavior near room temperature, eliminating the initial thermoelastic response of composites 1-4.

The SMA composite model closely matches the thermally-induced strain data for composites 1-3. The model for composite 4 matches well up to approximately 70°C, at which point, the assumed linear relationship between stress and temperature of the blocked ribbons begins to become inaccurate. Further, the high temperature behavior of composite 4 suggests that the $M - A$ transformation is nearly complete at 100°C, an unexpected result. Further study is required on the behavior of the SMA ribbons at high stresses and temperatures to improve upon the current model.

Due to the change in elastic moduli and generation of recovery stresses, SMA bearing materials can be used to tune the static and dynamic properties of a component. To investigate this, composites 1-4 were subject to static and dynamic testing. For static testing, the average axial deflection over a given load was measured at different temperatures. Composites 1-3 all exhibited increases in stiffness with increasing temperature due to the $M - A$ transformation of the embedded ribbons. The largest increase in stiffness is a 10.0% change over room temperature stiffness for composite 2 at 100°C. Composite 3, with a higher NiTi volume fraction should have surpassed this, however the loads applied cause the onset of the stress-induced $A - M^+$ transformation, resulting in a drop of the effective NiTi stiffness, decreasing the total composite stiffness at 100°C. Due to the fully detwinned state of the NiTi ribbons embedded within composite 4, the $M - A$ transformation is not completed. As a result, the composite stiffness does not increase over its room temperature value when heated.

Two dynamic properties, natural frequency and damping ratio, were measured for composites 1-4 subject to C-F and C-C boundary conditions at multiple temperatures. Similar to the static stiffness tests, the temperature dependence of the C-F, or cantilevered, boundary condition for all composites was affected by the phase of the embedded NiTi ribbons. Since the NiTi ribbons were embedded at or near the neutral axis of the samples, there is little change in bending stiffness of the beams due to the $M - A$ transformation. Composite 1, 5% NiTi, has a smaller drop in natural frequency with increasing temperature as compared to a solid Al beam due to the inclusion of NiTi. Composite 3, 20% NiTi by volume, exhibits a decrease in natural frequency at lower temperatures but returns to its room temperature

natural frequency between 70°C and 90°C due to transformation. Beyond 90°C, the natural frequency begins to decrease due to the dropping modulus of the Al matrix. Composite 2, with 15% NiTi by volume, has an increase in natural frequency between 70°C and 90°C of 0.6%. The increase, despite its smaller fiber volume fraction compared to that of composite 3, is believed to be due to a slightly higher thickness near the base of the cantilevered beam, resulting in a higher moment of inertia and bending stiffness of the NiTi ribbons at high temperatures. As a result, the NiTi ribbons have greater authority over bending stiffness and natural frequency of the composite 2. Similar to the static stiffness tests, the restricted $M - A$ transformation of the ribbons in composite 4 result in a decrease in natural frequency relative to room temperatures for all elevated temperature tests.

The C-C boundary condition (double clamped) elicits a significantly different response from the composites. Due to the lower CTE of composites 1-4 relative to Al 3003 fixture, changes in temperature cause a tensile load to develop along the axial direction of the composites. The tensile loads increase due to the CTE mismatch for all composites, but composites 2 and 4 also have contributions from the blocking stresses generated by the prestrained condition of the NiTi ribbons. As a result, composites 2 and 4 exhibit the largest increases in natural frequency at 100°C, 16.6% and 25.0%, respectively. Dynamic response calculations created with analytical dynamic models and the developed composite model show good agreement with the observed experimental results. Using the dynamic models, the stress-induced martensitic volume fraction of composite 2 was determined to be 1.0%. Since the thermally-induced strain model for composite 4 deviates from observed behaviors after approximately 70°C, the dynamic model overestimates the shift in natural frequency. However, if the thermally-induced strain data is used to correct the model, the calculated dynamic behavior agrees well with the observed results.

In both the C-F and C-C boundary conditions, damping ratios of the composites were found to be similar to that of the solid Al reference sample. While composites and SMAs in general exhibit higher damping ratios than isotropic materials, the root causes, high damping of the matrix, fiber-matrix friction, and stress-induced transformation of the SMA, are not present in these composites. The Al matrix has a low damping ratio, interface

studies have shown good mechanical bonding between the ribbons and matrix, and ribbon loads during these tests are insufficient to cause detwinning or transformation. It may be possible to observe higher damping ratios of SMA UAM composites if beam deflections are higher or if axial vibrations are used as dynamic excitation, thereby more directly loading the embedded ribbons. High damping composites could also be designed for bending applications by placing ribbons further away from the neutral axis.

The interface between the NiTi ribbons and Al matrix has been characterized through high magnification observations, composition analysis via EDS, and failure analysis via DSC. SEM images of a cross-section made from composite 5 show very close contact between the NiTi ribbon and Al matrix at the micron level. EDS analysis of four different areas indicate the presence of a persistent oxide layer and show no evidence of diffusion between the NiTi and Al. These results suggest that the NiTi-Al interface is dominated by mechanical interlocking and friction between the fiber and matrix.

Using DSC analysis and three samples from composite 6 provided consistent failure temperatures with an average of 68.9°C. Using the SMA-MMC model, this corresponds to a axial stress applied by the NiTi of 176 MPa which results in a shear stress at the interface of 7.36 MPa. This is an important parameter for the design of future SMA UAM composites as once the interface fails and SMA prestrain is recovered, the composite behavior is fundamentally different. This change in behavior is also shown in the DSC measurements over two separate heating cycles.

7.2 Contributions

The presented research has advanced the state-of-the-art of SMA composites in multiple ways. First, the new developed model represents a versatile framework for designing and describing the behavior of long-fiber reinforced SMA composites with arbitrary levels of fiber volume fraction and SMA prestrain. Further, the model is not limited to a specific SMA or matrix material. As long as material properties are well defined and fiber volume fraction and SMA prestrain are known, the composite can be modeled. This model improves over

others in the literature by eliminating the dependence on fitting parameters and formulating a continuous kinetic law over the mixed stress and temperature-induced transformation region of the SMA phase diagram. This model allows for rapid design iterations of SMA composites to obtain desired behaviors before committing material resources and time to creating an SMA MMC component.

In this research several SMA MMCs were manufactured with various fiber volume fractions and SMA prestrain levels through UAM. Fiber volume fractions in excess of 20% were obtained, comparable to the SMA MMCs constructed in the literature. However, unlike the state-of-the-art MMC processes used to create SMA composites, the low process temperatures inherent in UAM result in composites that maintain the repeatable nature of the embedded SMAs; this is not possible with any other MMC technique currently in existence as they require fusion or diffusion of the matrix requiring high temperatures which are detrimental to SMA behaviors. Preservation of the SMA behaviors allow for the creation of metallic structures with unique properties such as tailored CTE, tunable static stiffness, and thermally adjustable dynamic properties. While these have been investigated for SMA polymer composites, the metal matrix enables these composites to be used under harsh conditions, including high temperature, vacuum, and moist environments, where polymer composites are often not suitable.

The size of embedded fibers also represents a significant contribution and improvement upon the state-of-the-art. Prior UAM composites were limited to maximum fiber diameters of approximately 100 μm . Preliminary studies with HPUAM systems for this research accomplished embedding of 381 μm diameter wires culminating in embedding rectangular ribbons 762 μm wide and 254 μm thick utilizing only plastic flow of the matrix material during consolidation. The methods described in this research enable composites with larger fiber volume fractions while maintaining intimate contact between the fiber and matrix along the entire interface.

The unique properties enabled by the SMA behavior have been experimentally characterized. Tailoring of the CTE has been demonstrated utilizing prestrained NiTi ribbons and varying NiTi fiber volume fraction. Being able to tailor the CTE of a metal structure

has two advantages. First, by reducing the CTE of Al based structures, light weight, dimensionally stable components can be developed for environments with larger changes in ambient temperatures. Currently, iron based alloys such as Invar are used in such cases. By using an SMA MMC there is a significant weight reduction which, for example, translates into fuel savings for payloads on aerospace structures. By creating a composite with a negative CTE, solid-state actuation is built into structural components. This can ultimately be applied to morphing structures with little or no moving parts.

Stiffness and natural frequency tuning of SMA MMCs was accomplished as was quantification of the damping ratios. By adjusting the dynamic properties of a structure, tunable solid-state suspension systems can be designed allowing for active vibration attenuation by shifting natural frequencies.

The nature of bonding between the NiTi ribbons and Al matrix was determined to be mechanical in nature with no evidence of metallic or diffusion based bonding. Further, the shear strength of the interface was quantified. This is a critical aspect of SMA MMCs that had not been investigated for NiTi-Al UAM composites. By quantifying the shear strength, operational envelopes can be determined for SMA MMC components to avoid interface failure and loss of prestrain-dependent behaviors. Further, knowing the primary mechanism for load transfer, steps can be taken to increase the interface strength allowing for higher generation of recovery stresses, higher operational temperatures, and ultimately increased performance in the studied behaviors such as zero/negative CTEs and larger shifts in natural frequency.

The contributions to the state-of-the-art are summarized below:

- Development of a model to describe the behavior of current composites and aid in the development of future SMA composites
 - SMA model with a continuous kinetic law over the mixed stress and temperature-dependent transformation region
 - SMA composite model dependent only on material properties and composite properties

- Design and manufacturing of high SMA volume fraction MMCs at low temperatures through UAM
 - Demonstrated method to create composites with volume fractions over 20%
 - Developed method to embed SMA fibers with different levels of prestrain
 - Increased the maximum size of embedded fibers
- Experimental characterization of the thermally-dependent behaviors and properties of NiTi-Al UAM composites including characterization of the interface between the NiTi fiber and Al matrix
 - Demonstrated the ability to tailor composites CTE using SMA fiber volume fraction and prestrain
 - Characterized increase in static stiffness with increasing temperature and effect of a critical composite load
 - Demonstrated tunable natural frequency of SMA MMCs
 - Quantified the damping ratio of composites as a function of temperature
 - Determined the nature of the SMA-matrix interface and calculated interface ultimate shear strength

7.3 Future Work

The research presented brings into focus some opportunities for future work and improvement. These concepts are divided into their improvement upon the current contributions of this research.

- Modeling
 - Modeling of high temperature blocking behavior of SMAs will increase model accuracy of high prestrain composites at higher temperatures. This will avoid the underestimation of thermally-induced strain and overestimation of shifts in natural frequency at high temperatures.

- Integration of the SMA composite model into classical lamination theory will create new design possibilities with composites that can have controllable CTE and tunable stiffness in two dimensions. Further, by having multiple laminates with different fiber angles, it may be possible create thermally-activated complex curvatures and to tune individual mode shapes of dynamically excited composite structures.
- Composite design and manufacturing
 - The observed behaviors and model predictions show that using prestrained pseudoelastic NiTi will result in blocked behavior at room temperature, enabling a low average CTE between 25°C and 200°C of approximately $1 \mu\epsilon/^\circ\text{C}$. Further, by increasing fiber volume fraction, the model indicates that negative CTEs, or actuation properties, could be obtained. These behaviors motivate the construction of additional composites with these attributes in mind.
 - The research has shown unique behaviors of small scale composite samples. Using the emerging generation of HPUAM systems, creating thermally-invariant components in the deci/centimeter scale rather than the milli/micrometer scale is now a possibility. This is key step in developing structural smart composite components. Such components are under development, Figure 7.1, based upon the findings in this research.
- Experimental study
 - In this study, damping characteristics were quantified, but they were not a primary design consideration. An investigation into thermally activated UAM damping structures could be conducted studying the effect of fiber volume fraction of non-prestrained or critically preloaded SMA elements as well as the placement and total fiber volume fraction of the SMAs on the composite damping ratio. Further, if a material with a relatively high CTE, such as Al is used as the matrix, it may be possible to have temperature increases that create thermoe-

lastic loads on SMA elements, bringing them closer to their critical detwinning stresses and causing additional excitation to generate hysteretic minor loops, thus dissipating applied energy through transformation.

- The interface investigation has characterized the nature of the NiTi-Al bond and its strength. A natural extension to this work is the investigation of improving the interface strength. Two possible methods include deformation of the NiTi surface to promote more aggressive mechanical interlocking and removal of the oxide surfaces through mechanical or chemical means prior to embedding to promote diffusion and metallic bonding. Low temperature heat treatments may also improve bond quality between the NiTi and Al elements via diffusion.
- Just as high temperatures can deteriorate repeatable SMA behaviors, so can high load levels. While UAM is a low temperature process, there are significant loads applied to the fiber and matrix materials during consolidation. The effect of these loads on SMA behavior is currently unknown but may be important in designing composites with specific functional behaviors and merits additional investigation.

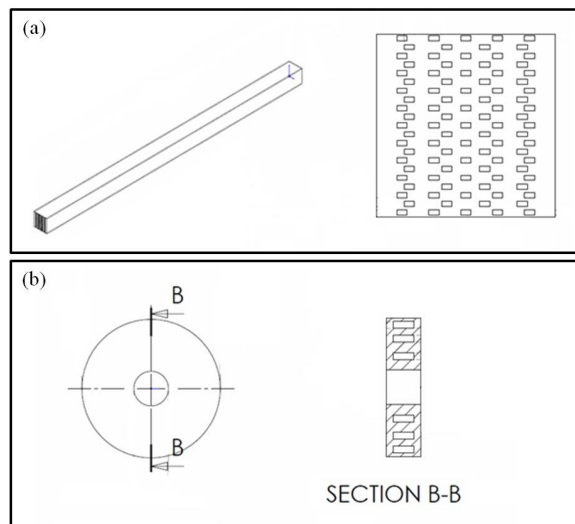


Figure 7.1: Thermally-invariant HPUAM SMA-Al composite components under development. These components combine the thermal-invariance of iron-based alloys such as Invar with the weight saving of aluminum alloys. (a) Longitudinally thermally-invariant structural beam. (b) Radially thermally-invariant bushing.

Appendix A

ADDITIONAL NUMERICAL SMA LOAD PATH SIMULATIONS

This appendix provides some additional simulations for combined thermal-mechanical load paths using the SMA model presented in Chapter 2. While the following load paths do demonstrate the flexibility of the SMA model and provide insight to the behavior of SMAs, they are not likely loadings to be encountered in an SMA composite. In an SMA composite, there would likely be no isobaric thermal loads due to differential CTEs of the SMA fibers and matrix and further, proportional loadings would likely have a positive stress-temperature slope. These simulations were made using SMA material properties given in Table A.1.

A.1 Piecewise Stress and Temperature Loading

Piecewise loadings are useful to demonstrate the one-way nature of the transformation regions. The following two plots increase stress and temperature independently and in turn before reducing each to their initial values. In both cases, the SMA begins as temperature induced martensite, $\xi_o = \xi_{To} = 1$. The first plot shown in Figure A.1, shows a clockwise rectangular load path, first increasing stress to 500 MPa, above the critical finish stress, and then increasing temperature to 150°C, sufficient to complete the $M^+ - A$ transformation. Stress and then temperature are brought back to their initial values, returning the SMA to its initial phase. From the phase diagram in Figure 2.2 (b), the load path causes transformation through regions 2a, 4, and 3 in order.

Table A.1: Material properties used for SMA model numerical examples.

Property	Description	Value
M_f	Martensitic Finish Temp	41°C
M_s	Martensitic Start Temp	50°C
A_s	Austenitic Start Temp	58°C
A_f	Austenitic Finish Temp	71°C
σ_{cr}^s	Critical Start Stress	50 MPa
σ_{cr}^f	Critical Finish Stress	63 MPa
C_M	Martensitic Stress Influence Coefficient	8.1 MPa/°C
C_A	Austenitic Influence Coefficient	8.1 MPa/°C
E_M	Martensitic Elastic Modulus	26 GPa
E_A	Austenitic Elastic Modulus	83 GPa
α	Coefficient of Thermal Expansion	10 $\mu\epsilon/^\circ\text{C}$
ϵ_L	Maximum Transformation Strain	6%

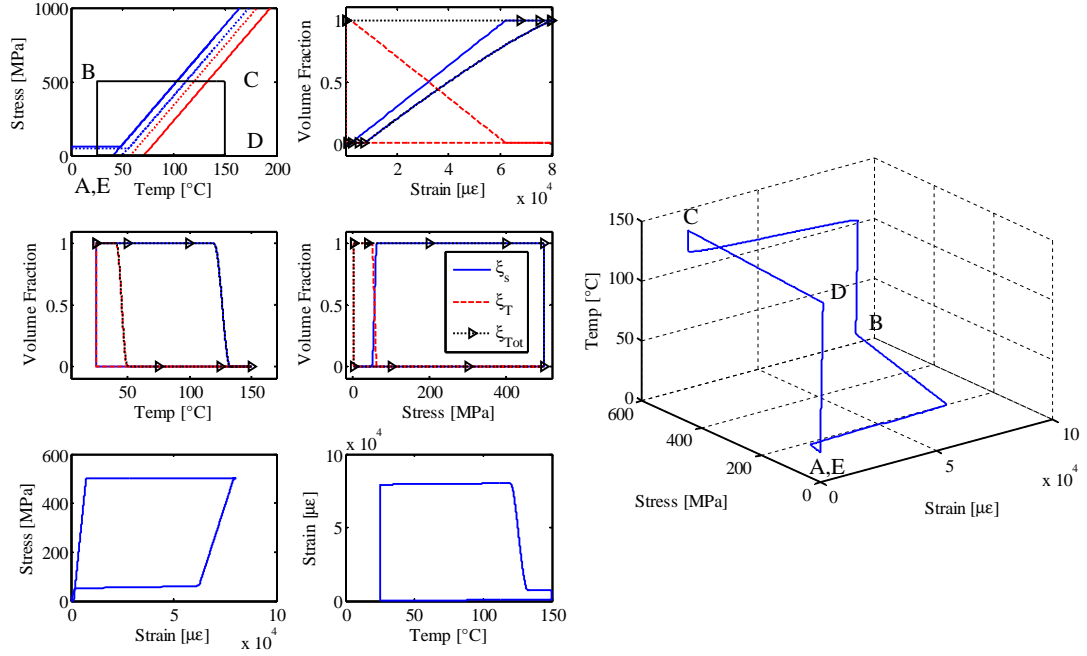


Figure A.1: Clockwise stress-temperature load path. $\xi_{T_o} = 1$, $T_o = 25^\circ\text{C}$, $\sigma_o = 0$ MPa.

Figure A.2 shows a load path identical in magnitude with the same initial conditions but in a counter-clockwise direction: temperature is first increased, followed by stress, then the temperature is reduced before the stress load is released. The result is that the SMA does not return to its original phase and retains residual transformation strain due to the one-way nature of the detwinning process. The initial heating transforms the twinned martensite to austenite. Subsequent loading is not sufficient to create stress-induced martensite at the current temperature but the subsequent drop in temperature decreases the temperature dependent critical start and finish stresses, allowing the isobaric transformation to stress-induced martensite. The unloading of the SMA results in only an elastic recovery of strain as the transformation from stress-induced martensite to temperature-induced martensite is not spontaneous.

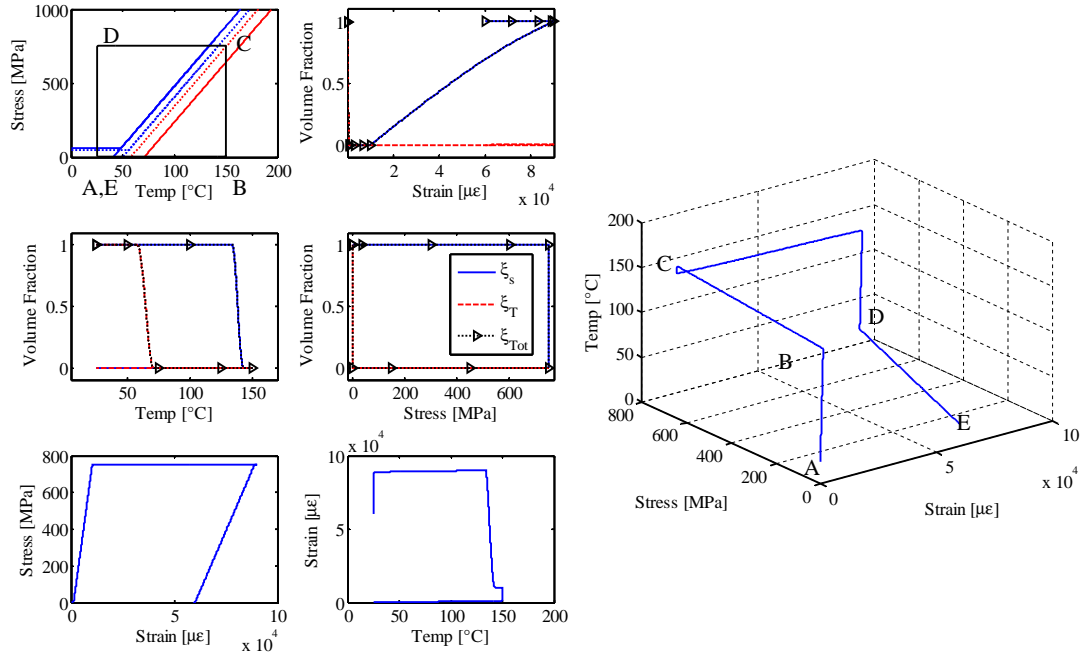


Figure A.2: Counter-clockwise stress-temperature load path. $\xi_{T_o} = 1$, $T_o = 25^\circ\text{C}$, $\sigma_o = 0$ MPa.

A.2 Proportional Loading

These two loadings demonstrate the same proportional stress-temperature loading traversing phase diagram regions 1, 2b, and 3, but begin when the SMA is in different phases. For the first loading, Figure A.3, the SMA is initially temperature-induced martensite. $\xi_o = \xi_{T_o} = 1$. The martensitic volume fraction-temperature and volume fraction-stress plots highlight the change in transformation regions by changing slope approximately where the stress-induced and temperature induced volume fractions are equal. Despite the change in rate of the volume fractions, the stress-induced volume fraction still evolves at the expense of the temperature-induced volume fraction and the total volume fraction is always equal to 1. Note that, even though the load path returns to its initial starting condition, the SMA does not return to its initial phase.

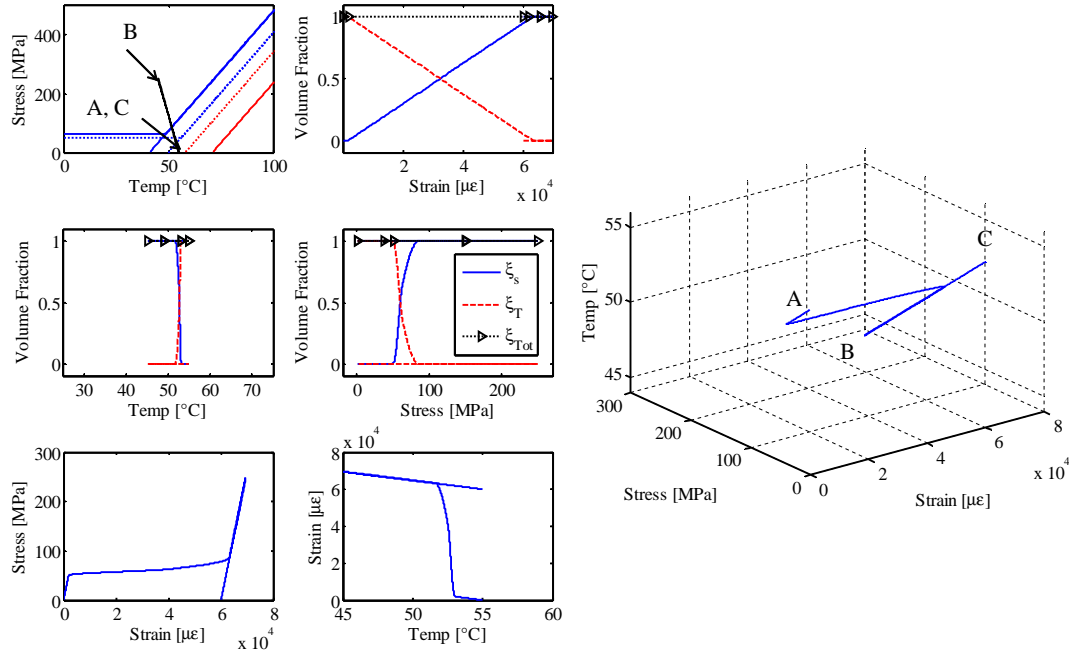


Figure A.3: Proportional stress-temperature load path traversing multiple transformation regions starting as martensite. $\xi_{T_o} = 1$, $T_o = 52^\circ\text{C}$, $\sigma_o = 0$ MPa.

The second case has the same loading through the low stress, mixed, and stress-induced martensite transformation regions but is applied to an initially austenitic SMA, $\xi_o = \xi_{T_o} = \xi_{s_o} = 0$. The main difference observed in stress-strain and strain-temperature plots in Figure A.4 is the increased slope in the initial thermoelastic region. This slope increase over that observed in Figure A.3 is due to the initial austenite phase and its increased modulus over the martensitic phase. In this load, the temperature-induced volume fraction increases prior to the increase of the stress-induced volume fraction. Soon after the load path enters into the mixed transformation region, the temperature-induced volume fraction begins to decrease as the stress-induced volume fraction evolves both through the increase in total volume fraction and in detwinning temperature-induced martensite.

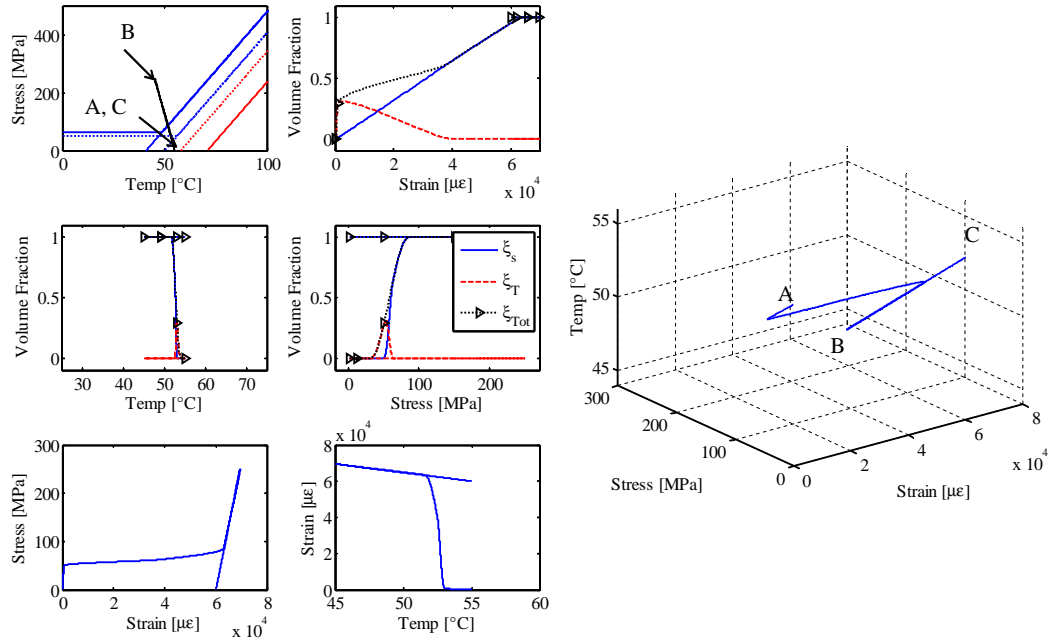


Figure A.4: Proportional stress-temperature load path traversing multiple transformation regions starting as austenite. $\xi_o = 0$, $T_o = 52^\circ\text{C}$, $\sigma_o = 0$ MPa.

The final proportional load demonstrates a minor loop. A reversal in loading during

transformation and then a second reversal continuing the initial load until the completion of transformation. In Figure A.5, the proportional loading is first halted and reversed approximately halfway through the $A - M^+$ transformation. Unloading is initially thermoelastic until the A_s^σ temperature is reached, whereupon the $M^+ - A$ transformation commences. This transformation is halted approximately midway through and reversed to complete the original $A - M^+$ transformation.

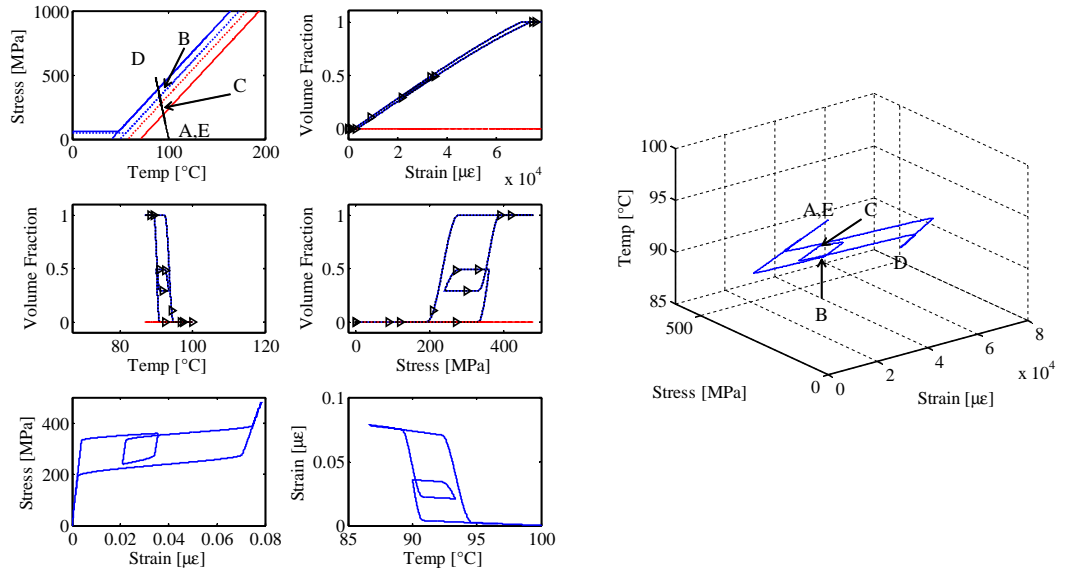


Figure A.5: Proportional stress-temperature load path with minor loop. $\xi = 0$, $T_o = 100^\circ\text{C}$, $\sigma_o = 0$ MPa.

A.3 SMA Model Code

This section give the m-code needed to run the preceding simulations in MATLAB.

```
1  %% Hahnlen Differential SMA Code
2  %This code will generate volume fraction values for arbitrary
3  %stress and temperature loading of an SMA for provided initial
4  %conditions. Input dsig and dT vectors as well as values for
5  %To, Sigo, zso, and zto. Material properties can be varied.
6  %Follows model outlined in Hahnlen PhD Dissertation (2012)
7  clc
8  clear
9  close all
10 %% Input the load path data and initial VF
11 dtim=.1;
12 t=0:dtim:1000+dtim;
13
14 %x=(50+1*(63-50)/4)/200
15 dsig=[0,0,1,0,-1,0,1,0,-1,0,0]; %MPa/sec
16 dt= [0,0,.08,0,-.08,0,.08,0,-.08,0,0]; %C/sec
17
18 sigi=0; %Initial Stress
19 Ti=25; %Initial Temp
20 zso=0; %Initial Stress Induced VF
21 zto=1; %Initial Temp Induced VF
22
23 tpk=[50.1,50.2,250.1,250.2,450.1,450.2,650.1,650.2,850.1,...
24      850.2,max(t)];
25 % Load Prescribe
26 %For single cycle paths need to clear out previous dsig, dt,
27 %and tpk, uncomment next two lines before uncommenting
28 \color{mgreen}29 %clear dsig dt tpk
30 %tpk=[250.1,250.2,500.1,500.2,750.1,750.2,max(t)];
31
32 t=0:dtim:1000+dtim;
33 tpk=[250.1,250.2,500.1,500.2,750.1,750.2,max(t)];
34 %for precoded load paths below
35
36 %dsig=[0,0,0,0,0,0,0,0]; %MPa/sec
37 %dsig=[2,0,0,0,-2,0,0]; %MPa/sec
38 %dt=[0,0,.4,0,0,0,-.4]; %C/sec
39 %dt=[0,0,0,0,0,0,0,0]; %C/sec
40
41 % % CW Rotation
42 % dsig=[2,0, 0,0,-2,0, 0]; %MPa/sec
```



```

43 % dt= [0,0,.5,0, 0,0,-.5]; %C/sec
44 %
45 % % CCW Rotation
46 % dsig=[0, 0,3,0, 0,0,-3]; %MPa/sec
47 % dt= [.5,0,0,0,-.5,0,0]; %C/sec
48
49 % % Proportional
50 dsig=[0,0,1,0,-1,0,0]; %MPa/sec
51 dt= [0,0,.4,0,-.4,0,0]; %C/sec
52
53 % %Trial Traces
54 %dsig=[0,0,0,0,0,0,0]; %MPa/sec
55 %dt=[.4,0,0,0,-.4,0,0]; %C/sec
56
57 %dsig=[0,0,0,0,0,0,0]; %MPa/sec
58 %dt=[0,0,.4,0,0,0,-.4]; %C/sec
59
60 % Hysteretic Partial Loop, change tpk!
61 %tpk=[210.1,210.2,285.1,285.2,500.1,500.2,850.1,...
62 %      850.2,max(t)];
63 %dsig=[2,0,-2,0,2,0,-2,0,0]; %MPa/sec
64 %dt=[-.02,0,.02,0,-.02,0,.02,0,0]; %C/sec
65
66 %dsig=[(50+3*(63-50)/4)/250,0, 0,0,-0.0,0, 0];
67 %dt=[0,0,.4,0,0,0,-.4]; %C/sec
68
69 %% Parameters
70 Em=26e3; %MPa
71 Ea=83e3; %MPa
72 alphaN=10e-6; %1/C
73 epl=0.06;
74 Ms=50; %C
75 Mf=41; %C
76 As=58; %C
77 Af=71; %C %
78 Cm=8.1; %MPa/C
79 Ca=8.1; %MPa/C
80 scrs=50; %MPa
81 scrf=63; %MPa
82 aa=pi/(Af-As);
83 am=pi/(Ms-Mf);
84
85 %% Preallocate-Create Empty Vectors for Speed
86 T=zeros(1,length(t));
87 Sig=zeros(1,length(t));
88 dSig=zeros(1,length(t));

```

```

89  dT=zeros(1,length(t));
90  Ass=zeros(1,length(t));
91  Afs=zeros(1,length(t));
92  Mfs=zeros(1,length(t));
93  Mss=zeros(1,length(t));
94  sgcrf=zeros(1,length(t));
95  sgcrs=zeros(1,length(t));
96
97  dzs=zeros(1,length(t));
98  dzt=zeros(1,length(t));
99  dztot=zeros(1,length(t));
100  Zt=zeros(1,length(t));
101  Zs=zeros(1,length(t));
102  Ztot=zeros(1,length(t));
103
104  ZTR=zeros(1,length(t));
105  ZSR=zeros(1,length(t));
106  ZTOTR=zeros(1,length(t));
107  dzst=zeros(1,length(t));
108
109
110  %% Load- Generates the Stress and Temperature Load Vectors
111  Sig(1)=sigi;
112  T(1)=Ti;
113
114  dSig(1)=dsig(1);
115  dT(1)=dt(1);
116  for i=2:length(t)
117      if t(i)>=0
118          Sig(i)=dsig(1)*(t(i)-t(i-1))+Sig(i-1);
119          T(i)=dt(1)*(t(i)-t(i-1))+T(i-1);
120      end
121
122      for j=1:length(tpk)-1
123          if t(i)>=tpk(j)
124              Sig(i)=dsig(j+1)*(t(i)-t(i-1))+Sig(i-1);
125              T(i)=dt(j+1)*(t(i)-t(i-1))+T(i-1);
126          end
127      end
128      dSig(i)=(Sig(i)-Sig(i-1))/dtime;
129      dT(i)=(T(i)-T(i-1))/dtime;
130  end
131
132  %% Initial Values
133  Zs(1)=zso;
134  Zt(1)=zto;

```

```

135 Ztot(1)=Zs(1)+Zt(1);
136 ztotr=Ztot(1);
137 ztr=Zt(1);
138 zsr=Zs(1);
139
140 %Critical Stress Determination based on T(t)
141 if T(1)>Mf+scrf/Cm
142     sgcrf(1)=(T(1)-Mf)*Cm;
143 else
144     sgcrf(1)=scrf;
145 end
146 if T(1)>Ms+scrs/Cm
147     sgcrs(1)=(T(1)-Ms)*Cm;
148 else
149     sgcrs(1)=scrs;
150 end
151
152 %Transformation Temperature Determination based on Sig(t)
153 Ass(1)=As+Sig(1)/Ca;
154 Afs(1)=Af+Sig(1)/Ca;
155 Mss(1)=Ms+Sig(1)/Cm;
156 Mfs(1)=Mf+Sig(1)/Cm;
157
158 % Double Check initial volume fractions
159 if T(1)>Ass(1) && Ztot(1)==1
160     disp('Nonsensical Starting Fractions! (Hi Temp)')
161 end
162 if T(1)<Mss(1) && Ztot(1)==0
163     disp('Nonsensical Starting Fractions! (Temp Ind)')
164 end
165 if Sig(1)>sgcrs(1) && Zs(1)==0
166     disp('Nonsensical Starting Fractions! (Stress Ind)')
167 end
168
169 %% Evolution from i=2 on
170
171 for i=2:length(t)
172     %Obtain the varying tran temps and crit stresses
173     %Critical Stress Determination based on T(t)
174     if T(i)>Mf+scrf/Cm
175         sgcrf(i)=(T(i)-Mf)*Cm;
176     else
177         sgcrf(i)=scrf;
178     end
179     if T(i)>Ms+scrs/Cm
180         sgcrs(i)=(T(i)-Ms)*Cm;

```

```

181     else
182         sgcrs(i)=scrs;
183     end
184     %Transformation Temperature Determination based on Sig(t)
185     Ass(i)=As+Sig(i)/Ca;
186     Afs(i)=Af+Sig(i)/Ca;
187     Mss(i)=Ms+Sig(i)/Cm;
188     Mfs(i)=Mf+Sig(i)/Cm;
189
190     %%% Ztot
191     if dT(i)<0
192         if Mfs(i) < T(i) && T(i) < Mss(i)
193             dztot(i)=-((1-ztotr)/2)*(sin(am*(T(i)-Mfs(i))))...
194                 *(am*(dT(i)-dSig(i)/Cm));
195             if dztot(i) < 0
196                 dztot(i)=0;
197             end
198         end
199     end
200     if dT(i)==0
201         if dSig(i)<0
202             if Ass(i) < T(i) && T(i) < Afs(i)
203                 dztot(i)=- (ztotr/2)*(sin(aa*(T(i)-Ass(i))))...
204                     *(aa*(dT(i)-dSig(i)/Ca));
205                 dzs(i)=zsr/ztotr*dztot(i); %by falling Ztot
206                 dzt(i)=ztr/ztotr*dztot(i); %by falling Ztot
207                 if ztotr==0
208                     dzs(i)=0;
209                     dzt(i)=0;
210                 end
211                 if dztot(i) > 0 %Condition Check/Warning
212                     dztot(i)=0;
213                     dzs(i)=0;
214                     dzt(i)=0;
215                     disp('Watch dztot')
216                 end
217             end
218         elseif dSig(i)>0
219             if Mfs(i) < T(i) && T(i) < Mss(i)
220                 dztot(i)=-((1-ztotr)/2)*(sin(am*(T(i)-Mfs(i))))...
221                     *(am*(dT(i)-dSig(i)/Cm));
222             end
223         end
224     end
225     if dT(i)>0; %Increasing T, M->A and M'->A
226         if Ass(i) < T(i) && T(i) < Afs(i)

```

```

227     dztot(i)=- (ztotr/2)*(sin(aa*(T(i)-Ass(i))))...
228         *(aa*(dT(i)-dSig(i)/Ca));
229         dzs(i)=zsr/ztotr*dztot(i); % by falling Ztot
230         dzt(i)=ztr/ztotr*dztot(i); % by falling Ztot
231         if ztotr==0
232             dzs(i)=0;
233             dzt(i)=0;
234         end
235     end
236     if dSig(i)/dT(i)>Cm && dSig(i)/dT(i)>Ca
237         if Mfs(i) < T(i) && T(i) < Mss(i)
238             dztot(i)=-((1-ztotr)/2)*(sin(am*(T(i)-Mfs(i))))...
239                 *(am*(dT(i)-dSig(i)/Cm));
240         end
241     end
242 end
243
244 %Zs (dSig/dT >= or less than Cm or equal to zero)
245 if Mfs(i) <= T(i) && T(i) <= Mss(i)
246     if Sig(i) < scrs
247         %temp only
248         dzt(i)=dztot(i);
249     end
250     if scrs <= Sig(i) && Sig(i) <= scrff
251         %mix region
252         delta=((1+zsr)/2)*((1-zsr)/2); %
253         kappa=((1-zsr)/2)*((1-zsr)/2); %
254         alpha=am*(T(i)-Mfs(i));
255         dalpha=am*(dT(i)-dSig(i)/Cm);
256         beta=pi/(scrs-scrff)*(Sig(i)-scrff);
257         dbeta=pi/(scrs-scrff)*dSig(i);
258         gamma=(1-zsr)/4;
259
260     dzs(i)=-gamma*sin(alpha)*dalpha*(cos(beta)+1)...
261         -gamma*sin(beta)*dbeta*(cos(alpha)+1);
262     dzst(i)=(-sin(alpha)*dalpha*(gamma*cos(beta)+delta)...
263         -sin(beta)*dbeta*(gamma*cos(alpha)+kappa));
264     dzt(i)=dztot(i)-dzs(i);
265
266     if dzs(i)<0 % dzs~<0 without dztot when dSig<0
267         dzs(i)=0;
268         dzt(i)=dztot(i);
269     end
270     if dzst(i)<0 % dzs~<0 without dztot when dSig<0
271         dzst(i)=0;
272     end

```

```

273
274         end
275         if Sig(i) > scrf
276             %stress only
277     dzs(i) = -( (1-zsr)/2 ) * ( sin(am*(T(i)-Mfs(i))) ...
278         * (am*(dT(i)-dSig(i)/Cm)) );
279         dzst(i) = dzs(i);
280         dzt(i) = dztot(i) - dzs(i);
281
282         if dzs(i) < 0 % dzs~<0 without dztot when dSig<0
283             dzs(i) = 0;
284             dzt(i) = dztot(i) - dzs(i);
285         end
286         if dzst(i) < 0 % dzs~<0 without dztot when dSig<0
287             dzst(i) = 0;
288         end
289     end
290 end
291 %Low Temp Detwin
292 if T(i) < Mfs(i)
293     if scrs <= Sig(i) && Sig(i) <= scrf %&& dSig(i) > 0
294         %stress only
295     dzs(i) = -(1-zsr)/2 * sin(pi/(scrs-scrf) * (Sig(i)-scrf)) ...
296         * dSig(i) * pi / (scrs-scrf);
297     dzst(i) = dzs(i);
298     dzt(i) = -dzs(i);
299
300     if dzs(i) < 0 %dzs~<0 without dztot when dSig<0
301         dzs(i) = 0;
302         dzt(i) = dztot(i);
303     end
304     if dzst(i) < 0 % dzs~<0 without dztot when dSig<0
305         dzst(i) = 0;
306     end
307 end
308 end
309 %% Numerical Integration and Return Points
310
311     Zs(i) = Zs(i-1) + dzs(i) .* dtime;
312     Zt(i) = Zt(i-1) + dzt(i) .* dtime;
313     Ztot(i) = Ztot(i-1) + dztot(i) .* dtime;
314
315     %%Return points- Establishes new initial VF's upon a
316     %%change in loading
317     if dzt(i) == 0 %No change in dzt, then no change in Zto
318         ztr = Zt(i);

```

```

319     end
320     if dzs(i)==0 %No change in dzs, then no change Zso
321         zsr=Zs(i);
322     end
323     if dztot(i)==0 %No change in dztot, no change in Ztoto
324         ztotr=Ztot(i);
325     end
326
327     if dT(i)==0 && dSig(i)==0 %All stop in loading
328         ztotr=Ztot(i);
329         ztr=Zt(i);
330         zsr=Zs(i);
331     end
332     if Zt(i)==1 %Fully twinned martensite
333         ztr=1;
334         zsr=0;
335         ztotr=1;
336     end
337     if Zs(i)==1 %Fully detwinned martensite
338         ztr=0;
339         zsr=1;
340         ztotr=1;
341     end
342     if T(i)<Mfs(i) && Sig(i)>=scrf %Fully detwinned martensite
343         ztr=0;
344         zsr=1;
345         ztotr=1;
346     end
347     if T(i)>=Afs(i) %Fully Austenite
348         ztr=0;
349         zsr=0;
350         ztotr=0;
351     end
352     ZTOTR(i)=ztotr;
353     ZTR(i)=ztr;
354     ZSR(i)=zsr;
355 end
356
357 En=Em.*Ztot+(1-Ztot).*Ea;
358 epN=alphaN.*(T-T(1))+(1./En).*Sig+epl.*(Zs-Zs(1));
359
360 %% Construction of Phase Diagram for Use in Figures
361 Sigeq=0:1000;
362 Teq=0:140;
363 eqT=zeros(1,length(Teq));
364 eqS=zeros(1,length(Sigeq));

```

```

365
366 eqTMs=zeros(1,length(Teq));
367 eqTMf=zeros(1,length(Teq));
368 eqMs=zeros(1,length(Sigeq));
369 eqMf=zeros(1,length(Sigeq));
370 eqAs=zeros(1,length(Sigeq));
371 eqAf=zeros(1,length(Sigeq));
372 for i=1:length(Teq) %%Temperature-Dependent Critical Stresses
373     if Teq(i)<Ms+scrs/Cm
374         eqTMs(i)=scrs;
375     else
376         eqTMs(i)=(Teq(i)-Ms)*Cm;
377     end
378     if Teq(i)<Mf+scrf/Cm
379         eqTMf(i)=scrf;
380     else
381         eqTMf(i)=(Teq(i)-Mf)*Cm;
382     end
383 end
384 for i=1:length(Sigeq) %Stress-Dep. Transfomration Temperatures
385     eqMs(i)=Ms+(Sigeq(i))/Cm;
386     eqMf(i)=Mf+(Sigeq(i))/Cm;
387     eqAs(i)=As+(Sigeq(i))/Ca;
388     eqAf(i)=Af+(Sigeq(i))/Ca;
389 end
390
391 %% Figure 1, Phase Diagram and Load Path
392 figure
393 plot(Teq,eqTMs,':b')
394 hold on
395 plot(Teq,eqTMf,'b')
396 plot(eqMs,Sigeq,':b')
397 plot(eqMf,Sigeq,'b')
398 plot(eqAs,Sigeq,':r')
399 plot(eqAf,Sigeq,'r')
400 plot(T,Sig,'k')
401 xlabel('Temp')
402 ylabel('Stress')
403 axis([0 200 0 500])
404
405 %% Figure 2, Multiplot
406 figure
407 subplot(3,2,1)
408 %Phase Diag
409 plot(Teq,eqTMs,':b')
410 hold on

```



```

411 plot(Teq,eqTMf,'b')
412 plot(eqMs,Sigeq,':b')
413 plot(eqMf,Sigeq,'b')
414 plot(eqAs,Sigeq,':r')
415 plot(eqAf,Sigeq,'r')
416 plot(T,Sig,'k')
417 xlabel('Temp [C]')
418 ylabel('Stress [MPa]')
419 axis([0 200 0 1000])
420
421 subplot(3,2,2)
422 plot(epN.*1e6,Zs)
423 hold on
424 plot(epN.*1e6,Zt,'--r')
425 plot(epN(1).*1e6,Ztot(1),'>k')
426 plot(epN.*1e6,Ztot,':k') %usd to create proper legend
427 plot(epN(1:1000:length(t)).*1e6,Ztot(1:1000:length(t)),'>k')
428 xlabel('Strain [\mu\epsilon]')
429 ylabel('Volume Fraction')
430 %legend('\xi_\sigma','\xi_T','\xi_{Tot}')
431 axis([min(epN).*1e6-20 max(epN).*1e6+20 -.1 1.1])
432
433 subplot(3,2,3)
434 plot(T,Zs)
435 hold on
436 plot(T,Zt,'--r')
437 plot(T,Ztot,':k') %usd to create proper legend
438 plot(T(1:1000:length(t)),Ztot(1:1000:length(t)),'>k')
439 xlabel('Temp [C]')
440 ylabel('Volume Fraction')
441 axis([min(T)-20 max(T)+20 -.1 1.1])
442
443 subplot(3,2,4)
444 plot(Sig,Zs)
445 hold on
446 plot(Sig,Zt,'--r')
447 plot(epN(1).*1e6,Ztot(1),'>k')
448 plot(Sig,Ztot,':k')
449 plot(Sig(1:1000:length(t)),Ztot(1:1000:length(t)),'>k')
450 xlabel('Stress [MPa]')
451 ylabel('Volume Fraction')
452 legend('\xi_s','\xi_T','\xi_{Tot}')
453 axis([min(Sig)-20 max(Sig)+20 -.1 1.1])
454
455 subplot(3,2,5)
456 plot(epN.*1e6,Sig)

```

```

457 xlabel('Strain [\mu\epsilon]')
458 ylabel('Stress [MPa]')
459
460 subplot(3,2,6)
461 plot(T,epN.*1e6)
462 ylabel('Strain [\mu\epsilon]')
463 xlabel('Temp [C]')
464
465 %% Figure 3, 3D Strain Stress Temp Plot
466 figure
467 plot3(epN.*1e6,Sig,T)
468 xlabel('Strain [\mu\epsilon]')
469 ylabel('Stress [MPa]')
470 zlabel('Temp [C]')
471 grid on

```

Appendix B

HIGH TEMPERATURE AND STRESS CYCLES OF NiTi RIBBONS

This section details the results of high temperature and stress cycles used to characterized the NiTi ribbons studied in this research. Higher stresses and temperatures were applied in a effort to obtain a superelastic stress-strain loop. If a full superelastic loop can be obtained, the effective austenite start and finish temperatures can be found through linear interpolation of the elastic regions and plateaus produced by the $M^+ - A$ transformation upon unloading. By determining these values at multiple stress levels, the values for C_A can be obtained and, ultimately, the stress free values of A_s and A_f .

Starting with 90°C tests, axial load was increased to 130 N (30 lbf), resulting in a axial stress of 690 MPa, to complete the detwinning plateau. Upon unloading, the strain of the ribbon did not return to its initial value and continued to accumulate strain for each subsequent cycle, shown in Figure B.1 (a). In an effort in promote the $M - A$ transformation, temperatures were increased to 100°C and 120°C, Figures B.1 (b) and (c), respectively. At higher temperatures, the effective σ_{cr}^s also increases resulting in an incomplete detwinning plateau at 120°C. A final set of cycles were conducted at 150°C with a maximum axial load of 156 N (35 lbf), resulting in a maximum stress of 804 MPa. The results from the fourth set of cycles is shown in Figure B.1 (d). Again, the applied load was not sufficient to complete the stress-induced $A - M$ transformation and each cycle resulted in more accumulated strain despite the increased temperature. As this was close to the observed yield strength of the SMA ribbons and the temperature was still not sufficient to complete the $M - A$

transformation upon loading, no further cycles were considered.

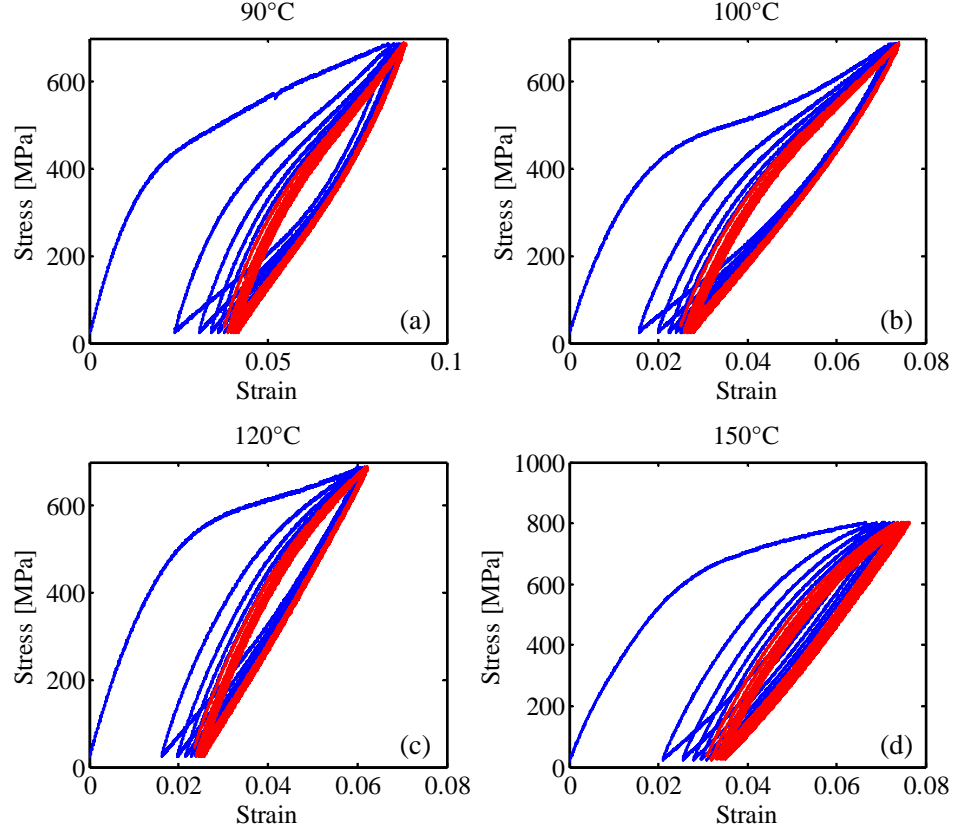


Figure B.1: Stress-strain cycle plots for NiTi ribbon at: (a) 90°C; (b) 100°C; (c) 120°C; (d) 150°C. Blue plots represent the first five cycles and red represent the last five cycles.

Upon zeroing the grip displacement, the ribbon had excess length due to the unrecovered transformation-induced strain. This strain could be mostly recovered by direct heating with a heat gun indicating that the unrecovered strain was likely not from a training phenomena and was possibly due to the unloading rate being too high. However, lower displacement rates, a minimum of 0.254 mm/min (0.01 in/min), for subsequent tests were still unable to allow a complete strain recovery. The relationship between the critical stresses, transformation temperatures, and the yield strength of this particular alloy are such that the material cannot be made to operate in the pseudoelastic regime.

Appendix C

STIFFENING EFFECT OF STRAIN GAGES ON HPUAM COMPOSITES

A study on the reinforcing effect of the strain gages on the NiTi-Al HPUAM composites is provided here. Generally, if a strain gage is applied to a specimen that is significantly thicker than the gage itself, the reinforcement from the gage is negligible. For composite specimens, a specimen height to gage height ratio of 10 is generally considered sufficient to ignore stiffening effects [79], however the HPUAM composites have a ratio of approximately 8.5. Due to the relative thinness of the composites, this study is meant to quantify the error induced by the addition of the gages.

When considering a long-fiber reinforced composite with a fiber orientation angle of 0° , the ratio of composite strain in the x direction, ϵ_{xo} , to gage strain in the same direction, ϵ_{xg} , is given by [79]

$$\frac{\epsilon_{xo}}{\epsilon_{xg}} = \left(1 + \frac{E_g}{\eta E_1} \right) \quad (C.1)$$

where E_g is the elastic modulus of the gage, E_1 is the elastic modulus of the composite along the fiber direction (coincident with the x direction for fiber orientation angles of 0°), and η is given by

$$\eta = \frac{h_s}{h_g} \quad (C.2)$$

where h_s is the thickness of the sample and h_g is the thickness of the gage.

Considering the worst-case scenario for the studied composites, E_1 will be taken as the

Table C.1: Properties used to quantify strain gage reinforcement.

Property	Description	Value
E_{Al}	Al modulus	69 GPa
E_M	Mart. modulus	17.9 GPa
E_g	Gage modulus	6.9 GPa (1×10^6 psi) ^a
h_s	Sample thickness	608 μm
h_g	Gage thickness	71 μm [89]
v	NiTi fiber volume fraction	20.6%, 15.2%

^aThis value is selected as a typical value for the gage backing material, phenolic resin [90, 91].

elastic modulus of composite 3, a 20% NiTi composite by volume, at low temperature. The elastic modulus is found through a rule of mixtures:

$$E_1 = E_{Al}(1 - v) + E_M v \quad (\text{C.3})$$

where E_{Al} is the elastic modulus of aluminum, E_M is the elastic modulus of martensite, and v is the NiTi fiber volume fraction.

Using the properties in Table C.1, the elastic modulus for the composite is found to be 58.5 GPa and the ratio of heights, η , for a single strain gage is 8.57. Using these values in (C.1), a value for the ratio of actual strain to measured strain is 1.014, meaning that the actual strain is 1.4% greater than the strain measured by the gage. If the case of composite 4 is considered with 15.2% NiTi by volume and two strain gages ($2 \times h_g = 142 \mu\text{m}$), the height ratio becomes 4.28 and the strain ratio becomes 1.026, the actual composite strain is 2.6% greater than the measured strain. In both cases, the reinforcing effect of the gages is deemed negligible and is not taken into account for analysis and discussion of the experimental results.

Though bending is not explicitly studied in this research, the stiffening effect of strain gages can be quantified for pure bending as well. The equation for the ratio of true sample strain to gage strain is [79]

$$\frac{\epsilon_{xo}}{\epsilon_{xg}} = \frac{4(E_1 C_2 + E_g C_3)}{E_1 h_s^3} \quad (\text{C.4})$$

where

$$C_1 = \frac{E_1\eta^2 - E_g}{2(E_1\eta + E_g)}, \quad (\text{C.5})$$

$$C_2 = 3d^2h_s - 3dh_s^2 + h_s^3, \quad (\text{C.6})$$

and

$$C_3 = 3d^2h_g - 3dh_g^2 + h_g^3. \quad (\text{C.7})$$

For (C.6) and (C.7)

$$d = C_1h_g. \quad (\text{C.8})$$

Using the properties in Table C.1, composite 3 has strain ratio of 1.032 and composite 4 has a strain ratio of 1.047, stiffening effects of 3.2% and 4.7%, respectively.

Appendix D

CHARACTERIZATION OF PSEUDOELASTIC NiTi RIBBON

Additional pseudoelastic ribbon was studied for construction of future HPUAM composites. The ribbon has a rectangular cross-section of $178\ \mu\text{m} \times 356\ \mu\text{m}$ ($0.007\ \text{in} \times 0.014\ \text{in}$). This alloy was subject to characterization experiments to verify manufacturer data and observe behaviors under various conditions. Characterization tests included a monotonic tensile test to failure, isothermal stress cycles at different temperatures, and blocked force testing.

D.1 Monotonic Tensile Test

An approximately 175 mm long section of pseudoelastic NiTi ribbon was used to conduct a monotonic tensile test to failure. The ribbon was placed in a universal tension/compression frame with an gage length of 50 mm (2 in) between the frame grips. Testing was conducted under displacement control at a rate of 13 mm/min (0.5 in/min). The resulting force displacement data was used to create a stress-strain plot for the test using the ribbon cross-sectional area and gage length. The resulting plot is shown in Figure D.1 and exhibits a low stress linear region, a stress plateau signifying the $A - M$ stress-induced transformation, a high stress linear region, and a plastic deformation region followed by failure. The stress plateau is relatively flat indicating that the load rate is low enough to ignore material heating from loading and sufficient to maintain the isothermal assumption. Using a 0.2% yield criterion from the second linear region, a yield stress of 1020 MPa is obtained. The coincident rupture and ultimate stresses are 1180 MPa. Extending the linear regression of

the second linear region back to zero stress, a recoverable strain of 6.3% is also found.

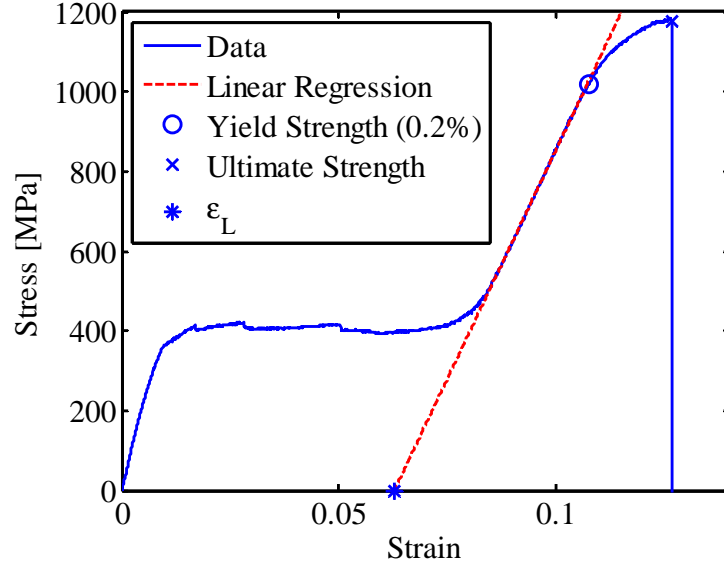


Figure D.1: Tensile failure stress-strain plot of pseudoelastic NiTi ribbon.

D.2 Isothermal Stress Cycles

Isothermal loading cycles were conducted at four different temperatures, 23°C, 40°C, 60°C, and 80°C. In each case, at least three sets of five successive load cycles were conducted going to a maximum of 44.5 N (10 lbf) which resulted in a maximum stress of 700 MPa. Using linear interpolation of the linear elastic regions and rising and falling transformation plateaus, critical detwinning start and finish stresses as well as their falling load counterparts, termed recovery start and finish stresses for the purposes of this appendix, were found for all cycle sets at each temperature.

Multiple load cycles were conducted at each temperature to observe the stability of the alloy. As seen in Figure D.2, there were slight difference between the stress-strain plots at each temperature between the first load cycles and last. Namely, stress plateaus and maximum recovery strains decrease slightly.

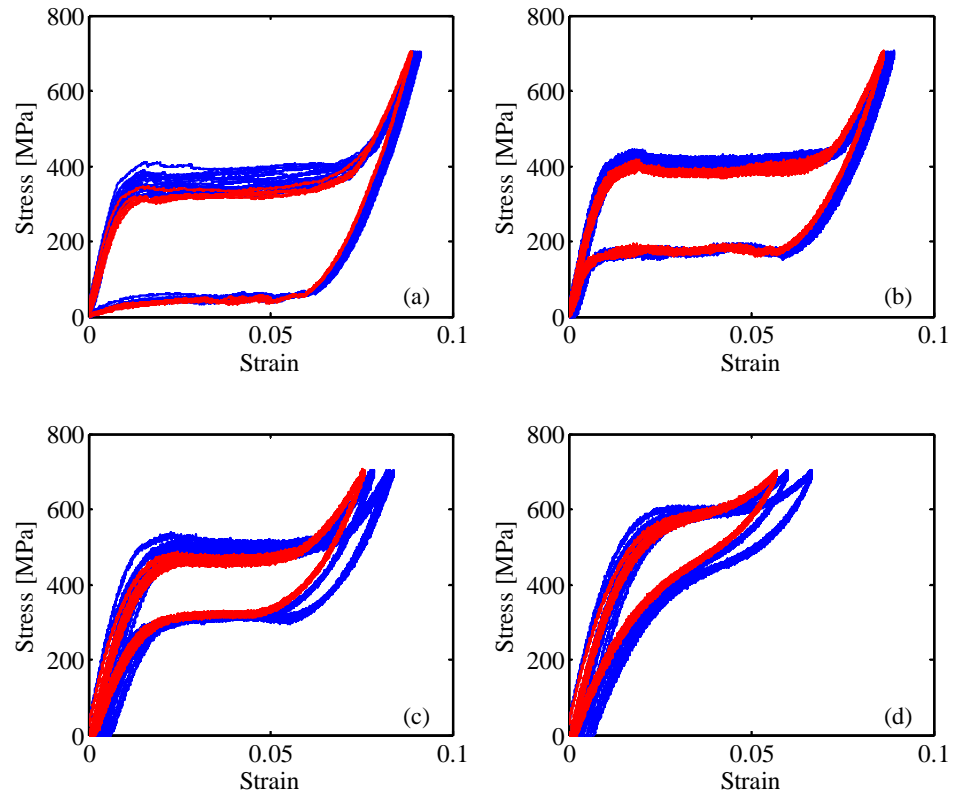


Figure D.2: Isothermal load cycles of pseudoelastic NiTi ribbon at (a) 23°C, (b) 40°C, (c) 60°C, and (d) 80°C. Last five cycles shown in red.

The critical and recovery stresses are plotted as a function of temperature in Figure D.3. In general, the relationship between stress and temperature appears linear for all temperatures except 80°C. At 80°C, however, the detwinning and recovery plateaus are not as well defined as they are in the other temperature cycles. For this reason, the 80°C values for critical detwinning and recovery stresses are omitted from the linear regression of the stress-temperature relationship shown in Figure D.4. By determining the relationship between the critical detwinning start and finish stresses the martensitic stress influence coefficient, C_M , can be determined from the slope of the line. The martensite start and finish temperatures can also be determined by finding where the linear regression lines intersect the zero stress axis. Similarly, by determining the linear relationship between the recovery start and finish stresses with temperature, the austenite stress influence coefficient as well as the austenite start and finish temperatures can be determined.

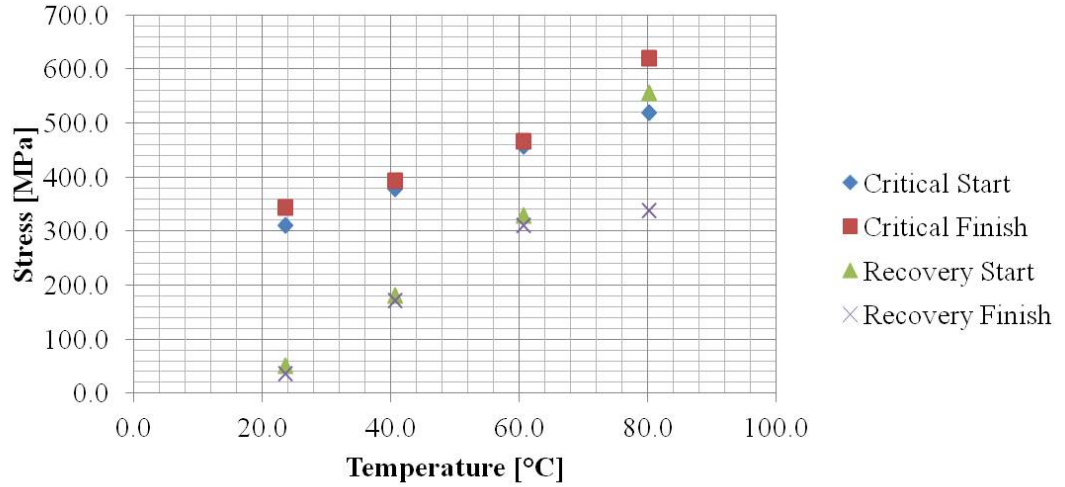


Figure D.3: Critical detwinning and recovery stresses versus temperature for a pseudoelastic NiTi ribbon.

The average of the slopes of the critical detwinning start and finish stresses yields a martensitic stress influence coefficient of 3.6 MPa/°C. The slopes of the recovery start and finish stresses provide a value of 7.4 MPa/°C for the austenitic stress influence coefficient.

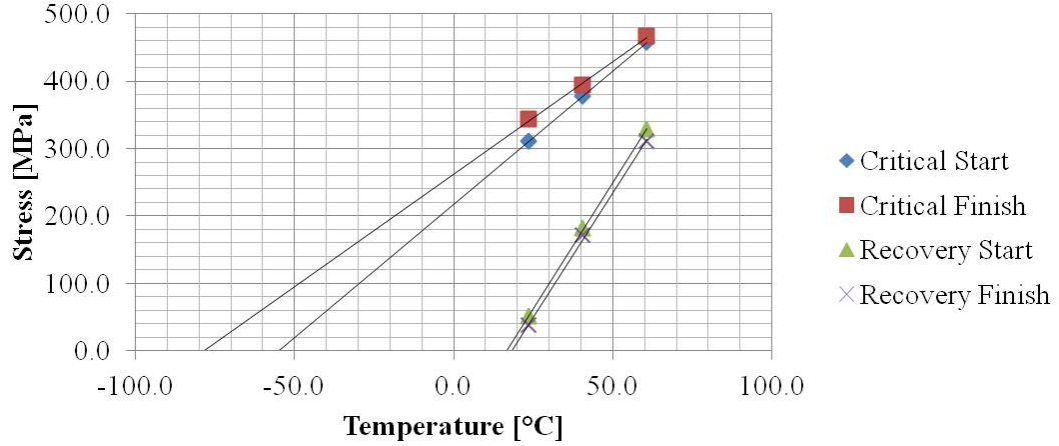


Figure D.4: Linear regression of critical detwinning and recovery stresses versus temperature for a pseudoelastic NiTi ribbon.

The critical detwinning start and finish linear regression lines intersect the zero stress axis at -78°C and -55°C which correspond to M_f and M_s , respectively. In a similar manner, the linear regression of the recovery start and finish stresses intersect the zero stress axis at 16°C and 18°C providing the values for A_s and A_f , respectively.

For the set of load cycles at each temperature the average slopes of the austenitic and martensitic elastic loading regions were determined. Due to the pseudoelastic nature of the ribbon, each load cycle provides two linear regions that can be used in determining the slope of the austenite elastic loading (at low loads) and martensite elastic loading (at high loads). On the stress-strain plots, these slopes correspond to the elastic moduli of their respective phases. The average value of the elastic moduli was found to be 24 GPa and 38 GPa for martensite and austenite, respectively. While the results show that the ratio between the martensite and austenite stiffness is correct, both values are approximately half of the manufacturer provided values, 41 GPa and 75 GPa. The likely cause of the discrepancy is the inability to directly measure ribbon deflection. Strain is derived from the grip displacement and ribbon length. Grip displacement includes deflections in the load train and does not account for specimen misalignment, both of which lower the measured stiffness and modulus of the sample being measured. The small size of the sample makes deflection measurements

through contact means, strain gages or extensometers, difficult. Further, there were no non-contact means immediately available to provide a more accurate measure of ribbon deflection. These same concerns are present in measuring the material properties of the shape memory ribbon in Chapter 3, however no corresponding manufacturer data were available for that alloy. In that case, because the literature data and measured modulus values were similar, the accuracy of the modulus calculation was assumed to be sufficient.

D.3 Blocking Stress Characterization

A different piece of the same alloy from the same material lot was used for blocking stress characterization. This ribbon was placed in the load frame, loaded to 44.5 N (10 lbf) and then the load was reduced to 22.2 N (5 lbf). This corresponds to a stress loading of 700 MPa followed by 350 MPa. From the preceding stress-strain plots, this would have caused a conversion to detwinned martensite which is not recovered upon unloading. At 350 MPa, the ribbon was excited by a DC electric current incremented 0.2 V at a time while load was measured using the tension frame load cell and temperature was monitored using a J-type thermocouple in contact with the ribbon. Heat transfer between the thermocouple and NiTi ribbon was augmented by thermal compound. A total of three thermal cycles were conducted, the first two going up to approximately 850 MPa to avoid yielding and the last going up to a temperature of 100°C. The resulting stress-temperature plot is shown in Figure D.5.

All three cycles are repeatable, exhibit low hysteresis, and are linear until approximately 80°C. Above 80°C, the stress begins to level off, similar to a behavior noted in the shape memory ribbon. Because the austenite start temperature is below room temperature, the pseudoelastic ribbon generates blocking stress immediately upon heating, making it an ideal material for controlling the CTE of a composite near room temperature.

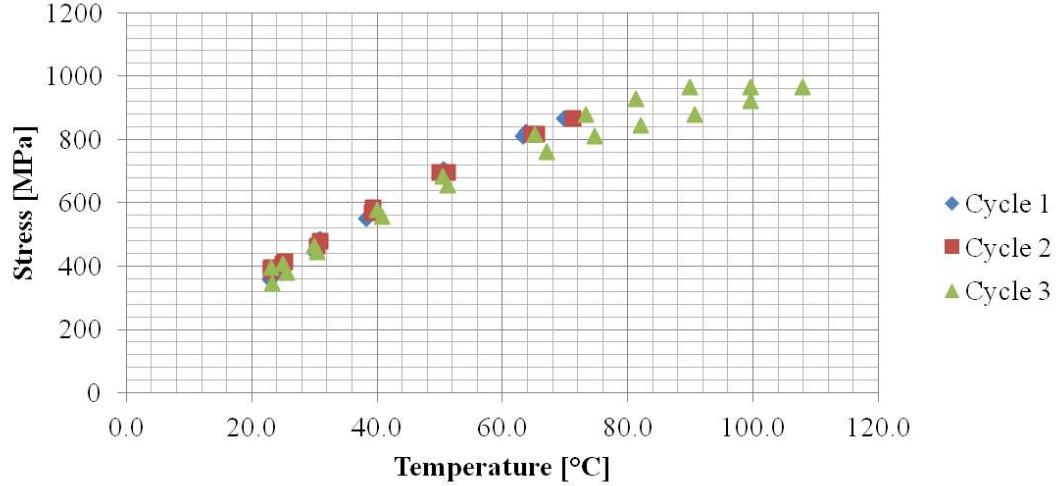


Figure D.5: Blocking stress versus temperature for the pseudoelastic NiTi ribbon.

D.4 Summary

The pseudoelastic NiTi ribbon was characterized through a combination of isothermal load cycles and blocking stress experiments. Due to the pseudoelastic nature of the alloy, more properties were able to be determined from the isothermal load cycles than were for the shape memory ribbon. A summary of material properties is given in Table D.1.

Table D.1: NiTi material properties obtained from characterization experiments.

Property	Description	Value	Source
M_f	Mart. Finish Temp	-78°C	Tensile Test
M_s	Mart. Start Temp	-55°C	Tensile Test
A_s	Aust. Start Temp	16°C	Tensile Test
A_f	Aust. Finish Temp	18°C	Tensile Test
C_M	Mart. Stress Influence Coefficient	$3.6 \text{ MPa}/^{\circ}\text{C}$	Tensile Test
C_A	Aust. Stress Influence Coefficient	$7.4 \text{ MPa}/^{\circ}\text{C}$	Tensile Test
E_M	Mart. Elastic Modulus	41 GPa	Manufacturer [58]
E_A	Aust. Elastic Modulus	75 GPa	Manufacturer [58]
ϵ_L	Maximum Transformation Strain	6.3%	Tensile Test
σ_y (0.2%)	Yield Stress	1070 MPa	Tensile Test
σ_u	Ultimate Stress	1180 MPa	Tensile Test

Appendix E

FIXTURE DRAWINGS

E.1 C-F Dynamic Fixture

This fixture was used for all dynamic testing of composites subject to a Clamped-Free (C-F) boundary condition. The fixture was constructed from Al 3003 H-14.

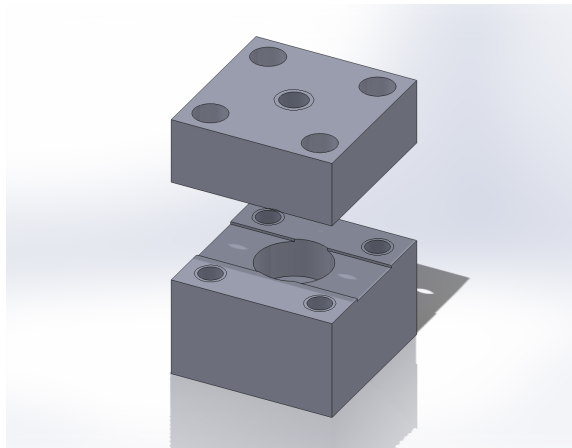


Figure E.1: Diagram of C-F Fixture.

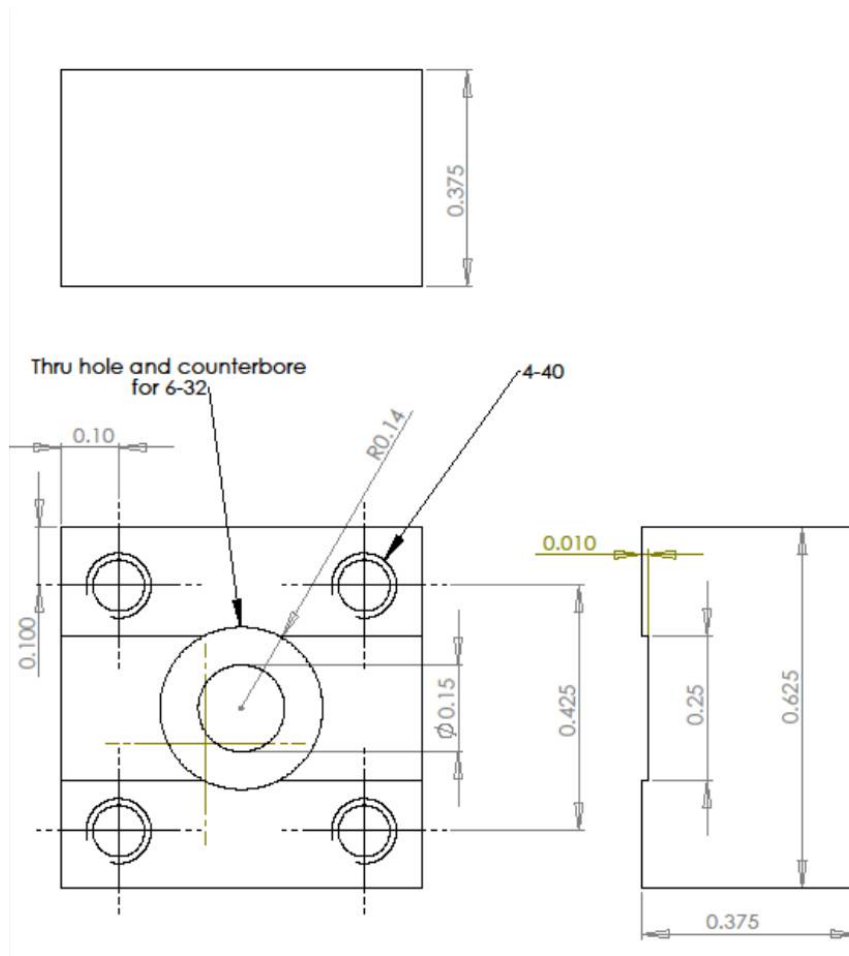


Figure E.2: Schematic for bottom of C-F Fixture. Dimensions in inches.

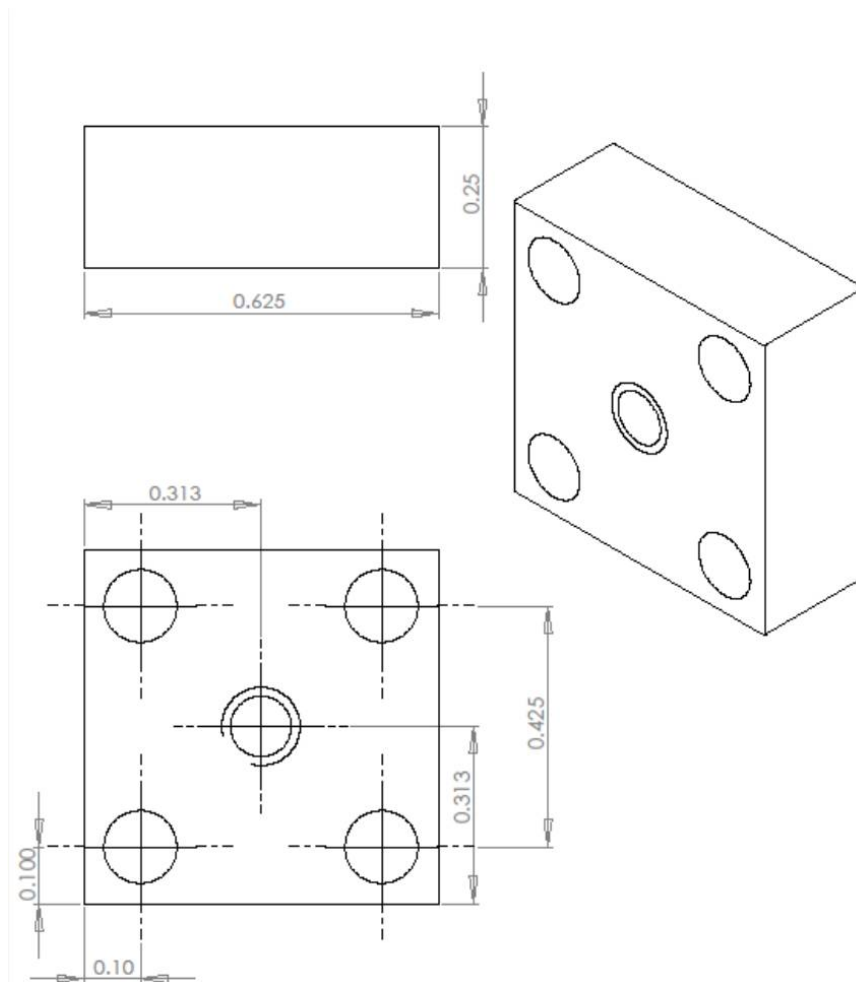


Figure E.3: Schematic for top of C-F Fixture. Dimensions in inches.

E.2 C-C Dynamic Fixture

This fixture was used for all dynamic testing of composites subject to a Clamped-Clamped (C-C) boundary condition. The fixture was constructed from Al 3003 H-14. The 4-40 bolts used to fasten all pieces together and clamp the composites must also be made of aluminum. During initial dynamic tests with steel bolts on a solid Al specimen, the natural frequency dropped with increasing temperature during heating but remained invariant during cooling. It is suspected that the different CTEs of the Al fixture and steel bolts combined with the slower heating time of the fixtured relative to the specimen caused a “ratcheting” phenomena; the specimen was able to slip within the grips slightly during heating as its temperature increased faster than the fixture. Upon cooling, the extra clamping force provided by the relatively low CTE steel bolts prevented the composite from slipping again and at low temperatures applied a compressive load, keeping the natural frequency depressed relative to the initial room temperature value. In addition to the Al bolts, this was prevented by applying a light coating of adhesive on the clamping surfaces during sample installation.

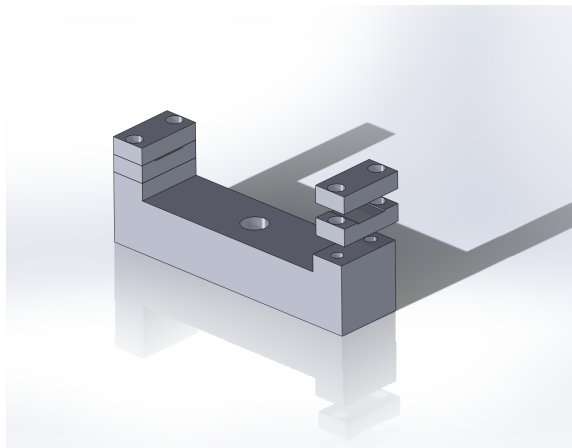


Figure E.4: Diagram of C-C Fixture.

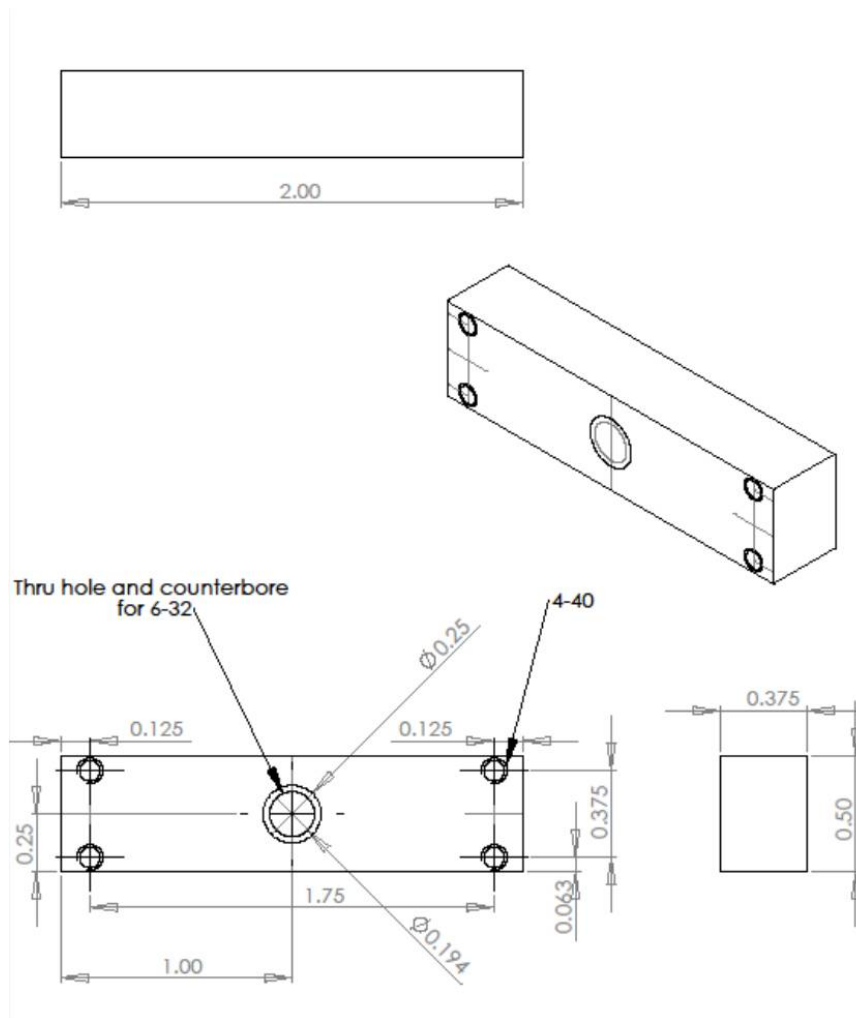


Figure E.5: Schematic for bottom of C-C Fixture. Dimensions in inches.

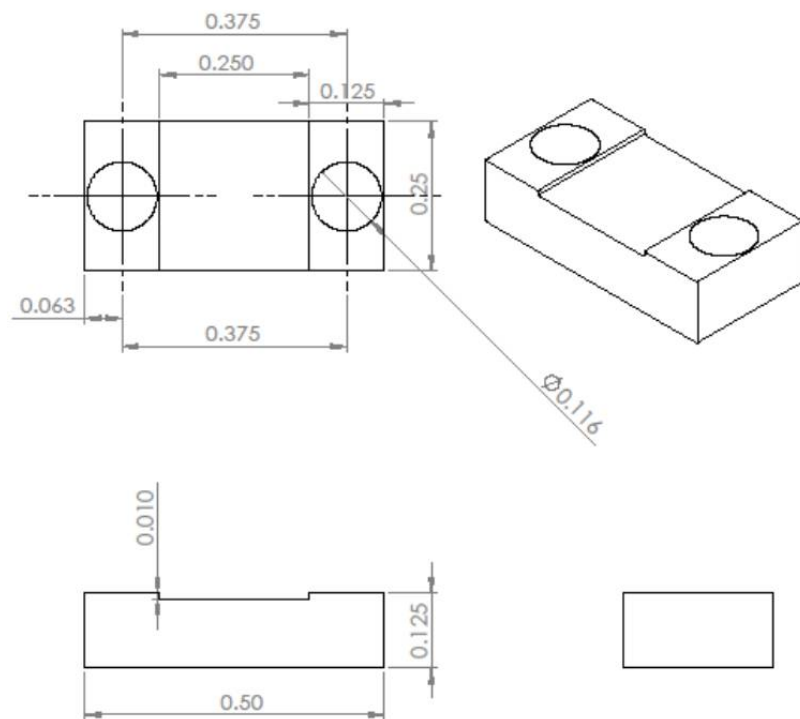


Figure E.6: Schematic for middle pieces of C-C Fixture. Dimensions in inches.

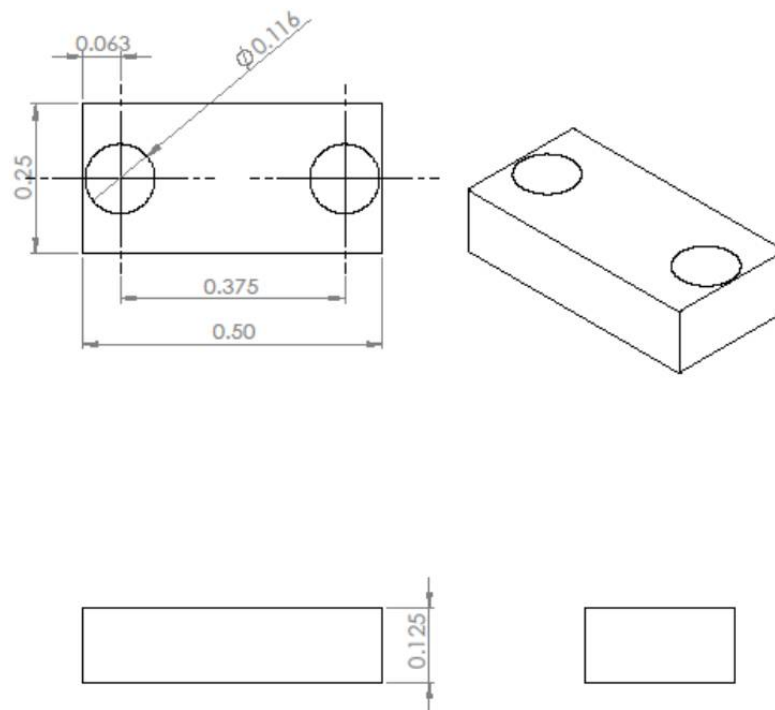


Figure E.7: Schematic for top pieces of C-C Fixture. Dimensions in inches.

E.3 HPUAM Mounting Plate

This schematic was used to construct the HPUAM base plate described in Chapter 3. Two versions of the base plate were constructed, the first from an Al 3003 H-14 and the second from steel. In both cases, a 3 in \times 4 in Al 3003-H14 sacrificial build plate is bolted to the base plate. The steel base plate is preferable for two reasons. First, the threaded holes that are used to mount the build plates are subject to loading from the ultrasonic vibrations applied by the horn. This causes the threads to wear and eventually fail in the Al plate. The threads in the steel plate have yet to show significant wear. Second, after welding tapes onto the Al build plate it would be partially welded to the Al base plate requiring a hammer and chisel to remove it before post-weld processing. While this is an interesting result and suggests the possibility of creating composite structures with larger Al pieces, it made composite finishing difficult. All composites discussed in this study were manufactured on the steel base plate.

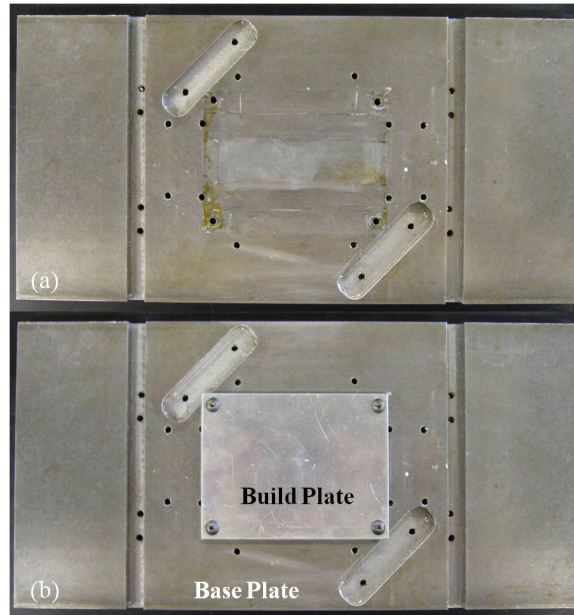


Figure E.8: HPUAM steel base plate (a) without build plate and (b) with build plate. Machined pockets at the corners of the build plate were machined after NiTi-Al composites for an unrelated embedding study.

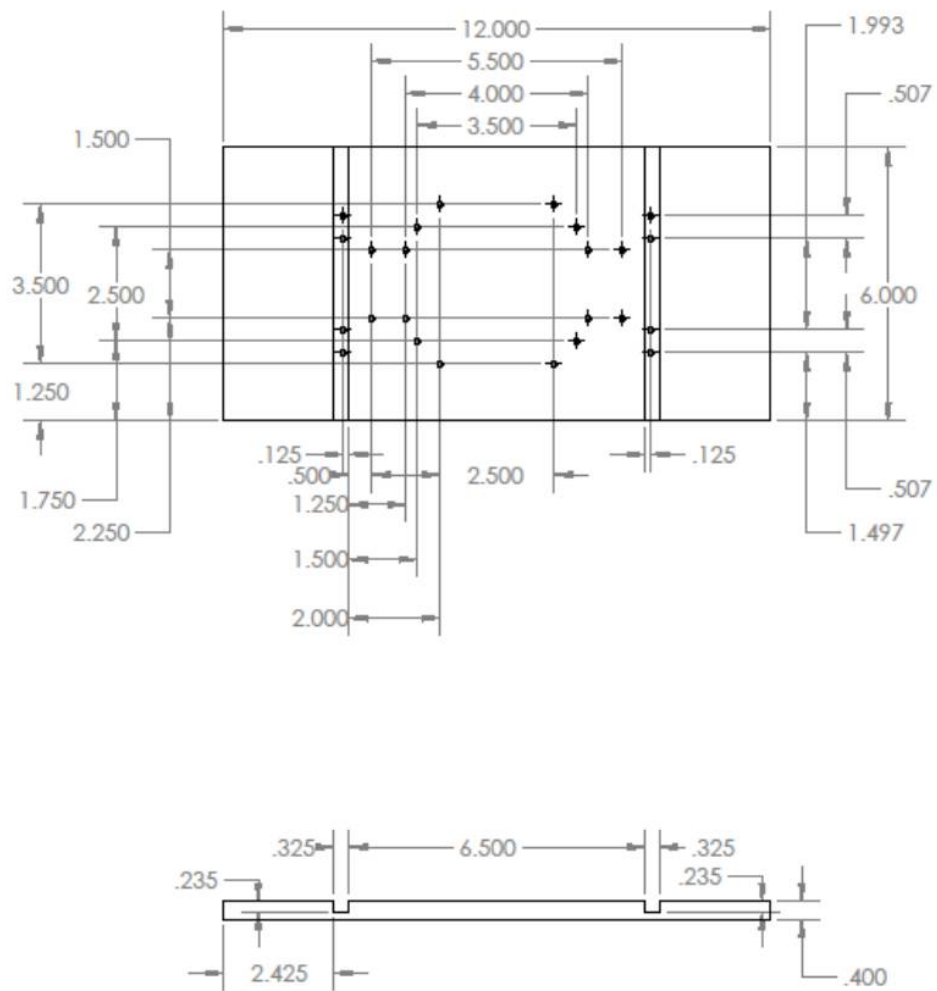


Figure E.9: Schematic for HPUAM base plate. Dimensions in inches, holes are all threaded for 8-32 bolts.

Appendix F

COMPOSITE TRANSIENT DYNAMIC BEHAVIOR

Composites 1-4 exhibited transient behavior during the first heating cycle of the C-C dynamic tests, as mentioned in section 5.3.2. Upon heating, the natural frequencies increased with increasing temperature but upon cooling, the natural frequencies dropped below their initial values. As seen in Table F.1, the initially observed natural frequencies are very close to the calculated values for each composite. Further, between the first and second thermal cycles, the peak natural frequencies of each composite did not vary significantly; the frequencies at 100 °C for both cycles are within 1% for all composites as shown in Table F.2. As shown in Chapter 5, the natural frequency change was stable for the second thermal cycle, with each composite returning to its lower room temperature natural frequency value upon cooling.

Table F.1: Calculated, initial, post-heating, and relative difference between room temperature natural frequencies of C-C dynamic test samples.

Sample	Calc. ω_n	Room Temp. ω_n [Hz]		Change
		Heating	Cooling	
Solid Al	2170	2277	2273	-0.1%
Comp. 1	2092	2013	1942	-3.5%
Comp. 2	1955	1902	1813	-4.7%
Comp. 3	1891	1947	1856	-4.7%
Comp. 4	1956	1965	1783	-9.2%

Table F.2: Comparison of the natural frequencies of composites 1-4 for the first and second heating cycles during C-C dynamic testing.

Sample	100 °C ω_n [Hz]		Change
	Cycle 1	Cycle 2	
Comp. 1	2011	2003	-0.4%
Comp. 2	2119	2106	-0.6%
Comp. 3	2041	2028	-0.6%
Comp. 4	2244	2228	-0.7%

Figure F.1 shows the natural frequencies of the composites as a function of temperature and their change as a function of temperature relative to the initial room temperature natural frequency. This is believed to be related to the transient behavior observed in constrained heating of SMAs illustrated in the initial heating of prestrained and constrained specimens discussed in Chapter 3 and Appendix D. Upon heating, the stress in the NiTi reaches a peak which then decreases during cooling to a value below the initially induced stress. This behavior was not observed in the C-F dynamic tests, further indicating that it is due to the constrained nature of the composite boundary condition for the C-C tests.

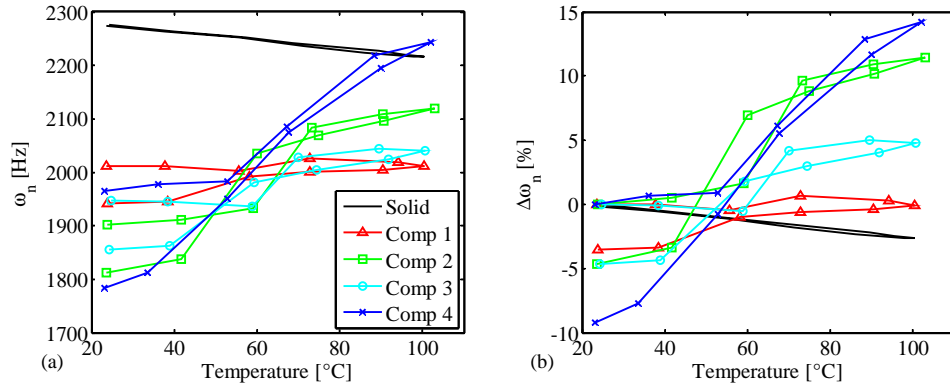


Figure F.1: Comparison of the first heating cycle responses of solid Al and composite 1-4 when subject to the C-C boundary condition: (a) Natural frequency; (b) Relative change in natural frequency.

Appendix G

MAXIMUM FIBER VOLUME FRACTION

G.1 UAM Composite Constraints

When considering long fiber reinforced composites, the practical limit for fiber volume fraction is considered to be approximately 70% [31]. However, the UAM process and ribbon geometry used in this research provide additional constraints upon the maximum theoretical volume fraction. First, the finite thickness of each tape layer provides a restriction on the maximum ribbon thickness; the ribbon cannot be greater than the combined thickness of two matrix tapes, though in practice it is shown that surplus tape thickness of $25.4\ \mu\text{m}$ (0.001 in) on the top and bottom of the embedded fiber can result in tape tearing and build failure as reported in Chapter 3. Second, in addition to the ribbon thickness constraint, tape layer thickness provides discrete heights within the composites at which ribbons can be placed. Third, to avoid matrix material build-up over multiple consolidated layers, ribbons must be spaced in a staggered pattern as shown in Figure G.1. This places a minimum on the lateral spacing of the ribbons equal to their width.

In considering an arbitrary rectangular cross-section composite, width of B and total thickness of H , with rectangular ribbons of width b and thickness t , additional constraints are applied for the analysis of the maximum fiber volume fraction. As seen in Figure G.1, a staggered spacing is used for alternating courses of embedded rectangular ribbons. The number of courses in this analysis, m , is arbitrary but always odd to allow for the largest number of embedded ribbons while the number of ribbons in each course alternates between n and $n - 1$. The spacing between ribbons in the same course is set equal to their width.

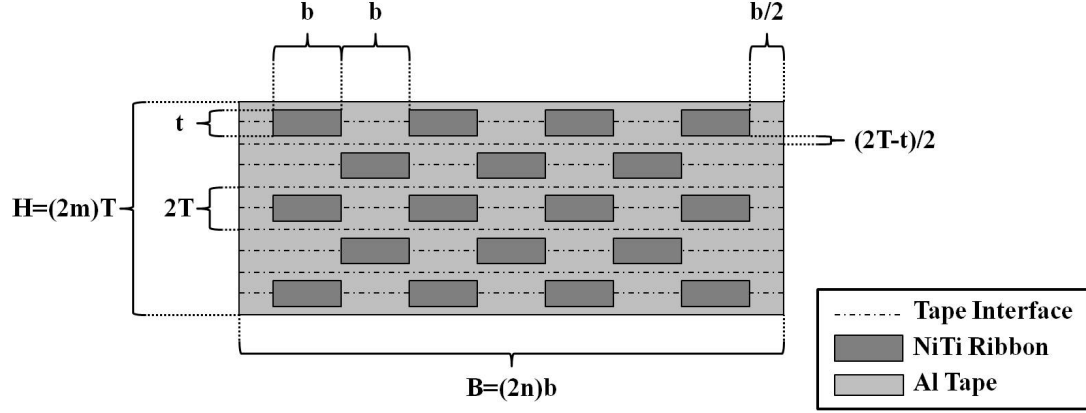


Figure G.1: Cross-section of a hypothetical rectangular ribbon multi-layer UAM composite with 5 courses and a maximum of 4 ribbons per course ($m = 5$, $n = 4$).

Spacing between the first and last ribbons and the edge of the composite for courses with n ribbons is set at $b/2$. Vertical spacing is calculated assuming equal deformation of the top and bottom tapes when embedding ribbons, using dimensions of the embedded ribbons and matrix tapes, with thickness T .

G.2 Volume Fraction Calculations

Volume fraction is calculated using A_{NiTi}/A_{Tot} assuming that the length of the fibers and matrix are equal. From Figure G.1, the total composite thickness is governed by the number of courses and given by

$$H = (2m)T. \quad (G.1)$$

Similarly, the total composite width is governed by the maximum number of ribbons in the courses:

$$B = (2n)b. \quad (G.2)$$

The total number of ribbons in a build with m courses and a maximum number of ribbons per course of n is given by

$$N = \left[\frac{m+1}{2} \right] n + \left[\frac{m-1}{2} \right] (n-1) \quad (G.3)$$

with the NiTi area given by

$$A_{NiTi} = N (bt) , \quad (G.4)$$

total composite area

$$A_{Tot} = BH, \quad (G.5)$$

and NiTi volume fraction given by

$$v = \frac{N (bt)}{BH} = N \frac{bt}{4mnbT} = \frac{N}{mn} \frac{t}{4T} = f(m, n) \frac{t}{4T}, \quad (G.6)$$

where $f(m, n)$ is named the fiber configuration function of the composite.

Expanding the fiber configuration function gives an equation dependent entirely upon m and n :

$$f(m, n) = \frac{N}{mn} = \left[\frac{m+1}{2} \right] \frac{n}{mn} + \left[\frac{m-1}{2} \right] \frac{(n-1)}{mn} = \frac{m(2n-1)+1}{2mn}. \quad (G.7)$$

By taking the derivatives of $f(m, n)$ with respect to m and n , it can be shown that increasing the number of courses, m , results in a decrease in volume fraction while increasing the maximum number of ribbons per course, n , increases the volume fraction:

$$\frac{\partial f(m, n)}{\partial m} = \frac{-1}{2m^2n} \quad (G.8)$$

and

$$\frac{\partial f(m, n)}{\partial n} = \frac{m-1}{2n^2m}. \quad (G.9)$$

From (G.8) and (G.9), it can be seen that the largest value for $f(m, n)$ is obtained when

$m = 1$, yielding $\frac{\partial f(m, n)}{\partial n} = 0$. This indicates that adding more ribbons to a composite

with one course has no effect on the total volume fraction if the previously mentioned array constraints are maintained. This analysis shows that the volume fraction equation, (G.6),

consists of a limiting value, $\frac{t}{4T}$, and the fiber configuration function, $f(m, n)$. The value for $f(m, n)$ can be used as a normalized volume fraction function to investigate the effect of total ribbon courses and number of ribbons per course on the composite volume fraction.

This is shown in Figures G.2 and G.3. As seen in the figures, the maximum volume fractions occur when $m = 1$. For any geometry where $m \neq 1$, increasing n to infinity approaches the limiting case where $m = 1$.

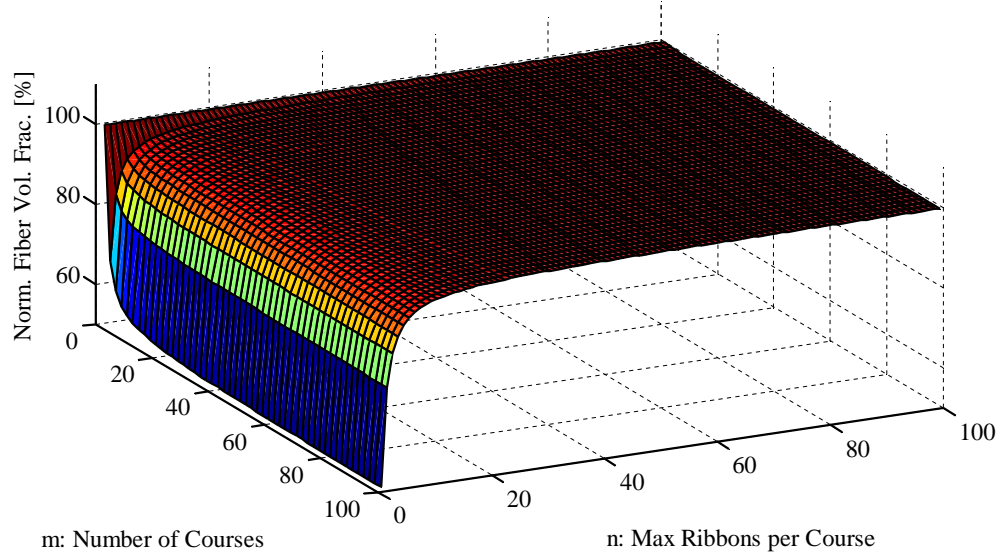


Figure G.2: Surface plot of normalized volume fraction as a function of number of ribbon courses, m , and maximum number of ribbons per course, n .

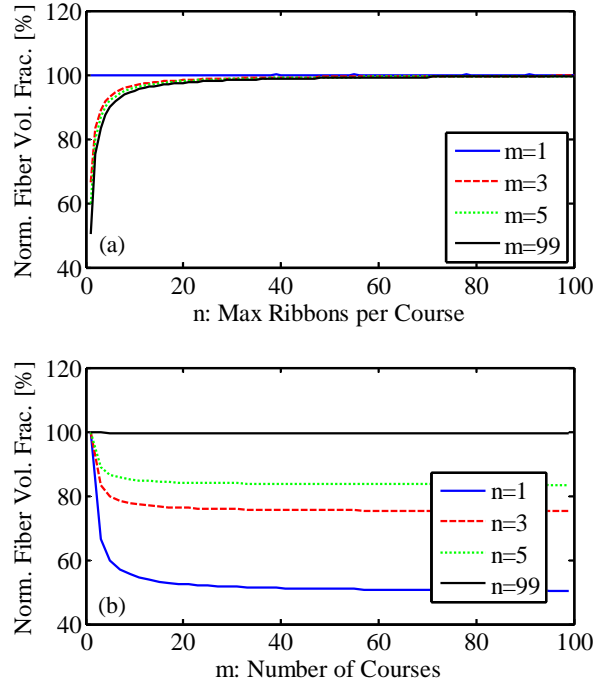


Figure G.3: Normalized volume fraction as a function of (a) maximum number of ribbons per course for prescribed number of courses; (b) number of courses for a prescribed maximum number of maximum ribbons per course.

The limit of fiber volume fraction is dependent upon the thickness of the ribbons and thickness of the matrix tapes used in the UAM process. This analysis is applied to two different NiTi ribbons, the shape memory ribbons discussed in the body of this dissertation and the pseudoelastic ribbons characterized in Appendix D. The geometries used in the analysis is given in Table G.1.

Table G.1: NiTi ribbon and matrix tape dimensions used in the maximum volume fraction analyses.

Parameter	Shape Memory Ribbon	Pseudoelastic Ribbon
t [μm]	254	178
b [μm]	762	356
T [μm]	152	152
$t/(4T)$	41.8%	29.3%

From Table G.1, the limiting volume fraction for composites with the shape memory ribbons is 41.8%. Figures G.4 and G.5 show the relationship between the fiber volume fraction, number of ribbon courses, and maximum number of ribbons per course.

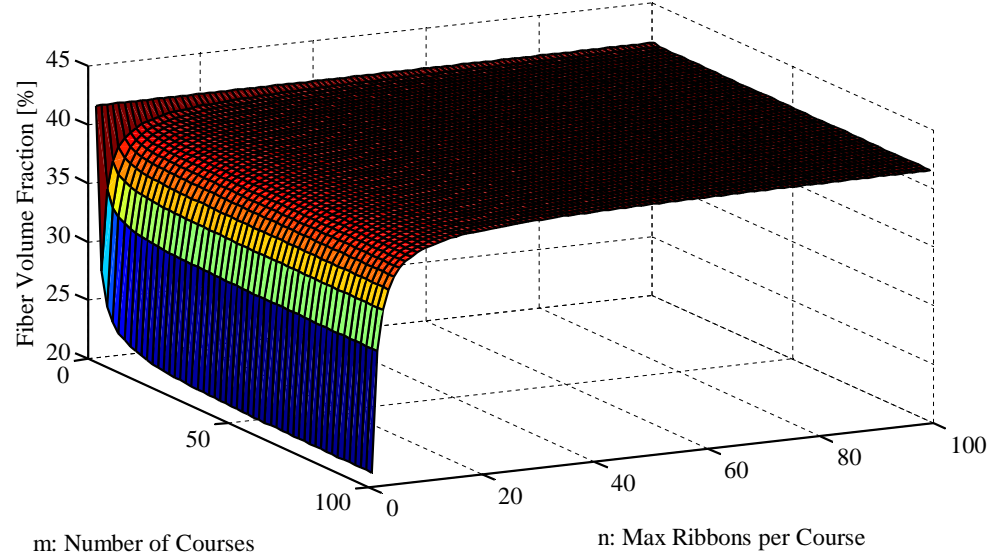


Figure G.4: Surface plot of shape memory NiTi volume fraction as a function of number of ribbon courses, m , and maximum number of ribbons per course, n .

From Table G.1, the limiting volume fraction for composites with the pseudoelastic ribbons is 29.3%. Figures G.6 and G.7 show the relationship between the fiber volume fraction, number of ribbon courses, and maximum number of ribbons per course.

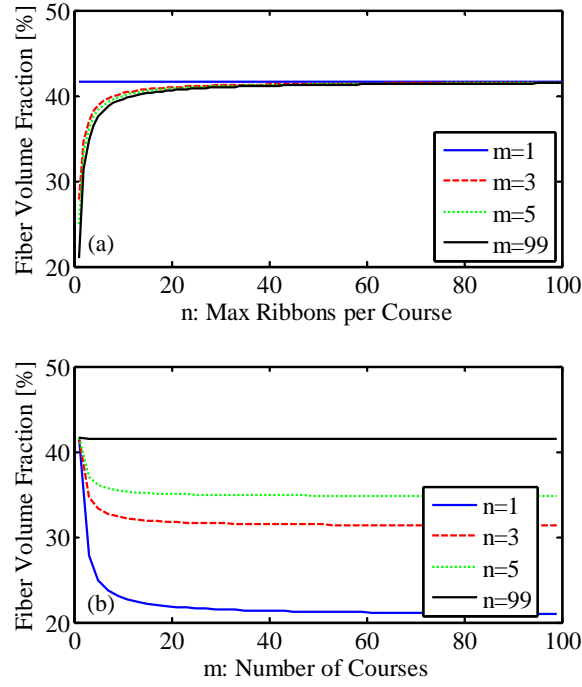


Figure G.5: Volume fraction of shape memory NiTi as a function of (a) maximum number of ribbons per course for prescribed number of courses; (b) number of courses for a prescribed maximum number of maximum ribbons per course.

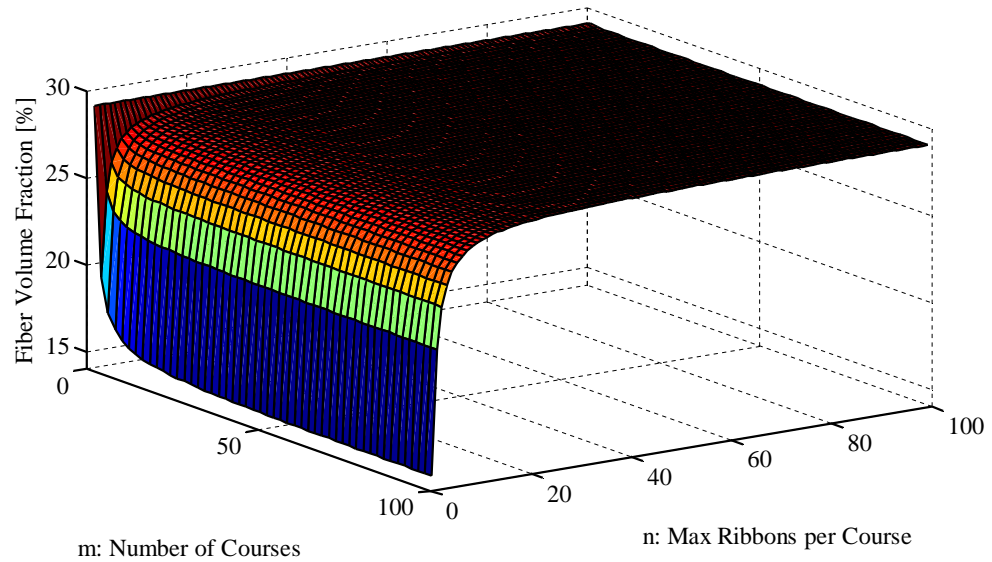


Figure G.6: Surface plot of pseudoelastic NiTi volume fraction as a function of number of ribbon courses, m , and maximum number of ribbons per course, n .

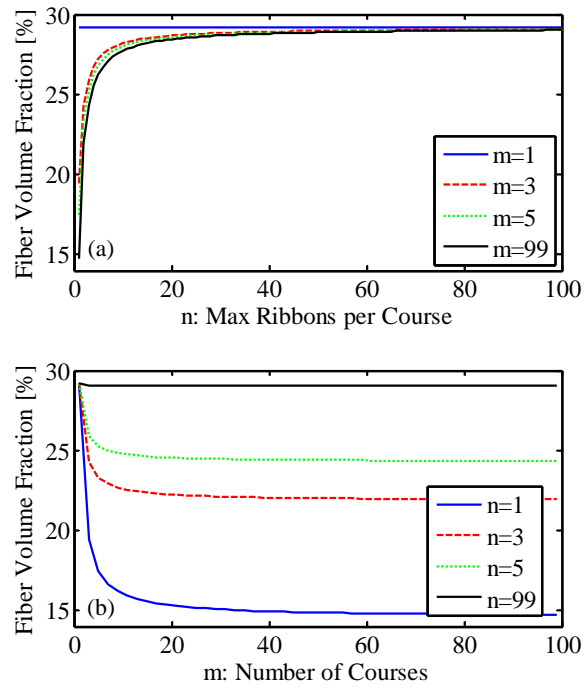


Figure G.7: Volume fraction of pseudoelastic NiTi as a function of (a) maximum number of ribbons per course for prescribed number of courses; (b) number of courses for a prescribed maximum number of maximum ribbons per course.

BIBLIOGRAPHY

- [1] D. F. Adams. *Reference Book for Composites Technology 2*, chapter Properties Characterization – Mechanical/Physical/Hygrothermal Properties Tests Methods, page 64. Technomic Publishing Company, Inc., Lancaster, PA, 1989.
- [2] W. D. Armstrong and H. Kino. Martensitic transformation in a NiTi fiber reinforced 6061 aluminum matrix composite. *Journal of Intelligent Material Systems and Structures*, 6:809–817, 1995.
- [3] W. D. Armstrong and T. Lorentzen. Fiber phase transformation and matrix plastic flow in a room temperature tensile strained NiTi shape memory alloy fiber reinforced 6082 aluminum matrix composite. *Scripta Materialia*, 36(9):1037–1043, 1996.
- [4] J. E. Bidaux, J. A. E. Manson, and R. Gotthardt. Active modification of the vibration frequencies of a polymer beam using shape-memory-alloy fibres. In *Third Conference on Intelligent Materials and Third European Conference on Smart Structures and Materials*, Thrid ICIM/ECSSM, pages 517–522, 1996.
- [5] R. D. Blevins. *Formulas for natural frequency and mode shapes*. Van Nostrand Reinhold Company, 1979.
- [6] J. G. Boyd and D. C. Lagoudas. A thermodynamical constitutive model for shape memory materials. Part I. The monolithic shape memory alloy. *International Journal of Plasticity*, 12(6):805–842, 1996.
- [7] J. G. Boyd and D. C. Lagoudas. A thermodynamical constitutive model for shape

- memory materials. Part II. The SMA composite material. *International Journal of Plasticity*, 12(7):843–873, 1996.
- [8] J. D. Bright and D. K. Shetty. Interfacial bonding and friction in silicon-carbide (filament)-reinforced ceramic and glass-matrix composites. *Journal of the American Ceramic Society*, 72(10):1897–1898, 1989.
- [9] L. Brinson. One dimensional constitutive behavior of shape memory alloys. *Journal of Intelligent Material Systems and Structures*, 4(2):229–242, 1993.
- [10] L. C. Brinson and M. S. Huang. Simplification and comparisons of shape memory alloy constitutive models. *Journal of Intelligent Material Systems and Structures*, 7:108–114, 1996.
- [11] F. C. Campbell. *Structural Composite Materials*, chapter Introduction to Composite Materials, pages 1–29. ASM International, Materials Park, OH, 2010.
- [12] R. B. C Cayless. *ASM Handbook, Volume 2: Properties and Selection: Nonferrous Alloys and Special-Purpose Materials*, chapter Alloy and Temper Designation Systems for Aluminum and Aluminum Alloys, pages 15–28. ASM International, Materials Park, OH, 1990.
- [13] R. Chandra, S. P. Singh, and K. Gupta. Damping studies in fiber-reinforced composites - a review. *Composite Structures*, 49:41–51, 1999.
- [14] C. Cismasiu and F. P. Amarante dos Santos. *Shape Memory Alloys*, chapter 7: Numerical simulation of a semi-active vibration control device based on superelastic shape memory alloy wires, pages 127–154. Sciyo, Rijeka, Croatia, 2010.
- [15] T. Clyne and P. Withers. *An Introduction to Metal Matrix Composites*. Cambridge University Press, Cambridge, UK, 1993.
- [16] M. Colakoglu. Factors effecting internal damping in aluminum. *Journal of Theoretical and Applied Mechanics*, 42(1):95–105, 2004.

- [17] J. A. Collins. *Elastic Instability and Buckling*, chapter 2: The Failure Prevention Perspective, pages 82–85. John Wiley & Sons, Inc., Hoboken, NJ, 2003.
- [18] J. P. Coughlin, J. J. Williams, and N. Chawla. Mechanical behavior of NiTi shape memory alloy reinforced Sn matrix smart composites. *Journal of Material Science*, 44:700–707, 2009.
- [19] E. De Vries. *Mechanics and Mechanisms of Ultrasonic Metal Welding*. PhD thesis, The Ohio State University, Columbus, OH, 2004.
- [20] Dynalloy, Inc. Dynalloy, Inc. FAQ - FLEXINOL Nitinol actuator wire. Website: <http://www.dynalloy.com/FAQ.php>, 2012.
- [21] A. Falvo, F. Furgiuele, and C. Maletta. Laser welding of a NiTi alloy: Mechanical and shape memory behaviour. *Materials Science and Engineering A*, 412:235–240, 2005.
- [22] A. Falvo, F. Furgiuele, and C. Maletta. Functional behaviour of a NiTi-welded joint: Two-way shape memory effect. *Materials Science and Engineering A*, 481-482:647–650, 2008.
- [23] C. M. Friend and C. R. D. Matthey. Active strain-energy tuning of low actuator-fraction shape-memory alloy (SMA) hybrid composites. *Materials Science and Engineering A*, 273-275:799–803, 1999.
- [24] Y. Furuya, A. Sasaki, and M. Taya. Mechanical properties of TiNi shape memory fiber/Al matrix composite. *Materials Transactions*, 34(3):224–227, 1993.
- [25] F. Gori, D. Carnevale, A. D. Atan, S. Nicosia, and E. Pennestri. A new hysteretic behavior in the electrical resistivity of Flexinol memory alloys versus temperature. *International Journal of Thermophysics*, 27(3):866–879, 2006.
- [26] K. Graff. *New Developments in Advanced Welding*, chapter Ultrasonic Metal Welding. Woodhead Publishing Limited, Cambridge, UK, 2005.

- [27] D. J. Hartl and D. C. Lagoudas. *Shape Memory Alloys*, chapter 2: Thermomechanical Characterization of Shape Memory Alloy Materials. Science and Business Media, LLC, New York, NY, 2008.
- [28] C. D. Hopkins. Development and characterization of optimum process parameters for metallic composites made by ultrasonic consolidation. Master’s thesis, The Ohio State University, Columbus, OH, 2010.
- [29] C. D. Hopkins, M. J. Dapino, and S. A. Fernandez. Statistical characterization of ultrasonic additive manufacturing Ti/Al composites. *Journal of Engineering Materials and Technology*, 132(4):041006–1–041006–9, 2010.
- [30] C. D. Hopkins, P. J. Wolcott, M. J. Dapino, A. G. Truong, S. S. Babu, and S. A. Fernandez. Optimizing ultrasonic additive manufactured Al 3003 properties with statistical modeling. *Journal of Engineering Materials and Technology*, 134(1):011004–1–011004–10, 2012.
- [31] D. Hull and T. Clyne. *An Introduction to Composite Materials*. Cambridge University Press, Cambridge, UK, 1996.
- [32] S. J. Hwang and R. F. Gibson. The use of strain energy-based finite element techniques in the analysis of various aspects of damping of composite materials and structures. *Journal of Composite Materials*, 26(17):2585–2605, 1992.
- [33] ASTM International. E8/E8M-11 standard test methods for tension testing of metallic materials, 2009.
- [34] Y. Ivshin and T. J. Pence. A constitutive model for hysteretic phase transition behavior. *International Journal of Engineering Science*, 32(4):681–704, 1994.
- [35] Y. Ivshin and T. J. Pence. A thermomechanical model for a one variant shape memory material. *Journal of Intelligent Material Systems and Structures*, 5:455–7473, 1994.

- [36] Johnson Matthey. Nitinol technical specifications: Transformation, physical, electrical, magnetic and mechanical. Website: <http://jmmedical.com/index.php?p=resources&id=221>, 2012.
- [37] K. D. Jonnalagadda, N. R. Sottos, M. A. Qidwai, and D. C. Lagoudas. Transformation of embedded shape memory alloy ribbons. *Journal of Intelligent Material Systems and Structures*, 9(5):379–390, 1998.
- [38] J. Kaufman, editor. *Properties of Aluminum Alloys: Tensile, Creep, and Fatigue Data at High and Low Temperatures*. The Aluminum Association, Inc. and ASM International, Materials Park, OH, 1999.
- [39] C. Kong and R. Soar. Fabrication of metal-matrix composites and adaptive composites using ultrasonic consolidation process. *Materials Science and Engineering A*, 412:12–18, 2005.
- [40] C. Kong, R. Soar, and P. Dickens. Ultrasonic consolidation for embedding SMA fibres within aluminium matrices. *Composite Structures*, 66:421–427, 2004.
- [41] C. Y. Kong and R. Soar. Method for embedding optical fibers in an aluminum matrix by ultrasonic consolidation. *Applied Optics*, 44(30):6325–6333, 2005.
- [42] D. C. Lagoudas, Z. Bo, and M. A. Qidwai. A unified thermodynamic constitutive model for SMA and finite element analysis of active metal matrix composites. *Mechanics of Composite Materials and Structures*, 3:153–179, 1996.
- [43] F. Lanza di Scalea. Measurement of thermal expansion coefficients of composites using strain gauges. *Experimental Mechanics*, 328(4):233–241, 1998.
- [44] K. Lau. Vibration characteristics of SMA composite beams with different boundary conditions. *Materials & Design*, 23:741–749, 2002.
- [45] K. Lau, L. Zhou, and X. Tao. Control of natural frequencies of a clamped-clamped composite beam with embedded shape memory alloy wires. *Composite Structures*, 58:39–47, 2002.

- [46] W. B. Lee, M. Jie, and C. Y. Tang. Constitutive modeling of aluminum matrix NiTi fiber-reinforced smart composite. *Journal of Materials Processing Technology*, 116:219–223, 2001.
- [47] D. J. Leo. *Engineering Analysis of Smart Material Systems*, chapter Shape Memory Alloys, pages 298–345. John Wiley & Sons, Inc., Hoboken, NJ, 2007.
- [48] Y. Li, L. Cui, Y. Zheng, and D. Yang. DSC study of the reverse martensitic transformation in prestrained TiNi shape memory alloy in different composites. *Materials Letters*, 51:73–77, 2001.
- [49] C. Liang and C. A. Rogers. One-dimensional thermomechanical constitutive relations for shape memory materials. *Journal of Intelligent Material Systems and Structures*, 1:207–234, 1990.
- [50] C. Liang and C. A. Rogers. One-dimensional thermomechanical constitutive relations for shape memory materials. *Journal of Intelligent Material Systems and Structures*, 8:285–302, 1997.
- [51] L. G. Machado and D. C. Lagoudas. *Shape Memory Alloys*, chapter 3: Thermomechanical Constitutive Modeling of SMAs. Science and Business Media, LLC, New York, NY, 2008.
- [52] H. Matsumoto. Electrical resistivity of NiTi with a high transformation temperature. *Journal of Materials Science Letters*, 11:367–368, 1992.
- [53] Memry Corporation. Physical properties of Nitinol. Website: <http://www.memry.com/nitinol-iq/nitinol-fundamentals/physical-properties>, 2012.
- [54] D. A. Miller and D. C. Lagoudas. Influence of cold work and heat treatment on the shape memory effect and plastic strain development of NiTi. *Materials Science & Engineering A*, 308:161–175, 2001.
- [55] K. Mizuuchi. The fabrication and thermomechanical behavior of Al and Ti SMA composites. *JOM*, 52(10):26–31, 2000.

- [56] C. Mou, P. Saffari, D. Li, K. Zhou, L. Zhang, R. Soar, and I. Bennion. Method for embedding optical fibers in an aluminum matrix by ultrasonic consolidation. *Measurement Science and Technology*, 20:1–6, 2009.
- [57] Nitinol Devices & Components. Material data sheet: Nitinol SM495 wire. Website: <http://www.nitinol.com/wp-content/uploads/2012/01/Material-Data-Sheet-Shape-Memory.pdf>, 2009.
- [58] Nitinol Devices & Components. Material data sheet: Superelastic Nitinol alloys. Website: <http://www.nitinol.com/wp-content/uploads/2012/01/Material-Data-Sheet-Superelastic.pdf>, 2012.
- [59] M. Parlinska, J. A. Balta, V. Michaud, J. E. Bidaux, J. A. Manson, and R. Gotthardt. Vibrational response of adaptive composites. In *Journal de Physique IV - Proceedings*, volume 11, pages 129–134, 2001.
- [60] M. Parlinska, H. Clech, J. A. Balta, V. Michaud, J. E. Bidaux, J. A. Manson, and R. Gotthardt. Adaptive composites with embedded shape memory alloys. In *Journal de Physique IV - Proceedings*, volume 11, pages 197–204, 2001.
- [61] A. S. Paula and F. M. Braz Fernandes. Structural and textural evolution during cold work in Ti-rich Ni-Ti shape memory alloy. In *European Symposium on Martensitic Transformations*, ESOMAT 06024, pages 1–6, 2009.
- [62] R. J. Perez, J. Zhang, M. N. Gungor, and E. J. Lavernia. Damping behavior of 6061Al/Gr metal matrix composites. *Metallurgical Transactions A*, 24A:701–712, 1993.
- [63] G. A. Porter, P. K. Liaw, T. N. Tiegs, and K. H. Wu. Fatigue and fracture behavior of nickel-titanium shape memory alloy reinforced aluminum composites. *Materials Science and Engineering A*, 314:186–193, 2001.
- [64] G. D. Janaki Ram, Y. Yang, and B. E. Stucker. Effect of process parameters of

- bond formation during ultrasonic consolidation of aluminum alloy 3003. *Journal of Manufacturing Systems*, 25(3):221–238, 2006.
- [65] S. Rawla. Metal-matrix composites for space applications. *JOM*, 53(4):14–17, 2001.
 - [66] R. A. Schapery. Thermal expansion coefficients of composite materials based on energy principles. *Journal of Composite Materials*, 2(3):380–404, 1968.
 - [67] D. Schick. Characterization of aluminum 3003 ultrasonic additive manufacturing. Master’s thesis, The Ohio State University, Columbus, OH, 2009.
 - [68] D. Schick, S. S. Babu, D. R. Foster, M. Dapino, M. Short, and J. C. Lippold. Transient thermal response in ultrasonic additive manufacturing of aluminum 3003. *Rapid Prototyping Journal*, 15(5):369–379, 2011.
 - [69] D. E. Schick, R. M. Hahnlen, R. Dehoff, P. Collins, S. S. Babu, M. J. Dapino, and J. C. Lippold. Microstructural characterization of bonding interfaces in aluminum 3003 blocks fabricated by ultrasonic additive manufacturing. *Welding Journal*, 89(1):105s–115s, 2010.
 - [70] D. K. Shetty. Shear-lag analysis of fiber push-out (indentation) tests for estimating interfacial friction stress in ceramic-matrix composites. *Communications of the American Ceramic Society*, 71(2):107–109, 1988.
 - [71] A. A. Shirzadi, H. Assadi, and E. R. Wallach. Interface evolution and bond strength when diffusion bonding materials with stable oxide films. *Surface and Interface Analysis*, 431:609–618, 2001.
 - [72] E. Siggard. Investigative research into the structural embedding of electrical and mechanical systems using ultrasonic consolidation. Master’s thesis, Utah State University, Logan, UT, 2007.
 - [73] J. Simpson and C. Boller. Performance of SMA-reinforced composites in an aerodynamic profile. In *Sensors and Smart Structures Technologies for Civil, Mechanical, and Aerospace Systems 2011*, Proc. SPIE 4698, pages 416–426, 2002.

- [74] P. Sittner, V. Michaud, J. A. Malta-Neumann, and J. Schrooten. Modeling and material design of SMA polymer composites. In *Proceedings of International Symposium on Smart Materials*, PRICM4, 2001.
- [75] P. Sittner, V. Michaud, and J. Schrooten. Modeling and material design of SMA polymer composites. *Materials Transactions*, 43(5):984–993, 2002.
- [76] P. Sittner and R. Stalmans. Developing hybrid polymer composites with embedded shape-memory alloy wires. *JOM*, 52(10):15–20, 2000.
- [77] P. Sittner, R. Stalmans, and M. Tokuda. An algorithm for prediction of the hysteretic responses of shape memory alloys. *Smart Materials and Structures*, 9(4):452–465, 2000.
- [78] P. Sittner, D. Vokoun, G. N. Dayananda, and R. Stalmans. Recovery stress generation in shape memory $\text{Ti}_{50}\text{Ni}_{45}\text{Cu}_5$ thin wires. *Materials Science and Engineering A*, 286:298–311, 2000.
- [79] G. Staab. *Laminar Composites*. Butterworth-Heinemann, Boston, MA, 1999.
- [80] K. Tanaka and R. Iwasaki. A phenomenological theory of transformation superplasticity. *Engineering Fracture Mechanics*, 21(4):709 – 720, 1985.
- [81] K. Tanaka, S. Kobayashi, and Y. Sato. Thermomechanics of transformation pseudoelasticity and shape memory effect in alloys. *International Journal of Plasticity*, 2(1):59 – 72, 1986.
- [82] A. D. Truog. Bond improvement of Al/Cu joints created by very high power ultrasonic additive manufacturing. Master’s thesis, The Ohio State University, Columbus, OH, 2012.
- [83] K. A. Tsoi, J. Schrooten, Y. Zheng, and R. Stalmans. Part I. Thermomechanical characteristics of shape memory alloys. *Materials Science and Engineering A*, 368:286–298, 2004.

- [84] K. A. Tsoi, J. Schrooten, Y. Zheng, and R. Stalmans. Part II. Thermomechanical characteristics of shape memory alloy composites. *Materials Science and Engineering A*, 368:299–310, 2004.
- [85] K. A. Tsoi, R. Stalmans, and J. Schrooten. Transformational behavior of constrained shape memory alloys. *Acta Materialia*, 50:3535–3544, 2002.
- [86] J. Uchil, K. K. Mahesh, and K. G. Kumara. Electrical resistivity and strain recovery studies on the effect of thermal cycling under constant stress on R-phase in NiTi shape memory alloys. *Physica B*, 324:419–428, 2002.
- [87] K. K. Umashankar, A. Abhinav, K. V. Gangadharan, and D. Vijay. Damping behaviour of cast and sintered aluminum. *ARPJ Journal of Engineering and Applied Sciences*, 4(6):66–71, 2009.
- [88] Vishay Precision Group. Document number 11071: 031CF General Purpose Strain Gages - Linear Pattern. Website: <http://www.vishaypg.com/docs/11071/031cf.pdf>, 2010.
- [89] Vishay Precision Group. Document number 11506: Gage Series - Stress Analysis Gages Technical Data. Website: <http://www.vishaypg.com/docs/11506/gageser.pdf>, 2010.
- [90] Vishay Precision Group. Tech Note TN-513-1: Measurement of thermal expansion coefficient using strain gages. Website: <http://www.vishaypg.com/docs/11063/tn5131tn.pdf>, 2010.
- [91] Vishay Precision Group. Tech Note TN-515: Strain gage rosettes: Selection, application and data reduction. Website: <http://www.vishaypg.com/docs/11065/tn-515.pdf>, 2010.
- [92] D. Vokoun, V. Kafka, and C.T. Hu. Recovery stresses generated by NiTi shape memory wires under different constrain conditions. *Smart Materials and Structures*, 12:680–685, 2003.

- [93] G. Wang. Welding of Nitinol to stainless steel. In *Proceedings of the International Conference on Shape Memory and Super Elastic Technologies*, pages 131–136, 1997.
- [94] Z. G. Wei, R. Sandstrom, and S. Miyazaki. Shape memory materials and hybrid composites for smart systems: Part II Shape-memory hybrid composites. *Journal of Materials Science*, 33:3763 – 3783, 1998.
- [95] Z. G. Wei, C. Y. Tang, W. B. Lee, L. S. Cui, and D. Z. Yang. Preparation of a smart composite material with TiNiCu shape memory particulates in an aluminium matrix. *Materials Letters*, 32:313–317, 1997.
- [96] M. Wu. Fabrication of Nitinol materials and components. In *Proceedings of the International Conference on Shape Memory and Superelastic Technologies*, pages 258–292, 2001.
- [97] X. D. Wu, J. S. Wu, and Z. Wang. The variation of electrical resistance of near stoichiometric NiTi during thermo-mechanic procedures. *Smart Materials and Structures*, 8:574–578, 1999.
- [98] Y. Yang, G. D. Janaki Ram, and B. E. Stucker. Enhanced diffusion and phase transformation during ultrasonic welding of zinc and aluminum. *Scripta Materialia*, 52:939–943, 2005.
- [99] Y. Yang, G. D. Janaki Ram, and B. E. Stucker. Bond formation and fiber embedment during ultrasonic consolidation. *Journal of Material Processing Technology*, 209:4915–4924, 2009.
- [100] Y. Yang, B. E. Stucker, and G. D. Janaki Ram. Mechanical properties and microstructures of SiC fiber-reinforced metal matrix composites made using ultrasonic consolidation. *Journal of Composite Materials*, 44(26):3179–3194, 2010.
- [101] J. Ye and A. K. Kaw. Determination of mechanical properties of fiber-matrix interface from pushout test. *Theoretical and applied fracture mechanics*, 32:15–25, 1999.

- [102] A. J. Zak, M. P. Cartmell, W. M. Ostachowicz, and M Wiercigroch. One-dimensional shape memory alloy models for use with reinforced composite structures. *Smart Materials and Structures*, 12:338–346, 2003.
- [103] C. Zhang and L. Li. A coupled thermal-mechanical analysis of ultrasonic bonding mechanism. *Metallurgical and Materials Transactions B*, 40B:196–207, 2009.
- [104] Y. J. Zheng, L. S. Cui, and J. Schrooten. Basic design guidelines for SMA/epoxy smart composites. *Materials Science and Engineering A*, 390:139–143, 2005.
- [105] Y. J. Zheng, J. Schrooten, K. A. Tsoi, and P. Sittner. Qualitative and quantitative evaluation of the interface in activated shape memory alloy composites. *Experimental Mechanics*, 43(2):194–200, 2003.
- [106] Y. J. Zheng, J. Schrooten, K. A. Tsoi, and R. Stalmans. Thermal response of glass fiber/epoxy composites with embedded TiNiCu alloy wires. *Materials Science and Engineering A*, 335:157–163, 2002.
- [107] J. Zurbitu, S. Kustov, A. Zabalet, E. Cesari, and J. Aurrekoetxea. *Shape Memory Alloys*, chapter 2: Thermo-mechanical behaviour of NiTi at impact, pages 17–39. Sciyo, Rijeka, Croatia, 2010.